Co-firing of Alternative Fuels in Cement Kiln Burners

Pedersen, Morten Nedergaard

Publication date:
2018

Document Version
Publisher's PDF, also known as Version of record

DTU Chemical Engineering
Department of Chemical and Biochemical Engineering

Co-Firing of Alternative Fuels in Cement Kiln Burners

Morten Nedergaard Pedersen

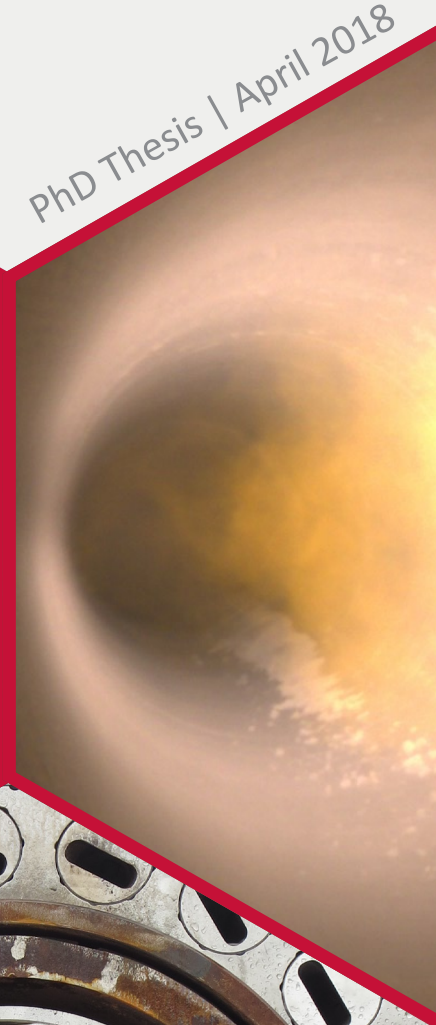

PhD Thesis | April 2018

DTU

Co-Firing of Alternative Fuels in Cement Kiln Burners

PhD Thesis

by

Morten Nedergaard Pedersen

Supervisors:

Kim Dam-Johansen, Technical University of Denmark

Peter Arendt Jensen, Technical University of Denmark

Sønnik Clausen, Technical University of Denmark

Lars Skaarup Jensen, FLSmidth A/S

Technical University of Denmark

Department of Chemical and Biochemical Engineering

CHEC Research Center

30th of April 2018

ABSTRACT

The production of cement is an energy intensive process, where, traditionally, 30 % of operating costs have been related to fuels. By increasing the use of alternative fuels in the industry, the operating costs can be significantly decreased. In addition, use of refuse derived fuels may limit the need for landfilling, and partly biogenic fuels can reduce CO_2 emissions from the industry. The utilization of alternative fuels in the cement rotary kiln appears to be mostly based on a trial and error approach. Fairly little systematic knowledge of the impact that these fuels have on flame behavior and cement clinker quality is available in the literature. This thesis attempts to give an increased fundamental understanding of these impacts. This is done through a literature survey highlighting the known challenges of alternative fuels firing, experimental studies conducted at full scale cement plants investigating the effect of cofiring on the kiln flame, and laboratory characterization of alternative fuels. Furthermore, a model is developed to describe the combustion in the cement kiln.

Alternative fuels for the cement industry can be both solid and liquid. Some of the most widely used are shredded tires, meat and bone meal, and solid recovered fuel (SRF). SRF is a fuel derived from the mechanical treatment of non-hazardous municipal or industrial waste. Compared to fossil fuels, most alternative fuels have a larger particle size, higher volatile and moisture contents, and a lower heating value. This makes their use in cement kilns challenging, as burnout takes longer, and flame temperatures are reduced. An increased understanding of these issues, and how to overcome them, are necessary to further increase the utilization of alternative fuels in cement kilns.

An experimental study was carried out at three different cement plants. The kiln flames were observed with a specially developed camera, which can be inserted in the kiln hood close to the burner and allows for detailed imaging of fuel and flame behavior. The difference between fossil fired flames and flames cofired with alternative fuels were studied. It was found that addition of alternative fuel to the flame would delay ignition by 1-2 meters and lower flame temperatures. At one plant the burner was changed. The design of the axial air injection was changed from an annular nozzle to multiple jet nozzles. The new burner decreased the ignition

length of the flame and increased the dispersion of alternative fuel in the kiln, which led to a higher clinker quality.

Additional measurements of the new burner were performed to study the impact of burner settings. Swirl air level and direction of the axial air, were found to impact the ignition of a petcoke flame. The air could also be used to disperse the SRF into the secondary air stream to aid ignition and burnout. The burner settings were linked to the cement clinker quality by means of a statistical analysis tool (Partial Least Squares Regression), which showed that the increased dispersion of SRF would increase the alite content of the clinker, indicating a higher quality.

SRF from two of the test plants and an additional plant was collected for fuel characterization. The fuels were classified using a wind sieve setup, which showed a distinction between light fuels used in the kiln and heavier fuels used in the calciner. A characterization of fuel composition, particle size distribution, and shape was made on two SRF samples. This resulted in a simplified description of the fuel that can be implemented in computational models.

A one-dimensional model was developed for the rotary kiln. The model describes and links together the fuel combustion, gas mixing, heat transfer, and clinker chemistry. The model calculates temperatures in the gas phase and clinker bed through the kiln and the clinker composition is given as output. Thus, the impacts of co-firing different alternative fuels can be studied. It is also possible to explore methods to reduce the negative effects of co-firing.

The model was used to study the influence of SRF co-firing in the kiln. It was found that increased shares of SRF, reduced flame and bed temperatures, which caused an increased free lime content in the clinker, indicating a decrease in clinker quality. These effects could to some extent be avoided by increasing the energy input to the kiln. An increased dispersion of SRF near the burner was also found to be beneficial, confirming the conclusions from the industrial tests.

RESUMÉ (ABSTRACT IN DANISH)

Produktionen af cement er en energiintensiv proces, hvor omkring 30 % af de løbende omkostninger traditionelt set er gået til brændsler. Disse omkostninger kan dog sænkes ved at øge brugen af alternative brændsler i cementindustrien. Derudover kan anvendelsen af affaldsbrændsler nedbringe nødvendigheden af lossepladser, og delvist organiske brændsler kan sænke industriens udledning af CO_2. Brugen af alternative brændsler i cement-roterovne beror mest på tidligere forsøg udført på de enkelte fabrikker. Systematisk viden omkring, hvordan disse brændsler påvirker flammen og cementkvaliteten, mangler i litteraturen. Denne afhandling forsøger at øge den fundamentale viden på dette område. Dette gøres ved at gennemgå litteraturen og belyse de kendte udfordringer ved at anvende alternative brændsler. Eksperimentelle studier udføres på storskala cementfabrikker, hvor den samfyrede flamme undersøges, og en karakterisering af alternative brændsler foretages i laboratoriet. Derudover udvikles en model til at beskrive forbrændingen i cementovnen.

De alternative brændsler, som bruges i cementindustrien, kan være både faste og flydende. De mest udbredte brændsler er opskårne dæk, kød- og benmel, samt fast affaldsbrændsel (Solid Recovered Fuel – SRF). SRF fremstilles ved en mekanisk behandling af ikke-giftigt husholdnings- eller industriaffald. Sammenlignet med faste fossile brændsler har de fleste typer af alternative brændsler en større partikelstørrelse, højere indhold af flygtige stoffer og fugt, samt en mindre brændværdi. Dette gør anvendelsen af alternative brændsler i cementovne udfordrende, da udbrændingstiden øges, og flammetemperaturen sænkes. En øget forståelse af disse begrænsninger og hvordan de kan overkommes, er nødvendig for yderligere at øge anvendelsen af alternative brændsler i cementovne.

Et eksperimentelt studie blev udført på tre forskellige cementanlæg. Flammerne i cementovnene blev observeret vha. et specialfremstillet kamera, som kan indføres igennem en inspektionslem i køleren og indsættes tæt på brænderen, hvilket muliggør detaljerede observationer af flammen og brændslets opførsel. Forskellen på flammer fyret med fossile og alternative brændsler blev undersøgt. Det blev konkluderet at brugen af alternative brændsler ville forskyde antændelsespunktet 1-2 meter og sænke flammetemperaturen. På et af anlæggene blev der foretaget en

udskiftning af brænderen. Designet blev ændret fra en brænder, hvor aksialluften indføres gennem en ringformet luftdysse, til flere stråledysser (jets). Den nye brænder sænkede antændingslængden af flammen og øgede spredningen af alternativt brændsel i ovnen, hvilket øgede cementklinker-kvaliteten.

Yderligere målinger på den nye brænder blev foretaget for at undersøge indflydelsen af brænderens indstillinger. Niveauet af swirl-luft (roterende) og retning af aksialluften kan påvirke antændingen af en petroleumkoks-flamme (petcoke). Luften kan også bruges til at sprede SRF ud i sekundærluften, hvilket gavner antændingen og udbrændingen. Brænderindstillingerne blev koblet til cementkvaliteten vha. en statistisk analyse (Partial Least Squares Regression), som viste, at den øgede spredning af SRF forhøjede indholdet af alit i klinkeren, hvilket indikerer en bedre cementkvalitet.

SRF fra to af testanlæggene, samt et andet anlæg, blev indsamlet for at foretage en brændselskarakterisering. Brændslerne blev klassificeret i en vindsigte, hvilket viste en klar forskel på lette brændsler, som bruges i cementovnen, og tungere brændsler, som bruges i calcinatoren. En yderligere karakterisering af to brændselsprøver blev foretaget for at bestemme størrelsesfordelingen og formen af partikler samt sammensætningen af brændslet. Dette arbejde resulterede i nogle simplificerende beskrivelser af brændslet, som kan implementeres i beregningsmodeller.

En endimensionel model blev udviklet for cementovnen. Modellen beskriver og sammenkæder forbrændingen, luftopblandingen, og klinkerkemien i ovnen. Modellen kan benyttes til at udregne temperaturprofiler i gasfasen og klinkerlejet gennem ovnen, hvorved klinkersammensætningen gives som output. Dermed kan effekten af samfyring med forskellige alternative brændsler evalueres. Det er også muligt at undersøge tiltag til at mindske den negative effekt af samfyring.

Modellen blev brugt til at undersøge indflydelsen af SRF-samfyring i cementovnen. Det blev konkluderet, at en øget andel af SRF sænkede gassens og klinkerlejets temperaturer, hvilket førte til en øget mængde fri kalk i klinkeren, som indikerer an lavere klinkerkvalitet. Ved at øge energiinputtet, kunne denne effekt dog delvist undgås. En øget spredning af SRF tæt på brænderen havde også en gavnlig effekt på indholdet af fri kalk, hvilket underbygger konklusionerne fra de industrielle undersøgelser.

PREFACE

This PhD project was carried out at the Combustion and Harmful Emissions Control (CHEC) Research Center of the Department of Chemical and Biochemical Engineering at the Technical University of Denmark (DTU). The project is part of the "Minerals and Cement Technology – MiCeTech" platform, which has been funded by the Innovation Fund Denmark, FLSmidth A/S, Hempel, and the Technical University of Denmark.

The supervisors for the project were professor Kim Dam-Johansen, senior researcher Peter Arendt Jensen, senior researcher Sønnik Clausen, and project manager Lars Skaarup Jensen (FLSmidth). I would like to thank them all for their help and guidance during this project.

The video probes used for the flame investigations were designed by Sønnik Clausen and manufactured by Jens Henry Poulsen of the workshop at the department. Their help in this has been vital and is much appreciated.

Mads Nielsen of FLSmidth has been a great travel buddy at our frequent visits to cement plants for measurements. He has been a key part of managing most of the industrial tests, for which I am very grateful.

I am also thankful to my colleagues at FLSmidth who have participated in the industrial tests, Christian Andersen, Morten Gabel, and Igor Pipiska. Furthermore, I appreciate the help provided by personnel at the cement plants during tests.

David Jayanth Isaac of FLSmidth has made the CFD simulations used in this project, for which I am also very grateful.

I would also like to thank Mohammadhadi Nakhaei for the collaboration and discussions on characterization of alternative fuels and their combustion.

Furthermore, I much appreciate the work done by students Patrick Pedersen, Casper Svith, Imran Khan, and Akhilesh Nair, who have been involved in the project.

Morten Nedergaard Pedersen

April 2018

CONTENTS

LIST OF FIGURES

LIST OF TABLES

ABBREVIATIONS

Abbreviation	Explanation
AF	Alternative Fuel
AR	Alumina Ratio
ASR	Alkali Sulfate Ratio
a.r.	As Received
CCAI	Calculated Carbon Aromaticity Index
CFD	Computational Fluid Dynamics
CIS	Commonwealth of Independent States
EC	Experimental Condition
ERZ	External Recirculation Zone
HC	HydroCarbon
HD	HotDisc
ID Fan	Induced Draft Fan
IFRF	International Flame Research Foundation
IRZ	Internal Recirculation Zone
LHV	Lower Heating Value
LSF	Lime Saturation Factor
MB	Main Burner
MBM	Meat and Bone Meal
MSEP	Mean Square Error of Prediction
MSW	Municipal Solid Waste
NIR	Near Infrared
PLSR	Partial Least Squares Regression
RDF	Refuse Derived Fuel
RMSE	Root Mean Square Error
RPM	Revolutions Per Minute
PC	PetCoke
SHW	Solid Hazardous Waste
SR	Silica Ratio
SRF	Solid Recovered Fuel
SS	Sewage Sludge
TGA	ThermoGravimetric Analysis
VDZ	Verein Deutscher Zementwerke (German Cement Works Association)
WBCSD	World Business Council for Sustainable Development
WSGG	Weighted Sum of Grey Gasses
XRD	X-Ray Diffraction
XRF	X-Ray Fluorescence

NOMENCLATURE

Roman	Explanation	Unit
A	Preexponential factor in Arrhenius expression	Unit dependent on order of reaction
A	Area	m^2
a	Weighting factor in WSGG model	-
Bi	Biot number	-
B_p	Secondary air requirement for stoichiometric fuel combustion	kg/kg fuel
$B_{p,exc}$	Excess air ratio for the secondary air	kg/kg secondary air
B_{PLSR}	Regression coefficients in PLSR model	-
C	Concentration	mol/m^3
C_{125}	Content of calcite particles larger than 125 µm	-
C_D	Drag coefficient	-
Cm_{RR}	Cumulative mass in Rosin Rammler distribution	wt%
Cp	Heat capacity	J/(kg*K)
Ct	Craya-Curtet parameter	-
D	Diffusion coefficient	m^2/s
d	Diameter	m
d_e	Equivalent diameter	m
d_{RR}	Characteristic dimeter in Rosin Rammler distribution	m
E	Energy	J
Ea	Activation energy in Arrhenius expression	J/mol
F	Force	N
Fr	Rotational Froude Number	-
Gr	Grashof Number	-
G_{opt}	Optimum burner momentum	N
G_X	Axial thrust	N
G_Y	Flux of angular momentum	N·m
g	Gravitational acceleration	m/s^2
H	Kiln bed height	m
H	Enthalpy	J/kg or J/mol
H_{cooler}	Clinker cooler heat transfer coefficient	W/(m K)
ΔH	Heat of reaction	J/kg
h	Heat transfer coefficient	$J/(s*m^2*K)$
I	Burner momentum	N
I’	Burner momentum normalized by burner power	N/MW
K	Parameter/constant in equation	-
k	Reaction rate constant	Unit dependent on order of reaction
L	Length	m
L_C	Chord of the sector covered by bed	m
l	Length or thickness	m
$l_{f,drop}$	Landing spot of fuel in the kiln	m
$l_{f,drop2}$	Spread on fuel landing spot	m

Roman	Explanation	Unit
l_m	Total path length for radiation	m
M	Molar mass	kg/mol
M_{SO3}	Sulfur Modulus	-
m	Mass	kg
$\dot{m}$	Mass flow rate	kg/s
m_{RR}	Characteristic mass in Rosin Rammler distribution	kg
N	Number	-
n	Kiln Rotational speed	1/s
$\dot{n}$	Mole flow rate	mol/s
n_{RR}	Spread parameter in the Rosin Rammler distribution	-
P	Power	W
Pr	Prandtl number	Pr
p	Pressure	Pa
Q	Heat flow	J/s
Q_{44}	Content of quarts particles larger than 44 µm	-
q	Heat flux	J/(m² s)
R	Reaction rate on mass basis	kg/(m³ s)
R'	Reaction rate on molar basis	mol/(m³ s)
Re	Reynolds number	-
Re_ω	Rotational Reynolds number	-
R_{gas}	Ideal gas constant	J/(mol K)
r	Radius	m
S	Swirl number	-
Sc	Schmidt number	-
Sh	Sherwood number	-
T	Temperature	K
T_q	Torque of kiln rotation	N·m
t	Time	s
t_p	Particle thickness	m
u	(Axial) Velocity	m/s
u_d	Dynamic mean velocity	m/s
u_k	Kinematic mean velocity	m/s
V	Volume	m³
V_{diff}	Diffusion volume	cm³/mol
v	Velocity	m/s
w	Tangential Velocity	m/s
X	Conversion	-
X_{PLSR}	Matrix of predictor variables in PLSR model	-
x	Axial distance	m
Y	Mass fraction	-
Y_{PLSR}	Matrix of response variables in PLSR model	-
$\hat{Y}_{PLSR}$	Predicted values of Y_{PLSR}	-
y	Molar fraction	-

Greek	Explanation	Unit
α	Absorption of radiation	-
γ	Ratio of specific heats	-
Δ	Change	-
δ_{ij}	Kronecker delta	-
ε	Emissivity of radiation	-
ε/k	Turbulent dissipation rate	1/s
η	Fraction of solid fill in kiln	-
θ	Angle subtended by solids at kiln centre	Radians
κ	Absorption coefficient in WSGG model	1/m or bar/m
λ	Thermal conductivity	J/(s*m*K)
μ	Dynamic viscosity	kg/(s*m)
ν	Kinematic viscosity	m^2/s
ξ	Bed angle of repose	Radians
ρ	Density	kg/m^3
σ	Stefan Boltzmann constant	$J/(s*m^2*K^4)$
$\sigma_{f,drop}$	Standard deviation on fuel landing spot	m
τ	Transmissivity for radiation	-
ϕ	Stoichiometry for reaction (mol based)	mol O_2/mol fuel
ϕ_m	Stoichiometry for reaction (mass based)	kg O_2/kg fuel
φ	Sphericity	-
ψ	Kiln slope	Radians
Ω	View factor for radiation	-
ω	Rotational speed	Radians /s

Subscript	Explanation
0	Initial
amb	Ambient
app	Approximate
b	Bed
bu	Bulk
char	Char
char,gsc	Char gasification
char,ox	Char oxidation
coat	Coating
cond	Conduction
conv	Convection
devol	Devolatilization
dry	Drying
edr	Eddy Dissipation Rate
ent	Entrainment
ex	Exit
exc	Excess
ext	External
f	Fuel
film	Film layer
fl	Flame
g	Gas
ht	Heat Transfer
i	Index
j	Index
k	Kiln
max	Maximum
n	Nozzle
o	Outer
p	Particle
prim	Primary air
RR	Rosin Rammler
r	Reaction
rad	Radiation
req	Requirement
res	Residence
s	Surface
sec	Secondary air
sh	Shell
vol	Volatiles
w	Wall
x	Axial direction
y	Vertical direction

1 INTRODUCTION

Concrete is the most utilized manmade material, with an annual production exceeding 1 m^3 per person worldwide. The success of concrete stems from its relatively low cost, low energy consumption, and the fact that it can be made from materials most abundant in the crust of the Earth [1]. Without reinforced concrete it would not have been possible to build modern landmarks such as the Burj Khalifa (Dubai) [2] or the Three Gorges Dam (China) [3]. Concrete consists of sand and gravel as aggregate particles that are held together by a binder, the cement. In some cases, steel can be added as reinforcement to further strengthen the concrete. 2000 years ago, the Romans used volcanic ash as the binder to build structures like the Pantheon, which still stands today [4,5]. Today, the main type of cement is Portland cement, which mainly consists of di- and tricalcium silicates. When the Portland cement is mixed with water it hydrates and hardens to bind together the stone and gravel in the concrete [6].

The extensive use of Portland cement clinker is, however, not without issues. The global cement production in 2017 amounted to 4.1 billion tons [7] and the cement industry is responsible for around 5 % of the worlds CO_2 emissions [8]. Furthermore, the manufacture of cement is highly energy intensive with the global average thermal energy usage being around 4.2 GJ/ton clinker, while the most efficient plants use 2.9 GJ/ton clinker [9]. This results in high costs related to fuels, which conventionally makes up for 30-40 % of the cement production cost [10].

Thus, there is a clear cost driver for the cement manufacturers to utilize cheap alternative fuels. However, alternative fuels also need to be readily available for the cement manufacturer and the legislation needs to be supportive. This is e.g. possible in the European Union where the landfilling of unprocessed waste has been banned, and a number of treatment plants upgrade the waste so it can be used as an alternative fuel in the cement industry [11]. Thus, the use of alternative fuels in the cement industry can also serve as a waste management option to reduce landfill and conserve fossil fuels. The increased use of alternative fuels and the reduction of fossil fuels may also contribute to reducing the CO_2 emissions from the industry [12].

1.1 Scope of Thesis

The objective of the work carried out in this PhD project is to gain increased systematic and scientific knowledge on the combustion of alternative fuels in the cement rotary kiln. With this knowledge, it will be possible to propose guidelines for the increased use of alternative fuels in the cement industry. The primary focus of this project was on the following two areas:

Large Scale Measurements

In connection with the development and commissioning of the FLSmidth Jetflex burner, several measurement campaigns were carried out at three different industrial scale cement plants.

The main aim of the measurements has been to get a better understanding of how the cement kiln flame is influenced by co-firing with alternative fuels, and how the co-fired flame can be optimized to give the best cement clinker quality.

Cement Kiln Modeling

In order to better understand the effect that alternative fuels have on the cement kiln process, it is desired to model the impact. In this way, the effect of the properties of alternative fuels, such as heating value, moisture content, and particle size, can be evaluated directly, through a simplified kiln and combustion model.

1.2 Outline of Thesis

The thesis is divided into three parts consisting of a literature survey (chapters 2-4), an experimental section (chapters 5-7), and a modeling section (chapters 8-9).

Chapter 2 will give a short introduction to the cement making process and an in-depth description of kiln burners. In chapter 3, a description of fuels used in the cement kiln is given, with a special focus on some of the challenges in utilizing alternative fuels. Typical measurements obtained at a cement plant to gauge the state of the process is covered in chapter 4.

The experimental section is covered in chapters 5-7. Chapter 5 and 6 covers the industrial tests, which investigates the effect of co-firing on the kiln flame using a specially developed kiln camera. Chapter 7 deals with a detailed characterization of SRF to obtain input parameters to combustion modeling.

Chapters 8 and 9 covers the model work. Chapter 8 begins with a review of the models for the rotary kiln found in the literature. This is followed by a review of the different mechanisms, e.g. heat transfer and combustion, occurring in the kiln. The knowledge is used to formulate mathematical models valid for the kiln. Chapter 9 contains model validation and results of the modeling work.

The final conclusions of the project are found in chapter 10.

1.3 Publications

During this PhD project the following journal article has been published:

M. N. Pedersen, M. Nielsen, S. Clausen, P. A. Jensen, L. S. Jensen, and K. Dam-Johansen, "Imaging of Flames in Cement Kilns To Study the Influence of Different Fuel Types," *Energy & Fuels*, vol. 31, no. 10, pp. 11424–11438, 2017.

Significant contributions (second author) have been made to the following conference article:

D. J. Isaac, M. N. Pedersen, D. Grévain, L. S. Jensen, and M. Nielsen, "Numerical Evaluation of Co-Firing Solid Recovered Fuel With Petroleum Coke in a Cement Rotary Kiln - A Case Example," in *Proceedings of The 12th International Conference on Computational Fluid Dynamics in the Oil & Gas, Metallurgical and Process Industries*, 2017, pp. 613–620.

In addition, the following manuscript has been submitted to the journal Energy and Fuels (second author):

M. Nakhaei, M.N. Pedersen, H. Wu, D. Grevain, L.S. Jensen, P. Glarborg, P.A. Jensen, K. Dam-Johansen, "Aerodynamic and Physical Characterization of Refuse Derived Fuel," *Energy and Fuels (Manuscript)*.

2 CEMENT PRODUCTION AND CHEMISTRY

The following chapter aims to give an overview of the basic principles of cement manufacturing. The primary focus will be on understanding the processes in the cement kiln and the impact of the kiln burner.

2.1 Production of Portland Cement

Ordinary Portland Cement (Type 1 Portland Cement in the USA) is the most common type of cement manufactured today and will be the focus of this chapter. Portland Cement can be used directly as is, or mixed with different additives, e.g. slag or fly ash, to form composite cements with various properties [11]. Other types of cement include rapid-hardening cement, manufactured with an increased alite content or finer grinding, sulfate resistant cement with lower aluminate content, and white cement, which have a reduced content of ferrite and is produced under reducing conditions [13].

The main raw materials used for cement production are naturally occurring limestone, shale, and sand, which are sources of $CaCO_3$, SiO_2, Fe_2O_3, and Al_2O_3.The materials are normally mined in a quarry, which should ideally be placed close to the cement factory, to reduce transportation costs. Raw materials that are relatively dry are usually preferred since removing excess water requires large amounts of energy [4]. Figure 2-1 provides an overview of the different processes in the cement plant after the raw materials have been mined and crushed.

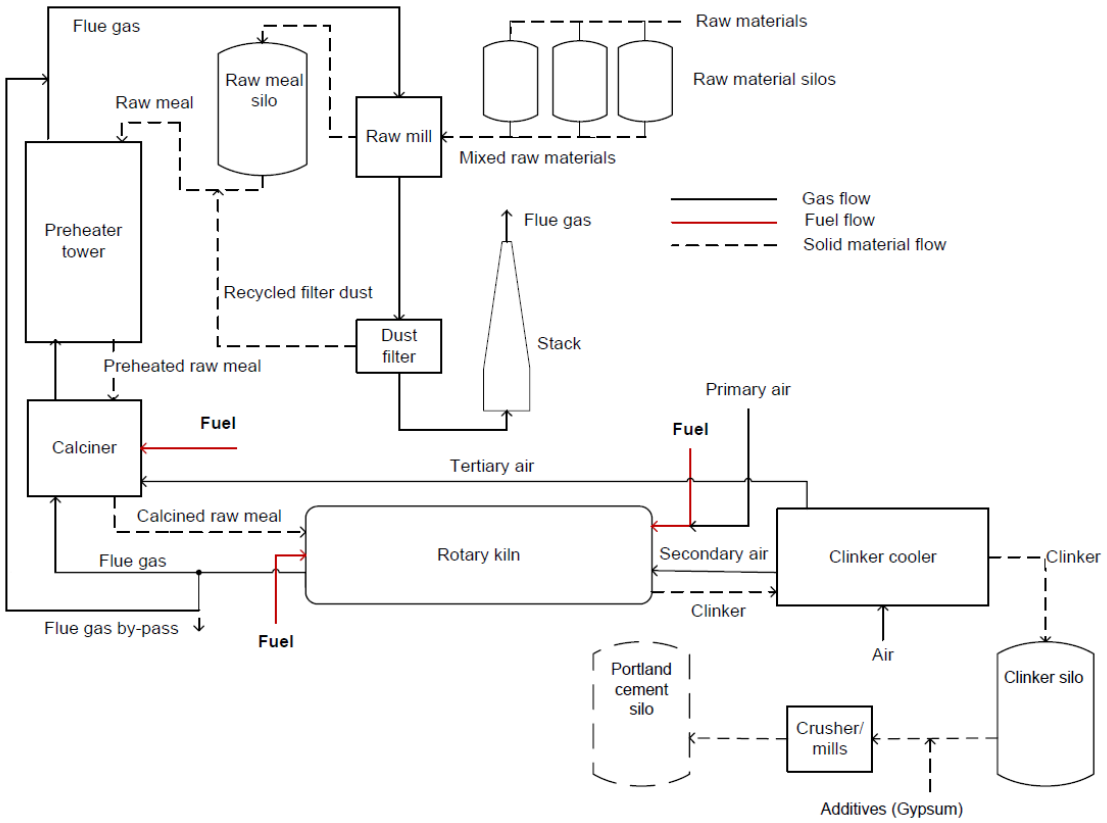

Figure 2-1: Process flow sheet of a cement plant with preheater tower consisting of cyclones and calciner [14].

The quarried raw materials are crushed to reach a size of 20-80 mm after which they are stored in a blending bed, which serves as storage and preliminary homogenization [15]. The raw materials are mixed and grinded in a mill to obtain a homogenous mixture with a particle size approximately between 5 and 125 µm. The small particle size is required to obtain proper reaction rates of the particles in the kiln. It is generally recommended that calcite particles are grinded finer than 125 µm and quartz is grinded finer than 45 µm [16]. Hot flue gasses from the preheater are typically used to dry the raw materials in the mill [6]. The milled and mixed raw materials is called raw meal. If further homogenization of the raw meal is required, it can be stockpiled in silos designed for blending [15]. It is important to mix the raw materials in the right proportions in order to get the proper composition required for the cement manufacture. Furthermore, a homogenous raw meal will yield the best and most stable product quality. In addition, a stable kiln feed reduces kiln instabilities and thus production costs [17].

After milling, the cement raw meal is led to the preheater tower, which consists of a series of cyclones. Modern cement plants usually have five or six cyclones depending on the drying requirements of the raw meal [18]. Older types of cement plants have fewer cyclone stages or none at all. In the preheater, the raw meal is heated by the hot gasses from the calciner and cement kiln and obtains temperatures up to 850 °C, while the gas is cooled from 1000 to 300 °C [4].

As the raw meal reaches temperatures around 700 °C the calcium carbonate begins to decompose forming calcium oxide [15]. The reaction is highly endothermic and consumes around 60 % of the thermal energy required in the cement process [4]. The energy for calcination is provided by combustion of fuels in the calciner, where the raw meal reaches temperatures between 800 and 900 °C and up to 95 % of the calcium carbonate is converted [18]. Around 50 % of the CO_2 emissions from cement manufacture are due to the decomposition of calcium carbonate [8].

From the calciner the material is admitted to the cement kiln where it is heated further and undergoes the reactions that gives the cement its characteristic attributes. The reactions will be discussed in detail in chapter 2.3. In the kiln the materials partly melt and form nodules known as clinker [6].

After the reactions in the kiln, the clinker is quickly cooled by ambient air in the clinker cooler. The preheated air from the cooler reaches temperatures of 1000 °C and is used as secondary air for the combustion process in the kiln [15]. Excess air from the cooler is used as combustion air in the calciner, so-called tertiary air. The cooled clinker is transported to storage until it is needed. The clinker typically has a size of 3-25 mm [14] and needs to be grinded to smaller and more uniform particle size in order to increase the reaction rate of the cement [4]. During the milling different additives such as gypsum, coal fly ash, or sand can be added to the cement in order to control the setting time of the cement [4]. The additives might replace a substantial amount of cement clinker in the finished cement and can reduce the energy requirement and CO_2 emissions of the manufacturing process [19].

2.2 Chemistry of Portland Cement

According to the European standard EN 197-1 [20], the requirements for Portland cement clinker are that calcium silicates constitute 2/3 of the clinker mass, the ratio of CaO to SiO_2 shall not be less than 2, and the content of MgO shall not exceed 5

wt%. The typical composition of Portland cement clinker can be seen in Table 2-1. Various additives and fillers can be added to substitute part of the clinker in Portland composite cements [20].

Table 2-1: Typical composition of Portland cement clinker [11].

	Name	Chemical formula	Cement Chemist Notation	Typical conc. (wt%)	Conc. range (wt%)
Major Components	Alite (tricalcium silicate)	$(CaO)_3 \cdot SiO_2$	C_3S	65	40-80
	Belite (dicalcium silicate)	$(CaO)_2 \cdot SiO_2$	C_2S	15	10-50
	Aluminate (tricalcium aluminate)	$(CaO)_3 \cdot Al_2O_3$	C_3A	10	0-15
	Ferrite (tetracalcium aluminoferrite)	$(CaO)_4 \cdot Al_2O_3 \cdot Fe_2O_3$	C_4AF	10	0-20
Minor Components	Free lime	CaO	C	1	0-3
	Magnesium oxide	MgO	M	2	0-5
	Dipotassium sulphate	K_2SO_4	$K\bar{S}$	1	0-2
	Disodium sulphate	Na_2SO_4	$N\bar{S}$	0.5	0-1
	Total concentration of non-specified impurities			<1	<1

The main components in the cement are alite, belite, aluminate, and ferrite. Alite is the most abundant mineral and is responsible for most of the strength development of the concrete [15]. The CaO in the cement clinker that has not combined with other components, is called free lime. Furthermore, the clinker can contain minor species such as MgO, K_2SO_4, and Na_2SO_4. In Table 2-1 the clinker minerals are listed in their pure forms, but in real clinker, smaller amounts of other oxides may be incorporated into the crystal structure as impurities [13].

In cement chemistry, a shortened notation is used for oxides, such as C for CaO and S for SiO_2 [13]. This is convenient to shorten the chemical formulas seen in Table 2-1. It is also common practice to report the composition of the clinker or raw meal on an oxide basis, e.g. K_2O or SO_3 [21], even though these components are not necessarily present in the kiln.

2.3 Clinker Reactions

Figure 2-2 is a simplified phase diagram showing how the different clinker phases are formed as the solids pass through the kiln system. The first steps of the cement clinker formation are taken in the preheater and calciner where the raw material is heated to temperatures of around 900 °C. This facilitates the decomposition of the calcium carbonate into calcium oxide:

$$CaCO_3 \rightarrow CaO + CO_2 \qquad \text{R 2.1}$$

The decarbonation reaction is an equilibrium reaction and the extent of the reaction depends both on the temperature and the partial pressure of CO_2 in the gas phase [6]. The reaction is also strongly endothermic, requiring 1800 kJ/kg $CaCO_3$ (at standard conditions) [14].

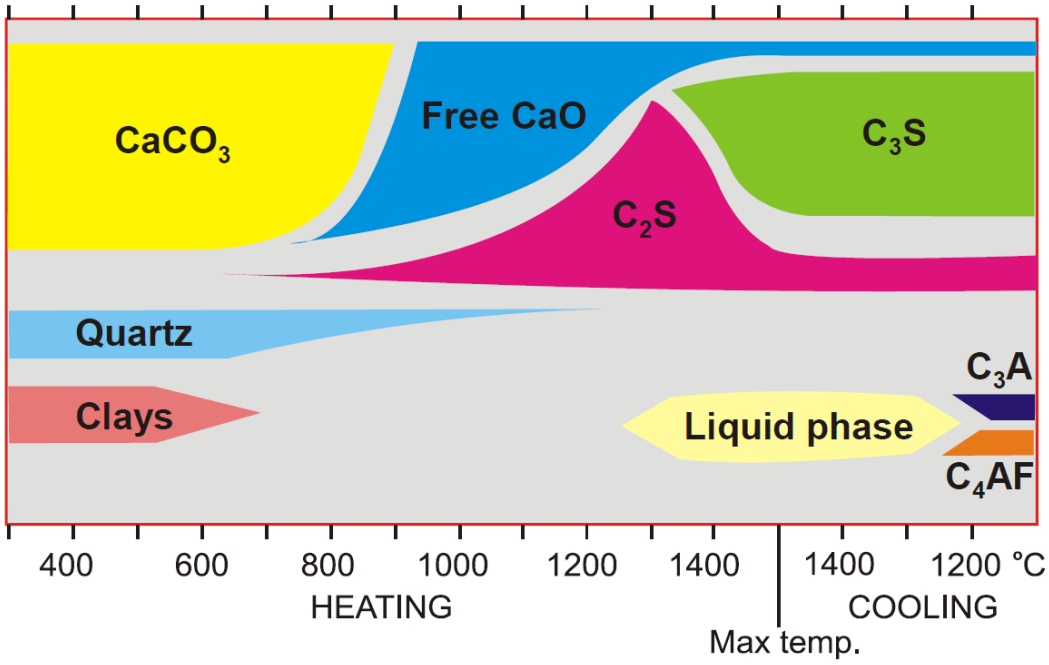

Figure 2-2: Simplified phase diagram showing the cement clinker reactions and corresponding temperatures as solids pass through the kiln system from left to right [22].

When the cement raw material enters the rotary kiln at temperatures around 900 °C, the remaining $CaCO_3$ is decomposed and the formation of the clinker phases begin [2]. Belite (C_2S) begins to form at temperatures above 600 °C [15], but is mainly formed in the kiln between 900 and 1250 °C as a solid-solid reaction between CaO and SiO_2 [2]. The reaction can in a simplified manner be represented as:

$$2CaO + SiO_2 \rightarrow (CaO)_2 \cdot SiO_2 \qquad \text{R 2.2}$$

This reaction equation shows the pure form of belite. Under industrial conditions several impurities are normally present which are incorporated in the various clinker phases [2]. The formation of belite reaches its maximum at around 1250 °C, after which it is consumed in the formation of alite (C_3S) [2]. Between 900 and 1250 °C the crystalline phases of aluminate (C_3A) and ferrite (C_4AF) are formed. The aluminate is formed as a reaction between CaO and Al_2O_3:

$$3CaO + Al_2O_3 \rightarrow (CaO)_3 \cdot Al_2O_3 \qquad \text{R 2.3}$$

The ferrite is formed in a reaction between CaO, Al_2O_3, and Fe_2O_3:

$$3CaO \cdot Al_2O_3 + CaO + Fe_2O_3 \rightarrow (CaO)_4 \cdot Al_2O_3 \cdot Fe_2O_3 \qquad \text{R 2.4}$$

Alumina and iron oxide are not essential constituents of the Portland cement clinker, but they serve as fluxing agents and lower the energy requirement of the process, making it more economical [4]. As the temperature increases above 1250 °C, the aluminate and ferrite phases begin to melt [2], and at 1450 °C as much as 20-30 % of the cement mix may have melted [13]. The molten phase serves the purpose of accelerating the clinker phase reactions by facilitating diffusion in the liquid phase, which is significantly faster than in the solid phase. This allows additional Ca to diffuse to and react with the belite to form alite:

$$2CaO \cdot SiO_2 + CaO \rightarrow (CaO)_3 \cdot SiO_2 \qquad \text{R 2.5}$$

In addition, the melt agglomerates the particles and binds them together forming clinker nodules while also reduces the amount of dust in the kiln [2]. The hot clinker should be swiftly cooled in the clinker cooler to prevent R 2.5 from occurring in reverse, which would lower the amount of alite.

2.4 Clinker Compositional Parameters

The clinker or raw meal composition is often described using a few key parameters related to the content of the different oxides.

The Lime Saturation Factor (LSF) is calculated based on the mass fraction of the 4 main clinker oxides [13]:

$$LSF = \frac{Y_{CaO}}{2.8 * Y_{SiO_2} + 1.2 * Y_{Al_2O_3} + 0.65 * Y_{Fe_2O_3}} \qquad \text{E 2.1}$$

If the LSF is unity, the oxides are present in proportions where they, in theory, combine fully yielding a clinker with zero free lime. If the LSF is above unity, then the amount of calcium is too high to be fully incorporated in the clinker minerals, and free lime will be present in the clinker. Typical values of LSF are in the range 0.92-0.98. The higher the LSF the more alite, C_3S, can be formed in the clinker [13].

Two other important metrics are the silica ratio (SR) and the alumina ratio (AR), also sometimes called alumina and silica modulus. They are defined as:

$$\boldsymbol{SR = \frac{Y_{SiO_2}}{Y_{Al_2O_3} + Y_{Fe_2O_3}}} \qquad \textbf{E 2.2}$$

$$\boldsymbol{AR = \frac{Y_{Al_2O_3}}{Y_{Fe_2O_3}}} \qquad \textbf{E 2.3}$$

The SR is normally in the range 2.0-3.0 and the AR 1.0-4.0. The SR governs the proportion of silicate phases to iron and alumina in the clinker. Increased values indicate that less melt, which is mainly caused by iron oxides and alumina, can be formed in the clinker. This causes the clinker reactions to occur slower, making the clinker harder to burn.

The AR describes the ratio between alumina and ferrite phases in the clinker. It governs the temperature at which the melt phase forms, which is lowered by increased iron content [23].

Another important equation is the Bogue formula [13,24], which may be used to estimate the composition of the four main clinker phases.

$$\boldsymbol{Y_{C_3S} = 4.0710\, Y_{CaO} - 7.6024\, Y_{SiO_2} - 6.7187\, Y_{Al_2O_3} - 1.4297\, Y_{Fe_2O_3}} \qquad \textbf{E 2.4}$$

$$\boldsymbol{Y_{C_2S} = -3.0710\, Y_{CaO} + 8.6024\, Y_{SiO_2} + 5.0683\, Y_{Al_2O_3} + 1.0785\, Y_{Fe_2O_3}} \qquad \textbf{E 2.5}$$

$$\boldsymbol{Y_{C_3A} = 2.6504\, Y_{Al_2O_3} - 1.6920\, Y_{Fe_2O_3}} \qquad \textbf{E 2.6}$$

$$\boldsymbol{Y_{C_4AF} = 3.0432\, Y_{Fe_2O_3}} \qquad \textbf{E 2.7}$$

In the above equations the measured free lime content should be subtracted the lime content before being applied. The Bogue formula may differ considerably from the actual phase composition, since pure clinker phases are assumed in the calculations, while impurities may be incorporated into the clinker in an actual kiln.

2.5 Clinker Burnability

The ease at which the clinker oxides react in the cement clinker is termed burnability. An easy burning clinker will form alite at relatively low temperatures, while a hard burning clinker will require higher temperatures. Thus, burnability is important for the energy consumption in the cement kiln. Historically, it has been easier to measure the free lime rather than the alite content, thus free lime content has been used to determine the completeness of the clinker reactions.

The burnability can be tested by burning raw meal in a laboratory oven. A procedure is to form small clinker nodules which are burned for 30 minutes at e.g. 1400, 1450, and 1500 °C [23]. The lower the free lime content after burning, the easier the clinker is to burn.

It is also possible to estimate the burnability theoretically using equations available in the literature. These equations attempt to estimate the free lime content, based on the raw meal composition and particle size. One example is given in E 2.8. The equation estimates the free lime in laboratory clinker burned for 30 minutes at 1400 °C [25].

$$\boldsymbol{Y_{CaO_f} = 0.33 * LSF + 0.0168 * SR - 0.353 + 0.93 * Q_{44} + 0.56 * C_{125}} \qquad \textbf{E 2.8}$$

The clinker thus becomes harder to burn by increased LSF and SR, which are related to the chemical composition. In addition, the content (mass fraction) of coarse quartz, Q_{44}, (SiO_2) and calcite, C_{125}, ($CaCO_3$) with particle sizes above 44 and 125 µm, also affects the burnability. These large particles are unable to react in the kiln due to diffusion limitations.

If the clinker burnability in a kiln changes due to changes in the raw meal kiln feed, it can be expected that the specific heat consumption of the kiln should be adjusted, to maintain a constant free lime content [26].

2.6 The Cement Rotary Kiln

The formation of cement clinker occurs in the rotary kiln. Figure 2-3 shows a rotary kiln and a grate cooler indicating the main temperature zones in the kiln. The cement rotary kiln is essentially a long cylindrical tube that acts as a large counter-current heat exchanger. At one end the raw materials, preheated and calcined in the cyclone

tower, are admitted at around 900 °C. At the other end of the kiln, fuel is being fired through the burner, to heat the material in the kiln to a maximum temperature of around 1450 °C. The kiln is composed of an outer steel shell, which is lined with refractory material that acts as thermal insulator and protects the outer shell [27]. The type of refractory bricks vary along the length of the kiln depending on the temperature of the material and gas [13]. In the hot parts of the kilns, where the clinker melts, a coating is formed on top of the refractory, which further helps insulate and protect the kiln walls [13].

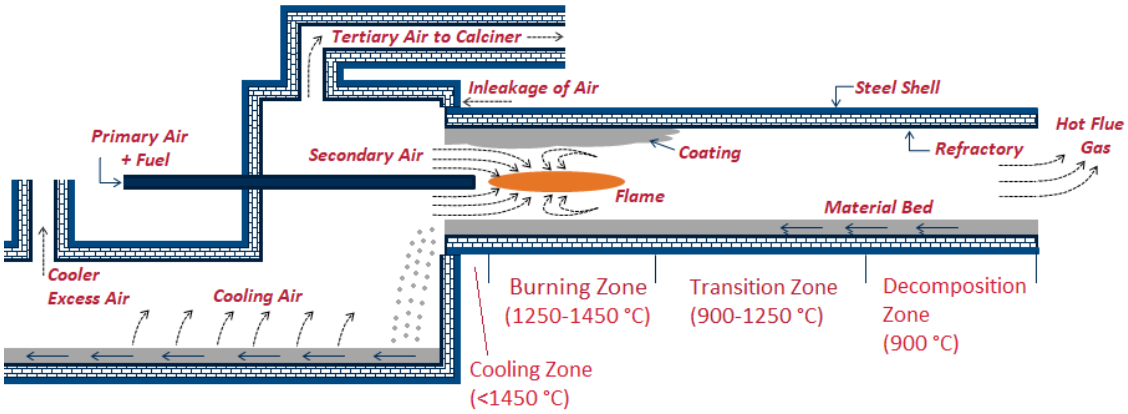

Figure 2-3: A burner in a grate cooler cement kiln indicating temperature zones in the kiln and different air flows.

The kiln is typically 50-100 meters long with diameters between 3 and 7 meters. Old wet kilns are long with L/d around 30, while modern pre-calciner kilns are shorter with L/d around 10-15 [6]. The kiln is tilted at 1-3° and rotates at 1-4 rpm to facilitate the movement of the raw materials from one end to the other. The residence time of the raw materials is typically 20-40 minutes with 10-15 minutes in the burning zone, the hottest part of the kiln [2,13]. The residence time of the gasses is around 5-10 seconds [28]. Typical production capacities are around 3,000 ton/day [11], but the largest kiln in the world has a capacity of 13,000 ton/day [29].

2.7 Combustion Air in the Cement Kiln

As indicated in Figure 2-3 several different types of air are relevant for the combustion process in the cement kiln. Primary air is injected through the burner and can be divided into transport air, axial air, and swirl air (also called radial or tangential air). The transport air is used to pneumatically inject the fuel into the kiln

at velocities around 30 m/s [27]. The axial and swirl air are used to control the flame shape [30]. The primary air constitutes around 5-15 % [31] of the air required to combust the fuel. Older generations of burners may have used up to around 30 % primary air [32].

The remainder of the combustion air is called secondary air. This is the air that is used to cool the hot clinker. Heat recuperation in the cooler preheats the secondary air to temperatures around 1000 °C before it enters the kiln [31]. The gasses are pulled through the kiln by an induced draft (ID) fan, which creates an underpressure in the kiln. The low pressure may cause some air, 2-10 %, to leak into the kiln between the rotating kiln and stationary cooler [27,32]. The air required to cool the clinker exceeds the amount of air necessary for the combustion in the kiln. Some of the excess air is used for the combustion in the calciner, so-called tertiary air. The remaining excess air leaves the clinker cooler and may be used elsewhere, e.g. for drying of raw materials [33].

A correct amount of combustion air is imperative for a high thermal efficiency in the kiln. If the amount of combustion air is too low, it results in unburned fuel and CO emissions from the kiln. On the other hand, excessive energy is required to heat up excess combustion air, which will cool the flame. An increase in the oxygen content at the kiln raw material inlet from 1 to 5 vol% will increase the specific heat consumption by approximately 10 % [32]. It is normally recommended that the oxygen content in the kiln exhaust gasses is in the range 0.7-3.5 vol% [34].

2.8 The Cement Kiln Burner

The kiln burner provides the thermal energy that is required to heat the raw meal from approximately 900 to 1450 °C, which facilitates the formation of a liquid phase and the initiation of the chemical reactions that form the cement clinker. Often the burner is referred to as the main burner, although in modern preheater and calciner plants, the larger share of fuel is fired at the calciner.

Most modern cement kiln burners are so called multichannel burners, which contain several channels and nozzles for injection of different kinds of fuel and air. An example of a modern multichannel burner is the FLSmidth Jetflex burner shown in Figure 2-4. The burner is designed with a large central channel for alternative fuels firing. The center is surrounded by a channel for swirl air, which is injected through

the slanted vanes giving a tangential motion of the air. Next follows two annular channels for pulverized fuel and gas, respectively. The burner has 20 axial air nozzles, which can be turned individually to shape the flame. The outside of the burner is lined with refractory to protect the steel from high temperatures. The size of the burner is dependent on its capacity, but it will typically be around 1 m in diameter, including 0.2 m of refractory. The length of the burner is typically 10-20 m, which is required since the burner must be long enough to reach through the kiln hood as shown in Figure 2-3.

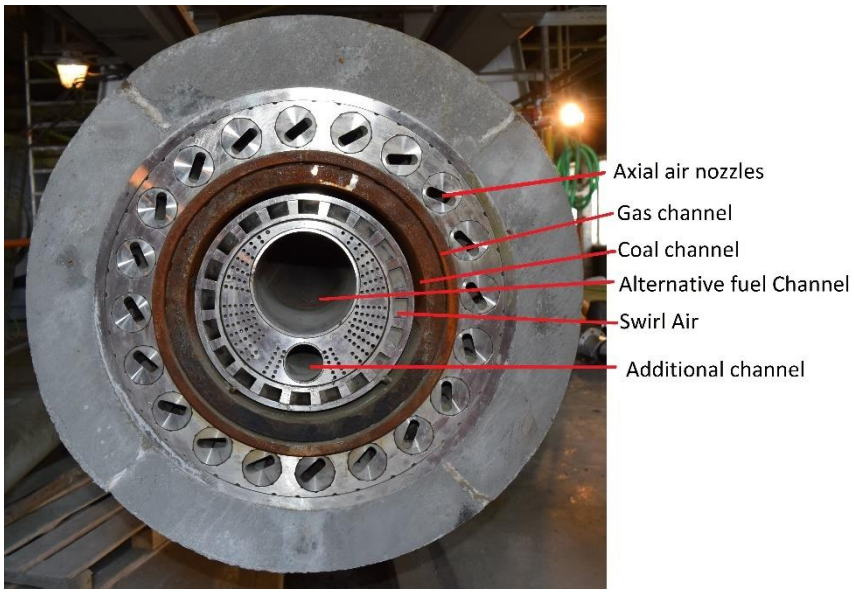

Figure 2-4: The Jetflex burner, a modern multichannel cement kiln burner from FLSmidth A/S. The additional channel can e.g. be used for oxygen enrichment, liquid fuel firing, or a flame detector.

To minimize the energy consumption in the rotary kiln it is important to achieve an efficient combustion process. Consequently, the ideal kiln burner should be able to [30,31,35,36]:

- Provide a high temperature flame maximizing heat transfer to the raw material
- Control the temperature and shape of the flame
- Obtain high product quality and production capacity
- Give stable process conditions
- Minimize the specific energy requirement

- Provide adequate and efficient mixing of the hot secondary air
- Obtain quick ignition and full conversion of fuel in suspension with a minimum of fuel dropout
- Produce a minimum of harmful emissions, e.g. NO_X.
- Use a minimum of excess air and primary air
- Be fuel flexible

Some of these points might be conflicting and the focus of the kiln burner may change between different cement plants or geographical regions, depending on e.g. legislation. For instance, there is a high focus on utilizing alternative fuels in the European cement sector, which may tend to increase process instability, which will be described in chapter 3.5.

2.9 History of Kiln Burner Design

Since the early 1900's the kiln burner has developed from being mainly coal fired to being mainly oil fired. During the oil crisis of the 1970's, the fuel was switched back to coal or petcoke. Recently, since the 1990's a demand for an increased amount of alternative fuels firing has arisen. In the meantime, environmental legislation has also become stricter, setting limits on emission of pollutants such as NO_X [30]. To adapt to the varying fuels and process requirements, the kiln burner has also developed, as shown in Figure 2-5.

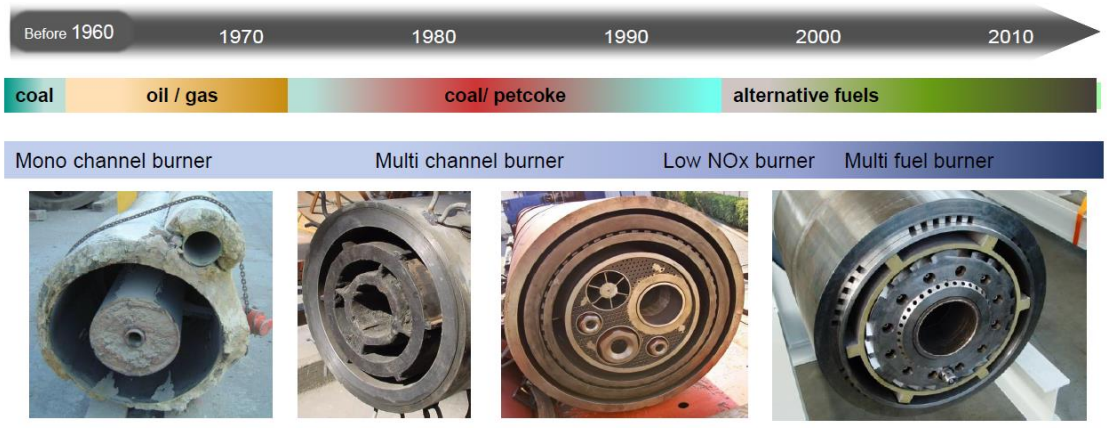

Figure 2-5: Development of the cement burner technology since 1960 and the main fuels used [30,37].

While the burners themselves have changed there has also been a change from direct firing to indirect firing since the 1970's. The directly fired burner is connected directly to the fuel mill. While this is a simple system it has the disadvantage that the primary air is used to dry the fuel before it is admitted to the kiln. This will result in larger amounts of primary air and unnecessary water in the kiln flue gas, which results in lower heat efficiency. It is also more difficult to regulate the system, since it is required to control the fuel feed to the mill and the mill speed simultaneously. In addition, if the mill breaks down it will lead to a kiln stop. In indirect fired systems, an intermediate storage for the pulverized fuel is installed after the mill. This reduces the disadvantages of the direct fired system, but also requires additional equipment. Another advantage of the indirect fired system is that one mill can feed both the kiln and the calciner [38,39].

2.9.1 Single Channel Burners

The early kiln burners were single channel burners typically fired with pulverized fuel, i.e. coal. Fuel and primary air are injected through a single channel and outlet velocities of the air is typically 40-60 m/s. They use a high amount of primary air (15-45 %) to ensure a high burner momentum. The burner momentum, I, is calculated by the axial velocity, u_{prim}, and mass flow, $\dot{m}_{prim}$, of the primary air according to E 2.9. A higher momentum gives a more efficient mixing of air and fuel in the kiln and thus promotes proper combustion of fuel. The momentum is often normalized, I', by the burner thermal capacity and is normally in the range 4-12 N/MW [31].

$$I' = \frac{I}{P_{burner}} = \frac{u_{prim} * \dot{m}_{prim}}{P_{burner}} \qquad \text{E 2.9}$$

In addition to the high amount of primary air, the disadvantages of single channel burners are that it is difficult to change the load (limited turndown ratio), consequently, they are difficult to manage during startup periods. Moreover, there is a very limited possibility to change the flame pattern during operation, since the amount of primary air and coal throughput should be proportionate. It is possible to gain some control by adjusting the primary air velocity and amount depending on the fuel load [35].

The flame can be sketched as in seen in Figure 2-6. The flame typically spreads with an angle around 10° and the mixing will typically be complete at around 3 kiln diameters downstream of the burner [40]. In the plug flow zone, after the mixing point, oxygen will mainly be supplied through diffusion [41]. Thus, the fuel burnout and CO reduction should preferably be completed ½ a kiln dimeter before the macro mixing is complete. Otherwise, the mixing intensity and combustion rate is lowered and unburnt fuel may cause reducing conditions in the clinker bed [40,41].

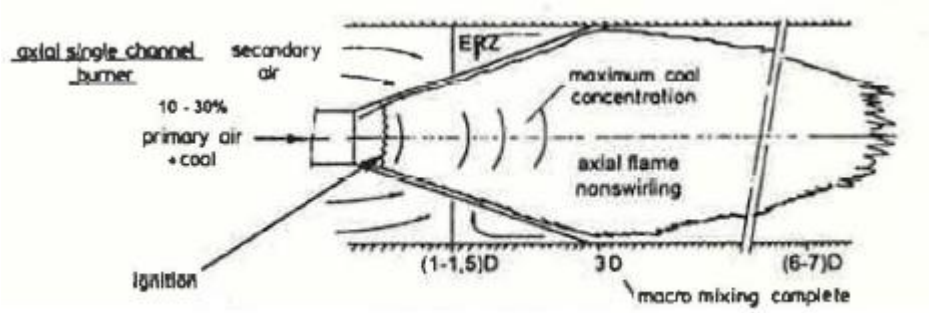

Figure 2-6: A typical axial flame from a single channel kiln burner [40]. ERZ = External Recirculation Zone

2.9.2 Multichannel Burners

The multichannel burner (three channel burner) was developed in the late 1970's. Separate channels were made for the coal and primary air, which allowed for a higher primary air velocity and introduction of swirl air. This created a better mixing of the fuel and hot secondary air than what was possible for the single channel burner and a better control of the flame [35]. The swirl air expands the flow of pulverized fuel and stabilizes the flame by creating an internal recirculation zone [42] as shown in Figure 2-7. The effect of swirl will be discussed in more detail in chapter 8.6. The high degree of flame shaping is beneficial to adjust a burner to the requirements of each single kiln system. It helps in kiln optimization, securing a stable coating formation, kiln shell temperature, and clinker quality [35]. Another advantage of the multichannel burner was that the high primary air velocities in the range 70-130 m/s made it possible to keep a high momentum by reducing the amount of primary air to 10-15 % of the combustion air, which gives a better heat economy [35]. The higher mixing that can be obtained with a multichannel burner will create a shorter, but higher temperature flame, which ensures better heat transfer to the clinker bed.

A sketch of the multichannel burner flame is shown in Figure 2-7. Compared to the single channel burner sketched in Figure 2-6, an internal recirculation zone is formed due to swirl flow. In addition, the mixing is completed closer to the burner.

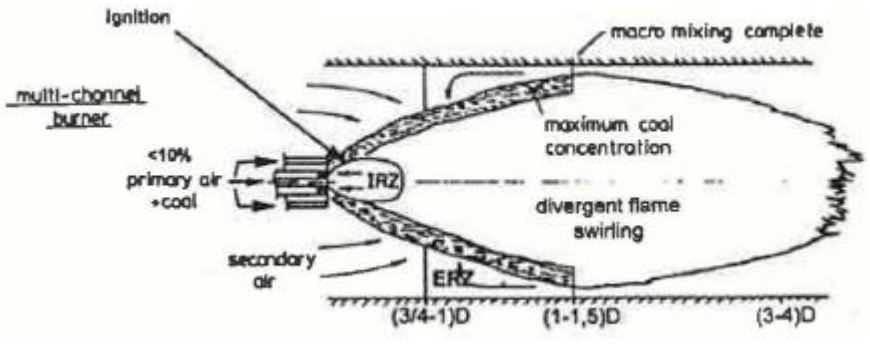

Figure 2-7: Multichannel burner coal flame [40]. ERZ = External Recirculation Zone, IRZ = internal Recirculation Zone.

The construction of the burner is normally a center channel for oil or gas surrounded by a jacket for swirl air, which gives the flame a divergent and rotating motion. The next outer channel is the coal channel, which is enclosed in an annulus or by jets for axial primary air. The coal is injected at around 20 m/s. The low coal velocities decrease wear and allows for better flame shaping. The amount of coal conveying air should be around 2-3 % of the combustion air (minimum 0.2 m^3/kg coal), in order to ensure pulse free flow [35].

2.9.3 Low Primary Air Burners

Low primary air burners, also often called low NO_X burners, were developed in the 1980's driven by stricter environmental legislation. NO_X formation increases with increasing temperature and oxygen availability. Thus the principles for lowering the NO_X are flame stabilization and recirculation of combusted gasses, concentrating the fuel along the center axis to prevent the fuel from leaving the flame, reduced primary air amount to 8-10 % (compared to 10-15 % in the multichannel burner), and more even heat distribution in the flame to avoid high peak temperature regions [42].

NO_X is mainly formed if the fuel is allowed to burn in oxygen rich conditions. Thus, low NO_X burners use a low amount of primary air, typically less than 10 %. This decreases the availability of oxygen in the hot part of the flames and lower the production of NO_X [30]. The lower primary air amount can be achieved by a redesign

of nozzles that allow for higher primary air velocities, thus keeping burner momentum at the same level [42].

Staged combustion, i.e. recirculation of combustion gasses to the burner, can also serve to lower NO_X emissions [35] and the concept is shown in Figure 2-8. The recirculated hot gasses will quickly heat up and ignite the fuels and they contain a low amount of oxygen, which limits the NO_X formation [40].

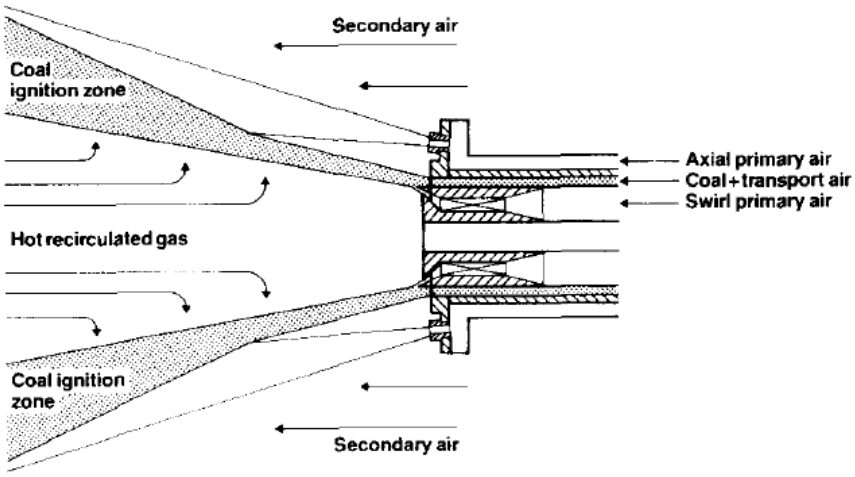

Figure 2-8: Flow pattern in a low NO_X burner [43]. Note that the swirl channel is located inside the coal channel.

The ignition point is also quite important for the NO_X formation [40,42]. Ignition close to the burner tip is preferred as it tends to lower the NO_X emissions [42]. If the ignition occurs far downstream in the kiln, more oxygen can be entrained into the flame leading to high NO_X levels [40,42]. The mono-channel burners create very high levels of NO_X since they have a late ignition. For multichannel burners, the effect of swirl was two-sided. The swirl creates an internal recirculation zone for fuel staging, while on the other hand an increased swirl also entrains extra air, which increases the oxygen availability [42]. The location of the swirl air channel compared to the fuel channel might also have an impact on the NO_X. If the swirl is placed on the inside of the coal channel, the air might throw the fuel into the hot secondary air, where it will burn at high oxygen concentrations being more prone to form NO_X [31,35].

The fuel type also has some influence on the NO_X formation. Depending on the coal characteristics, e.g. type, fineness, and volatile content, the ignition point might be influenced [42]. A high volatile coal has an early ignition, which can reduce NO_X formation [40]. The coal particle size may also play a role and a larger particle size

will delay the ignition and thus increase the NO_X [44]. On the other hand finer coal particles tend to burn at higher peak temperatures increasing the NO_X [40].

The low NO_X burners are typically not suitable for a high utilization of AF. The low amount of primary air and burner momentum is not sufficient to easily ignite the AF particles and fuel dropout of unburnt particles is likely to occur [30].

2.9.4 Alternative Fuels Burners

The current burner development aims to increase the share of alternative fuels and provide high fuel flexibility. The first trials to introduce alternative fuels into the rotary kiln were made through a separate pipe on top of the existing burner. However, this resulted in the fuel being carried over the top of the flame and dropping to the clinker bed unconverted [45]. Modern rotary kiln burners consist of multiple channels to increase the fuel flexibility, as shown in Figure 2-4. Different tubes and annular channels are applied with the possibility of burning both pulverized and lumpy solid fuels as well as liquids and gasses [30]. The channels for alternative fuels are located in the center of the burner to keep the fuel in the center of the flame as long as possible. Lumpy and fluffy solid fuels have a tendency to block pipes, thus a large round tube is preferred for these types of fuel [45]. The center fuel channel is typically surrounded by an annulus for pulverized fuels, i.e. coal or petcoke firing, and the primary air channels.

The difference between burners from different manufactures is the positioning of the primary air channels, which can be located inside or outside the annulus for pulverized fuel [46]. Another distinction is whether the air is injected in an annulus or through individual jets and how the primary air can be controlled to create axial momentum and swirl [46]. Burner manufacturers seem to prefer the jet design for axial primary air (see Figure 2-4). The merit of the jet design is an increased entrainment of hot secondary air between the primary air jets, which will increase the heating rate of the hard to ignite alternative fuels [46]. Nørskov [31] and D'Hubert [47,48] provides a survey and comparison of the state of the art burners currently available on the market.

2.10 Summary and Conclusions

Portland cement is the most commonly produced type of cement. It mainly consists of the calcium silicates alite and belite as well as ferrite, aluminate, and other minor components. The formation of cement clinker takes place inside a rotary kiln, where the materials are heated to 1400-1500 °C, to facilitate the proper reactions between the calcium and silica.

The high temperatures required in the kiln, makes the production of Portland cement clinker highly energy intensive. The energy is supplied by burning fuels at one end of the rotary kiln. In order to minimize the energy usage, the combustion process should be as efficient as possible. For this purpose, the design of the kiln burner has continuously evolved to allow combustion of different fuels, a higher flexibility, and to comply with stricter environmental legislation.

3 FUELS IN THE CEMENT INDUSTRY

The selection of fuel for the cement production is an important parameter for the cement plant, especially since the fuel often makes up a significant cost of the plant operation. Before a fuel is selected it is important to consider the following three parameters [39]:

- Costs, e.g. fuel purchase, availability, fuel handling, maintenance.
- Product quality, e.g. impacted by unburnt particles in the clinker
- Environmental impact, e.g. CO_2, CO, and NO_X emissions,

An example of how these factors may change and force plants to use new fuels has recently been seen in Egypt [49]. The Egyptian cement sector has traditionally relied on natural gas and oil as their main fuels. However, in 2013 the Egyptian government decided to promote the export of oil and gas, which reduced the availability for domestic industries. Thus, many cement manufacturers decided to start using coal or petcoke and are heavily investing in coal mills and other necessary equipment and process changes.

This chapter will give a short overview of different fuels widely utilized in the cement industry. They range from conventional fossil fuels such as coal, gas, and oil, to various alternative fuels. Furthermore, the potential negative impacts that alternative fuels can have on the kiln process, will be discussed.

3.1 Conventional Fuels Used in the Cement Industry

3.1.1 Coal

Coal is the most widely used fuel in the global cement industry [39]. Many plants switched from oil and gas firing to coal firing in the late 1970's due to a steep rise in the price of these fuels [15].

The rate of coal combustion is highly influenced by the particle size, the combustion time being roughly proportional to the diameter squared [39]. The smaller the particles, the faster they are heated and react, resulting in higher peak temperatures. The volatile content in the coal impacts the ease of ignition, and thus heavily affects the combustion in the kiln [40]. A rule of thumb for coal combustion says that the residue on a 90 μm sieve should not exceed 50 % of the volatile matter level [40]. E.g. a 20 % volatile matter coal would require that a maximum of 10 % of the coal is retained on a 90 μm sieve. A finer grinding than this may, all other things being equal, result in high peak temperatures and excessive NO_X formation [40]. In conjunction with the milling, the coal is dried to a moisture content of 0.5 to 2.0 %. A little residual moisture is preferable since the presence of OH radicals from the water will help ignite the coal [39].

When using coal, or other solid fuels, in the cement kiln it is important to consider that the ash will be incorporated into the cement clinker. This needs to be accounted for by a proper adjustment of the raw meal composition prior to the burning process [4]. It is also imperative that the ash particles are sufficiently small and injected far inside the kiln in order for the particles to be incorporated into the clinker phases, otherwise it could adversely affect the alite content in the clinker [4].

The types of coal fired in the cement kiln varies broadly from region to region depending on the coal availability. There can be quite a large variation between different coal types such as anthracite, bituminous coals, and lignite. Bituminous coals are most widely utilized in cement plants followed by subbituminous coals and lignite [39].

3.1.2 Petroleum Coke

Petroleum coke (petcoke) is a by-product from oil refining cracking processes. The oil is subjected to extreme conditions driving off the volatiles and leaving a solid

residue that is almost pure carbon [50]. As a by-product the price of petcoke is typically favorable compared to coals, and it has become a very widely used fuel in the cement industry [39].

A challenge compared to most coals is that petcoke is less reactive than coals. Petcoke has a low content of volatiles, normally 5-15 % [51]. This makes petcoke difficult to ignite compared to medium and high volatile coals, and once it is ignited, it only burns slowly. In order to ignite the petcoke as quickly as possible and allow full combustion of the particles, a fast mixing of secondary air and fuel is necessary [50], which provides oxygen to the fuel surface. Thus, the burner design should allow for higher momentum than during coal firing and single channel burners are not well suited for petcoke firing [50]. A fine grinding of the petcoke can also counter the low reactivity [51] as it increases the surface area of the fuel and thus contact with oxygen.

Another challenge in petcoke utilization is the high sulfur content, normally in the range 2-7 % [52]. The high input of sulfur may result in operational challenges in the cement kiln such as build-ups and blockages [53,54]. This is discussed in further detail in chapter 3.5.

3.1.3 Gas

Natural gas is the predominant type of gaseous fuel used in cement plants. It is typically supplied to the cement plant in pipelines at high pressure. Before the gas can be used it is necessary to reduce the pressure to 3-10 bar.

Since gas contains no ash components it is not necessary to adjust the cement raw meal mixture to account for the ash added as with the solid fuels [4]. A challenge with a gas flame is that it produces low amounts of soot and thus has a low radiance. However, the high amount of dust present in the cement kiln may alleviate this issue [4]. Gas is easy to ignite and is often used for heating up the kiln.

3.1.4 Oil

The oil used in cement kilns is normally heavy fuel oil (No. 6 fuel oil according to ASTM classification [55]) . Oil has a high viscosity and should be heated to around 50 °C in order to be easily pumped. In order to properly atomize the oil in the burner a further heating to around 120 °C is necessary [15]. A challenge with using oil is

that it, like petcoke, may contain high amounts of sulfur. For heavy fuel oil the sulfur content can be as high as 4 % [4].

The ease of oil ignition can be estimated by the Calculated Carbon Aromaticity Index (CCAI) [39]:

$$\boldsymbol{CCAI = \rho - 81 - 141 * log(log(\nu + 0.85))} \qquad \textbf{E 3.1}$$

Here the density, ρ [kg/m^3], and kinematic viscosity, ν [mm^2/s], are measured at 15 and 50 °C, respectively. Fuel oil with a CCAI between 800 and 870 is easy to ignite, while if CCAI is above 870, ignition may be difficult [39].

3.2 Drivers for Alternative Fuels Usage

During the last 20 years, an increased interest in alternative fuels for the cement industry has appeared. The primary drivers are cost, carbon dioxide emissions, and waste management, as further discussed in the following chapters.

3.2.1 Cost of Fuel

Energy accounts for 30-40 % of the operating costs of cement manufacturing when using fossil fuels [10], and is thus an important factor for any cement plant. The cost of various fossil fuels is indicated in Table 3-1.

Table 3-1: Relative cost of various fossil fuels per energy unit [39].

Fuel	Relative cost
Coal	100
Petcoke	30-50
Fuel oil	150-250
Natural gas	200-300

Table 3-1 shows that significant cost reductions are possible by choosing an appropriate fuel. Switching from coal to petcoke may cut fuel costs by up to 2/3, explaining why many cement plants have switched from coal to petcoke, even though it is a more troublesome fuel. Fuel oil and natural gas are around twice as expensive as coal, and relatively few plants use these fuels as their main fuel [11]. The solid fossil fuels are more cost effective, even though pretreatment in the form

of milling and drying is necessary, which results in increased investments costs for e.g. coal mills.

Waste derived alternative fuels may be significantly cheaper than the conventional fuels presented in Table 3-1. This is the primary driver for the increased use of alternative fuels in the cement industry. It has been estimated that a cement plant with an annual production of 1 million tons of cement, could save up to 2.4 million € annually, by replacing 30 % of fossil fuels with no-cost alternative fuels [56]. In some cases, the cement plant can be paid to accept alternative fuels [57].

3.2.2 Carbon Dioxide Emission Reductions

The cement industry is responsible for approximately 5 % of global anthropogenic CO_2 emissions [8]. Around 40 % of the emissions are due to fuel combustion [8]. Consequently, it is important that the cement industry contributes, if carbon emissions are to be reduced [19]. Table 3-2 contains an overview of the net CO_2 emission from various fuels often used in the cement industry, although significant differences can occur depending on the sourcing of the fuel, especially for RDF. Petcoke and coal are the most CO_2 intensive fuels, while the other types of fuel emit significantly less CO_2. Especially, RDF, animal meal, and wood result in lower CO_2 emissions since the fuels are wholly or partly biogenic and CO_2-neutral [58]. Thus, the use of alternative fuel could help in reducing the CO_2 emissions from the cement industry [56].

Table 3-2: Indicative net CO_2 emissions from various fuels used in the cement industry [59].

Fuel	Net CO_2 emission ($g\ CO_2/MJ$)
Petcoke	101
Coal	96
Natural gas	54
Used tires	85
Waste oil	74

Fuel	Net CO_2 emission ($g\ CO_2/MJ$)
Plastic	75
RDF	9
Animal meal	0
Waste wood	0

3.2.3 Waste Management

A third reason to use waste fuels in the cement industry is that it might help divert waste away from landfills [56]. Combustion in cement kilns is a good option to recover the energy in waste and conserve fossil resources [11]. The conditions in a cement kiln are well suited for the thermal destruction of organic molecules. The temperatures in the cement kiln exceed 1200 °C, the residence time is more than 2 seconds, and the oxygen concentration exceeds 3 %. This allows the cement kiln to have very few emissions of organic toxins such as dioxins and furans [60]. Thus alternative fuels can normally be combusted without causing excess gaseous emissions [60]. In the cement kiln, fuel ashes are also incorporated into the clinker, which eliminates the solid waste stream that is otherwise encountered during waste incineration [61]. This may make it more beneficial to burn waste in cement plants than in dedicated waste incinerators [61].

3.3 Use of Alternative Fuels

The use of alternative fuels in the cement industry for selected countries and regions is shown in Figure 3-1. The data have been taken from the World Business Council for Sustainable Development (WBCSD) Cement Sustainability Initiative, which collects data in the “Getting the Numbers Right” database [62]. The database covers numbers from more than 900 cement installations worldwide, which is around 20 % of the global production. The initiative best covers Europe where 95 % of cement producers reports to the database. In other regions the coverage is less, which may lead to somewhat skewed results [63].

Figure 3-1 shows that the use of alternative fuels is most advanced in the EU. Here the use began to increase during the 1990’s with 2 % of the energy being derived from alternative fuels. By 2000 this number had increased to 9 % and in 2013 to 37 %. Germany is one of the countries where the use of alternative fuels has progressed the most and alternative fuels provide above 60 % of the energy.

North America is the region with the second highest use of alternative fuels, totaling 15 % in 2013, which is close to the world average. China and India have only very small substitution rates. An improvement here could have a very large potential since they are the largest cement producers in the world with 59 and 7 %, respectively, of world production in 2017 [7]. Consequently, there is a large

potential for increasing the use of alternative fuels worldwide to a level near that in Europe. However, it does require significant infrastructure and well managed waste collection systems, which are not necessarily present outside of Europe and North America.

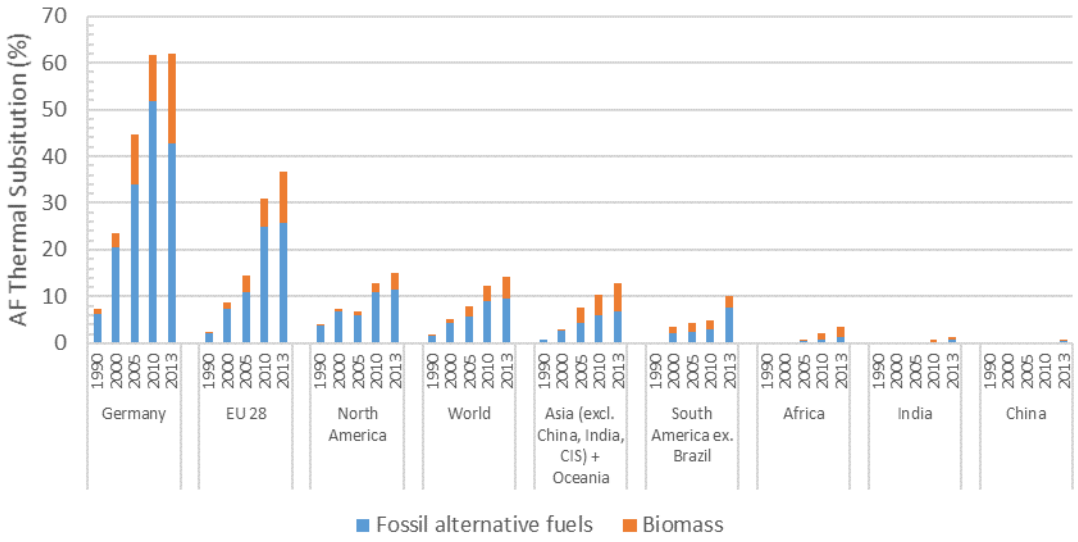

Figure 3-1: Use of fossil and biomass based alternative fuels in selected countries and regions [62]. Fossil alternative fuels include e.g. waste oil, tires, plastics, refuse derived fuel; biomass include e.g. agricultural waste, sewage sludge, charcoal. CIS = Commonwealth of Independent States.

In the European Union a framework for handling of waste and co-combustion of waste has been set up through the "Waste Framework Directive" (2008/98/EC) and the "Waste Incineration Directive" (2000/76/EC) [64,65]. The legislation defines when a waste can be incinerated and sets rules to minimize the environmental impact of waste incineration. Thus, a well-developed waste handling infrastructure is present in Europe, and waste fuel is easily accessible for cement manufacturers. In other parts of the world the use of waste products may be controversial since cement kilns are not subject to stringent emission control [9,66].

3.4 Types of Alternative Fuels

Alternative fuels for the cement industry spans a wide variety of different fuels that can be of either fossil or biogenic origin. Examples of commonly used fuels of fossil origin are: waste oil, used tires, plastics, and solvents, while biomass fuels include: agricultural waste, waste water sludge, rice husks, and charcoal [57,66].

Furthermore, alternative fuels can be either gaseous, liquid, or solid, where solid fuels are most widely utilized [28]. The fuels may be further subdivided into various categories relating to e.g. size [10].

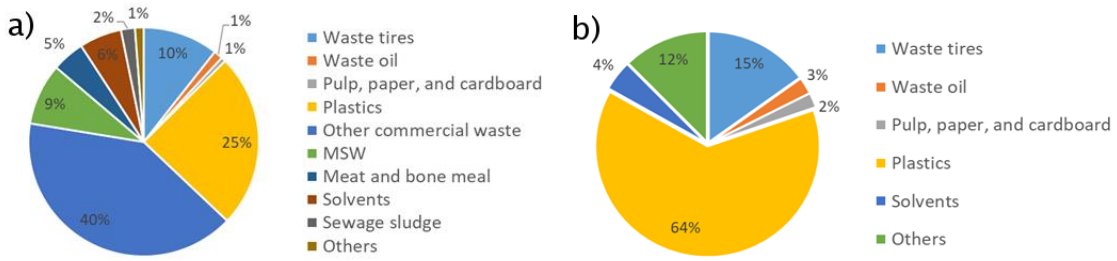

Figure 3-2: Distribution of alternative fuels in the German (a) and Austrian (b) cement sectors in % of annual thermal use in 2015 [67,68].

Figure 3-2 shows the distribution of various kinds of alternative fuels in the German and Austrian cement sectors. These countries utilize some of the highest amounts of alternative fuels. It is seen that the largest fraction of fuel is plastics and commercial waste. Waste tires also constitute a large fraction of the fuels used in these countries. The use of biomass derived fuels: paper, sewage sludge, meat and bone meal, wood, and agricultural residue contribute less than 10 % of the thermal share in these two countries. An increased use of these fuels may be beneficial for the CO_2 emissions in the cement industry.

3.4.1 Solid Recovered Fuel

The largest fraction of alternative fuels in the German and Austrian cement industries is plastics and commercial waste. In a broader sense these fuels are typically called Refuse Derived Fuel, RDF, or Solid Recovered Fuel, SRF.

There appears to be no clear definition of RDF in the literature. Typically, RDF is meant as the combustible fraction of municipal solid waste, but the definition can also be broader covering a range of different commercial wastes such as: packaging, tires, biomass, and waste oils [69]. Within the European union SRF is defined as "*fuels prepared from nonhazardous waste to be utilized for energy recovery in waste incineration or co-incineration plants regulated under community environmental legislation*" [70]. The quality of SRF is assured through a number of standards within the framework of the European Committee for Standardization Technical Committee 343 (CEN/TC 343) [71].

SRF is produced from municipal solid waste, industrial or commercial waste. The waste may be processed in mechanical or mechanical-biological treatment plants, where the combustible fractions of the waste are separated out to be utilized for co-combustion. The treatment differs depending on the source of the waste material and the quality requirements for the processed SRF [72]. Normally the treatment consists of various steps of shredding and sieving to reduce and homogenize the particle size and remove fines. The fines typically consist of non-combustibles or organic material with a high water content. Additional steps of the process are magnetic separators to separate out iron and use of Near Infrared (NIR) spectroscopy to separate out chlorine rich parts. Organic material can be removed by biological composting, which also dries the material due to the heat released by the biological decomposition [73]. The finished product has a more uniform quality, higher heating value, and lower moisture content than the raw waste [72].

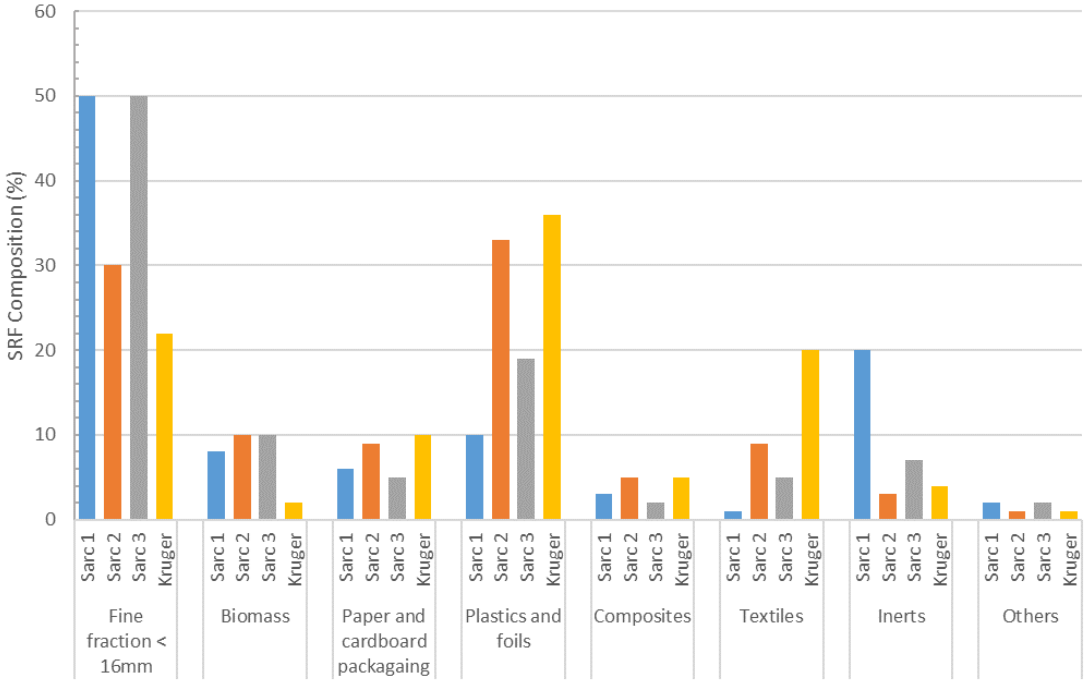

Figure 3-3: Composition of Solid Recovered Fuel based on visual sorting [74,75].

An example of the composition of different SRF's based on the works of Sarc and Lorber [75] and Krüger et al. [74] is shown in Figure 3-3. The figure underlines the differences between SRF from different sources. The largest part of the SRF is fines, which are particles less than 16 mm, and thus difficult to define. Plastics also contribute a large fraction of the SRF composition and so does textiles and paper.

The SRF can also contain significant amounts of inert materials such as metals, glass, and stones.

The wide difference in SRF composition is also mirrored in the combustion behavior of the fuel. Fuel rich in paper and plastics tends to have a high heating value, while fuel rich in biomass and inerts has a low heating value [75].

The composition of SRF varies widely from different manufacturers [73], but the quality from a single supplier can also vary substantially based on the origin of the source material [75,76]. Vainikka et al. [77] reported on the fuel quality from one supplier of SRF where the SRF was sampled over 4.5 years. Table 3-3 shows the large span of quality that was found in the study.

Table 3-3: Example on the quality variation of SRF. Measurements based on one SRF supplier over 4.5 years [77].

	Min.	Mean	Max.
Moisture (wt% as received)	7.9	16.7	40.4
Ash (wt% dry matter)	4.5	8.9	20.2
Lower Heating value (MJ/kg as received)	13.3	19.0	24.2

Some cement plants have a direct discharge of SRF from trucks to firing in the kiln without intermediate storage. This can obviously result in significant changes when trucks from different suppliers are handled. Other cement plants have an intermediate storage, where the SRF is mixed and homogenized prior to use. An example of such a system is the FLSmidth Feedex reclaimer [78]. This will to some extent lower the short-term variations in fuel quality, but not eliminate it completely.

3.5 Challenges of Alternative Fuels Firing

The benefits of utilizing alternative fuels in the cement industry have been outlined above in chapter 3.2. However, the utilization of alternative fuels also introduces some challenges since most alternative fuels are vastly different from conventional fossil fuels. This chapter will give an overview of some of the challenges typically encountered when using alternative fuels.

3.5.1 Experiences of Alternative Fuels Co-Firing

Lockwood and Oy [79] presented an early review of RDF co-firing in a cement kiln. They noted that the RDF combustion requires more combustion air and generates more flue gas, which reduces the thermal efficiency of the kiln. Thus, the specific heat consumption is increased, and production may be limited, if the kiln system cannot cope with the increased flue gas amount. They concluded that the upper limit of RDF use would be 10-15 percent of the total fuel consumption.

The Cemflame 3 experiments [80] aimed to evaluate the effect of co-firing coal with different alternative fuels, such as sewage sludge and plastic waste. Experiments were made in a pilot scale cement kiln simulator of 9 m length and 0.78 m in diameter. In total, 240 different flames were investigated. The main problems of the alternative fuels are their particle size, which results in lower combustion and heat release rates than the solid fossil fuels. It was recommended that the specific surface area of particles should be at least 100 m^2/kg (approximately corresponds to $d_p =$ 600 µm for $\rho_p = 1000$ kg/m^3), to obtain burnout in the gas phase of an industrial cement kiln.

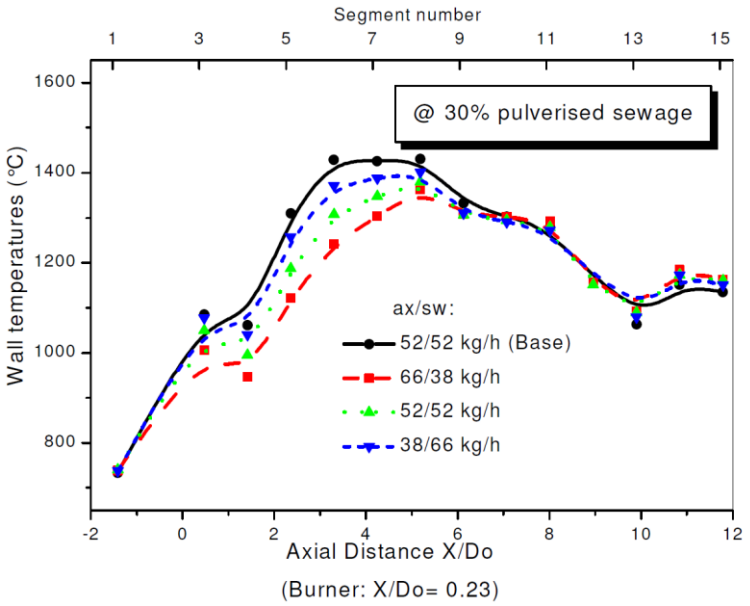

Figure 3-4: Effect of the amount of swirl and axial air on a flame co-fired with 30 % pulverized sewage sludge and comparison to coal flame (base). The temperatures are measured as kiln wall temperature [80].

The influence of burner settings was also investigated in the Cemflame 3 experiments. The swirl could help move the ignition point of the co-fired flame

closer to the burner and increase flame temperatures. This in turn increases the heat flux to the kiln simulator wall and the temperature of the wall. An example is shown in Figure 3-4 for a flame co-fired with 30 % pulverized sewage sludge. It is noticed how the cofired flame results in lower wall temperatures than the baseline coal flame. For the co-fired flame, the wall temperature is increased by increasing the swirl air.

Ariyaratne et al. [81,82] have made some detailed tests of the influence of co-firing meat and bone meal (MBM) [81] and solid hazardous waste (SHW), which consisted of organic solvents mixed with wood chips [82]. In these tests, the co-firing rate was increased stepwise, and the effect on clinker quality and other operational data were measured. The data from the MBM tests are shown in Figure 3-5. The main limitation was found to be an increased free lime content in the clinker, which was believed to be caused by lower flame temperatures [83,84]. CaO and P_2O_5 in the MBM ash could also have a negative impact on free lime content. It was found that the upper limit for co-firing was 20 and 40 % of the energy input, for the SHW and MBM, respectively. The SHW had a considerably larger particle size, which explains its lower co-firing limit.

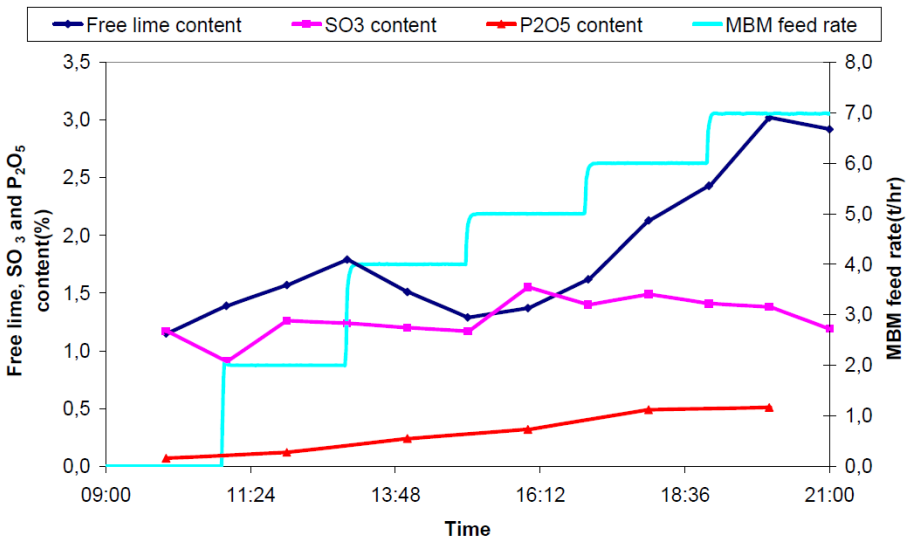

Figure 3-5: Free lime, SO_3, and P_2O_5 content in clinker for different MBM feed rates [81].

Nørskov [31] studied the effect of injection velocity of dried sewage sludge on the kiln system. It was found that an injection velocity of 30 m/s was to be preferred compared to 48.5 m/s. With the high injection velocity, it was possible to achieve up

to 6 % substitution of the petcoke energy, but with the low injection velocity 10-12 % substitution was achieved. The low injection velocity results in more fuel burning closer to the burner, which releases the fuel energy in the clinker burning zone, where it is required. With the higher injection velocity, more fuel energy is released downstream of the clinker burning zone. The main limitation of sewage sludge use turned out to be a higher evaporation of sulfur, which led to blockings in the calciner. To reduce the sulfur evaporation, it was necessary to increase the kiln inlet oxygen concentration from 1-2 vol% to 5 vol%.

The examples presented here demonstrates common issues encountered when co-firing alternative fuels. The different limitations will be discussed in further detail in the following chapters.

3.5.2 Fuel Composition

The composition of alternative fuels is different from fossil fuels, as indicated in Table 3-4. Typically, the volatile content will be higher and consequently the char/fixed carbon content will be lower. This is most likely a positive attribute of the alternative fuels, since fuel with a high volatility are easier to ignite. In addition the char that is produced from biomass is also more reactive than coal char [85]. For pine wood particles of around 3 mm in diameter combusted in 20 % oxygen, the devolatilization and char burnout both takes approx. 2-4 seconds [86]. When the oxygen concentration is lowered to around 10 %, the char combustion takes 4-5 times as long as the devolatilization [87]. Consequently, the char combustion is highly dependent on the amount of oxygen available, while the devolatilization only requires sufficient heat, and when the volatiles are released they burn quickly, if they can be mixed with oxygen.

The minor elements contained in alternative fuels can be mixed with the clinker in the kiln and have a significant impact on the clinker reactivity or the process stability [88]. The most significant species are sulfur and chlorine. Sulfur can be beneficial in low amounts in the clinker, since $CaSO_4$ melts at low temperatures and acts as a fluxing agent in the kiln [13]. However, sulfur in excess of 1.2 % may decrease the alite content and stabilize belite and free lime [13,89]. Excessive chlorine in the clinker may cause corrosion of steel reinforcement in the final concrete [13] and the level of chlorine in Portland cement is typically limited to 0.1 % [4]. The impacts of

circulation of these species is discussed in chapter 3.5.7. While the sulfur content of SRF is low, the chlorine content is relatively high compared with coal or petcoke.

Table 3-4: Proximate and ultimate analysis of select fuels used in the cement industry.

Parameter	Unit	Bitum. coal[a]	Pet-coke[b]	Oil[c]	Pine Wood[d]	Polyet-hylene[d]	SRF[e]	MBM[f]
Moisture	wt% a.r.	3.0	-	-	8.4	0	16.7	4.0
Volatiles	wt% dry	39.4	11.0	-	81.5	98.6	70.8	63.4
Ash	wt% dry	14.1	1.2	-	0.1	1.4	8.9	28.2
Fixed Carbon	wt% dry	46.5	87.8	-	18.4	0.03	13.2	8.3
C	wt% dry	68.7	86.5	85.7	51.6	83.7	54.7	49.1
H	wt% dry	4.9	3.6	10.9	6.1	15.5	7.7	7.2
N	wt% dry	1.1	1.8	0.2	0.1	0.01	0.7	10.1
S	wt% dry	1.8	5.5	2.6	0.1	0	0.18	0.5
O	wt% dry	9.5	1.7	0.5	42.0	0	36.7	4.9
Cl	wt% dry	0.03	0.02	-	0	0	0.41	0.20
Na	wt% dry	0.08	0.05	-	0	-	0.14	0.42
K	wt% dry	0.38	0.42	-	0.02	-	0.09	0.08
LHV	MJ/kg dry	27.8	34.1	40.2	19.0	42.2	23.2	19.4

a: Data from [90] based on average of 11 samples. Na and K content from [91] based on 5 samples.
b: Data from [92] based on average of 22 samples. Cl, Na, and K from [93]
c: Data from [94].
d: Data from [95]. Na and K from [96]
e: Data from [77]. Volatiles and fixed carbon from [97].
f: Data from [83]; Cl, Na, and K content from [98].

Other trace elements that may influence the clinker quality are alkalis and phosphorous. Sodium and potassium are important for binding sulfur in the clinker, but may also inhibit alite formation or cause expansion of the concrete leading to cracking [14]. Phosphorous is especially high in meat and bone meal, and has a tendency to stabilize belite and lower the alite formation in the kiln [28,88].

3.5.3 Particle Size

Solid fossil fuels, like coal and petcoke are normally grinded to below 100 µm, before being fired in the kiln. This is necessary to ensure a fast heating and ignition of the fuels, as well as a fast burnout. However, the water content and soft paper and plastic fractions makes milling of SRF more problematic than milling of coal, and the metal and glass content of SRF may result in significant wear of the mills [99]. Thus, comminution of the particles can be quite expensive, and it is preferably avoided. SRF particle size can be up to 100 mm [100], which can be utilized in cement calciners equipped with auxiliary combustion devices such as the FLSmidth Hotdisc

[101] or the Thyssenkrupp Prepol step combustor [102]. If direct firing in the kiln is desired, the particle size will have to be smaller, typically < 30 mm as determined by sieving [100].

The consequence of the larger particle size is a longer ignition and combustion time [87], which may move the combustion zone further into the kiln and reduce the flame peak temperature. In addition, unburnt particles can, depending on the residence time in the flame, fall unconverted into the clinker bed. Here the fuel depletes the oxygen, resulting in local reducing conditions, which is described in further detail in chapter 3.5.6.

Normally, 40 % of the fuel energy needed in the cement process is fired in the kiln, while the rest is fired in the calciner [31]. Due to the longer combustion time of SRF, the fuel energy may not be released in the clinker burning zone, but rather further upstream in the kiln. This may lead to a higher share of fuel in the main burner of between 50-60 % of the total thermal input. Thus, the alternative fuel is used to substitute calciner firing, rather than fossil firing at the main burner.

3.5.4 Moisture Content

The moisture content in SRF is generally high and may vary between 10-40 %, as seen in Table 3-3. This has primarily three negative effects on the fuel: increased density, increased conversion time, and lower peak temperature.

The moisture content in the fuel will increase the particle density, which makes wet particles heavier than dry ones. An increased particle mass will influence the particle terminal velocity and inertia. Consequently, it will be more difficult to keep wet particles in suspension in the kiln and influence the particle flow by the burner primary air.

Increased moisture content increases particle conversion times, since additional energy is required to evaporate the water and heat the particles. For wood particles this results in a delayed ignition time, which may be increased by a factor 10 [87], when the moisture content is increased from 10 to 40 wt%. The devolatilization time may be increased by a factor 2 [87,103]. This will evidently move the main combustion zone further into the kiln and increase the risk of non-complete particle conversion.

Lastly, the moisture content significantly reduces the peak temperature in the combustion zone, since less heat is carried per unit of fuel and significant amounts of energy is used to evaporate the added water. The effect of the moisture on the temperature can be sketched by calculating the adiabatic flame temperature at different moisture contents, as shown in Figure 3-6. Here it is seen that increasing the moisture content of SRF from 0 to 50 %, may decrease the adiabatic flame temperature by more than 500 °C. Since the heat transfer from gas to clinker bed is mainly radiation based and highly dependent on the temperature, such a temperature difference may result in significantly lower heat transfer rates.

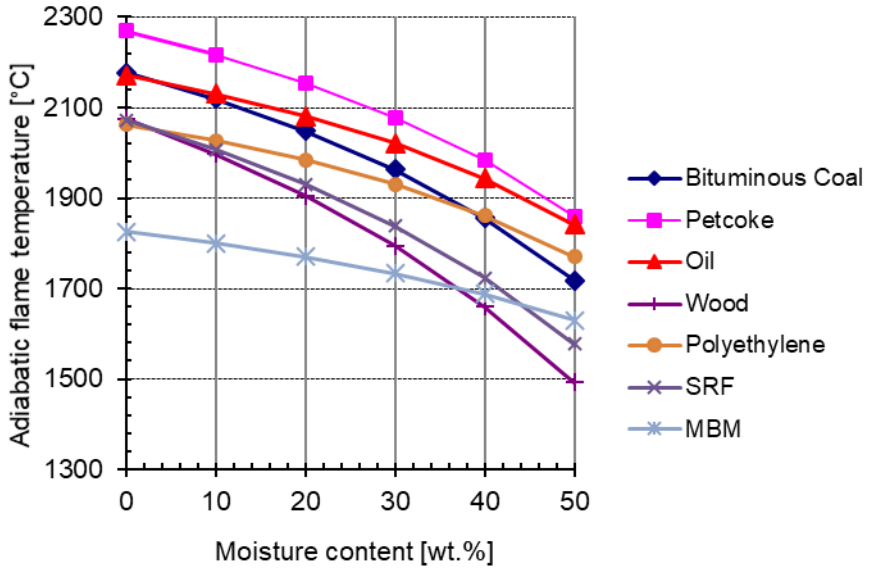

Figure 3-6 Adiabatic flame temperature for various fuels from Table 3-4 calculated at different moisture contents at an air to fuel ratio of 1.

3.5.5 Kiln Dust

A high dust load in the rotary kiln can be very problematic since it limits heat transfer from the flame to the clinker bed. Inside the kiln, saltation is the main form of particle entrainment [104]. Saltation is a type of particle transport where large particles are picked up by the air, but due to their size they fall back into the bed, rebounding or ejecting other particles [27]. If light particles are present they may follow the gas flow out of the kiln [105]. The most influential parameter on particle elutriation and dust formation is thus the average gas velocity [104]. Saltation is limited in the burning zone where the clinker melts and form nodules [105].

However, an insufficient temperature and melt formation limits agglomeration and dusty clinker can be formed [25]. If under-burnt clinker enters the cooler, large amounts of fine dust particles are carried with the secondary air into the burning zone limiting the visibility and severely cooling the burning zone [34].

3.5.6 Reducing Conditions

As mentioned in section 3.5.3, one of the disadvantages of the large particle size of most alternative fuels, is that fuel may drop unconverted to the clinker bed, consume the oxygen and result in local reducing conditions.

One adverse effect of reducing conditions is that Fe^{3+} can be reduced to Fe^{2+}, which results in a loss of ferrite phase (C_4AF) and an increase in aluminate content (C_3A). The formed FeO may also substitute CaO in C_3S. Thus, an effective increase of LSF, SR, and AR is observed, and the clinker becomes harder to burn. To compensate, the temperature needs to be raised, creating larger alite crystals and a poorer cement quality. FeO can also replace CaO in the alite, which is more prone to decompose to belite and free lime upon cooling, and with a lower alite content the compressive strength of the cement is lowered [106,107]. The adverse effects of reducing conditions may to a high extent be lowered if the clinker is rapidly cooled from above 1250 °C in air [107].

The indicator for reducing conditions in the kiln is typically a brown color of the clinker, especially in the center, compared to its normal dark grey. It is the calcium aluminate ferrite (C_4AF) that colors the cement. Pure C_4AF is brown, but when magnesium ions (Mg^{2+}) are incorporated in the crystalline phase, the color changes to grey. When the iron is reduced from Fe^{3+} to Fe^{2+}, under reducing conditions, it can displace the Mg^{2+}-ions, which affects the color of the clinker [107,108]. It is normal for some Fe^{3+} to be reduced to Fe^{2+} in the hottest parts of the kiln, but it will normally be re-oxidized during cooling, if oxygen can diffuse into the center of the clinker nodules. Thus, peak temperatures and clinker nodule size and porosity also affects the clinker color [109]. If the clinker produced in a reducing atmosphere is rapidly cooled from above 1250 °C in oxidizing conditions, the brown color can be avoided [107].

3.5.7 Circulation of Volatile Species

Under normal kiln conditions, evaporation of sulfur, chlorine, and alkali occurs in the hot parts of the flame zone. The volatility is heavily influenced by temperature, retention time in the burning zone, particle size, and concentration of sulfur and oxygen in the kiln atmosphere [110]. Since the escape of volatile species from the solids is dependent on the particle size and surface area, it will be most prominent during the early stages of clinkering, before the grains have sintered together [111]. The species that do not fully evaporate in the kiln, leaves the kiln with the clinker.

The evaporated species are transported with the kiln gas towards the inlet of the kiln, where they may condense on or react with the colder dust from the preheater and calciner. In this way, the volatile species are returned to the kiln, and a circulating pattern is established, which can lead to accumulation of volatile species in the kiln. As the concentration of volatile species increase they can condense on surfaces in the kiln, preheater or calciner, where it can lead to blockages and ring formation, severely affecting the process operation by a restriction of material and gas movement. [13].

Local reducing conditions can enhance the evaporation of sulfur, which can take place at lower temperatures than in oxidizing conditions. The sulfur release is e.g. enhanced by the reaction with CO in R 3.1 or the shift of equilibrium in R 3.2, when oxygen is depleted [112]:

$$\boldsymbol{CaSO_4(s) + CO(g) \rightarrow CaO(s) + SO_2(g) + CO_2(g)} \qquad \textbf{R 3.1}$$

$$\boldsymbol{CaSO_4(s) \rightleftharpoons CaO(s) + SO_2(g) + \frac{1}{2}O_2(g)} \qquad \textbf{R 3.2}$$

Measurements made in a pilot rotary kiln simulating the conditions of the kiln raw material inlet, indicate that the evaporation of sulfur mainly occurs if fuel devolatilization occurs in the clinker bed [54]. If these results are valid for the hotter parts of the rotary kiln, they may indicate that sulfur evaporation can be limited if fuel devolatilization occurs in suspension, while char oxidation can be allowed in the bed.

The sulfur can form different chemical compounds, depending on the availability of other species in the kiln, which may influence the volatility of sulfur. The following order of combination of the volatiles has been observed [110]:

1. Chlorine has a strong affinity for K and Na and forms KCl and NaCl. The remaining chlorine forms $CaCl_2$.
2. The residual alkalis combine with sulfur to K_2SO_4 or Na_2SO_4. If an excess of alkali is present they can be present as carbonates or hydroxides [112].
3. The residual sulfur combines with calcium to form $CaSO_4$.

The volatility of chlorine is very high and normally most of the chlorine evaporates in the burning zone of the kiln. However, the volatility of sulfur is very dependent on the specific compound. At the high temperatures in the kiln $CaSO_4$ is fairly volatile, while alkali sulfates are less volatile. Thus a measure for the tendency of sulfur evaporation is given by the sulfur modulus (MSO_3), calculated based on the mass fraction of sulfur, potassium, and sodium [23]:

$$\boldsymbol{MSO_3 = \frac{\frac{Y_{SO_3}}{80}}{\frac{Y_{K_2O}}{94} + \frac{Y_{Na_2O}}{62}}} \qquad \textbf{E 3.2}$$

The coefficients of the equation are equivalent to the molar mass of the involved species. A MSO_3 value around 1 is considered sufficient to ensure a surplus of alkalis to combine with the sulfur. In this case, the sulfur volatility (defined in E 3.3) is in the range 0.3-0.5, while if there is a surplus of sulfur over alkalis most of the sulfur evaporates and the volatility is 0.9-1. Generally, a value above 0.7 indicates too high sulfur recirculation, meaning that sulfur will accumulate in the kiln system. The volatility is defined as [110]:

$$\boldsymbol{SO_{3,vol} = 1 - \frac{Y_{SO3}\ clinker}{Y_{SO3}\ hot\ meal}} \qquad \textbf{E 3.3}$$

Another definition of the SO_3 available to form $CaSO_4$ is given as excess SO_3. The formula is given in E 3.4 and indicates the amount of sulfur not bound by alkali sulfates. If there is no significant excess SO_3 the sulfur volatility will be low around 0.35, but it will increase with additional excess SO_3 [113].

$$\boldsymbol{Excess\ SO_3 = Y_{SO3} - 0.85\ Y_{K2O} - 0.65\ Y_{Na2O}} \qquad \textbf{E 3.4}$$

The build-ups in the kiln and preheater are primarily a mixture of K_2O, SO_3, CaO, and Cl^-, the exact combination differs widely depending on the location and the operating conditions at the specific plant [114]. Common minerals found in rings and deposits in the kiln and preheater are listed in Table 3-5.

Table 3-5: Typical compounds found in deposits in the cement kiln and preheater [23,112].

Name	Formula	Typical Location
Spurrite	$(2CaO{\cdot}SiO_2)_2{\cdot}CaCO_3$	Lower cyclones
Ellestadite	$Ca_{10}(SiO_4)_3(SO_4)_3X_2$ Where X = OH, F, Cl	Riser duct
Sulfospurrite	$(2CaO{\cdot}SiO_2)_2{\cdot}CaSO_4$	Kiln rings
Anhydrite	$CaSO_4$	Cyclones and riser duct

While the sulfur content in alternative fuels such as SRF is significantly lower than that of coal or petcoke, and the alkali content is similar, the chlorine content is significantly higher, see Table 3-4. The build-up tendency in the kiln and preheater is significantly increased when both sulfur and chlorine is present, as indicated by Figure 3-7. This explains the potential increased deposit formation from alternative fuels, even though the sulfur input from the fuel is significantly lowered. KCl promotes the formation of deposits, either by condensing on lime dust to form a sticky surface leading to agglomeration and build-ups [115] or acting as a mineralizer in the formation of spurrite [116]. Another adverse effect of high chlorine concentration is that it promotes corrosion in the kiln [117].

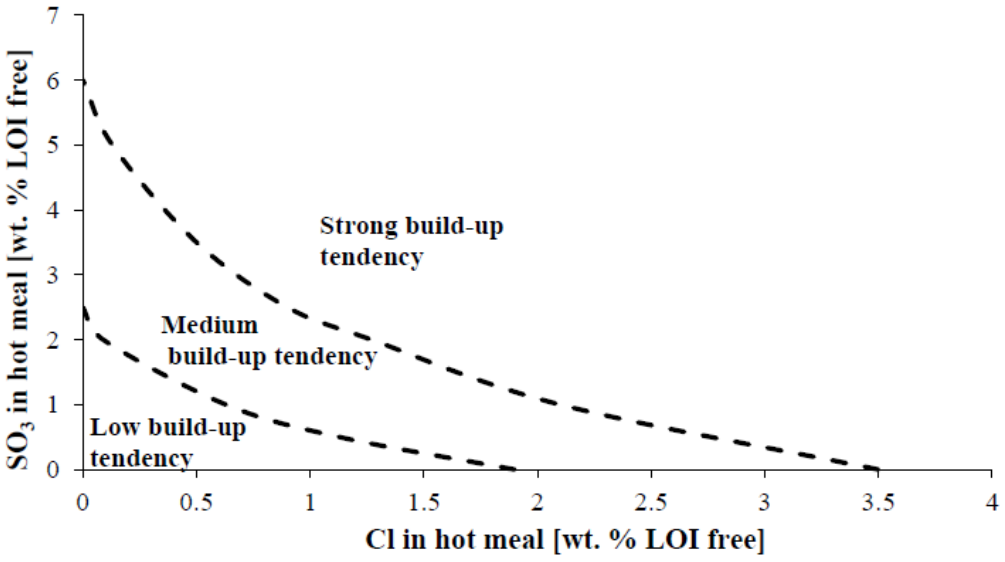

Figure 3-7: Build up tendency as function of SO_3 and Cl in the hot meal [112].

A more detailed description of the circulation of volatiles, especially sulfur, is given by Choi and Glasser [111], Nielsen et al. [14,53,118], and Cortada Mut et el. [54,112,119].

3.5.8 Chlorine Bypass

To minimize the problems caused by recirculating species and deposits, a bypass can be installed at the kiln inlet. This is typically needed to achieve high degrees of alternative fuels firing, without excessive build-up problems. The bypass works by extracting a fraction of the hot air at the kiln inlet, where the concentration of chlorine is high. The hot air is then mixed with cold air in a quench chamber in order to condense the chlorine [28].

A disadvantage of a kiln bypass is that hot gas is removed from the preheater causing a considerable heat loss. Additionally, large amounts of bypass dust has to be disposed of [120]. In order to decrease the heat and material loss, the particles can be separated in a cyclone, since small particles have a high concentration of chlorine, while the large particles are mainly cement raw meal and can be returned to the kiln [120]. At plants utilizing large amounts of alternative fuels, the bypass dust amount can reach as much as 10,000 ton per year [121]. Thus, the companies Holcim and A TEC have developed a system called ReduDust, where the chlorine is removed from the bypass dust. This creates a KCl rich salt that can be sold for industrial purposes and the cleaned bypass dust can be used in the cement grinding [122].

3.6 Summary and Conclusions

There are several considerations to make when a fuel is selected for use in the cement kiln. Fuel cost, environmental impact, and potential impact on the kiln process are some of the factors that should be considered. Traditional use of fossil fuels account for approximately 30 % of the operating costs at a cement plant. Thus, a high incentive to use cheaper alternative fuels is present. Furthermore, the utilization of waste fuels can divert waste away from landfills and partly biogenic fuels has the potential to reduce CO_2 emissions.

The most common alternative fuels include shredded tires, meat and bone meal, and Solid Recovered Fuel (SRF). The properties of most alternative fuels are very different from fossil fuels. The main challenges are related to a larger particle size,

higher moisture content, and decreased combustion temperatures. Consequently, the introduction of alternative fuels can cause different issues in the cement kiln. Decreased temperatures can cause a lower cement quality and potentially increase amounts of dust in the kiln. The longer combustion time can result in unconverted fuel in the bed, which induces local reducing conditions. This can promote sulfur recirculation, which may cause blockages in the kiln system. Another adverse effect of reducing conditions, is the discoloration of clinker and reduced quality.

The discoloration and lower clinker quality caused by reducing conditions, may to some extent be reverted if the clinker is rapidly cooled in an oxidizing atmosphere. Sulfur evaporation may be limited if the fuel undergoes devolatilization before it enters the bed.

4 KILN PROCESS MONITORING

Monitoring and control of the kiln combustion is paramount for obtaining a good product quality as well as stable and economical production. As already discussed in previous chapters the quality of alternative fuels can change quite drastically over time, especially SRF as seen in Table 3-3. As an example, the moisture content and the heating value may change, which can alter the temperature in the clinker burning zone. Thus, monitoring of the combustion is particularly important when dealing with high amounts of alternative fuels.

This chapter aims to give an overview of methods that can be used to monitor the cement kiln processes. The measures discussed here can help determine how co-firing with alternative fuels influence the kiln. As such the methods are important for the industrial tests, described in chapters 5 and 6.

4.1 Clinker Quality

The primary objective of the kiln is to create a cement clinker of high quality. This is achieved as a combination of residence time and temperature in the burning zone. If the burning zone is too cold or the clinker passes through it too quickly, it will result in under-burnt clinker. In the under-burnt clinker, the clinker reactions have not reached a sufficient conversion, which results in reduced reactivity and strength of the concrete. In addition, high amounts of free lime may create destructive expansion [13]. Conversely, if the clinker is over-burnt at too high temperature or time, the clinker mineral crystals grow too large, and the clinker will be difficult to grind [17].

As an indicator for the completeness of the clinkering reactions the free lime content is often used. The free lime content is the CaO in the clinker that has not combined with SiO_2, Al_2O_3, or Fe_2O_3. If the free lime content is increasing, it indicates that the burning zone is cooling, and vice versa. The free lime content should normally be around 1 % (Table 2-1). The simplest method for measuring if the clinker is burnt correctly is to fill a cone of 1 litre volume and fill it with loosely packed clinker. The mass should preferably be in the range around 1.25-1.35 kg/l. A lower density indicates under-burning, while a higher density indicates over-burning [13]. More precise measurements of free lime content are also available [123].

Today, X-ray fluorescence (XRF) and X-Ray diffraction (XRD) methods are used in many cement plants. The methods give a possibility to determine the complete elemental analysis (XRF) and quantify the crystalline phases (XRD) of the clinker. XRD is a powerful tool that can be used to directly measure the clinker phases and amount of free lime, and thus directly gives a measure of the clinker quality [124,125]. The plant operator can use this information to determine if the clinker is adequately burned and make appropriate adjustments.

A drawback of using clinker measurements as the primary means of control is that there is a significant time lag between the time of sampling and the analysis. Typically, it might take up to 45 minutes from a clinker is discharged at the cooler until it is ready in the laboratory. Furthermore the analysis may take between 30 and 90 minutes [17]. Thus, it is also important for the operator to keep an eye on other more rapid, but indirect measures, to monitor the kiln.

4.2 Burning Zone Temperature

The burning zone temperature is important to monitor closely. The temperature can be measured in different manners through e.g. thermocouples, radiation pyrometers or acoustic pyrometers [126]. The use of thermocouples can often be used to measure the secondary air temperature in the kiln hood and the temperature in the kiln inlet. To measure the temperatures in the flame or burning zone, pyrometric methods based on infrared light are normally used [127]. Other indicators of the burning zone temperature are NO_X in the kiln inlet or kiln torque.

4.3 Gas Measurements

The gasses at the kiln inlet are normally measured for the contents of O_2, CO, and NO_X, which gives an indication of the quality of combustion and conditions in the kiln. The benefits of monitoring the kiln off gases are e.g. kiln performance gains, energy conservation, emission reductions, and improved production quality [128].

The measurement of oxygen at the kiln inlet is important for controlling the combustion in the kiln. If the oxygen concentration becomes too low there is a risk of reducing conditions, which impacts clinker quality and sulfur evaporation as discussed in chapters 3.5.6 and 3.5.7. In addition, the presence of CO in the kiln inlet may be increased if insufficient oxygen is present. This can result in a heat loss and significant pollution, if it is not oxidized in the calciner. On the other hand, a too high oxygen content results in a diluted off gas with lower peak temperature, since the excess air needs to be heated by the combustion. The oxygen content at the kiln inlet should preferably be in the range 0.7-3.5 % [34].

Measuring the NO_X level in the kiln inlet can give an indication of the burning zone temperature [127]. The majority of NO_X from the cement kiln is thermal NO_X, while smaller amounts are fuel and prompt NO_X , thus the formation is highly dependent on the temperature in the burning zone [129]. The NO_X level from the kiln may be reduced in the calciner where fuel is injected into oxygen deficient areas [129].

Getting reliable gas measurements at the kiln inlet can, however, be difficult. The high temperature, high dust load, as well as corrosive and condensable species in the kiln inlet challenge the design of gas extraction probes. The design of probes must entail cooling, cleaning and gas extraction, but the complex design is also more prone to failure [128].

4.4 Kiln Torque

The measurement of the kiln torque, as main drive power consumption or amps, can give a relative estimate of the kiln burning zone temperature. As the temperature increases in the kiln the amount of molten material in the kiln will also increase. This causes the material in the kiln to be carried further up the side of the kiln as it rotates, which increases the required torque to rotate the kiln. The amount of material in the kiln also affects the torque. If e.g. the coating thickness changes, this

can also influence the kiln torque [17]. The power consumption is a function of the torque required to turn the kiln and the rotational speed:

$$P_k = 2\pi n T_q \qquad \text{E 4.1}$$

Here P_k is the power consumption of the kiln, n is the rotational speed (rot/s) and T_q the torque.

4.5 Kiln Cameras

Cameras can be placed in the kiln hood of the cement kiln and be used to observe the near burner region of the kiln. A typical flame image from a kiln camera is shown in Figure 4-1. Using this information, it can be monitored how the flame ignition point, shape, or intensity changes when e.g. changing fuels and the operators can adjust accordingly.

Figure 4-1: Image from a kiln camera showing the combustion in the kiln [130]. The hot clinker bed can be seen on the left side. Unignited pulverized fuel is seen directly in front of the burner. The combustion zone (bright area at center) is further removed from the burner.

The German Cement Works Association (VDZ) has used kiln cameras to evaluate the effect of fuels and burner settings on the kiln flame. However, only very sparse information was published on this area [30,131]. There are also examples in the literature of such cameras being used for modeling and control of the kiln process. Lin et al. [130] have attempted to predict the NOx emission from a cement kiln based on partial least squares regression (PLSR). They showed the information from a camera in combination with regular process measurement can be used to give a

better prediction of NOx than using the process measurements alone. The company Powitec [132] also uses flame images in their automatic control for kiln burners.

4.6 Kiln Scanners

Another method to monitor the kiln is the use of infrared scanners to measure the temperature of the outside kiln shell [133]. The kiln scanner can be used to monitor for high temperatures on the kiln shell, so called hotspots, which may indicate damage to the refractory or loss of coating. The kiln shell temperature will also change depending on the temperatures inside the kiln. Nørskov [31] showed how co-firing with dried sewage sludge can affect the kiln shell temperature profile, as shown in Figure 4-2. Lower temperatures are seen in the area 22-27 m, and higher temperatures are seen around 18-20 m, which may indicate spilling of the alternative fuel into the clinker bed in this area.

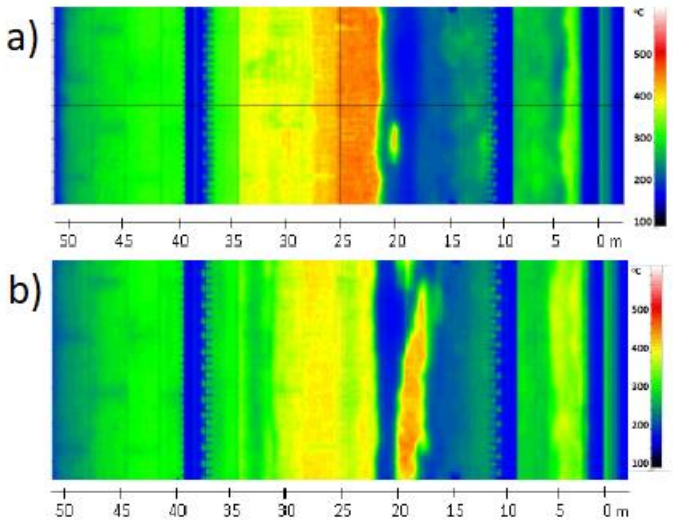

Figure 4-2: Kiln shell temperatures when firing petcoke (a) and co-firing with 10 % sewage sludge by energy (b). Temperatures are lower around 22-27 m when co-firing, but higher around 18-20 m [31].

4.7 Measures Against Changing Conditions

If the conditions in the kiln changes, there are several control options possible for the kiln operator, to revert the kiln back to stable conditions.

If the oxygen concentration becomes too low or CO spikes are observed in the kiln off gasses, not enough air is available in the kiln. The air level can be increased by increasing the draft in the kiln by adjusting the ID fan.

The burner primary air, axial and swirl air, can be used to influence the flame shape. If the burning zone is too cold, it might be necessary to increase the flame intensity, which can be achieved by a higher momentum or swirl air. If hot spots on the kiln scanner are detected, the temperature may be too high, or the flame can be impinging on the refractory. This might be remedied by lowering the swirl, which tends to narrow the flame.

Plants that fire large amounts of alternative fuels normally also utilize a fossil fuel such as coal or petcoke. If the burning zone temperature decreases due to e.g. too much water in the alternative fuel, it will be common to increase the amount of fossil fuel, to increase the temperature.

The kiln rotational speed can be used to control the residence time of the clinker in the kiln. If the clinker is overburnt, the residence time in the burning zone can be reduced by increasing the rotational speed of the kiln.

If the other factors fail to make an impact it is also possible to change the kiln feed. With a lower kiln feed, it is easier to adequately burn the clinker, and the kiln will be less sensitive to changes.

Furthermore, it is also possible to increase the firing in the calciner to increase the calcination degree, which lowers the fuel requirement in the kiln.

4.8 Summary and Conclusions

To ensure a good and stable product quality it important to monitor the kiln process. This is especially the case when utilizing alternative fuels, as their quality, e.g. moisture content and heating value, can change significantly over time, which can influence the combustion process. The quality of clinker samples can be determined by use of X-ray fluorescence (XRF) and X-ray diffraction (XRD). However, it is also important to monitor more indirect measures, which offer a quicker response. These include e.g. gas measurements, burning zone temperatures, and the kiln torque. Changes to the kiln flame, such as intensity and ignition point, can be monitored via a camera.

5 Effect of Alternative Fuels Co-firing on Kiln Flame

The experimental part of this PhD project constitutes two studies that were made in industrial cement kilns. Furthermore, a characterization study of SRF was made to obtain parameter inputs for combustion modeling purposes.

The first study, described in this chapter, investigates the effect of alternative fuels co-firing on the cement kiln flame. This was done with a camera specially developed to be inserted in the kiln hood, close to the flame. This allows for detailed imaging of the flame. Measurements were performed at three different cement plants. At one of these plants the kiln burner was changed to the FLSmidth Jetflex burner, which allows for a comparison of two burners. This work has been published as:

M. N. Pedersen, M. Nielsen, S. Clausen, P. A. Jensen, L. S. Jensen, and K. Dam-Johansen, "Imaging of Flames in Cement Kilns To Study the Influence of Different Fuel Types," *Energy & Fuels*, vol. 31, no. 10, pp. 11424–11438, 2017.

The second study sought further details into the possibilities of adjusting the flame of the Jetflex burner. Furthermore, it was investigated how the burner settings can influence co-firing. Details of these experiments can be found in chapter 6.

The characterization study of SRF can be found in chapter 7. The results of the study have been written into an article manuscript that has been submitted to the journal Energy and Fuels:

M. Nakhaei, M.N. Pedersen, H. Wu, D. Grevain, L.S. Jensen, P. Glarborg, P.A. Jensen, K. Dam-Johansen, "Aerodynamic and Physical Characterization of Refuse Derived Fuel," *Energy and Fuels (Manuscript)*.

5.1 Description of Test Cement Plants

Measurements were carried out at three different European cement kilns all producing ordinary Portland cement clinker. Brief details of the plants are given below. Details of the fuels used at each plant are collected in Table 5-1.

Plant 1 produces around 3,500 ton clinker per day and has a kiln with a diameter of 5 m and 77 m length. It is equipped with a 5 stage preheater, in-line calciner, and an FLSmidth HOTDISC device, primarily burning coarse SRF, providing energy to the calciner. Under normal conditions approx. 65 MW is fired in the kiln with 70 % of the energy being from SRF and the remainder from petcoke. The plant maintains a kiln inlet oxygen concentration of 4-5 %.

Plant 2 operates a semi-dry process with a capacity of 4,300 ton of mineralized clinker per day. It is equipped with a 2-string 5 stage preheater and in-line calciner, where the main fuel is SRF supplemented by coal. The kiln has a diameter of 4.75 m and is 74 m long. In the kiln, the fuel energy input is 70 MW with the main fuel being a mix of 75 % coal and 25 % petcoke. As alternative fuel SRF or granulated tires can be used in amounts of up to approximately 10 or 30 % of the energy input, respectively. The oxygen concentration at the kiln inlet is 5-6 %.

Plant 3 has a clinker capacity of 3,100 ton per day in a kiln of 5 m in diameter and length of 68 m. The plant has a 5-stage preheater, an in-line calciner, and FLSmidth HOTDISC, burning primarily whole tires and coarse SRF <120 mm. In the kiln, petcoke is used as the main fuel. The plant uses several types of alternative fuels in the kiln with the largest fraction being SRF and smaller amounts of dried sewage sludge or waste oil contributing up to 50 % of the energy in the kiln. The total energy input of fuel in the kiln is around 65 MW. Due to defunct equipment, the oxygen concentration at the kiln inlet was not monitored during the measurement campaign; however, it is likely around 5 %.

The three plants have different burners from major burner suppliers. At plant 1 the burner was recently changed to the Jetflex burner from FLSmidth. This allowed a comparison of two different burners at the same site. The Jetflex burner is described in chapter 2.8.

Details of the fuels used at the three plants are shown in Table 5-1. The analysis of the fuel is on a wet basis. The samples for coal and petcoke listed for Plant 2 and 3 are taken from the stock at the respective plants. Thus, the moisture content is relatively high compared to that of Plant 1. Before being used in the kiln the solid fossil fuels are grinded in mills to a particle size < 100 µm and dried to a moisture content of approx. 2 % at Plant 2 and 0.6 % at Plant 3. An example of the SRF used at the different plants is given in Figure 5-1.

Table 5-1: Properties of the fuels utilized at the cement plants. Data are on an as received basis. Moisture and ash in coal and petcoke depends on sampling before (Plant 2 and 3) or after milling (Plant 1).

		LHV	Moist.	Ash	Vol.	S	Cl	Particle Size	Typical use
Plant	Fuel	MJ/kg	wt%	wt%	wt%	wt%	wt%		% or t/h
1	Petcoke	32.3	0.9	7.2	13.8	3.4	0.04	3.5 % > 90 µm sieve	20-40 % energy
1	SRF	17.5	19.8	15.5	45.9	0.5	0.66	< 30 mm	60-80 % energy
2	Coal	25.2	11.9	6	34	0.44	0.02	13 % > 90 µm sieve	7
2	Petcoke	30.7	8.8	0.58	9.8	5.89	44 (ppm)	13 % > 90 µm sieve	2
2	SRF	18.7	17.3	12.5	-	-	-	-	1.5
2	Granulated tires	34.4	1.5	6	-	-	-	-	3
3	Petcoke	31.9	6.1	1.3	11.8	5.5	-	3.5 % > 90 µm sieve	4
3	SRF	19.3	21.5	-	-	0.29	1	Max 30x30x2 mm	5
3	Sewage Sludge	13.8	9.2	28.2	-	-	-	-	1

Figure 5-1: SRF used at plant 1 (a), Plant 2 (b), and Plant 3 (c).

Another important aspect of how the burners operate, is the use of primary air which is used to shape the flame [30]. This is typically divided into axial air, which adds axial momentum to the flame, and swirl (radial) air, which may create internal recirculation zones and stabilize the flame [35,42]. Transport air is also used to pneumatically convey the fuel through the burner. In addition air is used to cool the burner, often called central air, and occasionally some air can be used to disperse alternative fuels [31]. Table 5-2 contains an overview of the primary air used at the kiln burners at the three different cement plants.

Table 5-2: Amount and pressure of primary air typically used in the burners at the three cement plants. Plant 3 uses a burner with no separate swirl air channel.

	Plant 1		**Plant 2**	**Plant 3**
	Old Burner	New Burner		
Primary Air Amount (m^3/h) (Excl. transport air)	12000	12000	6200	6600
Axial Air Pressure (mbarg)	230	210	300	220
Swirl Air Pressure (mbarg)	240	150	40	-
Other Air Pressure (mbarg)	50	10	70	100
Transport Air Amount (m^3/h)	4000	4000	4400	4200
Fraction Primary Air (% of total combustion air)	~20	~20	~13	~10

5.2 Kiln Camera Probe

The cameras used in the cement kilns are typically installed at the back of the kiln hood to be protected from the high temperatures in the kiln. However, the view can be obstructed by large amounts of dust in the kiln hood [130]. For this work, a portable kiln camera was developed. The camera used was an IDS camera (model number UI-5240CP-C-HQ) with a resolution of 1.3 megapixels and a maximum

framerate of 50 frames per second. The camera was placed in an approximately 2 m long water cooled probe, Figure 5-2a. The probe was made of concentric stainless steel tubes with cold (~10 °C) cooling water flowing at the center and the hot (~60 °C) return water at the outside. The camera lens was covered by a neutral-density filter, with optical density 1, to reduce the light intensity and protect the camera from thermal radiation. Compressed air is passed through the probe and helps keep the filter clean from dust and provides additional cooling of the camera. The camera probe can be inserted through the side of the kiln hood close to the burner tip as shown in Figure 5-2b+c. This makes it possible to get a clear image of the burner compared to conventional cameras, which are placed further away from the burner.

Figure 5-2: a) The camera inserted in the probe. b) Camera probe inserted through side of kiln hood. c) Camera probe inserted next to kiln burner.

5.3 Description of Flame Images

The main objective of this study has been to get an increased understanding of the effect that alternative fuels have on the flame in the cement kiln based on visual observations. Several hours of video footage under different operating conditions have been recorded at the cement plants included in this study. In the following sections those hours of video recordings are condensed into a few representative images of the flames.

The sketch in Figure 5-3a shows how the camera is inserted through the side of the kiln hood and the approximate field of view into the kiln. The Image in Figure 5-3b shows the typical view seen with the camera. On the right side of the image the burner tip is seen. The fuel is injected through the burner forming a dark flame plume, which expands and becomes wider as it moves away from the burner. At

some point the fuel is ignited, giving a bright high intensity region. Below the fuel plume, the hot clinker bed at the bottom of the kiln can be seen. Above the fuel plume the opposite kiln wall can be observed. It is slightly darker than the clinker, indicating a lower temperature. The camera can be moved around, which will change the view. For instance, the camera can be turned downwards under the fuel plume, to observe if fuel drops to the clinker bed.

In the following the ignition point is defined as the distance from the burner where a sudden change in image intensity is observed. The distance will be measured along the center of the fuel plume. In Figure 5-3b this is seen as the point where the dark fuel plume changes color to bright yellow/white. As seen in the image this occurs earlier at the top and bottom of the flame plume compared to the center, but the center value will be used as the ignition point.

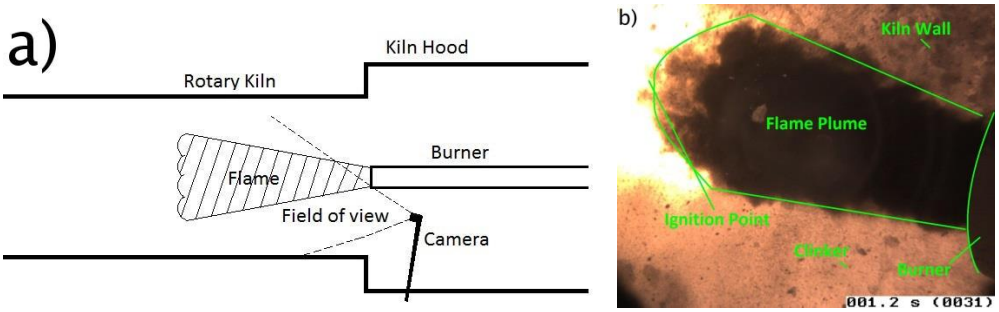

Figure 5-3: a) Sketch of the camera view (top view). b) Explanation of camera view.

The cement flame is characterized by a high degree of turbulent motion, which means that it is constantly fluctuating. In addition, there can be various amounts of dust in the kiln, which can influence the visibility. The images in Figure 5-4a-c are taken 0.4 seconds apart and show how the flame ignition point and plume width change. To limit the effect of the short term variations an average frame can be produced. The greyscale image in Figure 5-4d s has been averaged over 5 seconds. This concept will be used through the remainder of the paper, where images in color are single frames from the recorded videos and images in greyscale are averaged over 5 seconds. In the images, the distance to the burner tip has been estimated, with the numbers indicated in meters. This will help estimate how much e.g. the ignition point is changed by different fuel types. The description of how the distances are estimated can be found in the supporting material of the published article [134].

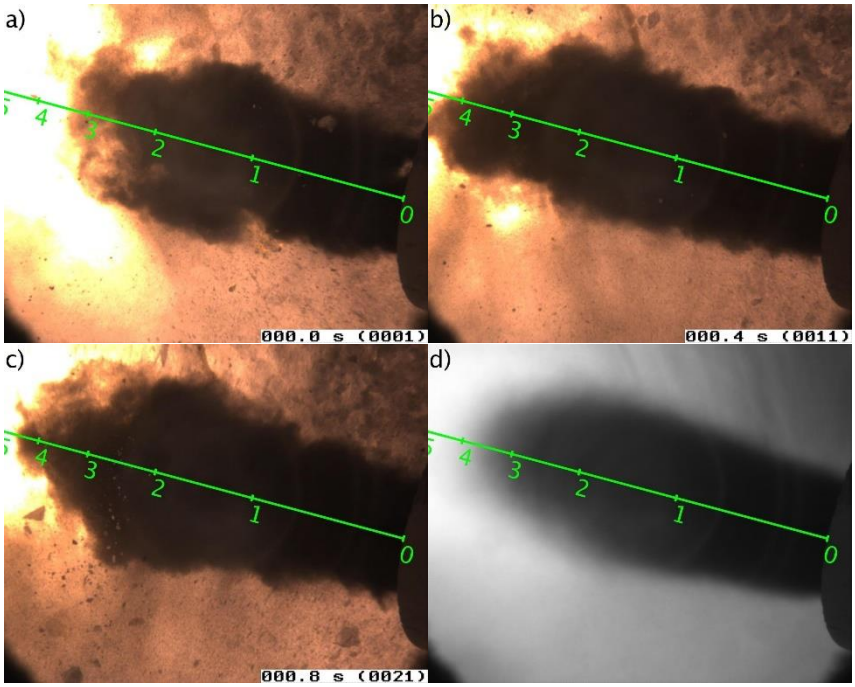

Figure 5-4: Images taken 0.4 seconds apart showing the fluctuations in the kiln flame. d) Frame averaged over 5 seconds. Images from Plant 1 during full petcoke load.

5.4 Results from Plant 1

5.4.1 Petcoke Fired Flame

A wholly petcoke fired flame from the old and new burners used at Plant 1 is seen in Figure 5-5. First of all, it is noticed that the petcoke is ignited relatively far from the burner with the earliest ignition approximately 3 meters from the burner tip. This is generally one of the issues of using petcoke in the cement kiln and is caused by the low volatile content of petcoke compared to coal, see Table 5-1 [50,51]. It is seen that the new burner (Figure 5-5c+d) ignites the petcoke earlier than the old burner (Figure 5-5a+b). As shown in Figure 5-4 the ignition point can fluctuate more than 1 meter in a short time, but on average the new burner has an ignition point between 3 and 4 meters from the burner, while the ignition point of the old burner is more than 4 meters away, outside the frame of the image. The earlier ignition is caused by a more effective entrainment of the hot secondary air into the fuel stream, which allows for a faster heat up of the fuel. This is primarily achieved by three measures on the new burner. The swirl channel is located inside the coal channel on the new burner, while it was located on the outside on the old burner. This has a tendency to push the fuel outwards, where it meets with the hot secondary air [35]. In addition, the swirl channel vanes are angled more, which gives

a higher tangential velocity to induce swirling motion and increase mixing. Lastly, the axial air jets of the new burner will allow for an increased secondary air entrainment compared to an annular air channel [36,46]. It is generally thought to be beneficial with a high amount of entrainment and early ignition as this gives a short high temperature flame, where heat can easily be transferred to the clinker. An early ignition can also help reduce NO_x since less oxygen has had time to entrain into the flame [40,42]. On the other hand, when the swirl channel is located inside the petcoke channel, the fuel is pushed out into more oxygen rich conditions, which may increase the NO_x [35,40,42].

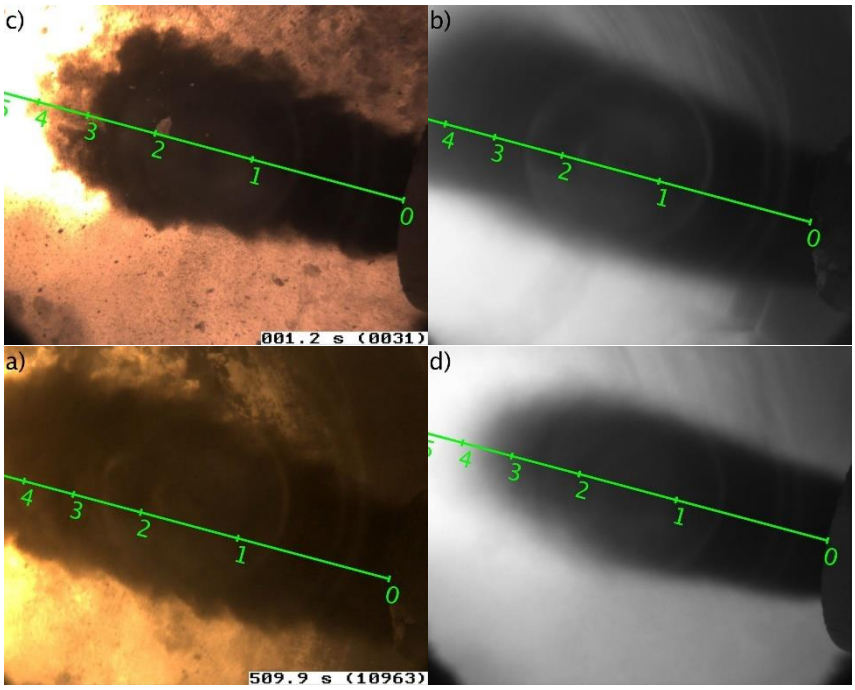

Figure 5-5: Images during full petcoke firing of old burner (a+b) and new burner (c+d). Old burner operating with 250 mbarg swirl air pressure and new burner operating with 190 mbarg swirl air pressure.

5.4.2 Co-Fired Flame

Most of the time Plant 1 operates with a co-firing scenario where 60-80 % of the energy input is supplied by SRF. The ratio between the fuels is used to control the burning zone temperature and will typically be influenced by quality variations in the SRF. I.e. if the moisture content of the SRF increases and the heating value decreases, it will be necessary to increase the amount of petcoke to keep the temperature constant. Images of the co-firing case are seen in Figure 5-6. The flame plume is narrower and lighter in color compared to the full petcoke cases shown in

Figure 5-5 and the ignition point of the flames is moved further away from the burner. For the old burner, Figure 5-6a+b, the ignition is still outside the image frame, more than 5 meters from the burner tip. For the new burner, Figure 5-6c+d, the ignition point is around 5 meters from the burner, which is 2 meters further away than when only petcoke was fired. The difference is caused by SRF, which delays the ignition due to a longer heating time, caused by a larger particle size and high moisture content. The narrower fuel plume is likely caused by a lower amount of petcoke being used than in Figure 5-5. The petcoke is added through an annular channel close to the edge of the burner, with the swirl channel located inside. Thus, it is fairly easy to disperse the petcoke outwards compared to the SRFæ

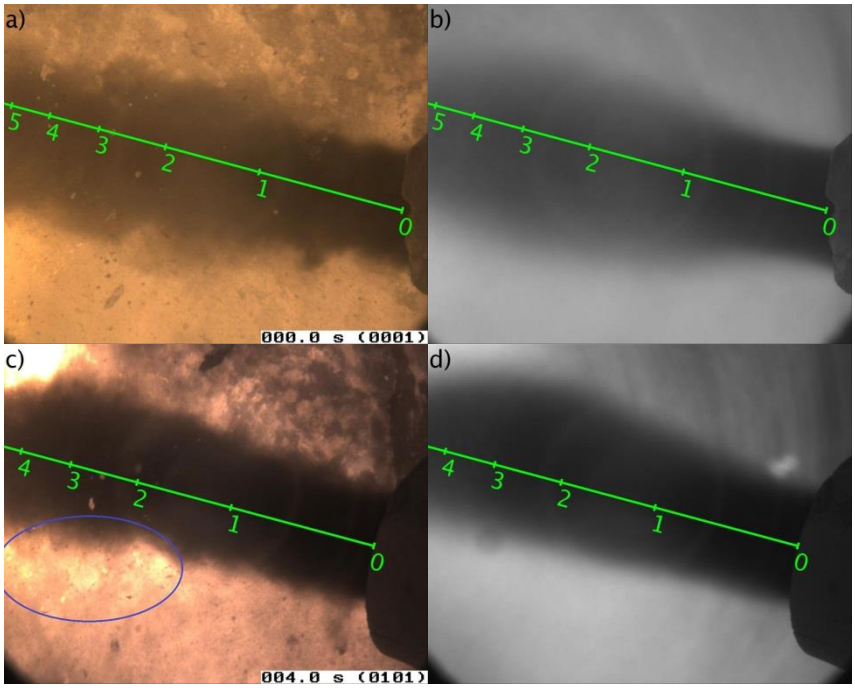

Figure 5-6: Images during co-firing of petcoke and SRF of old burner (a+b) and new burner (c+d). The old burner operates with 80 % energy by SRF and 240 mbarg swirl air pressure. The new burner operates with 70 % energy by SRF and 180 mbarg swirl air pressure.

In the lower left corner of Figure 5-6c some burning particles can be seen. These are SRF particles whirled out of the flame due to the swirling flow. When they enter the hot secondary air, it is possible to ignite the particles faster than in the cold fuel plume. The amount of SRF that is whirled out of the flame can to some extent be controlled by the swirl, as shown in Figure 5-7. Here a flame with 180 mbarg swirl air pressure is compared to one with 100 mbarg swirl air. With the increase in pressure, the exit flow velocity of the tangential swirl air is increased, which

increases the angular momentum and the swirl intensity [135]. Burning SRF particles can be seen as small specks of light on the darker background and have also been highlighted by blue circles. With the high amount of swirl more SRF particles are seen to burn outside the main flame. Almost twice as many particles are marked in Figure 5-7a compared to Figure 5-7b. It is unfortunately not certain whether this can be considered as a representative measure of the amount of SRF burning outside the flame. Thus, if a specific cement plant is vulnerable to particles burning in the clinker, i.e. local reducing conditions; it may be beneficial to lower the swirl. However, this will also have a negative effect on the mixing and the flame intensity, causing the ignition to take place further inside the kiln. This is also shown in this image, where the flame intensity in the upper left corner is much higher with the high swirl. The images in Figure 5-7 are recorded with a different view than previous images. The camera has been turned to look further down the kiln, and the tip of the burner is outside the image on the right side. It has not been possible to estimate the distance in these images, since no reference size is present. In the previous pictures the burner is used as size reference.

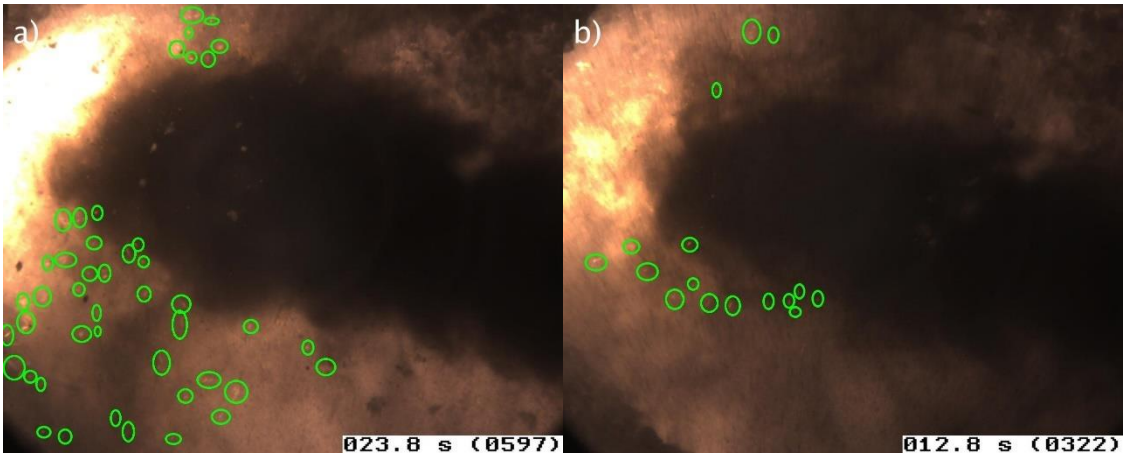

Figure 5-7: Co-firing with the new burner at Plant 1 with 180 (a) and 100 (b) mbarg swirl air pressure. Burning SRF particles are highlighted by green circles. Distances are not indicated in the figure since no reference size is present.

5.4.3 SRF Fired Flame

The petcoke that is fired in an annular channel around the SRF blocks for a clear view of the SRF flow and combustion behavior. At plant 1 it was possible to turn off the petcoke for a brief period to study how the SRF behaves when injected into the kiln. In Figure 5-8 these results are presented. A small amount of residual petcoke is present in the annular channel in the pictures of the old burner (Figure 5-8a-c). The

fuel flow from the old burner is characterized by a low degree of dispersion, where the fuel follows the initial injection trajectory. The low degree of fuel dispersion is detrimental to the combustion of the fuel, since it creates a dense cold core in the flame, which inhibits ignition.

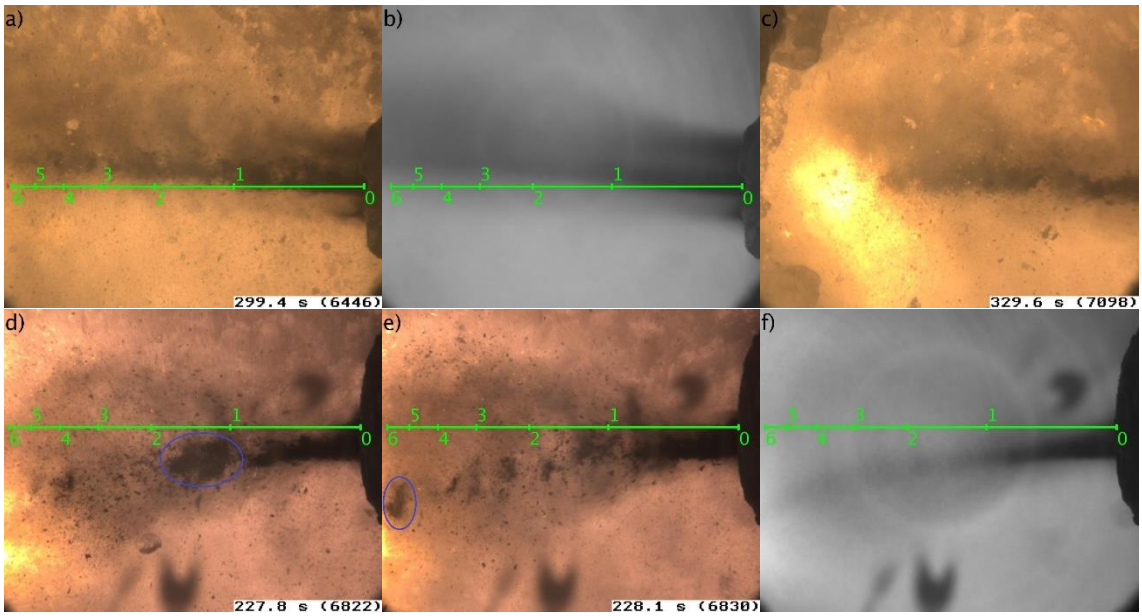

Figure 5-8: Images during 100 % SRF firing for old burner (a+b+c) and new burner (d+e+f). The old burner operates a swirl air pressure of 240 mbarg. The new burner with a swirl air pressure of 150 mbarg. The camera has been turned further downstream in image c, than in the other images.

When the camera view is changed, Figure 5-8c, it can be seen how the particles continue far inside the kiln without being ignited. It can be assumed that the particles will eventually land in the clinker bed largely unconverted. The new burner is better at dispersing the SRF particles. After an initial ~1 m where the SRF is densely packed, it starts to spread out. Some particles still tend to follow the injection trajectory, which can be observed in the averaged image of Figure 5-8f. This is primarily caused by denser lumps of particles, which are difficult to disperse. One such lump can be tracked in Figure 5-8d and e, which are taken 0.3 seconds apart. These lumps are most likely caused by the feeding system. In this case the SRF is fed through a rotary feeder located ~20 meters behind the burner. The feeder rotates, and its compartments are blown clean by the conveying air, which tends to generate the fuel lumps, which can be observed at the burner tip. With a more uniform feeding, it would likely be easier to disperse the particles properly.

The total primary air flow for the two burners is the same at approx. 12,000 m^3/h, but the old burner operates at a significantly higher swirl pressure, 240 mbarg compared to 150 mbarg. This should allow for a higher tangential velocity and the possibility to obtain a higher angular momentum. However, as evident from the images, the swirl is not utilized to affect the flow of SRF. The design of the new burner with a higher angle of the swirl vanes and the channel located close to the SRF seems highly beneficial for the dispersion of SRF in the kiln.

The main advantage of the higher dispersion of particles is a better mixing with the hot secondary air, which leads to an earlier ignition. Some burning particles can be observed in the top and bottom left corners of the images in Figure 5-8d and e, when the fuel leaves the cold fuel core. The high degree of fuel spreading also causes some of the fuel particles to be whirled out of the flame by the centrifugal forces generated by the swirl. In the cement industry, this is traditionally viewed as a negative thing, since it can lead to local reducing conditions in the kiln bed, which promotes brown clinker, stabilization of belite, and increased sulfur evaporation [106–108,111,119]. However, this does not appear to be a specific issue at the plant, where, generally, the quality of the clinker is good, with an alite content above 65 wt.%. Brown clinker and build-ups have not been reported by the plant operators, which suggest that the plant is insensitive to reducing conditions. In fact, it may be beneficial to purposely spread the fuel near the kiln outlet, where the oxygen concentration is high and the clinker nodules are already formed, since the evaporation of sulfur will be limited by the smaller surface area for evaporation [111]. In addition, the energy contained in the fuel will be released before the clinker burning zone and contribute to increasing the temperature here, presumably yielding an increased cement quality. Experiments carried out by Nørskov [31] have shown that injecting alternative fuels too far into the kiln limits the possible substitution in the cement kiln, and just substitutes calciner firing. This will be discussed in further detail later.

Table 5-3 contains measures of the key parameters for the burner performance. The data are averages from one month of operation. Most importantly, with the new burner it was possible to achieve an increased use of SRF while the petcoke consumption was lowered, resulting in a higher energy share of SRF. At the same time the clinker alite content, which is a measure of the quality, increased. Operation of the old burner was supported by oxygen enrichment at the burner where 460

Nm^3/h of oxygen was used to increase the combustion quality. With the new burner this was not necessary, and the oxygen was only used on a few test days. The clinker production was slightly lower with the new burner. In conclusion, the changes in the design were shown to give an earlier ignition and increased dispersion of SRF, resulting in an improved performance.

Table 5-3: Comparison of key operating parameters for the old and new kiln burners at Plant 1. Values are averages for one month of operation. Ignition point data from Figure 5-5 and Figure 5-6.

	SRF Energy Share	**Clinker Alite Content**	**Oxygen enrichment at burner**	**Clinker Production**	**Ignition Point**
	%	wt%	Nm^3/h	t/h	m
Old Burner	62.7	65.3	460	147	Petcoke: >4 m Co-firing: >5 m
New Burner	67.5	67.5	37	144	Petcoke: 3-4 m Co-firing: 5 m
Change in %	7.7	3.5	-91.9	-1.8	-

5.5 Results from Plant 2

The fuel dosing during the test day at Plant 2 and the kiln drive power consumption are shown in Figure 5-9. The power consumption of rotating the kiln is often used as a relative measure of the kiln temperature [17]. As the temperature rises, more material will melt inside the kiln, which will make it more difficult to rotate the kiln, increasing the kiln torque and power consumption. However, the power will also be influenced by other factors such as the amount of material in the kiln or the rotational speed.

Before 13:00, the kiln was fired exclusively with a mix of coal and petcoke. At 13:15 the SRF amount was increased to 1.5 t/h. This level can normally be tolerated at the plant without issues. Just after 16:00 the SRF firing was increased to 4.5 t/h for 20 minutes, while the coal was reduced to 7.5 t/h. There are generally large fluctuations in the kiln drive power consumption during the day even though the kiln firing is kept constant. This is caused by changes in the kiln feed and calciner firing, which are not shown here. However, as the SRF is increased to 4.5 t/h there is a sudden large drop in the kiln power, which is clear when observing Figure 5-9b, where the gradient of the power consumption is shown. A rapid increase is seen as the SRF is reduced back to 1.5 t/h. The drop in power consumption can indicate a lower

temperature in the kiln, which will lower the cement quality. The kiln operator also reported an increased amount of dust in the cooler with increased SRF. This may indicate increased sulfur volatilization caused by local reducing conditions.

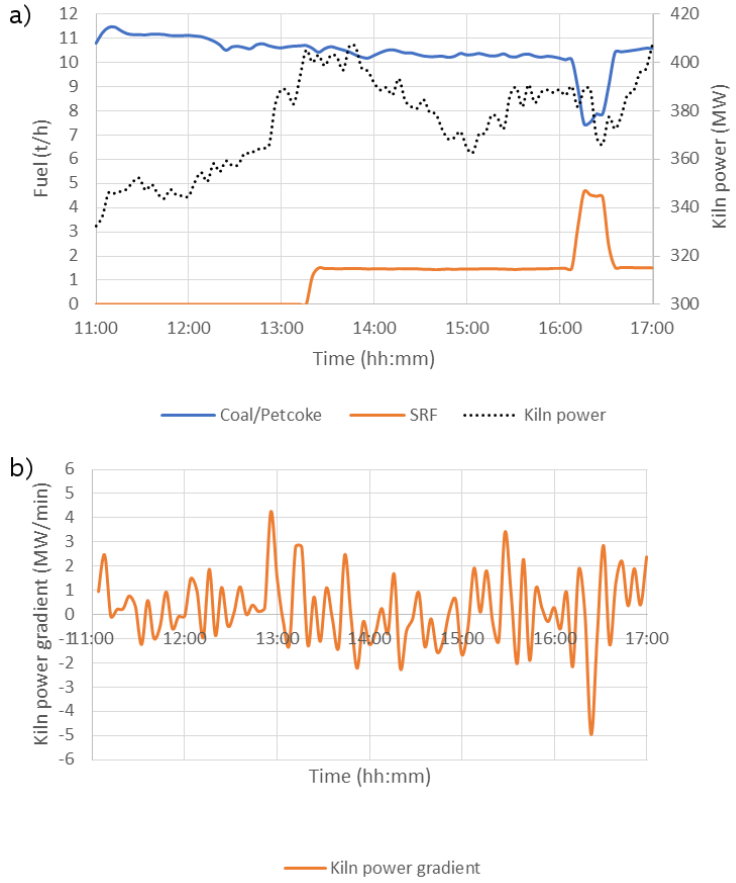

Figure 5-9: a) Fuel dosing of coal/petcoke, and SRF and the kiln drive power consumption (secondary axis) during the test day. b) Gradient of the power consumption. Data from Plant 2.

5.5.1 Fossil Fuel Fired Flame

The fossil fired flame from Plant 2 is shown in Figure 5-10. The plant fires a mix of 75 % of coal and 25 % petcoke. The flame is seen to ignite very close to the burner, around 1-2 meters from the tip, compared to the 3-4 meters at Plant 1, which was shown in Figure 5-5. This is generally due to the high volatility of the coal, compared to petcoke, see Table 5-1. The flame is seen to ignite in an uneven pattern, which is clear in Figure 5-10a and c. The burner is designed with a number of axial air jets surrounding the coal inlet. Four larger gaps are made between some of the jets, which allows for a place where additional secondary air can entrain into the fuel jet. This heats up the fuel quickly and ignites it. The three images in Figure 5-10

underline the turbulent nature of the kiln flame, which constantly fluctuates. In Figure 5-10a, the ignition point is very close to the burner, while it is more removed in Figure 5-10b.

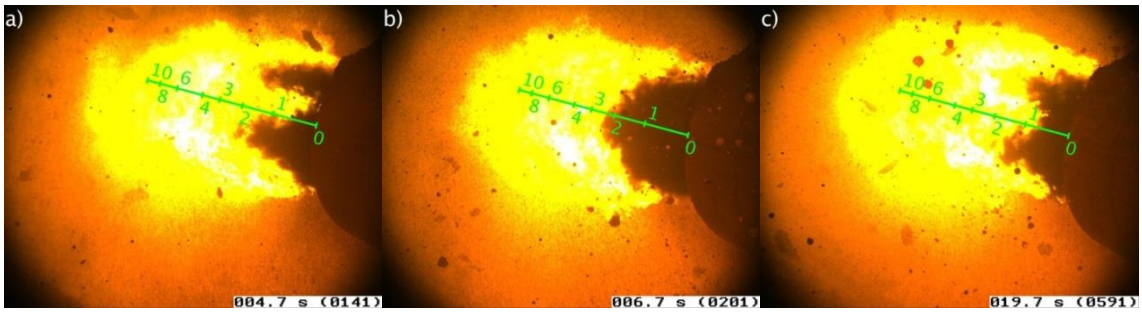

Figure 5-10: Images of the coal/petcoke fired flame with 10.5 t/h coal/petcoke.

5.5.2 Co-Fired Flame

Example images from the recorded videos with SRF co-firing are seen in Figure 5-11. The ignition point is between 2-4 meters from the burner, which is 2 meters further away than in the coal fired flame. The flame also appears less intense, indicating a lower flame temperature. This is a similar observation to the co-firing case seen at Plant 1 and is likely caused by a reduction in the coal amount and a longer heating and burning time of the larger SRF particles, which delays the ignition.

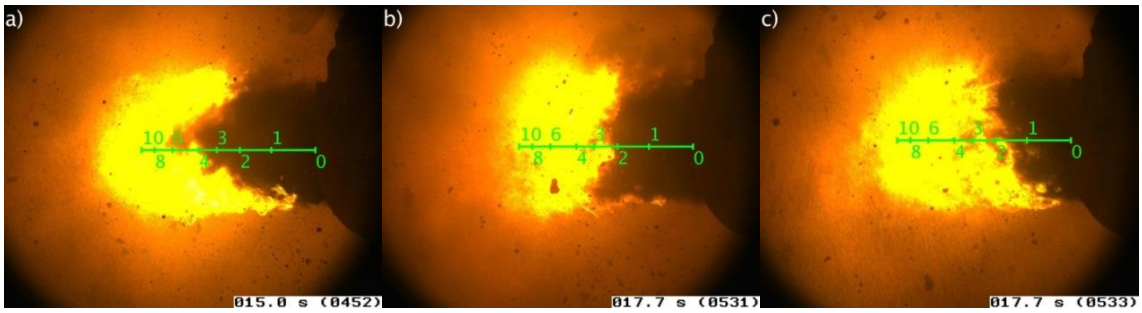

Figure 5-11: Images of co-firing of coal/petcoke with SRF. 7.5 t/h coal/petcoke is used with 4.5 t/h SRF (30 % SRF energy input).

The flame appears to ignite earlier at the bottom. This may be due to high radiation from the hot clinker below the flame, which gives an uneven heating of the fuel. It may also be caused by the flow of the secondary air from the clinker cooler, which is mainly coming from below [136]. The ignition at the side is no longer as pronounced as for the coal fired flame, although it is still seen to some extent e.g. in Figure 5-11c. The longer ignition time and lower flame intensity are expected to cause a lower temperature near the burner, which also lowers the clinker burning zone temperature. As seen in Figure 5-9, there is also a slight reduction in the kiln

drive power consumption, when the SRF firing is increased to 4.5 t/h. This is also an indication of a lowered temperature in the kiln caused by the SRF.

A side by side comparison of the coal/petcoke fired flame and the flame co-fired with SRF is shown in Figure 5-12. In this figure, the videos have been averaged over 5 seconds. This evens out the turbulent changes, which are observed in Figure 5-10 and Figure 5-11 and makes the comparison more straightforward. It becomes evident how the ignition point is moved away from the burner, when SRF is fired and how the intensity of the flame is also lowered, indicating a lower temperature.

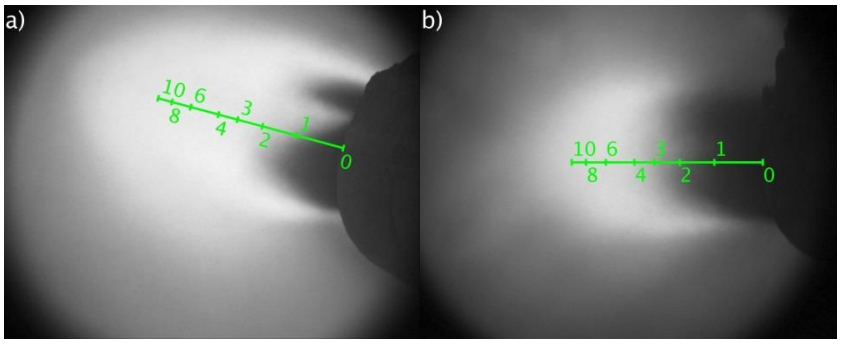

Figure 5-12: Comparison of the coal/petcoke fired flame (a) with the SRF co-fired flame (b). Images are averaged over 5 seconds.

Figure 5-13 shows a view under the flame along the wall of the kiln. This is done by turning the camera downwards compared to the normal view used in Figure 5-10 and Figure 5-11. This view gives an opportunity to track if particles have dropped out of the flame. During full fossil fuel firing, there is no fuel to be seen outside the flame as indicated in Figure 5-13a. When SRF is added to the flame, some particles fall out of the flame and they burn on the wall or charge as shown in Figure 5-13b+c. Only a very small number of particles are observed to drop out of the flame. It can thus be concluded that most of the SRF stays in the flame, until the particles cannot be tracked any longer due to the limited visibility. However, there are signs that the particles are not fully converted in the flame and will cause reducing conditions further downstream in the kiln.

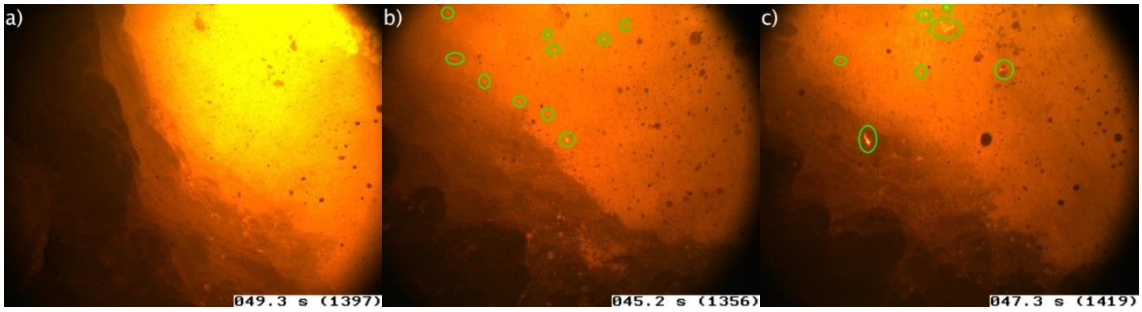

Figure 5-13: View along the kiln wall and charge under the burner for coal-fired case (a) and co-fired case (b+c). The kiln wall is seen in the left side of the images. The kiln bed can be seen on the right side of the images having a more orange color than the wall. Burning particles are bright spots in the images, which have been highlighted with green circles.

The high amount of SRF firing, 4.5 t/h, was only upheld for 20 minutes before the amount was reduced to 1.5 t/h. The kiln operator reported an increased dust load during the testing and there were indications of a lower kiln temperature based on the kiln drive power consumption (see Figure 5-9). The increased dust load is presumably caused by local reducing conditions, since the SRF is not fully converted while in suspension. The reducing conditions promote the decomposition of $CaSO_4$ and the evaporation of SO_2, which results in recirculation and accumulation of sulfur [119]. The sulfur creates a separate melt that is immiscible with the main clinker phases and has a low viscosity and surface tension [137]. It may thus have an adverse effect on the clinker nodulization and increase the dust load [25], if too much sulfate melt is present. Excessive dust in the cooler and kiln inhibit the heat transfer and cools the burning zone [104]. Comparing the images from Plant 2 with those of Plant 1 also show a significantly lower visibility in Plant 2, presumably due to a high dust load. One of the reasons for this is that the kiln manufactures mineralized clinker, where fluoride and sulfur are used as mineralizers/fluxes to lower the burning zone temperature requirement [138,139]. Mineralized clinker may be burnt at temperatures around 200 °C lower than normal clinker [138]. This may first appear promising for the use of alternative fuels (AF), which tend to burn at lower temperatures [83]. However, the mineralized clinker is also more sensitive to process changes [140] and as observed at Plant 2, even relatively small amounts of AF cannot be handled, due to increased sulfur volatility.

5.6 Results from Plant 3

The fuel dosing used during the test day at Plant 3 is shown in Figure 5-14a and selected process measurements are shown in Figure 5-14b.

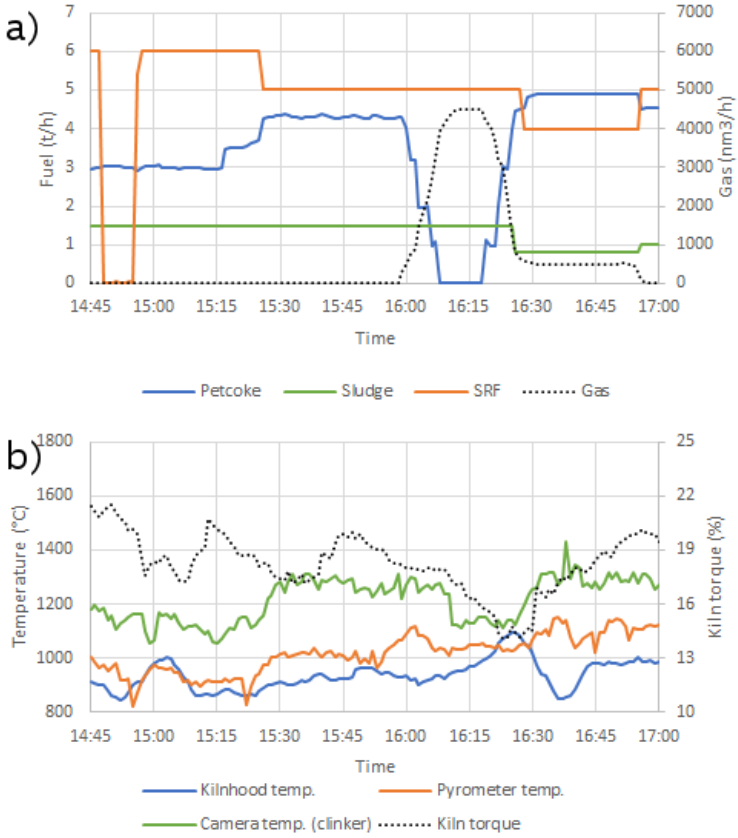

Figure 5-14: a) Fuel dosing to the kiln burner during the test day. b) Temperatures as measured by pyrometer, thermographic camera, kiln hood thermocouple and the kiln torque during the test day. Data from Plant 3.

Specifically, the measurements include the kiln torque and a number of temperature measurements to indicate the kiln burning zone temperature. The plant uses an infrared pyrometer and thermographic camera to gauge the temperature in the near burner zone of the kiln as well as a thermocouple measuring the temperature in the kiln hood. Initially, the SRF dosing has been 6 t/h, but due to a low temperature in the kiln, at 15:30 the dosing was lowered to 5 t/h and the petcoke dosing increased. This resulted in a temperature increase, which can be seen by the pyrometer or camera temperature in Figure 5-14b. The petcoke was deliberately shut off from 16:00 to 16:30, in order to better observe the SRF flight behavior in the kiln. In the meantime, natural gas was used instead to keep the energy input to the kiln constant.

5.6.1 Co-Fired Flame

The co-fired flame from Plant 3 is shown in Figure 5-15. It takes approximately 4 meters from the burner tip before the flame is ignited. This is somewhat similar to what was seen in Plant 1, where petcoke and SRF is also used, while Plant 2 had a very early ignition due to the volatile coal. The images in the figure also underline the large changes that can occur in kiln conditions when firing alternative fuels. The images of Figure 5-15b and c are recorded one hour apart, and the intensity in Figure 5-15c is much higher, indicating a higher burning zone temperature. This is caused by increasing the petcoke dosing by 1 t/h and reducing the SRF dosing by 1 t/h. The change is also consistent with the higher temperature measurements, as seen in Figure 5-14.

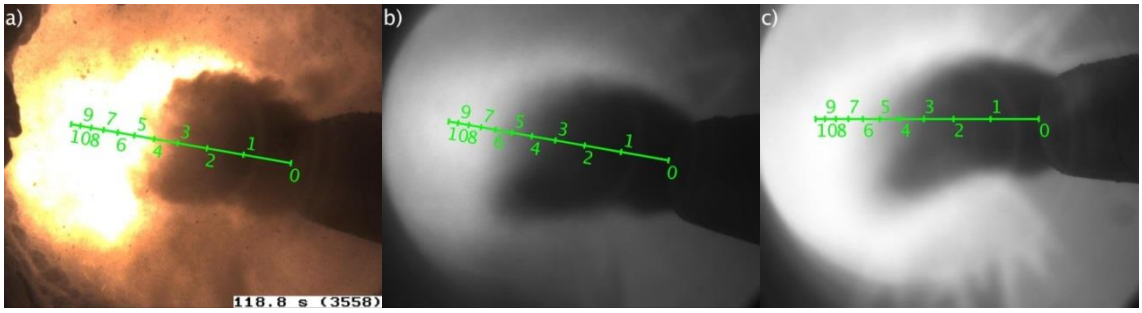

Figure 5-15: Flame of petcoke co-fired with SRF and sewage sludge. a+b) 3 t/h petcoke, 1.5 t/h sewage sludge, 6 t/h SRF (60 % AF energy input), recorded at 14:56. c) 4.3 t/h petcoke, 1.5 t/h sewage sludge, 5 t/h SRF (45 % AF energy input), recorded at 15:45.

The flame at Plant 3 is sometimes very divergent compared to Plant 1 and 2, which can cause the flame to impinge on the bed as shown in Figure 5-16a. This should generally be avoided since it may overheat the refractory and contribute to local reducing conditions [31]. The design of the burner differs from that used at the other plants. The other burners have separate channels for axial and swirl air, while the Plant 3 burner has only one channel, where the swirl level is adjusted by increasing the tangential angle of the air inlets. If the angle becomes too high, it seems that the burner lacks axial momentum to stabilize the flame, causing a very diverging flame. A relatively small amount of SRF particles are whirled out of the flame close to the burner as also indicated in Figure 5-16a. Further inside the kiln, just around the point where the petcoke ignites approximately 6 meters from the burner, some burning particles can be observed in the kiln bed, see Figure 5-16b. In the videos,

several burning particles can be seen around this point, which indicates that it is where the SRF particles begin to drop out of the flame.

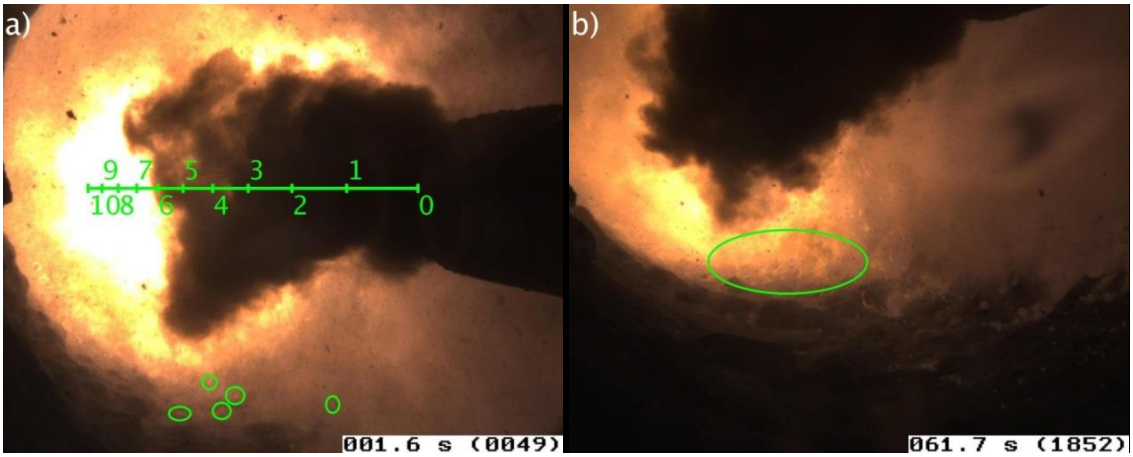

Figure 5-16: View of the co-fired flame from the side (a) and under the burner (b). Flames in bed are located by green circles. Fuels: 4.3 t/h petcoke, 5 t/h SRF, 1.5 t/h sewage sludge (45 % AF energy input).

5.6.2 Flame with Natural Gas

The SRF is fired through a pipe at the center of the burner, which is surrounded by an annular channel for the injection of petcoke. Similarly to Plant 1 the visibility of the SRF flow is obstructed by the petcoke. In an attempt to understand the SRF flow better, the petcoke was turned off for a brief amount of time. To keep the heat input to the kiln, gas was supplied instead, as shown in Figure 5-14 at around 16:15. While the gas flow is increased, from 0 to approx. 500 Nm^3/h, the ignition point moves closer to the burner tip from approx. 6 meters to 2 meters, see Figure 5-17. The combustion also becomes more intense, with the image becoming more oversaturated. It would seem that this could be quite a viable method to increase the ignitability of the co-fired flame and obtain a high temperature region close to the burner. However, the price of natural gas in most countries will probably make this kind of operation unfeasible. Per unit of energy, gas may be more than four times as expensive as petcoke [39]. The pyrometer measuring the flame temperature is seen to increase from around 1000 °C to 1050 °C, with a peak at 1100 °C, around the time where the petcoke dosing is lowered. The kiln hood temperature increases in the same period, which also indicates an increased temperature near the kiln outlet. The temperature measured by the kiln camera installed at the plant, however, has a lower reading, while the gas is being fired. The kiln torque is also seen to decrease, which may indicate less heating further inside the kiln. Gas flames normally produce

small amounts of soot compared to coal flames, which results in a lower flame emissivity [4]. The heat transfer from flame to clinker bed can thus be inhibited. This could explain the lower clinker temperatures measured by the camera and the lower kiln torque.

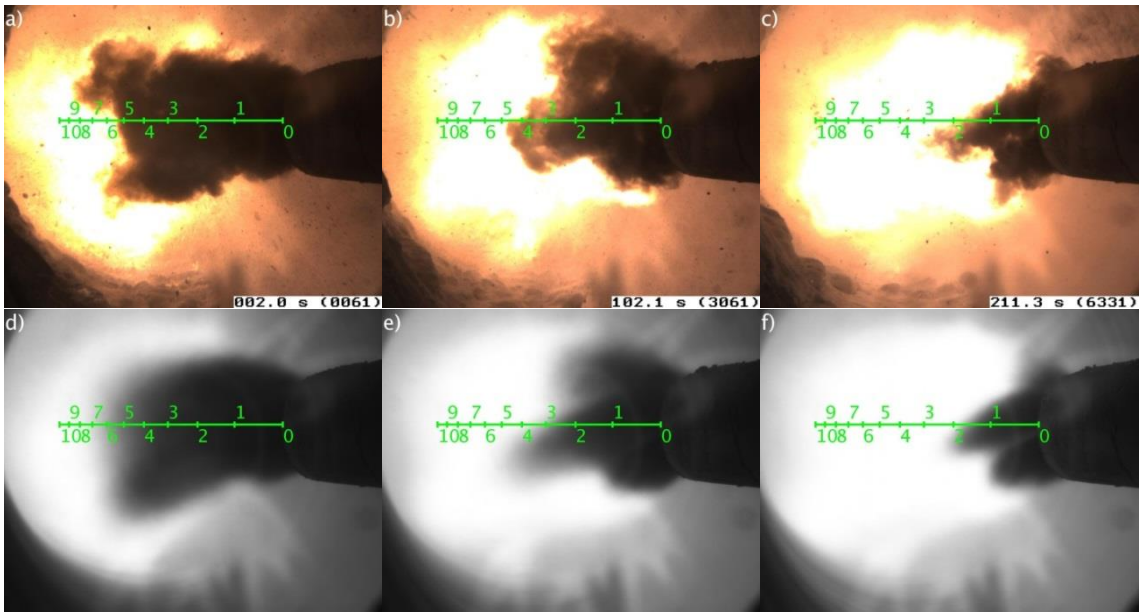

Figure 5-17: Different flame shapes while the gas flow is increased over 200 seconds from 0 (a+d) to 500 (c+f) Nm³/h. Petcoke dosing is constant at 4.3 t/h. Top row shows single frames and bottom row are images averaged over 5 seconds.

Some images of the SRF and gas fired flame without petcoke are shown in Figure 5-18. The visibility of the SRF changes from frame to frame as shown in the sequence of images in Figure 5-18, which is mainly due to the natural variations in flame ignition. In Figure 5-18b it is seen that the SRF is quite hard to ignite, and it passes at least 6 meters from the burner tip without being ignited, and then disappears in the gas flame. It is very likely to continue further inside before being properly ignited and the conversion in the flame may be low.

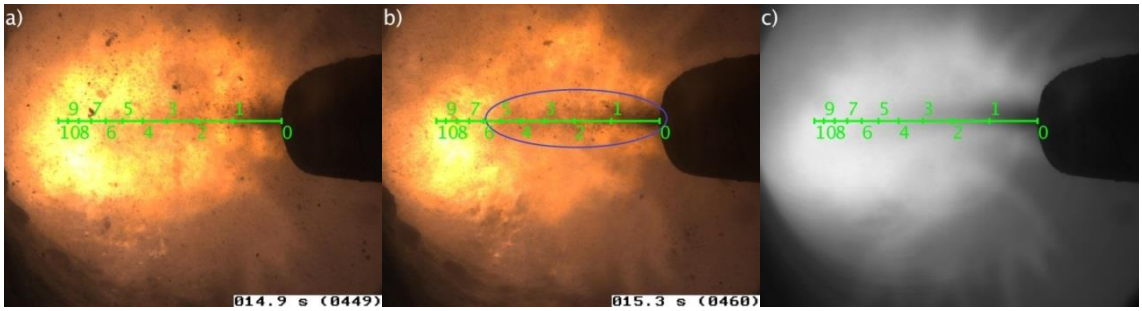

Figure 5-18: SRF and gas fired flame. 5 t/h SRF, 1.5 t/h sewage sludge, and 4500 Nm³/h natural gas (45 % AF energy input).

The SRF is not packed as densely as seen in Plant 1 (see Figure 5-8) when it enters, which is likely due to a lower feeding rate. The dispersion of the SRF appears to be better than for the old burner in Plant 1, and similar to what is achieved for the new burner at Plant 1. A significant amount of small flames can be seen in the bed, in the lower part of the images of Figure 5-18. This indicates that a large fraction of the SRF may burn in contact with the clinker rather than in suspension.

5.7 Limiting Factors for Alternative Fuels Firing

It is highly beneficial to understand the limiting factors for alternative fuel (AF) firing in order to eventually increase the amount of AF firing. Thus, some of the issues encountered at the three plants when firing AF will be discussed in further details here.

Plant 1 fires the highest amount of alternative fuels in the kiln of the three plants studied here. The plant produces clinker with an alite content above 65 %, which is a typical level for Portland cement [11]. Issues with brown clinker or build-ups in the kiln or preheater have not been observed during the measurements with SRF. The plant has a chlorine by-pass and several air blasters are installed in the preheater tower to combat build-ups. The main limitation is the lower combustion temperatures obtained during SRF co-firing. If the SRF firing gets too high, the kiln temperature is lowered. Thus, petcoke is needed to create a high temperature zone to obtain an adequate clinker quality. The petcoke is also used to adjust the burning zone temperature when the SRF heating value or moisture content changes. The plant has previously used oxygen enrichment in the kiln to stabilize the operation at high SRF firing and lower the petcoke consumption. The installation of the new burner has been beneficial for Plant 1. It has been possible to increase the alite content of the clinker, which resulted in increased compressive strength of cement mortar. Furthermore, the substitution with SRF was increased and oxygen enrichment was no longer used. The main difference between the designs of the two burners has been discussed in chapter 5.4, and is related to the mixing intensity achieved by the burners and the ability of the new burner to spread the SRF in the combustion zone.

Plant 2 fires the lowest amount of AF and has a low tolerance. This appears to be mainly caused by the manufacture of mineralized clinker, which is more sensitive to

reducing conditions since the sulfur loading is higher than for ordinary clinker. The limit of SRF firing appears to be around 2 t/h, while the plant can tolerate up to 3 t/h of the granulated tire. In a study by Nielsen et al. [53], tire granulate was found to be able to release more sulfur from cement raw materials than plastic and wood, which are the main constituents of SRF. Thus, the reason that a higher amount of granulated tire can be tolerated, is most likely related to the smaller particle size. This results in a faster conversion of the fuel, resulting in less fuel ending up in the kiln bed to induce reducing conditions.

Plant 3 uses an intermediate amount of alternative fuels in the kiln. The produced clinker has an alite content above 60 % (calculated by Bogue formulas [13,24]). Plant 3 sometimes encounters problems with reducing conditions, when firing too much alternative fuels. This is seen as brown cores in the cement clinker and some deposit build-ups in the calciner and cement kiln. The plant recently installed a by-pass to reduce the volatile circulation, which is expected to alleviate some of the problems with build-ups, and may allow for a further increase in the use of alternative fuels.

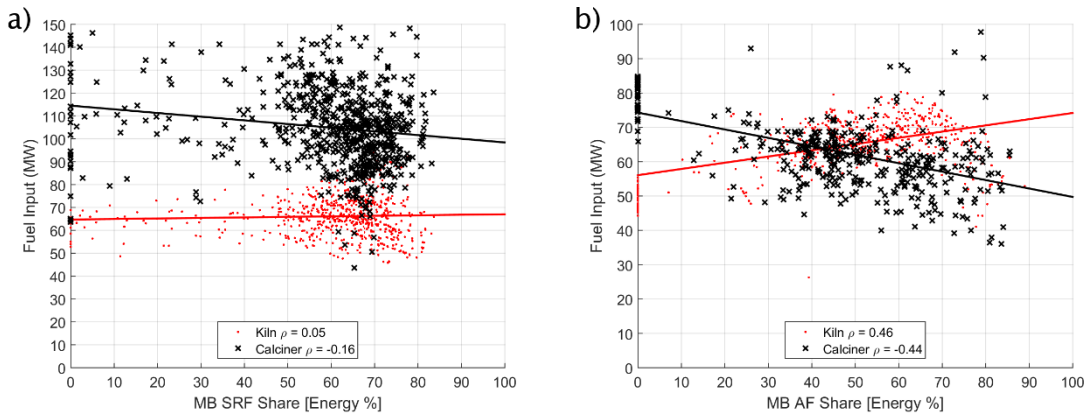

Figure 5-19: Relationship between the energy from alternative fuels firing at the main burner (MB) and the energy input in the kiln (red dots) and the calciner (black x) for Plant 1 (a) and Plant 3 (b). Data are based on hourly averages for one month of operation. ρ is Pearson correlation coefficient.

An interesting difference between Plant 1 and Plant 3 is shown in Figure 5-19. The figure shows the relationship between the fraction of alternative fuels firing at the main burner and the energy input at the main burner and calciner (Hotdisc included) for Plant 1 (Figure 5-19a) and for Plant 3 (Figure 5-19b). The data plotted in the figure are based on hourly averages from one month of operation giving a

large degree of data scatter. The Pearson correlation coefficient [141] has been calculated as a measure for the relationship between the variables.

Normally, around 60 % of the total fuel used in the cement process will be fired in the calciner and the remainder in the kiln. This is because the calcination of limestone is highly endothermic requiring 1800 kJ/kg [142]. This is also the balance at both plants when no AF is fired in the kiln. At Plant 1, the heat input at the burner and calciner is rather independent of the amount of AF fired at the main burner. However, at Plant 3, the energy input at the kiln is increased as the amount of AF in the kiln is increased, while the firing in the calciner is reduced. This shifts the balance between kiln and calciner firing and when high amounts of AF are utilized around 60 % of the energy is fired in the kiln. This indicates that the fuel energy from the AF is not released quickly enough to contribute to increasing the clinker burning zone temperature, and rather substitutes firing in the calciner. At Plant 1, the correlation is small, indicating that the fuel fired in the main burner is actually utilized in the kiln. Thus, there are indications that AF burns closer to the kiln exit at Plant 1 than at Plant 3. Nørskov [31] made some experiments with different injection velocities of AF and found that an injection velocity of 30 m/s was to be preferred over a velocity of 50 m/s. The high injection velocity causes the fuel to be injected too far into the kiln, and the energy is not released in a proper location to contribute in rising the clinker temperature. It is possible that a lower injection velocity of AF at plant 3 could ensure that the SRF is not injected too far into the kiln, which allows for the energy to be released in the clinker burning zone.

Another large difference between the plants is their tolerance to reducing conditions. At Plant 1 neither brown clinker or deposits were observed during testing, at Plant 2 the dust load in the kiln is increased when utilizing high amounts of AF due to sulfur evaporation, and at Plant 3 brown clinker and deposits are sometimes encountered. The difference may largely be caused by the sulfur evaporation in the kiln. The sulfur evaporation may be limited if there is a high amount of alkalis in the clinker, since alkali sulfates are less volatile than calcium sulfate. One measure is the sulfur modulus calculated as [23]:

$$\boldsymbol{MSO_3 = \frac{\frac{Y_{SO_3}}{80}}{\frac{Y_{K_2O}}{94} + \frac{Y_{Na_2O}}{62}}} \qquad \textbf{E 5.1}$$

The sulfur modulus calculated for the clinker of the three plants is on average 0.64, 1.51, and 0.84. A value around 1 is adequate to ensure that there is sufficient alkali to combine with the sulfur [23]. It can thus be seen that Plant 2 operates at a high sulfur modulus, due to the high input of sulfur in the mineralized clinker, but this also means that it is more susceptible to sulfur evaporation caused by reducing conditions. The sulfur modulus for Plant 1 and Plant 3 are low enough that most of the sulfur should be able to combine with alkalis. However, comparing the fuels of Plant 1 and 3 (Table 5-1), it is seen that the sulfur content of the petcoke used in Plant 3 is higher than that in Plant 1 and the chlorine content of the SRF is higher. The plant will thus have a higher input of sulfur and chlorine through the fuel, which may set a limit for the utilization of alternative fuels. In addition, Plant 3 did not have a by-pass to lower the amount of recirculating species. Thus, Plant 3 is likely to be more vulnerable to reducing conditions causing sulfur evaporation and deposits than Plant 1.

Brown core clinker is also sometimes encountered at Plant 3. The brown color is caused by a reduction of Fe^{3+} to Fe^{2+}, which may substitute MgO in the ferrite phase (C_4AF), which otherwise gives cement its dark grey color. The reduced iron can also affect the formation of alite, lowering the cement quality [106–108]. Alternative fuels are burned in contact with the bed in both Plant 1 and Plant 3, but Plant 1 tolerates it better, with no formation of brown clinker. It may be related to where the AF mainly burns, which was discussed above and illustrated in Figure 5-19. If the AF burns too far inside the kiln it may drop into a bed of un-nodulized clinker, with a large surface area which may be more prone to iron reduction [111]. If the AF mainly burns close to the burner where the nodules have already formed, the surface area for evaporation of sulfur and iron reduction is significantly smaller and the oxygen concentration will be higher. The brown clinker cores may also be related to the rate of clinker cooling. Locher [107] showed that the adverse effects of burning under reducing conditions could be limited by a rapid cooling from 1250 °C in air. Perhaps high clinker porosity will be beneficial to counter brown cores, since it will help oxygen to diffuse in and reoxidize the clinker during cooling.

In summary, all three plants are limited by the conversion rate of the alternative fuels. For Plant 1 the main limitation is that the AF does not burn quickly enough to obtain sufficiently high temperatures. Thus, some petcoke is needed to maintain a

high temperature and proper heat transfer to the clinker. At Plant 2 and Plant 3 the main limitation is that the fuel is not converted quickly enough before ending in the bed, eventually leading to localized reducing conditions in the kiln. It would be interesting to study if the utilization could be improved by drying or milling of SRF to obtain faster conversion of the fuel. Excess heat typically available in the off-gasses could be used to dry alternative fuels, but milling of SRF is difficult due to the soft paper and plastic fractions and impurities that may damage the mill [99].

5.8 Conclusions

A specially developed camera setup has been used to study the kiln flames at 3 different cement plants. The probe was designed so it could be inserted directly in the cement kiln hood where the temperature is around 1000 °C and the dust load is high. This allowed for a detailed study of the influence of alternative fuels on the cement kiln flame.

An overview of the flames studied at the three different cement plants is given in Table 5-4. Adding alternative fuel to the flame had at all three cement plants a negative impact on the flame. At Plant 1 the ignition point was between 3-4 meters from the burner tip when petcoke was fired alone, and when SRF was added to the flame the ignition point was between 5-6 meters from the burner tip. At Plant 3 the ignition point was at a similar distance while co-firing petcoke and SRF. The flame at Plant 2 ignited within 1 meter. A mix of coal and petcoke was used, which ignites more readily than the petcoke at Plant 1 and 3 due to a higher volatile content of the coal. At Plant 2 the ignition point was also shifted approx. 2 meters when SRF was added to the flame. At all three plants, the flame intensity was also lowered when using AF, which indicates a lower combustion temperature. This is mainly due to the high moisture content and large particle size of alternative fuels compared to conventional fuels, which results in a lower conversion rate of the fuel. At Plant 2 and Plant 3 measurements of the kiln drive power consumption also suggested that the temperature in the kiln was decreased when co-firing AF. The lower temperatures in the kiln may negatively affect the clinker quality.

Table 5-4: Overview of the impact of alternative fuels on the flame ignition point at the three cement plants. C: Coal, PC: Petcoke, SRF: Solid Recovered Fuel, SS: Sewage Sludge.

	Plant 1				**Plant 2**		**Plant 3**	
	Old Burner		New Burner				Old Burner	
Flame	Fossil	Co-fired	Fossil	Co-fired	Fossil	Co-fired	Co-fired 1	Co-fired 2
Figure	5-5a+b	5-6a+b	5-5c+d	5-6c+d	5-11+ 5-13a	5-12+ 5-13b	5-16c	5-18c+f
Fuel (t/h)	-	-	-	-	PC: 2.1 C: 8.4 SRF: 0	PC: 1.5 C: 6 SRF: 4.5	PC: 4.3 SRF: 5 SS: 1.5	PC: 4.3 SRF: 5 SS: 1.5 Gas: 500 Nm^3
AF Energy Share (%)	0	80	0	70	0	30	45	45
Ignition Point (m)	> 4	> 5	3-4	~5	1-2	2-4	~4	~2

At all three plants, it was observed how some of the SRF drops out of the flame and burns in contact with the cement clinker. At Plant 2 and 3 this leads to problems with sulfur evaporation or brown cored clinker, while Plant 1 appears to be more robust to local reducing conditions. Why this is the case is not fully understood, but Plant 2 is sensitive to reducing conditions due to manufacturing mineralized clinker and has a high sulfur modulus, which makes sulfur evaporation more probable. Between Plant 1 and Plant 3 there may be a difference in where the SRF mainly burns or there could be a difference in the cooling which can prevent reduced clinker.

The burner design does have a significant influence on the flame. The burner design at Plant 2 could create ignition sources, by allowing secondary air to be entrained into the fuel stream in a few locations. A clear difference in the two burner designs tested at Plant 1 was also observed. The change from an annular axial air channel to axial air jets benefited the ignition when using petcoke. The design of the swirl channel influences the flame swirl level, increasing the dispersion of SRF particles in the flame. The old burner at Plant 1 had very little dispersion of the SRF. This creates a cold core of SRF in the flame, which will be difficult to ignite and the SRF will continue far into the kiln and eventually land in the clinker bed, likely largely unconverted. Alternatively, the SRF can be spread as much as possible, which occurs with the new burner at Plant 1. This will evidently result in more SRF dropping out

of the flame and ending up in the clinker bed close to the burner. On the other hand, the energy in the fuel will be released earlier, contributing better to maintain a high temperature in the clinker burning zone. Based on the results presented here, the second option with a high degree of fuel dispersion appears beneficial. It may also reduce the problems with localized reducing conditions induced by fuel in the bed, since the fuel will be in contact with nodulized clinker, which has a relatively small surface area, in the part of the kiln where the oxygen concentration is highest. By changing the burner at Plant 1, it was possible to increase the alite content of the clinker while increasing the substitution of SRF.

6 Effect of Burner Settings on the Cement Kiln Flame and Clinker Quality

It is fairly well known how burner settings, such as axial momentum and swirl, can influence the solid fossil fuel flame on factors like ignition, temperature, and NO_X formation. For a co-fired flame this knowledge is more limited. It is generally understood that the burner should allow a fast mixing of secondary air and alternative fuel in order to promote ignition [30,46]. Detailed studies of the burner settings have been made in the Cemflame 3 experiments (see chapter 3.5.1 and 9.1.1), while one study [143] (see chapter 8.1.2) used CFD simulations to study different operating conditions, amongst them swirl level, when co-firing in a cement kiln.

A more detailed understanding of the influence of burner settings on the co-fired kiln flame is thus beneficial. To this end, further experiments were made using the Jetflex burner installed at Plant 1. The aim was to understand the impact that burner settings, e.g. swirl, has on the co-fired flame, and investigate which approach is best suited to optimize the flame characteristics and clinker quality. The kiln camera was used to study the near burner changes in the flame pattern using different burner settings, while a statistical analysis (Partial Least Squares Regression) was

performed on collected operating data to relate the burner settings to the clinker quality.

6.1 The Jetflex Burner Settings

The FLSmidth Jetflex burner has previously been described (see chapter 2.8). The Jetflex burner has a number of different possibilities to influence the flame shape. The amount and velocity of axial air, swirl air, and central air (for cooling) can be adjusted by valves controlling the flow and thus the air pressure and velocity to each channel. The axial air provides axial momentum to the flame, while the swirl air is introduced tangentially giving the flow a swirling motion. This is a common way of controlling the flame shape [30,35,42,144]. The flow of central air is small and used to cool the burner front plate.

The 20 axial air nozzles of the burner can be turned individually 360°, which can further impact the flame. The axial air nozzle openings are flat and have a slight offset of 10°. The nozzle position is defined as 0° when the offset is pointing towards the burner center and 180° when the offset is pointing away from the burner center.

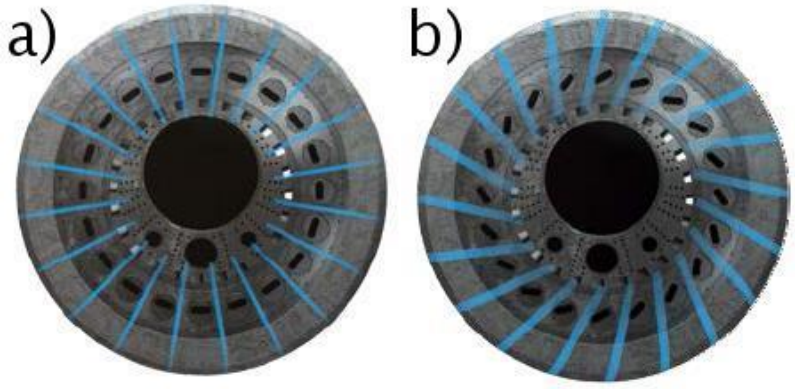

Figure 6-1: The Jetflex axial air nozzles can be turned allowing different nozzle configurations such as: a) All nozzles pointing inwards 0°. b) All nozzles turned 30° [145]. The blue lines indicate the entrainment of secondary air into the burner jet.

Nozzle configurations of 0° and 30° are shown in Figure 6-1a and b. When the nozzles are at 0° the configuration almost resembles an annular channel for the axial air, and the entrainment of secondary air is low. When the nozzles are at 30°, the annular configuration is broken up, which allows for extra space between the nozzles for entrainment of secondary air [46], as indicated by the blue lines in Figure 6-1.

Furthermore, it is possible to switch the fossil fuel from being fired through the conventional annular channel to be mixed with the alternative fuel and be fired through the large central pipe. This allows for a reduced amount of cold transport air, benefiting the specific heat consumption in the kiln.

Lastly, it is possible to retract the center of the burner, including the swirl channel, as shown in Figure 6-2. When the swirl air reaches the tip of the burner it can suddenly expand, which creates a stronger recirculation zone in front of the burner. In cold testing of the burner it was found that this could help disperse the alternative fuel [145].

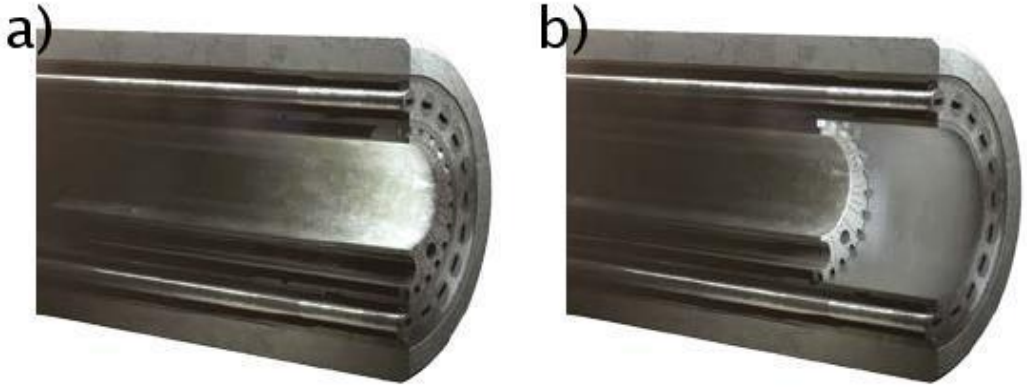

Figure 6-2: Burner in normal operation (a) and with retracted center (b) [145].

6.2 Calculation of Burner Momentum and Swirl

Valves at the burner air channels are used to control the air flow in the axial and swirl channels. When both valves are fully open the pressure in both the swirl and axial channels are around 180 mbarg. Closing the swirl valve causes the flow and pressure of swirl air to decrease, while the axial air flow and pressure is increased, since the primary air fan is giving a constant air flow to the burner. The exit velocities at the swirl and axial nozzles can, for isentropic flow, be calculated by [146]:

$$v_{ex} = \sqrt{\frac{2\gamma}{\gamma - 1}\frac{R_{gas}}{M_{air}} T_{burner}\left(1 - \frac{p_{ex}}{p_{burner}}^{\frac{\gamma-1}{1}}\right)} \qquad \text{E 6.1}$$

In the equation v_{ex} is the exit gas velocity from the nozzle, R_{gas} is the gas constant, M_{air} is the molar mass of air, T_{burner} is the temperature of air in the burner, p_{ex} is the

pressure at the nozzle exit (ambient pressure), p_{burner} is the pressure in the burner, and γ is the ratio of specific heats.

With additional data on the burner geometry and nozzle areas it is possible to calculate the mass flow of swirl and axial air, and thus the burner momentum:

$$I = \dot{m}_{ex}\, u_{ex} = \rho_{ex}\, A_{ex}\, u_{ex}^2 \qquad \text{E 6.2}$$

Here I is the burner momentum, $\dot{m}_{ex}$ is the air mass flow, ρ_{ex} is the air density at the nozzle exit, A_{ex} is the nozzle area, and u_{ex} the axial gas velocity at the nozzle.

The swirl number in its common definition proposed by Beér and Chigier [135,147], is difficult to compute without detailed flow measurements, which were not performed here. Thus, a simplified swirl number is used instead. The number is calculated based on maximum axial and tangential velocities, u_{ex} and w_{ex}, respectively, measured at the nozzle exit [148]:

$$S_{app} = \frac{\frac{w_{ex}}{2u_{ex}}}{1 - \frac{w_{ex}}{2u_{ex}}} \qquad \text{E 6.3}$$

The relevant operating pressures for the performed tests and corresponding nozzle velocities, axial momentums and the approximated swirl number are given in Table 6-1.

Table 6-1: Overview of burner pressures and corresponding velocities, axial momentum and the approximated swirl number.

Swirl Pressure	Axial Pressure	Swirl air velocity	Axial air velocity	Axial Momentum	Approximated Swirl Number
mbarg	mbarg	m/s	m/s	N/MW	-
10	240	42	234	9.6	0.07
30	235	72	232	9.7	0.12
50	230	93	229	9.8	0.17
80	225	116	227	10.0	0.22
100	220	130	225	10.0	0.26
150	200	156	216	9.9	0.34
180	190	170	211	9.8	0.40

6.3 Flame Measurements

The data presented in this chapter are comprised of video recordings with the kiln camera obtained at Plant 1 (described in chapter 0). The video footage has been acquired over several visits to the test cement plant stretching over one year, in

which several hours of video footage have been recorded. From this data a few representative images have been selected and presented here.

In the following chapters images shown in color are single frames from the recorded videos. Images in gray scale are averages over 5 seconds (around 150 frames). These are presented to reduce the frame to frame variation. Two different approaches are used to further highlight the difference between burner settings, as will be explained later. The following chapters will first discuss the influence of swirl and nozzle configuration on the petcoke flame, and afterwards the attention will be turned to the flame co-fired with SRF.

6.3.1 Petcoke Flame

6.3.1.1 Effect of Swirl Air

The effect of changing the swirl air pressure on the petcoke flame is shown in Figure 6-3.

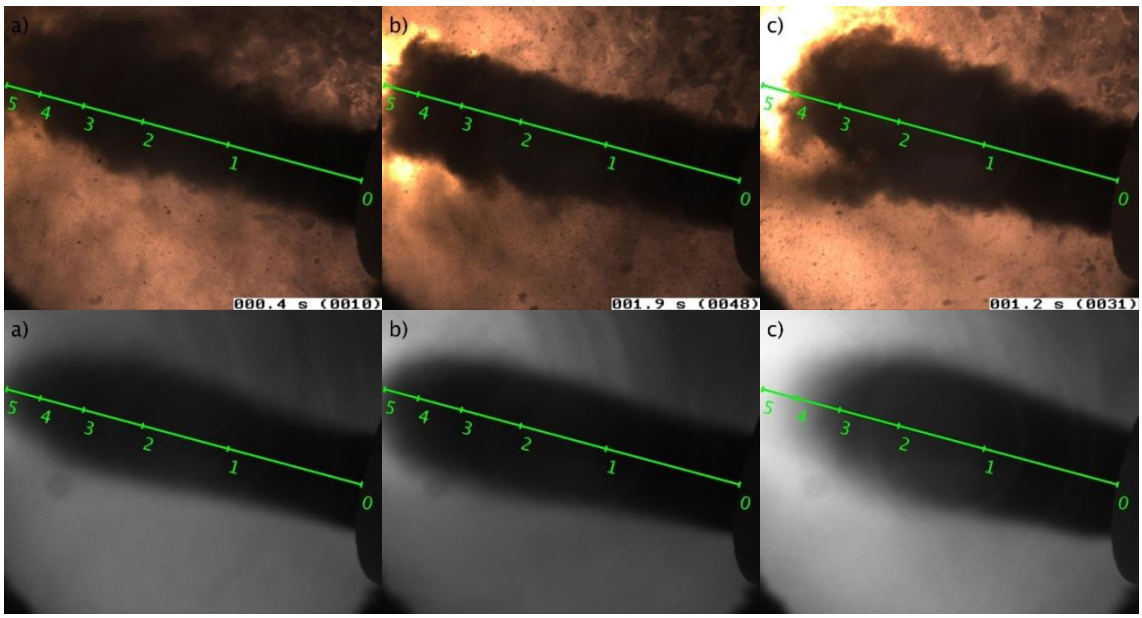

Figure 6-3: Effect of swirl air pressure on the petcoke flame with axial air nozzles at 30°. Swirl pressure of a) 30 mbarg, b) 80 mbarg, c) 180 mbarg.

Petcoke flames with swirl air pressures of 30, 80, and 180 mbarg are shown in Figure 6-3, with the axial air nozzles being at 30°. The swirl increases the width of the flame plume, which causes an increased mixing of fuel with the hot secondary air surrounding the flame plume. This causes an earlier ignition which is moved from around 5 meters when the swirl pressure is 30 mbarg (Figure 6-3a) to between 3 and 4 meters when the swirl pressure is 180 mbarg (Figure 6-3c).

In order to further highlight the difference between the burner settings Figure 6-4 is presented. The recorded color-video frames are converted to a series of 8-bit grayscale images, having an intensity scale from 0 to 255. An intensity value of 0 is black, and a value of 255 is white. In each image the intensity profiles along the horizontal centerline (green lines in Figure 6-3) and perpendicular to the centerline 1 m in front of the burner are determined. These are then plotted over time to yield Figure 6-4, which indicates how the image intensity changes over time (x-axis) and distance (y-axis). The color on the plots indicates the image intensity, with dark blue being low image intensity, indicating cold areas such as the unignited fuel plume, and yellow being high image intensity, indicating hot areas such as the ignited fuel. A simplified example of the approach is presented in Appendix A, for additional clarity.

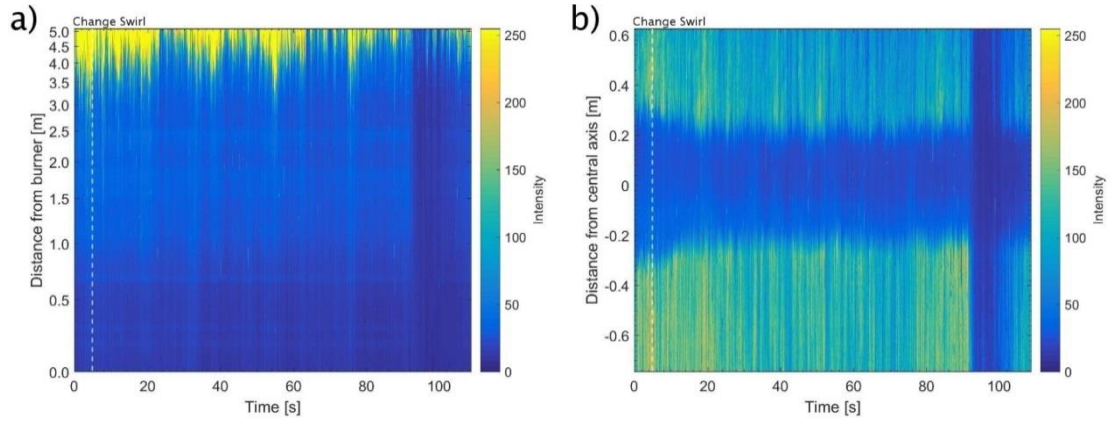

Figure 6-4: Intensity profiles over time when swirl pressure is changed from 180 to 30 mbarg. a) along the horizontal centerline, and b) across the image 1 m in front of the burner.

Figure 6-4 shows how the flame is impacted when the swirl pressure is lowered from 180 mbarg to 30 mbarg, at 5 seconds. In comparison the images in Figure 6-3 shows how the flame appears before and after similar changes. The low intensity region in the center of the Figure 6-4b indicates the dark petcoke plume seen in Figure 6-3. The swirl is changed by closing a valve at the burner, which gives an almost immediate effect on the flame. The reduction of the swirl pressure is seen to give a contraction of the flame plume in Figure 6-4b between 5-15 seconds. The swirl also impacts the ignition point of the flame as shown in Figure 6-4a. Here it can be seen that the bright yellow region, which represents a high image intensity and fuel ignition, becomes smaller after 20 seconds. Thus, the ignition point is moved further away from the burner. The figure also indicates the constantly changing

nature of the flame. In Figure 6-4a, it can be seen that the flame burns back and ignites earlier at around 40, 60, and 80 seconds. This could possibly be linked to some pulses in the fuel flow or changes in the air flow around the burner. For instance, the kiln rotates at approximately 3 RPM, which coincides with the frequency of the flame pattern. In addition, a dark band is seen in the region 90-100 s, which is caused by excessive dust from the clinker cooler obstructing the flame view. The dust is likely caused by the emptying of air blasters that are installed in the cooler to prevent buildups, so-called 'snowman' formation.

6.3.1.2 Effect of Nozzle Configuration

The effect of nozzle configuration on the petcoke flame is shown in Figure 6-5 and Figure 6-6. Nozzle configurations of 0, 30 and 180° are shown for a highly swirled flame with swirl pressure of 180 mbarg. With the nozzles at 0° the flame is ignited between 4 and 5 meters from the burner. When the nozzles are turned to 30° or 180°, the ignition occurs between 3 and 4 m. The flame plume before ignition has a similar width when the nozzles are at 0 and 30°, but is widened when the nozzles are turned to 180°. In Figure 6-6 it is seen how the image intensity changes when the nozzles are turned from 0 to 180°. The 20 axial air nozzles are rotated one at a time and takes longer than when the swirl is changed. The first nozzle is changed at 20 seconds, while the last is changed at 180 seconds. The flame plume is widened (Figure 6-6b), especially between 80-120 seconds, and the ignition is moved closer to the burner (Figure 6-6a).

It is shown how the nozzles can help influence the mixing of hot secondary air and fuel. When the nozzles are in 0°, the configuration is relatively closed, and the jets mimic an annular channel where the entrainment of hot secondary air into the fuel stream is slow, which results in a later ignition of the petcoke. Turning the nozzles outwards to 180°, gives extra space for the fuel stream to expand and widens the fuel plume. This slows the fuel stream and gives an increased mixing of hot secondary air, which results in an earlier ignition. It appears that a similar ignition length can be achieved by just turning the nozzles to 30°. In this case the nozzle configuration is more open than in 0°, see Figure 6-1, and allows increased amounts of secondary air to be entrained into the fuel jet, moving the ignition point closer to the burner, without expanding the fuel plume as much as when the nozzles are at 180°.

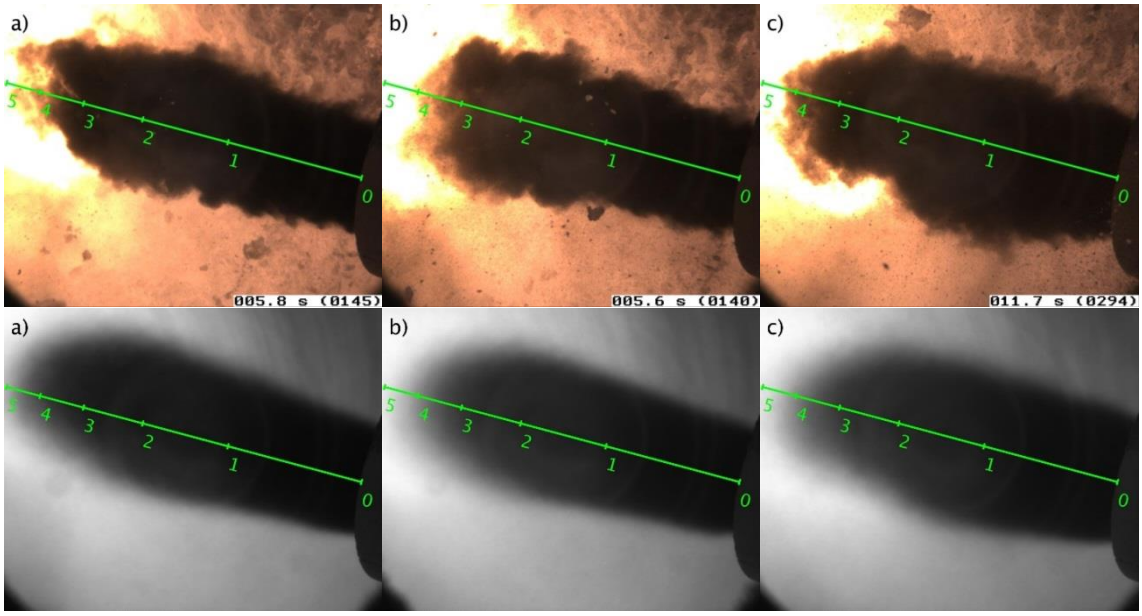

Figure 6-5: Effect of axial air nozzle configuration on the petcoke flame with swirl pressure of 180 mbarg. Axial air nozzle position of a) 0°, b) 30°, c) 180°.

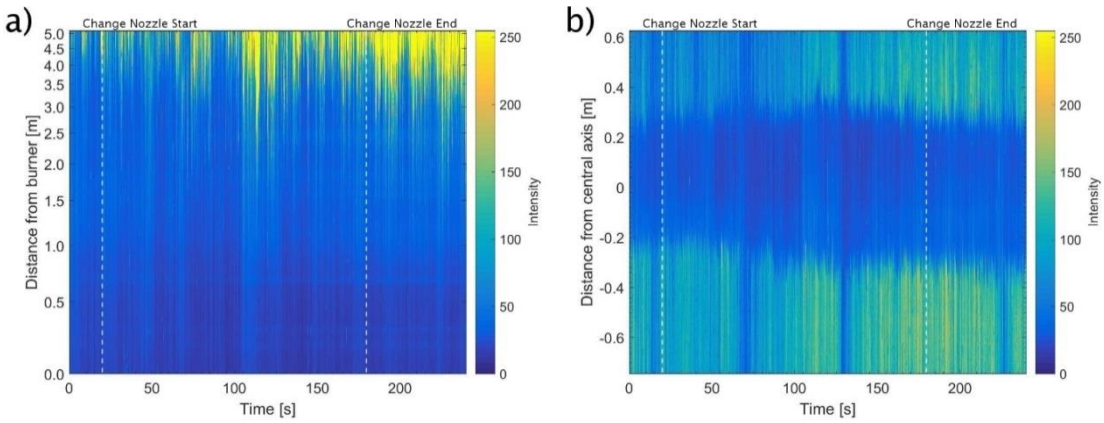

Figure 6-6: Intensity profiles over time when nozzles are changed from 0 to 180°. a) along the horizontal centerline, and b) across the image 1 m in front of the burner.

The impact of swirl and nozzle configuration is compared in Figure 6-7. The graphs compare the image intensity of the averaged frames in Figure 6-3 and Figure 6-5. Figure 6-7a shows the image intensity along the horizontal centerline and thus indicates the point of ignition, as the distance where the intensity begins to increase sharply and approaches a value around 200. With the nozzles at 30° this is mainly impacted by increasing the swirl to 180 mbarg. With the swirl at 180 mbarg, the ignition point is similar with nozzles at 30 and 180°. Turning the nozzles to 0° delays the ignition from approximately 4.5 m to 5.0 m.

Figure 6-7b shows the intensity across the flame plume 1 m in front of the burner and indicates the width of the flame plume. The unignited flame plume is dark,

resulting in low image intensity. Thus, the flame plume width can be compared by comparing the width of the intensity dip observed in Figure 6-7b. The flame plume is widest at ~55 cm, when the swirl is high at 180 mbarg and the nozzles are turned outwards to 180°. It is narrowest with ~30 cm, when nozzles are at 30° and swirl at 30 mbarg.

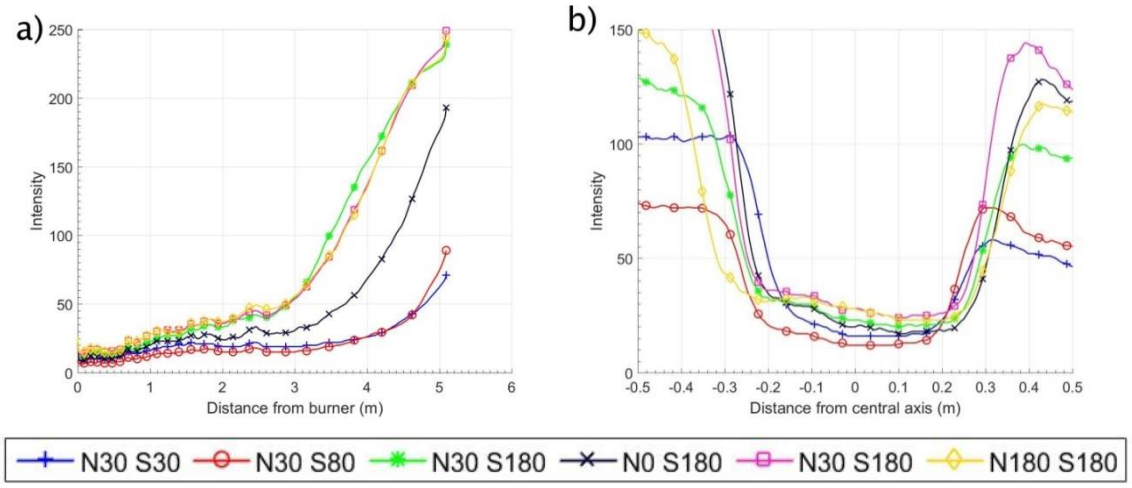

Figure 6-7: Intensity profiles for the petcoke flame images with different swirl (S in mbarg) and nozzle configurations (N in °) a) along the horizontal centerline, and b) across the image 1 m in front of the burner.

Based on the performed tests it is concluded that the petcoke flame can be adjusted by both changing the swirl and the axial air nozzle configuration of the Jetflex burner. It is possible to both influence how fast the fuel expands and the ignition point. The optimal settings will likely wary between plants. Normally, it is of interest to have a high temperature flame, which creates effective heat transfer to the clinker bed. However, a too high temperature may harm the kiln refractory or lead to excessive NOx [30,31,35,36]. Thus, for a hard to ignite fossil fuel such as petcoke it may be necessary to have a high swirl and nozzle offset to facilitate ignition. With a more volatile and easy to ignite coal, lower swirl and a low nozzle offset can be used. To reduce NOx emissions from the kiln it is important to limit the oxygen availability in the high temperature combustion zone. This can possibly be achieved by having the nozzles at 0° where mixing of fuel and secondary air is limited.

6.3.2 Co-fired Flame with Petcoke in Annular Channel

In this chapter the effects of swirl air and nozzle configuration on the co-fired flame with petcoke in the annular channel are investigated.

6.3.2.1 Effect of Swirl Air

An example of how the swirl influences the co-fired flame is seen in Figure 6-8 and Figure 6-9. Here the axial air nozzles are at 60° and the swirl level is increased from 50 to 150 mbarg. The plume is widened by the increased swirl level. However, the ignition point does not appear to be changed significantly. Image intensity is increased slightly in the lower left corner of the image Figure 6-8b.

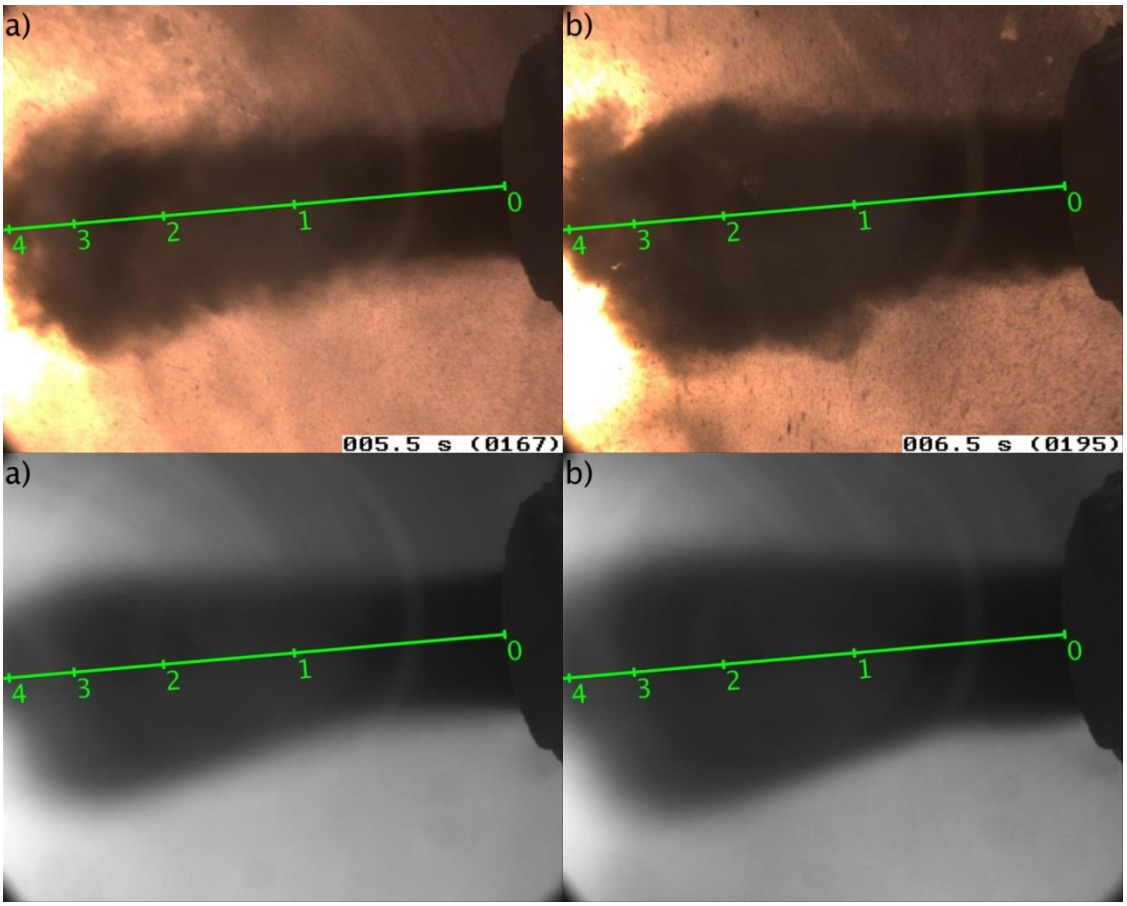

Figure 6-8: Effect of swirl pressure on the co-fired flame with axial air nozzles at 60°. Swirl pressure of a) 50 mbarg, b) 150 mbarg. SRF contributes 60 % energy.

Figure 6-9 shows how the image intensities change over time as the swirl air pressure is increased from 50 to 150 mbarg is seen. The change occurs between 10 and 15 s and widens the flame plume. The ignition point is not influenced, likely because it is further than 4 m from the burner and thus not shown in the images above.

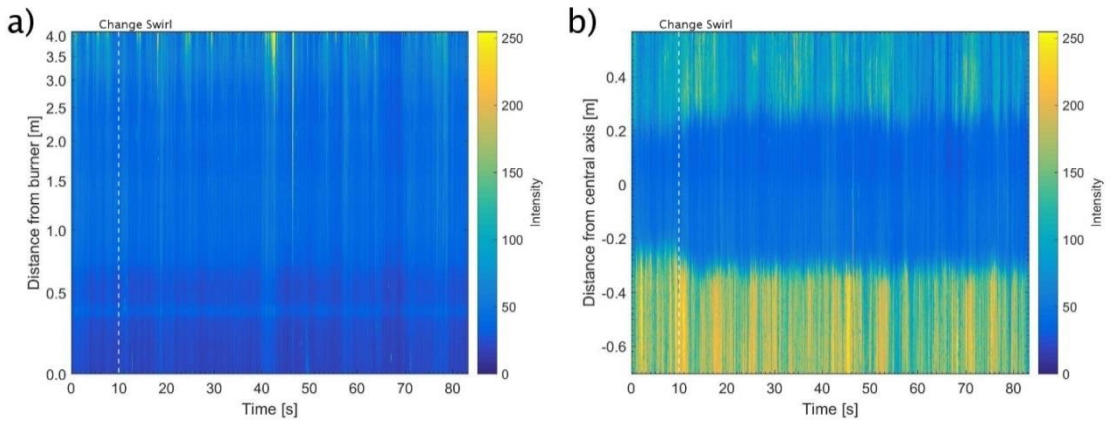

Figure 6-9: Intensity profiles over time when swirl pressure is changed from 50 to 150 mbarg. a) along the horizontal centerline, and b) across the image 1 m in front of the burner.

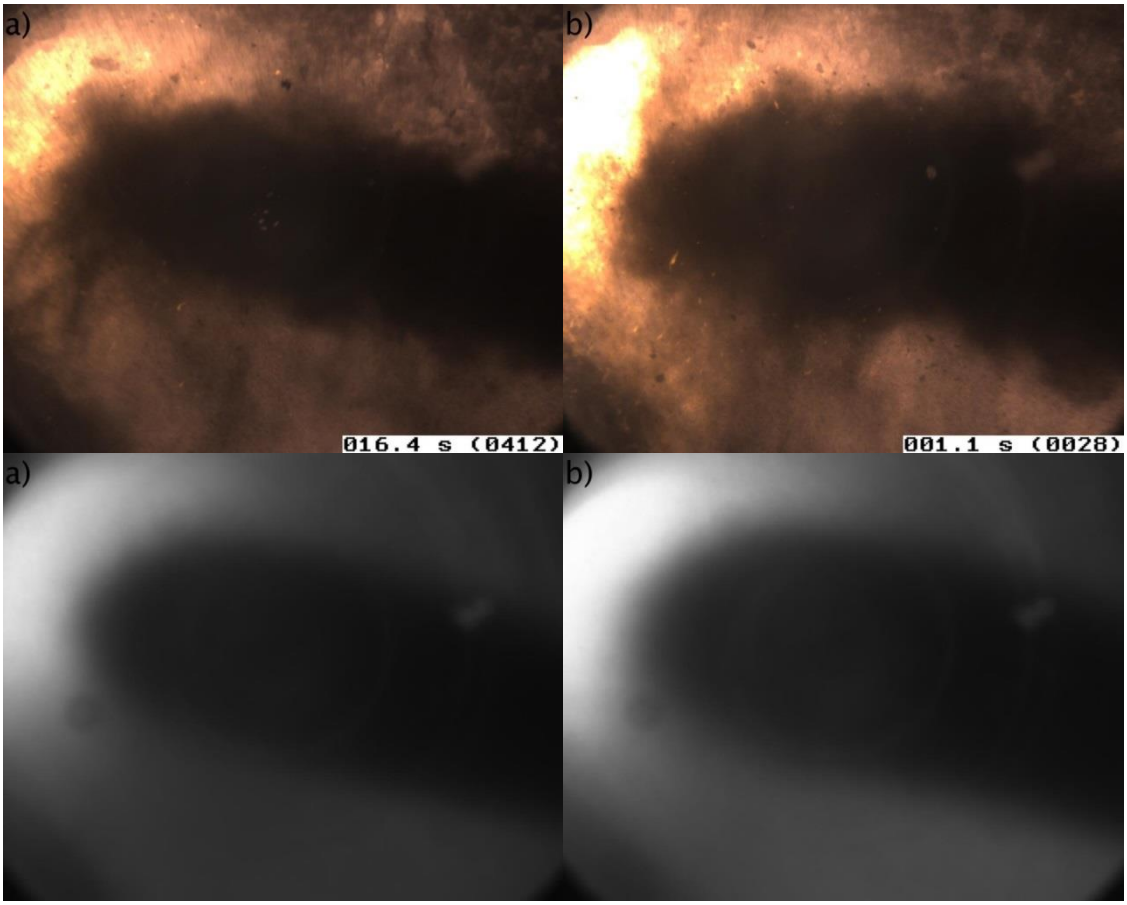

Figure 6-10: Effect of swirl pressure on the co-fired flame with axial air nozzles at 30° using alternative camera view. Swirl pressure of a) 100 mbarg, b) 180 mbarg. SRF contributes 70 % energy.

The images presented in Figure 6-10 shows a different view where the camera has been turned more downstream in the kiln to better observe the region where the flame ignites. The burner is used as a size reference to determine the length of the

flame in previous images. With the different view, the burner tip is no longer visible, and it is not possible to determine distances in the image. In this case a swirl level of 100 and 180 mbarg with nozzles at 30° is compared. An increased high intensity region is observed, indicating that the swirl helps boost the combustion, resulting in increased temperatures closer to the burner. It can also be observed how additional SRF is falling out of the main fuel plume, when the swirl is increased. The SRF particles are seen as orange specks, indicating that they ignite as they leave the petcoke plume and enter the hot secondary air, mainly below the petcoke plume.

6.3.2.2 Effect of Nozzle Configuration

Figure 6-11 and Figure 6-12 show an example of the effect of the nozzle configuration on the co-fired flame.

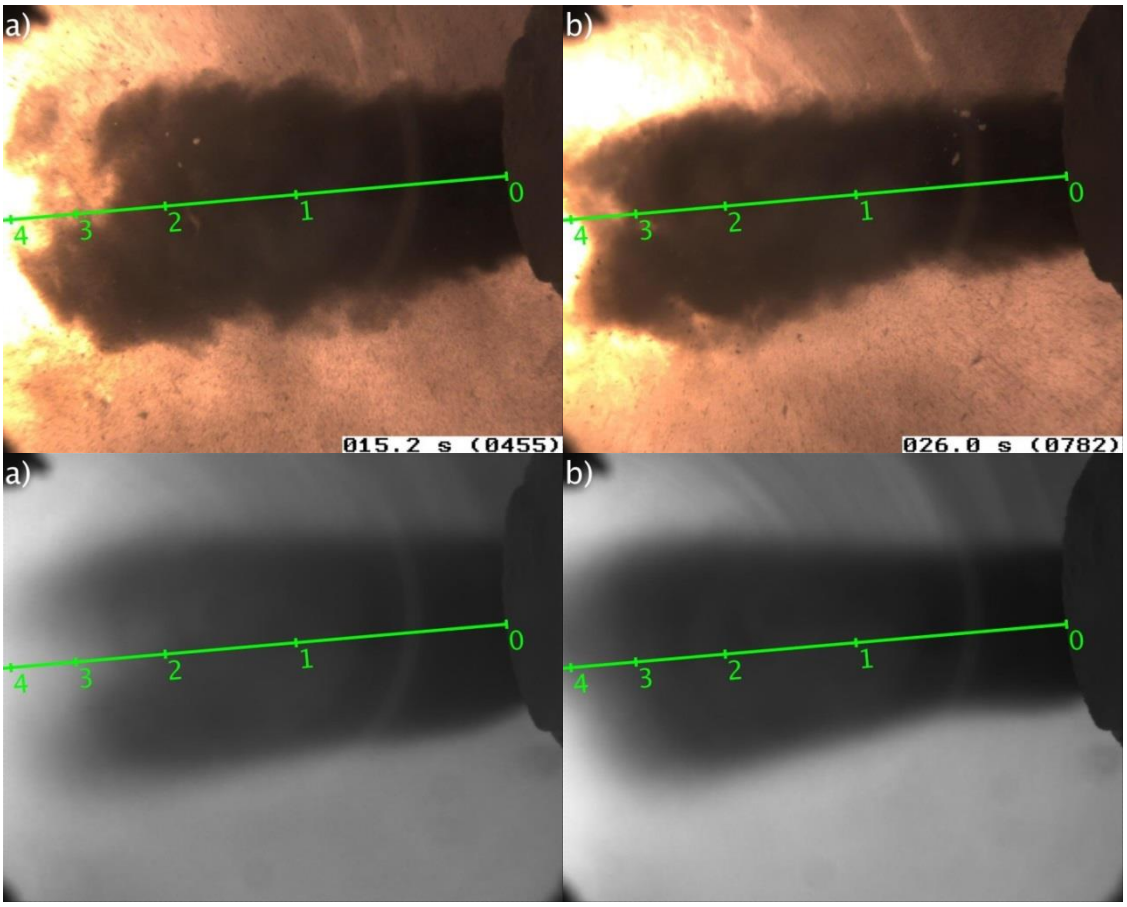

Figure 6-11: Effect of axial air nozzle configuration on the co-fired flame with swirl pressure of 150 mbarg. Axial air nozzle position of a) 180°, b) 60°. SRF contributes 60 % energy.

The effect of having the nozzles at 180° instead of 60° is to expand the fuel jet faster. This is most notably seen close to the burner. When the nozzles are at 60° an expansion of the fuel plume is seen from around 0.8 m in front of the burner. With

the nozzles in 180°, the fuel plume is widened almost at the burner front and keeps a more uniform width. The width at a distance of 3 m appears similar. The ignition point benefits slightly from the faster expansion obtained by having the nozzles at 180°.

In Figure 6-12 the effect of changing the nozzles from 180 to 60° is illustrated. The change starts at around 30 s and continues until 270 s. Since the nozzles are changed one at a time a brief period with an asymmetric nozzle configuration is obtained. This initially makes the flame plume expand downwards in the period 30-60 s, as observed in Figure 6-12b. As the bottom nozzles are then adjusted, the bottom of the flame plume contracts. As the remaining top nozzles are turned from 180 to 60° a contraction of the top of the flame plume is also observed between 200 and 270 s. The narrow flame plume also affects the ignition point as shown in Figure 6-12a, which moves further away from the burner.

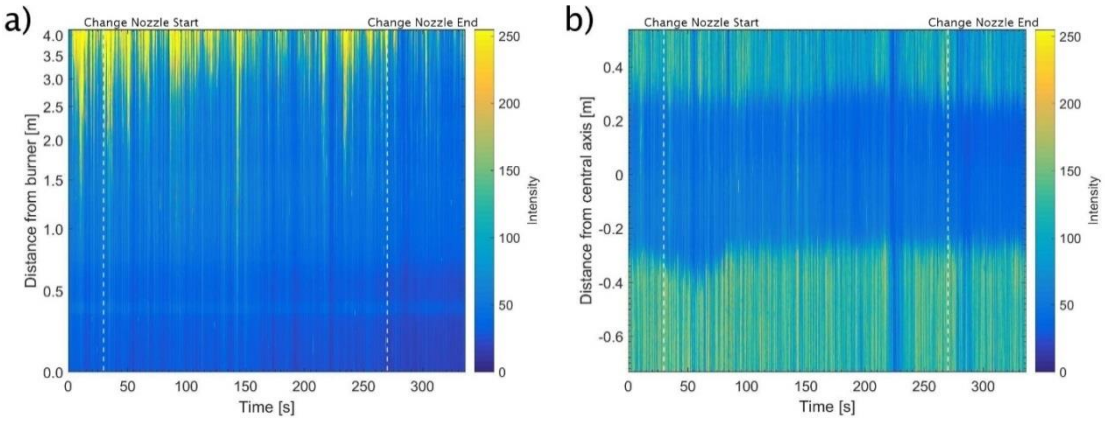

Figure 6-12: Intensity profiles over time when nozzles are changed from 180 to 60°. a) along the horizontal centerline, and b) across the image 1 m in front of the burner.

The intensity profiles in Figure 6-13 summarize and compare the impact of swirl and nozzle configuration for the co-fired flame. The ignition point (Figure 6-13a) is not influenced much by changing the swirl between 50 and 150 mbarg. Turning the nozzles to 180° results in an ignition point around 4 m from the burner tip. The flame plume width (Figure 6-13b) is increased by higher swirl and nozzle configuration angle. The plume width is ~30 cm with nozzles at 60° and swirl at 50 mbarg, while it is ~50 cm with nozzles at 180° and swirl at 150 mbarg. There is a difference in the plume width and ignition point between the repeat cases with nozzles at 60° and swirl 150 mbarg (red and green graphs). The images shown in Figure 6-8, used to create the blue and red curves, were recorded one hour earlier than those in Figure

6-11, used to create the green and black curves. This could result is some differences in the kiln state. For instance, a higher temperature in the kiln hood was measured during the latter set of videos. This could impact ignition, and explain why the green graph of Figure 6-13a obtains a higher intensity than the red graph, which are made with similar burner settings. Thus, the state of the kiln can influence the repeatability of experiments. However, many experiments are made within short time intervals, as shown in e.g. Figure 6-12, where the state of kiln does not have time to change. However, comparisons of operation on different days, should be analyzed with care.

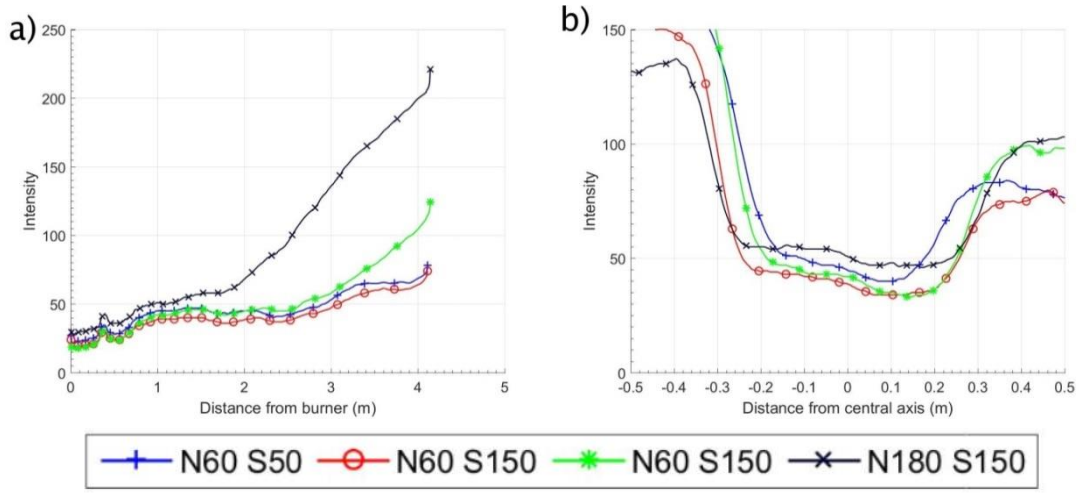

Figure 6-13: Intensity profiles for the co-fired flame images with different swirl (S in mbarg) and nozzle configurations (N in °) a) along the horizontal centerline, and b) across the image 1 m in front of the burner.

In comparison to the petcoke flame the co-fired flame is more difficult to ignite when the nozzles are at 60° and the swirl air pressure is either 50 or 150 mbarg. Changing from low to high swirl does not have the same impact on ignition point as for the petcoke flame. Changing the nozzles to 180° has a larger effect in this case, which gives an ignition point at around 4 m that is similar to the petcoke flame. However, the intensity does not reach near 250 as it does for the petcoke flame.

6.3.3 Co-fired Flame with Petcoke in Central Channel

As already mentioned a special feature of the Jetflex burner is that the petcoke can be switched from being fed in the regular annular channel to the central channel where it is mixed with the SRF. In this chapter setting changes are investigated with the petcoke in the central channel.

6.3.3.1 Effect of Swirl Air

Switching the petcoke from the annular to central channel has a relatively large impact on the flame appearance as seen when comparing Figure 6-14 with Figure 6-8. With the petcoke in the central channel, the fuel plume is initially narrow. However, with higher degree of swirl the fuel quickly expands to be as wide as when petcoke is injected through the annular channel. The SRF appears to be more dispersed with burning particles above and below the main fuel plume. When petcoke and air is in the annular channel it may act as a barrier that restricts the flow of SRF, which is not the case with petcoke in the central channel. With the petcoke in the central channel, the fuel plume also appears more transparent. This could perhaps be caused by some of the petcoke sticking to the larger SRF particles. The ignition of the petcoke seems to be easier, when it is fired through the annular channel. In Figure 6-14 the majority of the fuel is not ignited within the image frame. Only the SRF particles that are whirled out into the hot secondary air are ignited. When the petcoke is fed through the annular channel, it may be easier to mix with the secondary air, aiding ignition. Furthermore, as it encases the SRF the petcoke will absorb most of the thermal radiation from the kiln walls, which results in a faster heating.

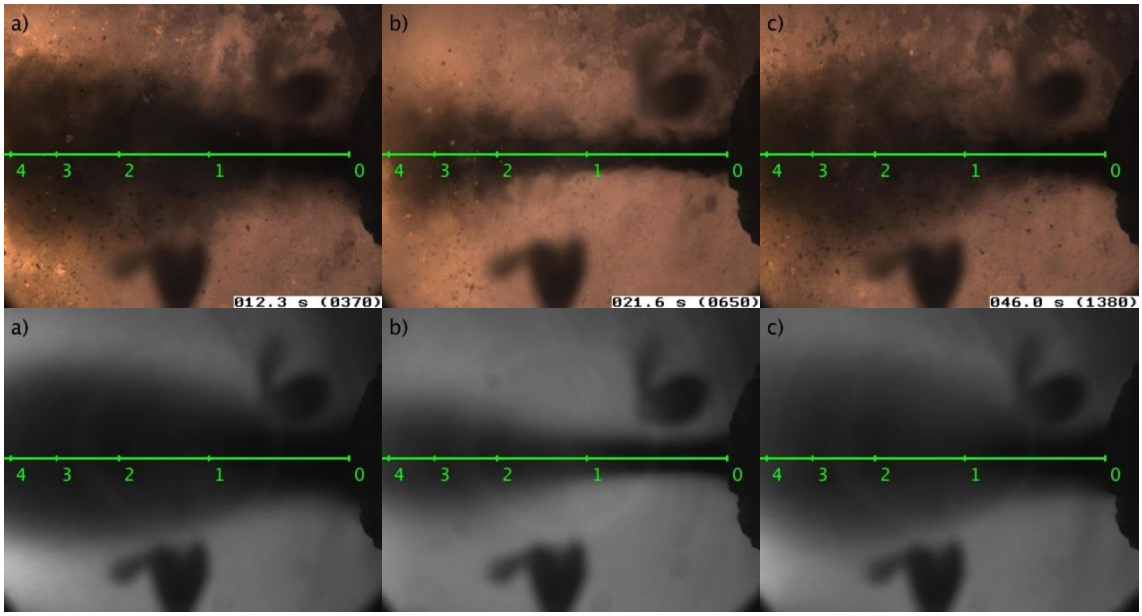

Figure 6-14: Effect of swirl pressure on the co-fired flame with axial air nozzles at 60° and petcoke in center. Swirl pressure of a) 150 mbarg, b) 10 mbarg c) 180 mbarg. SRF contributes 65 % energy.

Changing the swirl air pressure when the petcoke is in the central channel is seen to have a large effect on the flow of fuel as shown in Figure 6-14 and Figure 6-15. The image sequence in Figure 6-14 shows an initial swirl pressure of 150 mbarg, it is then reduced to 10 mbarg, and increased to 180 mbarg. The difference between the 150 and 180 mbarg is slight, but turning the swirl pressure to 10 mbarg has a very large effect. In this case the fuel is hardly dispersed in the kiln, resulting in a very narrow fuel plume. Observing the intensity plots in Figure 6-15 it is seen that the change in swirl has no influence on the ignition point, but a large impact on how well the fuel is dispersed in the kiln cross section. With higher swirl, the dispersion of the fuel happens rapidly around 0.5 meters, which may be caused by a recirculation zone that that serves to break up the fuel.

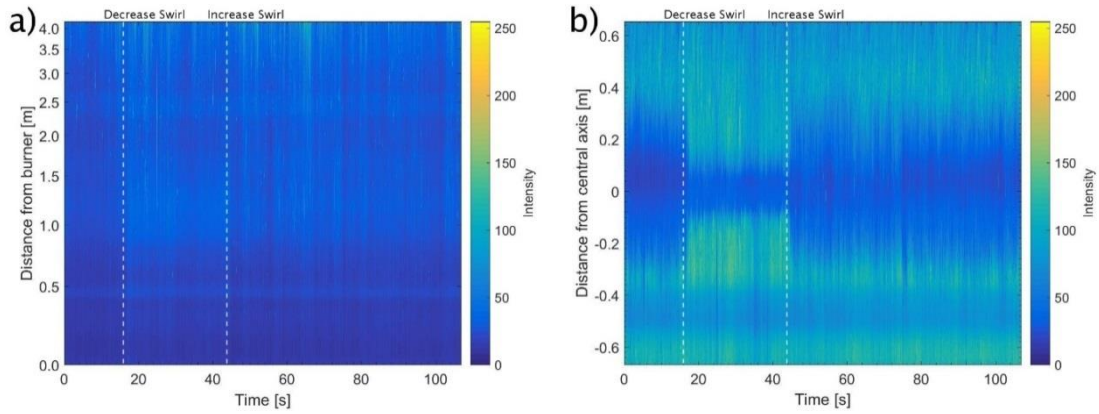

Figure 6-15: Intensity profiles over time when swirl pressure is changed from 150 to 10 to 180 mbarg. a) along the horizontal centerline, and b) across the image 1 m in front of the burner.

The images presented in Figure 6-16 shows a different view where the camera has been turned more downstream in the kiln to better observe how the SRF behaves further from the burner. The swirl pressure has a large influence of how the SRF is dispersed in the kiln. When the swirl is high, the SRF is easily whirled out of the petcoke plume, where it begins to burn as it enters the hot secondary air. Much of the fuel is seen to be burning close to the walls and will be in contact with the clinker. With the lower swirl level, less of the SRF is whirled out of the petcoke plume, and it does not ignite. It will instead travel further into the kiln, and eventually burn further away. Comparing the images to those in Figure 6-10 more SRF is whirled out of the central petcoke plume. Likely, this is because the SRF flow is no longer restricted by the petcoke and transport air in the annular channel.

It is often reported that unconverted fuel in contact with the clinker may cause local reducing conditions [46], which can increase volatile circulation [111,119] and cause brown clinker with reduced quality [106–108]. However, these negative effects were not observed during testing, even though large amounts of particles can be seen burning at the walls and in contact with the clinker, when the swirl level is high. With the low swirl level, the SRF particles are likely to end up in the clinker regardless, since the temperature and conversion is low in the central part of the fuel plume. This cannot be observed in the videos, since it occurs too far from the burner, and the view is obstructed by the petcoke flame and clinker dust.

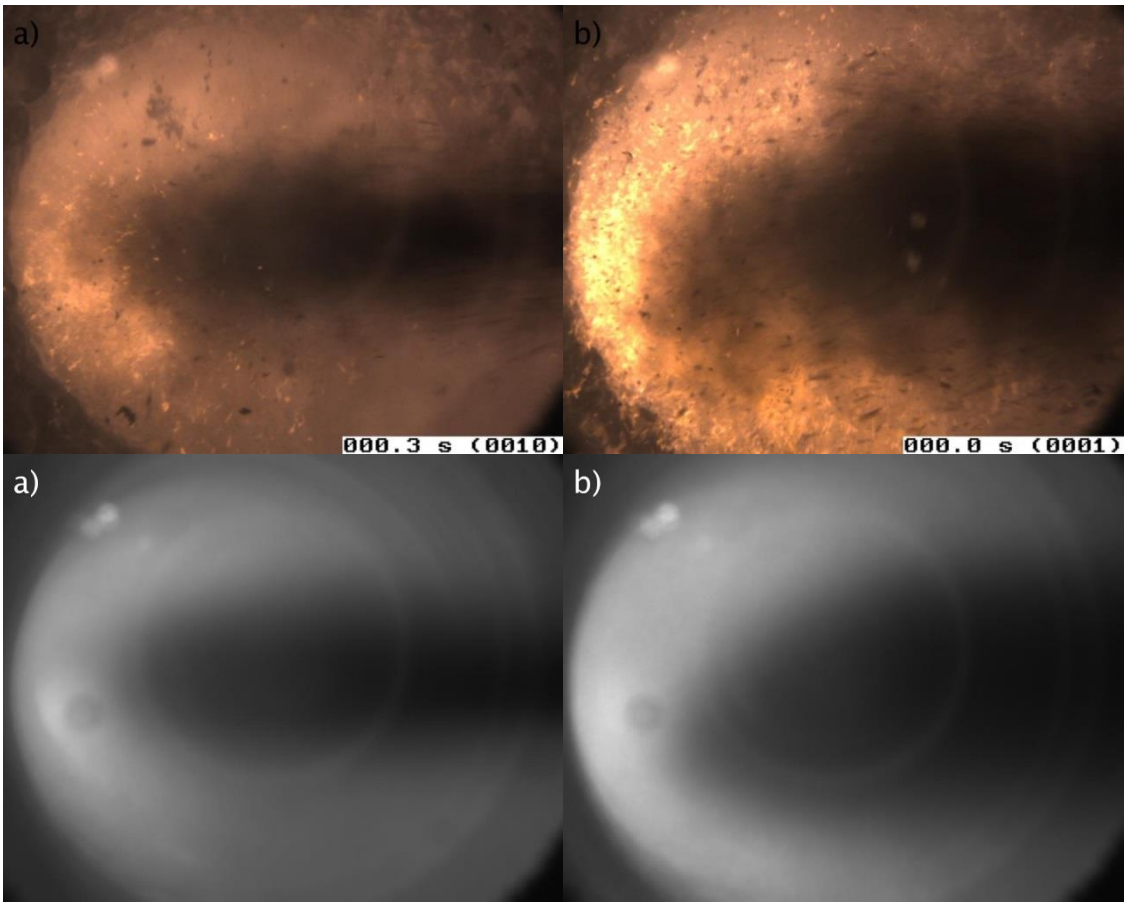

Figure 6-16: Effect of swirl pressure on the co-fired flame with axial air nozzles at 30° and petcoke in central channel. Swirl pressure of a) 50 mbarg, b) 180 mbarg. SRF contributes 70 % energy.

6.3.3.2 Effect of Nozzle Configuration

The effect of changing the axial air nozzles is shown in Figure 6-17 and Figure 6-18. An interesting behavior is observed here. The fuel plume expands as expected when nozzles are changed from 0 over 30 to 60°. However, when the nozzles are then turned to 180°, the plume is narrower than in 30 or 60°.

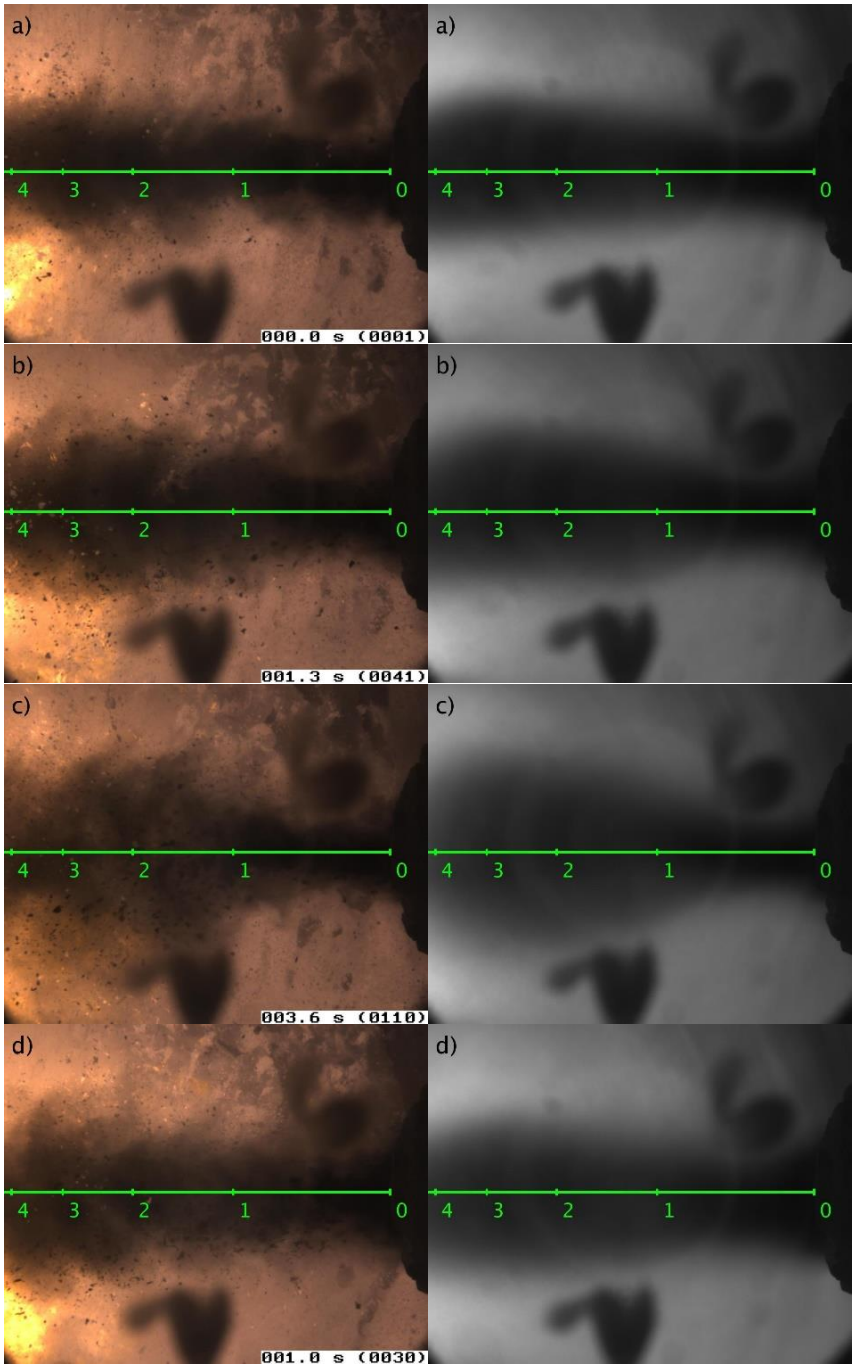

Figure 6-17: Effect of axial air nozzle configuration on the co-fired flame with swirl pressure of 150 mbarg. Axial air nozzle position of a) 0°, b) 30° c) 60°, d) 180°. SRF contributes 65 % energy.

When the nozzles are at 30 or 60° a sudden expansion of the fuel occurs around 0.5 m in front of the burner. When the nozzles are at 180°, this sudden expansion is less pronounced, and instead the fuel plume is wider at the burner front. A similar behavior was observed when the petcoke was in the annular channel as shown in Figure 6-11. It is possible that the change of nozzle configuration changes the

location or size of the internal recirculation zone, which affects the dispersion of SRF.

It is observed that the SRF does not ignite within the first 5 meters in the central part of the fuel plume. It only ignites when it is dispersed into the hot secondary air surrounding the fuel plume. Thus, no impact on the nozzles is observed along the horizontal centerline in Figure 6-18a. There is a change in the spreading of the fuel and the width of the fuel plume as observed in Figure 6-18b. As the nozzles are changed, the plume is shifted downwards from around 70 to 110 s. The plume stabilizes more around the center when the remaining nozzles are adjusted around 250-300 s.

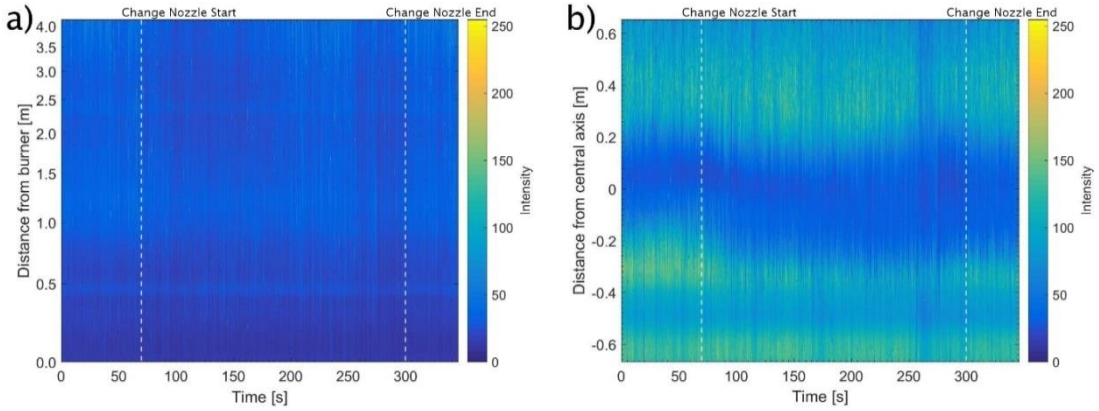

Figure 6-18: Intensity profiles over time when nozzles are changed from 0 to 180°. a) along the horizontal centerline, and b) across the image 1 m in front of the burner.

The impact of swirl and nozzles when the petcoke is fired through the central channel is summarized and compared in Figure 6-19. In the horizontal direction the settings have little impact on the observed intensity, see Figure 6-19a. The intensity is generally below 50, indicating no ignition of the fuel in the central part of the fuel plume. The width of the fuel plume and the spreading of the fuel is indicated by Figure 6-19b. Here a significant impact is seen when the swirl is lowered to 10 mbarg (red curve), which results in a very narrow fuel plume. The nozzle configuration of 30 or 60° (magenta and yellow curves) shows only minor differences. The largest difference is seen between 0 and 180° (black and dark green curves). Observing the intensity dip in Figure 6-19b, the curve for 180° is shifted to the left compared to the curve for 0°. This indicates that the fuel is pushed more downwards, which is also evident comparing Figure 6-18a and d.

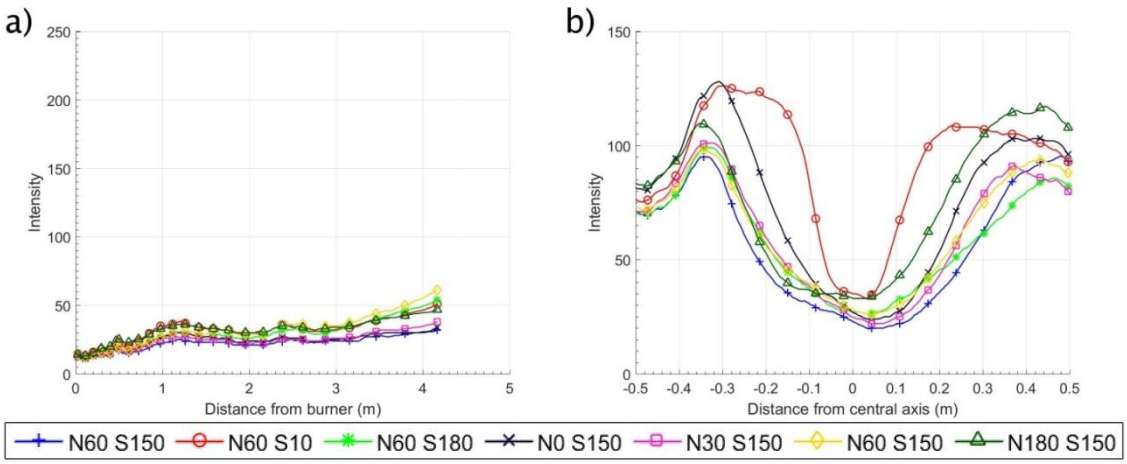

Figure 6-19: Intensity profiles for the co-fired flame with petcoke in central channel images with different swirl (S in mbarg) and nozzle configurations (N in °) a) along the horizontal centerline, and b) across the image 1 m in front of the burner.

6.3.4 Retraction of the Central Channel

The last feature of the burner that will be discussed here is that the center of the burner can be retracted, while petcoke and SRF is fired through the central channel.

Figure 6-20a shows the flame with the center in the normal position, with a swirl of 180 mbarg and nozzles at 180°. In Figure 6-20b, the center is retracted. The effect is that the fuel is slightly more dispersed in the immediate vicinity of the burner within 20 cm. In Figure 6-21b, the image intensity is slightly lower with the center retracted, than when it is in the normal position. Further from the burner the difference is not discernible. The plots with intensity changes over time are not shown here, since the difference is too small to be discerned on that kind of plot.

A scaled down version of the burner was tested in cold flow, before the industrial tests were performed. In the cold tests, retracting the center had a large impact on the fuel flow in front of the burner, compared to what is seen here. The reason is likely a higher flowrate and forward momentum of the fuel and transport air in the industrial tests, compared to the cold tests. The additional forward momentum makes it more difficult to change the flow direction of the fuel.

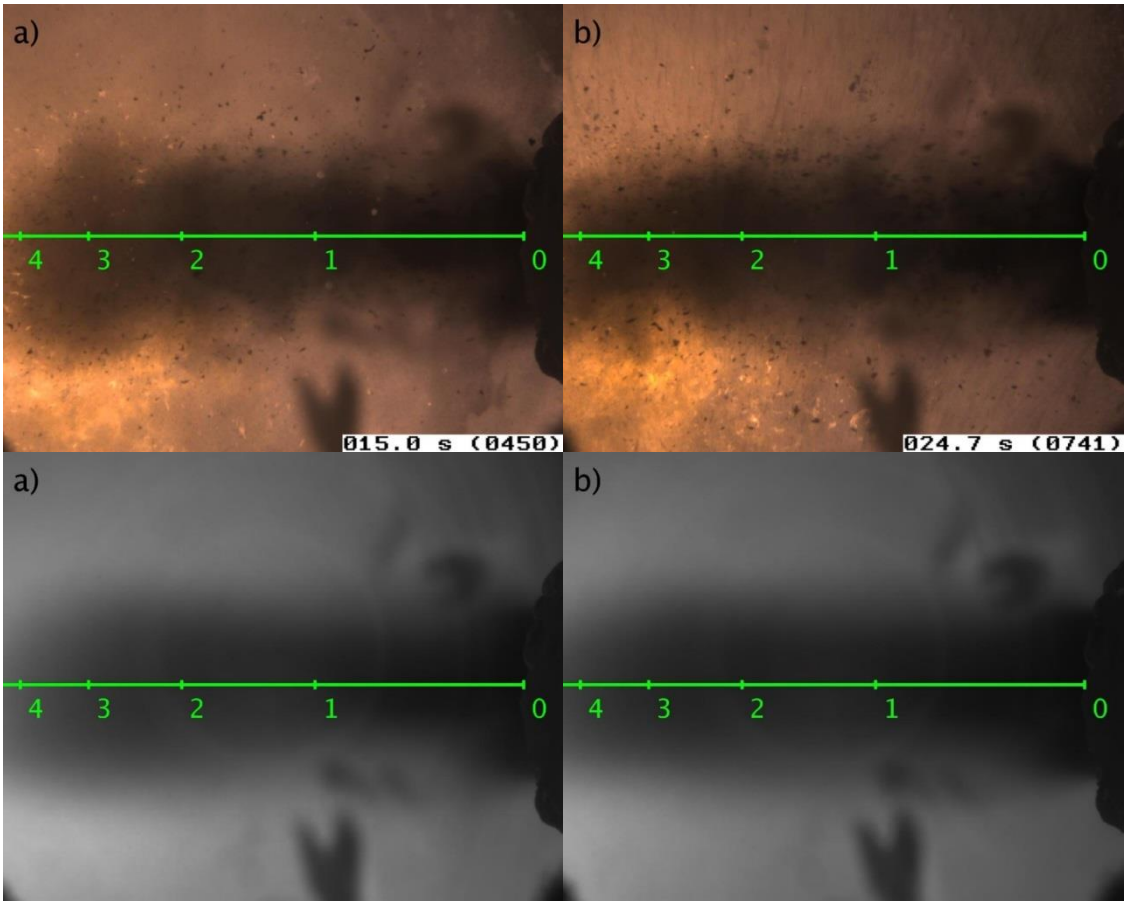

Figure 6-20: Effect of retracting burner center with axial air nozzles at 180° and swirl 180 mbarg. a) Center normal, b) Center Retracted. SRF contributes 90 % energy.

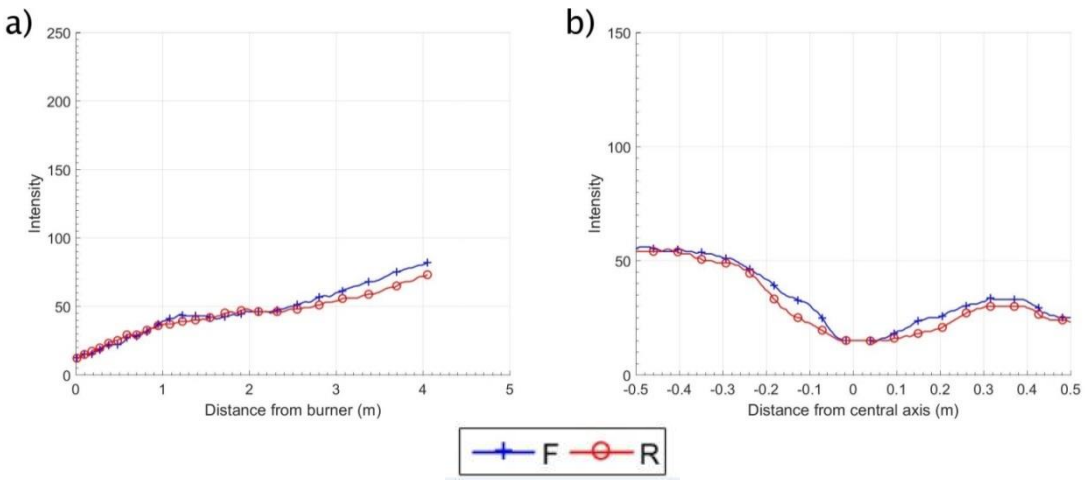

Figure 6-21: Intensity profiles for the images with center forward (F) or retracted (R) a) along the horizontal centerline, and b) across the image 0.1 m in front of the burner.

6.4 Statistical Data Analysis

In order to determine the optimal conditions for the operation of the burner when co-firing SRF a series of different burner settings were tested over 6 days according to the schedule in Table 6-2. The purpose was to test the impact of the different settings described earlier in this report and couple their impact to the cement clinker quality, which is measured as the clinker alite content. Alite (Ca_3SiO_5 or C_3S in cement chemist notation) is the main phase of interest in the Portland cement clinker [11].

Table 6-2: Overview of burner setting tests.

Test number	Test time (hours)	Fuel pos.	Axial pressure (mbarg)	Swirl pressure (mbarg)	Nozzle position (°)	Center Position
1	3.2	Center	210	200	180	Forward
2	16.7	Annular	210	200	180	Forward
3	8.1	Center	210	200	180	Forward
4	17.2	Annular	210	200	180	Forward
5	0.5	Center	210	200	180	Forward
6	2.2	Center	210	200	180	Back
7	1.4	Annular	210	200	180	Forward
8	11.6	Center	210	200	180	Forward
9	3.0	Annular	210	200	180	Forward
10	2.6	Center	210	200	180	Forward
11	1.5	Center	220	130	150	Back
12	1.2	Center	235	82	150	Back
13	1.3	Center	242	56	150	Back
14	1.8	Center	215	140	150	Back
15	2.4	Center	210	170	60	Forward
16	26.4	Annular	210	170	60	Forward
17	44.4	Annular	220	150	60	Forward

In order to determine the impact of the burner settings, and potential other process variables, on the clinker alite content, Partial Least Squares Regression (PLSR) is used. PLSR is a statistical tool to handle multivariate data [149–152], and can be used for e.g. process analysis and monitoring [152,153]. Within the cement industry PLSR has previously been used to predict quality and emissions [130,154–156].

The process variables are collected in a matrix, X_{PLSR}, that are used to describe the alite content, Y_{PLSR}. The PLSR model determines a number of regression coefficients, B_{PLSR}, that can be used to estimate Y_{PLSR} by the matrix $\hat{Y}_{PLSR}$ according to [153]:

$$\hat{Y}_{PLSR} = X_{PLSR} B_{PLSR} \quad \text{E 6.4}$$

There are a number of different methods to determine the most influencing variables for the PLSR [157]. One of the simpler methods is to observe the association between predictor variables and the response by observing the regression coefficients in the PLSR, i.e. B_{PLSR}. In this way the impact of some of the burner settings can be determined [153].

In the PLSR model 23 measured variables are used to predict the clinker alite content. An overview of the measured variables is given in Table 6-3. Of most interest here are the variables related to the burner settings, such as swirl air pressure and the nozzle configuration. In addition, some other variables that may have an influence on the clinker quality, such as fuel dosing, are also added to the X-matrix. Furthermore, the composition of the clinker, measured as Lime Saturation Factor (LSF), Silica Ratio (SR), and Alumina Ratio (AR), is included. Most of the X variables are continuous measurements, but two categorical variables are also used. Petcoke can be fired through the central (assigned 1) or the annular channel (assigned -1), and the burner center can be retracted (assigned 1) or in normal position (assigned -1).

The PLSR data analysis is performed in Matlab 2015b. The raw data are firstly reviewed, and obvious outliers are removed. For the data in question this was mainly related to the gas concentrations at the kiln raw meal inlet. Oxygen concentrations above 10 % are generally uncommon and may be caused by leakage of false air, thus these data were removed together with the corresponding CO and NOx measurements. The rotational speed of the kiln, also had some outliers, which also caused outliers in the kiln power consumption.

The clinker is sampled every two hours (with some exceptions), and the clinker phases are determined by X-ray diffraction [125] to determine the alite content. The process data are logged on a minute basis, which causes relatively large scatter in the data. Thus, to reduce the data scatter and number of process measurements, the measurements in the time interval 60 minutes before each clinker sample were averaged, to yield the value that is used in the regression. Afterwards the data were mean centered and normalized to standard deviation 1. In total 57 data points were used in the regression.

Table 6-3: Overview of variables used to predict the clinker alite content in the PLSR model.

Variable Name	Description	Unit
SR	Silica Ratio measured in the cement clinker	-
Nozzle Conf.	Nozzle Configuration – Angle of the axial air nozzles on the burner	°
Kiln Power	Power consumption of the kiln drive. Value will tend to increase at higher kiln temperatures	kW
LSF	Lime saturation factor in the cement clinker	-
SRF to MB	SRF fired in the main burner	ton/h
Kiln Hood T	Temperature in the kiln hood. Approximates the secondary air temperature	°C
Retracted Center	If the burner center is retracted (1) or if it is at normal position (-1)	-
Swirl P	Burner swirl pressure	mbarg
MB Total Power	Total heat input in main burner	MW
NOx at Kiln Inlet	NOx measured at the kiln raw material inlet	ppm
Petcoke in Center	If the petcoke is fired through the central channel (1) or in the annular (-1)	-
PC to Calciner	Petcoke fired in the calciner	ton/h
Calciner Total Power	Total heat input in the calciner	MW
Axial P	Burner axial pressure	mbarg
Kiln RPM	Rotational speed of the kiln in revolutions per minute	RPM
PC to MB	Petcoke fired in the main burner	ton/h
SRF/Rot.	Ratio of amount of SRF fed to main burner to the rotational speed of the SRF feeder	ton/h/%
SRF to Calciner	SRF fired in the calciner	ton/h
O2 at Kiln Inlet	Oxygen measured at the kiln raw material inlet	%
Kiln Feed	Amount of raw material fed to the kiln	ton/h
HD Total Power	Total heat input in the Hotdisc	MW
AR	Alumina ratio measured in the cement clinker	-
CO at Kiln Inlet	CO measured at the kiln raw material inlet	%

The number of latent variables is determined by computing the Mean Square Error of Prediction (MSEP) [158] as determined by 10-fold cross validation [159], which is shown in Figure 6-22a. The minimum value of the MSEP is achieved for 4 PLS components. The resulting measurement and model predictions are shown in Figure 6-22b. The data are shown in normalized form. The model follows the overall trend well, but seems to be unable to capture some of the outliers of lower alite content.

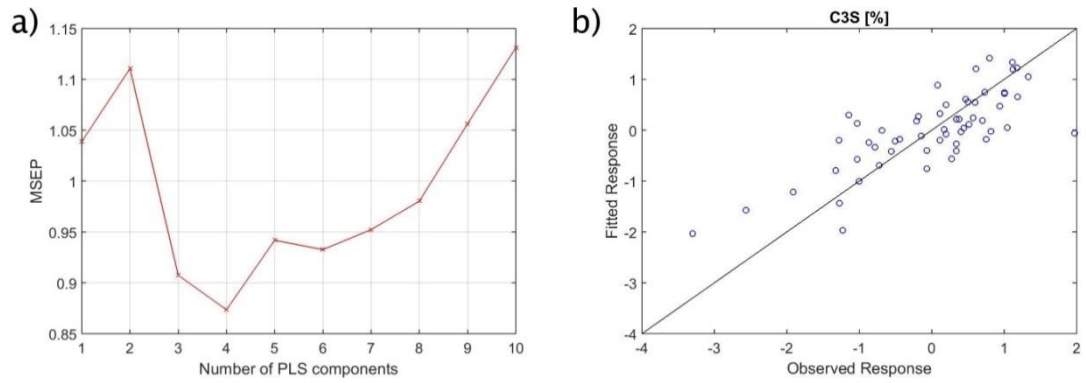

Figure 6-22: a) MSEP values as function of number of latent variables in PLSR. b) Comparison of measured and modeled values of clinker alite content using 4 latent variables, in normalized form.

6.4.1 Impact of Process Variables

The regression coefficients for the PLSR model, B_{PLSR}, are shown in Figure 6-23.

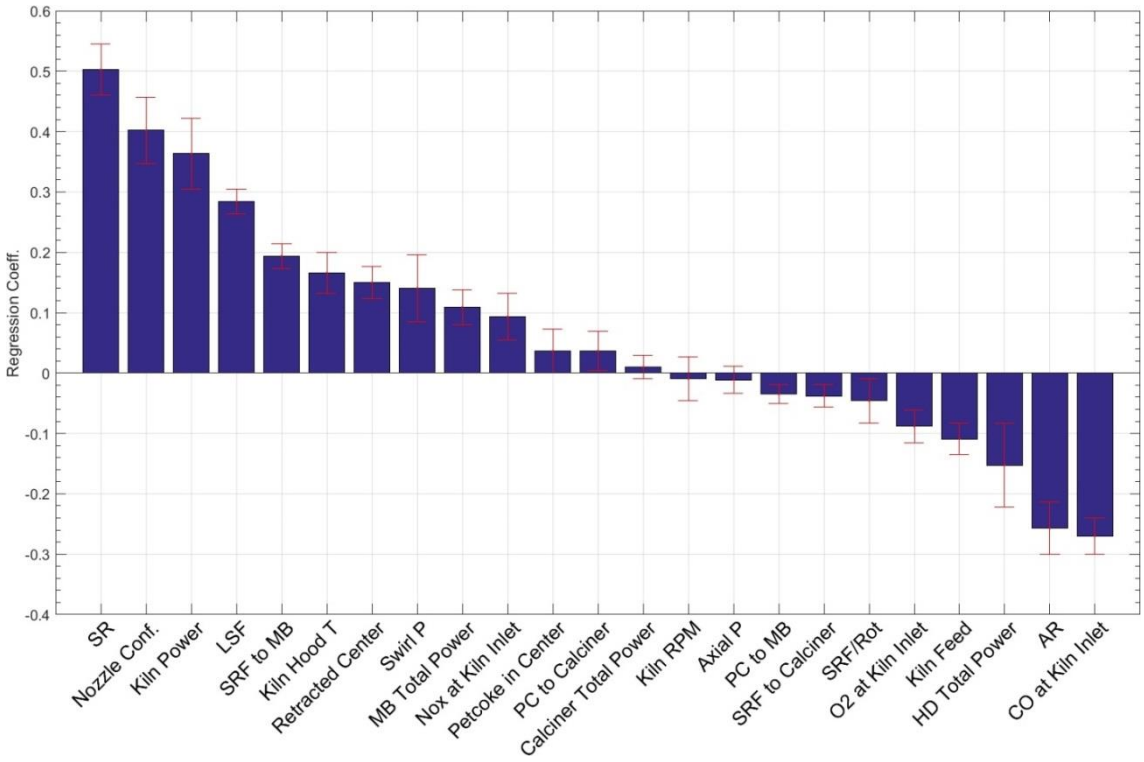

Figure 6-23: Regression coefficients in the PLSR model ($\hat{Y}_{PLSR} = X_{PLSR}B_{PLSR}$). Error bars are 95 % confidence interval determined by 10-fold cross validation. Variables are explained in Table 6-3.

Before focusing on the effect of burner settings, the effect of other variables will be reviewed, to determine if the regression predictions are reasonable. It is seen in Figure 6-23 that some of the parameters that yield high alite content are related to

the kiln temperature. Kiln power, kiln hood temperature and NOx at the kiln inlet all have a positive impact on the clinker quality. With high temperatures in the kiln the amount of melt in the kiln is increased, which increases the required torque and power consumption to rotate the kiln [17]. The formation of NOx will generally increase with increased temperatures as well [41].

Other factors that have a positive impact on the alite content are the clinker lime saturation factor (LSF) and silica ratio (SR), which are related to the composition of the clinker. With higher values of these ratios more lime and silica are present in the clinker, which can combine to form the alite. On the other hand, an increased LSF and SR increases clinker burnability. At the other end of the spectrum the clinker alumina ratio (AR) has a negative impact. With increased iron content the factor is lowered, which favors the reaction of lime and silica to form alite [34].

It is seen that SRF fired in the main burner (SRF to MB) presumably has a positive impact on the clinker quality, while increasing the petcoke (PC to MB) has a negative impact. Since SRF is more difficult to combust and burns at lower temperatures, this appears counterintuitive. However, since high amounts of SRF firing is the normal at this plant, high amounts of petcoke indicates an upset kiln. Typically, the plant operators will increase the amount of petcoke when the kiln temperature is lowered, thus it would likely coincide with lower alite content. It is also observed that the clinker alite content is increased with the total energy input to the kiln (MB Total Power). Another factor that is related to the fuel is the SRF/Rot, this measure is calculated as the amount of SRF fed to the kiln divided by the rotational speed of the SRF weigh feeder. If the SRF is dense, i.e. has high moisture content, the same mass can be fed with lower rotational speed than when the SRF is less dense, i.e. dry. The measure thus indicates the humidity of the SRF fed to the burner, and indicates that a higher humidity, which results in higher SRF/Rot numbers, has a negative impact on the alite content.

The factors that can have a negative impact on the alite content are e.g. kiln feed, as well as oxygen and CO at the kiln raw meal inlet. With an increased raw meal feed rate to the kiln, alite content will decrease, since the temperature decreases with more material present in the kiln. Too much oxygen in the kiln raw meal inlet indicates an excessive air to fuel ratio. This lowers the adiabatic flame temperature [34], which could lead to lower alite content. On the other hand, the oxygen content

should not be too low, since that will inhibit combustion. Spikes of CO may indicate an incomplete combustion, which will also negatively impact the clinker alite content.

It is interesting that the model indicates that firing of SRF in the Hotdisc (HD) should decrease the alite content. Perhaps excessive firing in the Hotdisc rather than in the calciner can negatively impact the calcination degree of the raw meal as it enters the kiln. The fuel burned in the Hotdisc is also of a relatively low quality, and expected to have a high content of impurities, such as metals and glass. Large silica particles originating from glass may have difficulties reacting with the lime in the kiln due to diffusion limitations [25], which could lower the alite content.

Based on this review of impact of different process measurements, it appears that the PLSR model is reasonable and that most measures behave as expected. Thus, the attention will now be turned to the effect of the burner settings.

6.4.2 Impact of Burner Settings

Increasing the swirl level (Swirl P) or the nozzle configuration (Nozzle Conf.), i.e. turning the nozzles outwards to a larger angle, appear to have a positive impact on the clinker alite content. From the observations made with the camera, it is seen that increased swirl or nozzle angle will help disperse SRF into the secondary air stream and ignite it. For a co-fired flame with the petcoke in the annular channel, higher swirl and nozzle configuration can also help ignite the petcoke faster. It is believed that spreading the SRF near the burner end will cause a more rapid combustion of the fuel, which contributes to increasing the temperature in the clinker burning zone. With a low swirl, the fuel will burn too far inside the kiln and not contribute energy, where it is required the most.

It appears beneficial to have the petcoke in the central channel rather than the annular channel, although the value of the regression constant has a high deviation. Based on the visual observations of the flame, this may be caused by the increased dispersion of SRF in the kiln, when it is not enclosed by the petcoke. Petcoke in the annular channel can also shield the SRF from radiation, meaning that it will take longer to heat and ignite the SRF.

A retracted center may also increase the alite content of the clinker. Based on the videos this appears to slightly increase the dispersion of the SRF when the petcoke

is fed through the central channel. However, the burner was only operating for 8 hours with a retracted center during the test of 146 hours. This is perhaps too few operating hours to make concrete conclusions.

6.5 Conclusions

The recently developed Jetflex cement kiln burner from FLSmidth has several different possibilities to shape the flame. This gives a flexible burner where it is possible to adjust the flame as e.g. fuel type or quality changes. In addition to the adjustment of axial momentum and swirl level, it is possible to direct the axial air using rotatable axial air nozzles and the petcoke can be switched from being fired in a conventional annular channel, to being mixed with the SRF in a large central pipe. It is also possible to retract the central part of the burner. Using a specially developed camera probe it has been possible to investigate and quantify how the different burner features impact the flame in the cement kiln.

When the kiln operates solely on petcoke it is possible to impact the ignition point of the flame by adjusting the swirl and the nozzle configuration, changing it from approximately 5 m to 3.5 m from the burner. The co-fired flame is harder to ignite and the effect of swirl and nozzles on the ignition point of the co-fired flame is less pronounced. When the petcoke is fired with the SRF through the central channel, instead of in the annular channel, ignition of the petcoke is more difficult. However, it becomes easier to disperse the SRF into the hot secondary air, which helps igniting the SRF. Increasing swirl or nozzle angle can increase the dispersion of SRF, but it will also whirl the SRF out of the main fuel plume. This causes it to burn on the kiln walls and in contact with the cement clinker. Retraction of the central part of the burner slightly improves the dispersion of the SRF.

The effect of burner settings were coupled to the cement clinker quality, by analyzing recorded operating data using Partial Least Squares Regression. Based on this analysis it can be concluded that increasing the swirl and turning the axial air nozzles to a larger angle, has a positive effect on the clinker alite content. Firing the petcoke through the central channel and retracting the central channel also had a positive effect on the clinker quality. The overall effect of these four measures is to increase the dispersion of the SRF near the burner. Presumably this will help establish a high temperature zone where alite can be formed.

7 PHYSICAL CHARACTERIZATION OF SRF

The classification system of the European standard CEN/TS 15359 classifies SRF based on the heating value and content of chlorine and mercury [160]. However, this classification is not detailed enough to determine how the fuel will burn in a cement kiln. Normally it is also required to know the moisture content of the fuel, and the particle size. For a cement kiln burner, a common size limitation for SRF is that particle size should be smaller than 30 mm [100] and predominantly two-dimensional. However, this is a vague definition and may be difficult to observe in practice. More detailed guidelines for the properties of SRF may help cement manufacturers assure the SRF quality and better determine limitations of co-firing.

Additionally, a thorough understanding of fuel properties on a particle level is necessary to create a detailed input for computational models. The parameters should include:

- Particle size/mass distribution and shape
- Composition of fuel
- Combustion kinetics

The particle size and shape are important for the combustion and flow behavior of the fuel. Larger particles take longer to heat and convert, while a larger surface area decreases conversion times. Furthermore, light and heavy particles are influenced differently by air flows. The composition of the fuel, with respect to e.g. proximate

and ultimate analysis is also important for the combustion behavior. Lastly, the rate at which the fuels react will also impact the combustion process.

Considering the large size of alternative fuels, generally above 1 mm, it is believed that the primary limitations for combustion are heat and oxygen transfer to the particle. Thus, it is more important to focus on an accurate description of the particle size and shape, rather than a detailed kinetic mechanism for combustion. This is the foremost purpose of a physical characterization method of SRF, which is covered in this chapter. Furthermore, the overall heat and mass balances obtained by a proximate, ultimate, and heating value analysis, are also important.

The work presented in this chapter has been carried out in collaboration with fellow PhD student, Mohammadhadi Nakhaei. An article manuscript [161] covering this work, with Mohammadhadi Nakhaei as first author, has been submitted to the journal Energy and Fuels.

7.1 Characterization of SRF in Literature

SRF is highly heterogeneous, consisting of different materials, as outlined in chapter 3.4.1. The main parts of the combustible fractions can be derived into biomass, paper & cardboard, plastics, and textiles (see Figure 3-3).

Liedmann et al. [162] attempted to characterize RDF and suggested a method for implementing the RDF particles into a CFD model for use in a power plant. Other articles by the authors used the same approach to model the co-firing in a cement kiln [143,163]. The RDF was divided into five groups: 2D foils, 3D plastics, paper & cardboard, textiles, and fines. Proximate and ultimate analysis and heating value was determined for each fraction. The mass of particles from each fraction was determined, and the sphericity was calculated based on images of the particles. Aerodynamic properties, drag and lift coefficients, were determined in a drop shaft.

Thermogravimetric Analyses (TGA) of different materials from SRF are quite abundant in the literature [164–166]. They show that different kinds of paper and cardboard, which are based on lignocellulosic materials, have a very similar devolatilization behavior, with the main mass loss occurring between 300-400 °C. Different kinds of plastic (except polyvinylchloride) also behave similarly with the main mass loss occurring between 400-500 °C. Of these plastics, polyethylene is the most widely used plastic [167], and will also be present in the largest amount in SRF

[164,168]. Polyethylene is almost completely volatile, while the lignocellulosic biomass will leave a char upon devolatilization [164,166]. Furthermore, it is also possible to see two distinct steps of mass loss in SRF samples during devolatilization, as e.g. shown in Figure 7-1. The size of the steps vary based on the content of plastics and biomass [165].

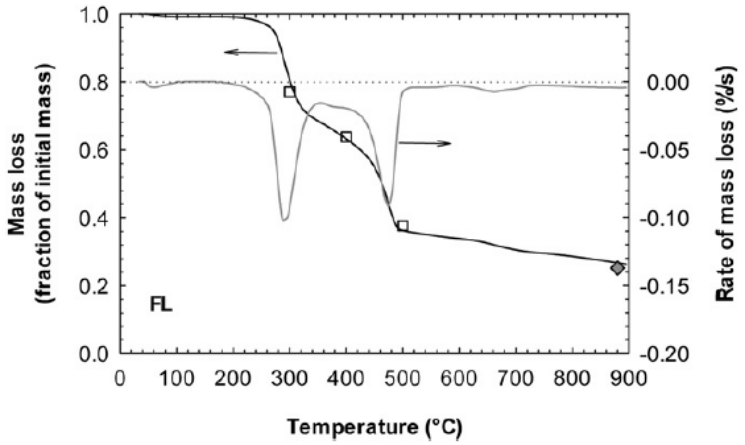

Figure 7-1: TGA experiment of SRF sample showing two distinct mass loss steps [165].

Consequently, to simplify the combustion model for SRF, it will be natural to split the SRF particles into a cellulosic biomass fraction and a plastic. The textile fraction can also be split into two, since it for the most part will consist of either natural fibers, e.g. cotton, or artificial fibers, e.g. nylon or polyester, which also decompose in the temperature range 400-500 °C [169]. If this approach is followed, it is only necessary to split the SRF sample into two fractions with different chemical/combustion properties, compared to the five different fractions proposed by Liedmann et al. [162]. A further detail of the size distribution and shape for particles in both fractions is still necessary.

7.2 Wind Sieve Setup

A regular sieving analysis is often inappropriate to characterize the size of SRF [170]. Since particles are only separated by their size, differences in particle shape may impact results significantly. If particles are instead separated by their terminal velocity, both the particle mass and shape will affect the classification. A simple example is presented in Table 7-1.

Assuming a sieve with an aperture size of 1 mm, a flat cuboid particle of dimensions 1x1x0.1 mm may be retained while a spherical particle of diameter 0.8 mm will pass.

However, since the spherical particle has a higher volume and lower surface area, one would expect it to burn slower than the flat particle. If the particles are instead separated by their terminal velocity, the flat particle has a smaller terminal velocity, which is consistent with it burning faster.

Table 7-1: Example calculations on particle shape. Terminal velocity determined at 20 °C with assumed drag coefficient of 0.44.

Particle shape	Particle size	Equivalent diameter	Volume	Surface area	Projected area	Terminal velocity
	mm	mm	mm^3	mm^2	mm^2	mm/s
Spherical	0.8	0.80	0.27	2.0	0.50	1.6
Cuboid	1x1x0.1	0.58	0.10	2.4	1.0	0.88

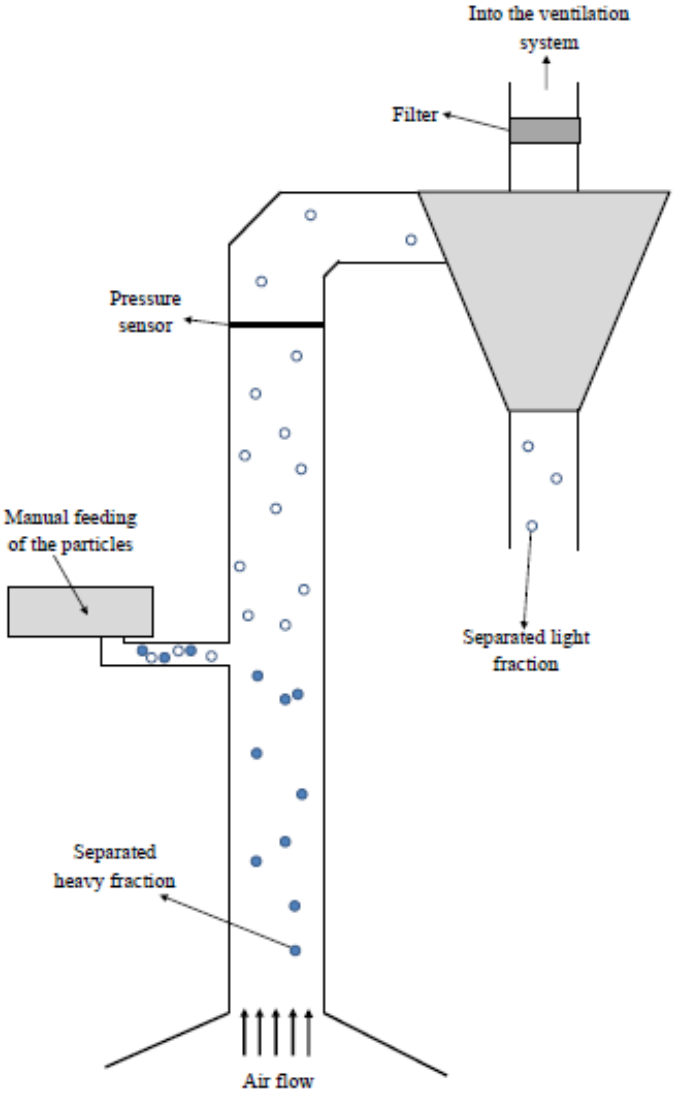

Figure 7-2: Sketch of the wind sieve setup used to characterize alternative fuels.

A wind sieve setup has been used to characterize the SRF. A sketch of the setup is shown in Figure 7-2. The sieve separates particles based on their terminal velocity. Particles are fed into a tube of diameter 24 cm and height 333 cm. The air velocity in the tube is maintained at a set-point controlled by a Pitot tube. Particles are fed at the middle of the tube, and particles with a terminal velocity higher than the set point will fall down, while the remaining particles are carried upwards with the air stream. The heavy fraction of particles is collected in a tray at the bottom, and the light fraction of particles is separated using a cyclone and collected at the top. The heavy fraction is collected and inserted into the wind sieve again using a higher air velocity. Thus, a particle sample can be fractioned into multiple groups based on terminal velocity.

7.2.1 Results from Wind Sieve Tests

Six different RDF samples obtained from three different cement plants were tested in the wind sieve. An overview of the fuels is given in Table 7-2. Industrial flame measurements were performed at Plant 1 and Plant 2 (see chapters 5 and 6). The samples are all SRF, except for RDF-C, which is the granulated tire used in the main burner at Plant 2. The samples were dried at 105 °C for three hours before being tested in the wind sieve. The high temperature was chosen to also disinfect the samples. No significant melting of plastic particles was observed at this temperature.

Table 7-2: Details of the fuels tested in the wind sieve.

RDF Sample	Place of Use	LHV	Moisture	Ash
		MJ/kg	wt%	wt%
A	Plant X Calciner	-	-	-
B	Plant 1 Kiln	15.4	21.4	17.6
C	Plant 2 Kiln	31.4	1.5	6.0
D	Plant 2 kiln/calciner	18.7	17.3	12.5
E	Plant 2 calciner	17.8	18.5	13.0
F	Plant 1 Hotdisc	14.6	29.9	19.2

Results of the wind sieve characterization are shown in Figure 7-3. The fuels appear to be divided into three main groups, light fuel (RDF-C), medium fuel (RDF-A, RDF-B, RDF-D), and heavy fuel (RDF-E and RDF-F).

RDF-C and RDF-D were both burned in the kiln at Plant 2 during the industrial flame imaging tests. The upper limitation of firing is around 3 t/h for RDF-C and 2 t/h for RDF-D. Higher degrees of alternative fuels firing tends to result in reducing conditions, which is a sign of the particles not being fully converted in the flame. The wind sieve analysis shows that RDF-C is significantly lighter, and it is thus expected to be converted faster than RDF-D. Thus, higher degree of co-firing can be achieved using RDF-C. RDF-E is also used at Plant 2, but only in the calciner. This fuel is seen to be significantly heavier than the fuels used in the kiln.

RDF-B and RDF-F are both used at Plant 1. RDF-B is used in the main burner in the kiln, while RDF-F is used in the Hotdisc [101]. The Hotdisc is designed to burn large particles that are converted too slowly to be burned in the kiln or calciner. Thus, it is reasonable that RDF-F is heavier than the RDF-B.

RDF-A is used in the calciner of Plant X. The distribution is very similar to that of RDF-B. Thus, it should be possible to use the same fuel in the kiln.

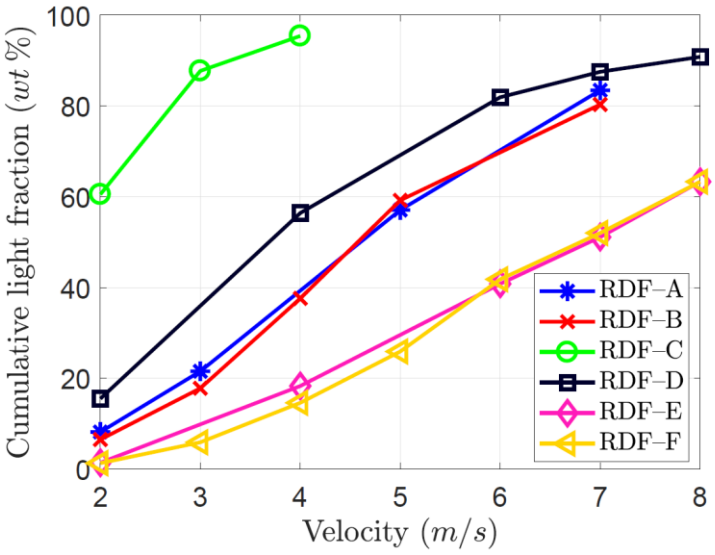

Figure 7-3: Results of wind sieve characterization of various RDFs.

A well-known rule of thumb for the particle size of coal for use in cement kilns, states that the residue at a 90 µm sieve should be maximum half of the volatile content [40]. It would be beneficial if a similar simple rule could be proposed for the use of RDF.

Co-firing of SRF at Plant 1 averages around 70 % of the energy input (see Table 5-3). It is expected that a fuel should behave similarly to RDF-B in the wind sieve, to be suitable for a high degree of co-firing. Therefore, to achieve above 50 % energy substitution in the kiln it is suggested that the fuel should have at least 20, 60, and 80 wt% light fraction tested at 3, 5, and 7 m/s, respectively, similarly to RDF-B.

This is an early suggestion for how the wind sieve analysis can be used to gauge fuel quality for the cement kiln. Further tests are necessary to make more concrete conclusions.

At Plant 2 co-firing only reached 30 % energy using RDF-C and 10 % using RDF-D, even though these fuels are lighter than RDF-B used at Plant 1. Thus, other limitations than the particle size contribute to limiting the use of RDF. The limitation at Plant 2 appears to be a kiln that is more sensitive to reducing conditions than Plant 1.

7.3 Manual Fractionation of SRF

Samples of RDF-A and RDF-B were collected from the wind sieve to make an in-depth analysis of the two samples.

In the wind sieve, samples were fractionated into five groups according to their terminal velocities. Terminal velocity ranges for the groups were <2, 2-3, 3-5, 5-7, and >7 m/s. Each of the five groups were first sieved to remove fines smaller than 2 mm. These particles were too small to reliably determine in which group they belong. The remaining fuel was manually sorted and classified into four groups: plastic, biomass, textiles, and inert. The sorting was based on a visual characterization based on particle texture. Results of the sorting are shown in Figure 7-4.

For both RDF samples the amount of plastics in the light fractions (lower terminal velocity range) is high. In the heavier fractions the plastic is reduced, and the amount of biomass is increased. This is likely because a high amount of the plastic is from packaging foil, which has a high surface to mass ratio, which means that it has low terminal velocity. The biomass particles are mainly thicker paper and cardboard pieces and woodchips, which are heavier than the plastic foils. The amount of inert is also highest in the fraction 5. These are mainly metals and stone, which are quite dense, and thus have a high terminal velocity.

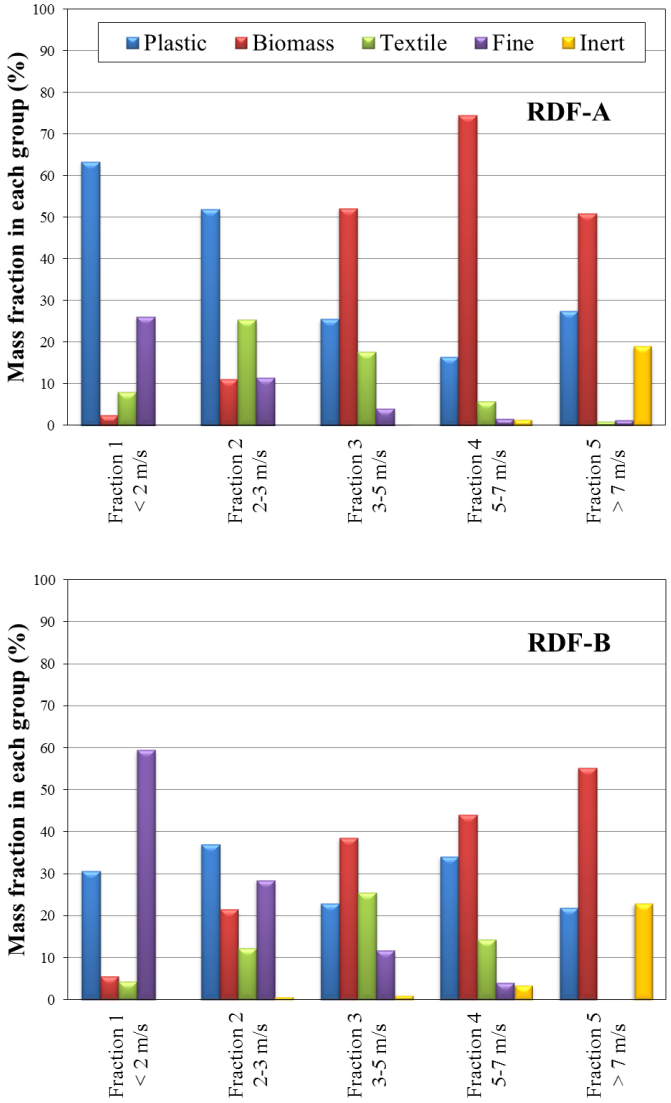

Figure 7-4: Results of manual sorting and classification of RDF-A and RDF-B. Fines are particles under 2 mm as determined by sieving.

The main distinction between the two RDF samples is that RDF-A is richer in plastics in the light factions and the amount of fines is somewhat higher in RDF-B.

7.4 Particle Mass Distribution

The biomass and plastic particles of each fraction (20 samples in total) were reduced to a subset with 50-100 particles by the quartering method [171]. The mass of each particle was measured on a scale. Subsequently, the data were fitted to a Rosin-Rammler distribution [172,173]:

$$Cm_{RR}(m_p) = 100 - \left(100 * exp\left(-\left(\frac{m_p}{m_{RR}}\right)^{n_{RR}}\right)\right) \qquad \text{E 7.1}$$

Cm_{RR} is the cumulative mass, m_p is the particle mass, m_{RR} the characteristic mass (equivalent to the 63rd percentile), and n_{RR} is the spread parameter.

The Rosin-Rammler distribution was initially developed to describe the particle distribution of coal [172], but has also been found to be valid for shredded refuse fuel [174].

The mass distribution of the biomass and plastic fractions of RDF-A and RDF-B are shown in Figure 7-5. The parameters for the fitted Rosin-Rammler distributions are given in Table 7-3.

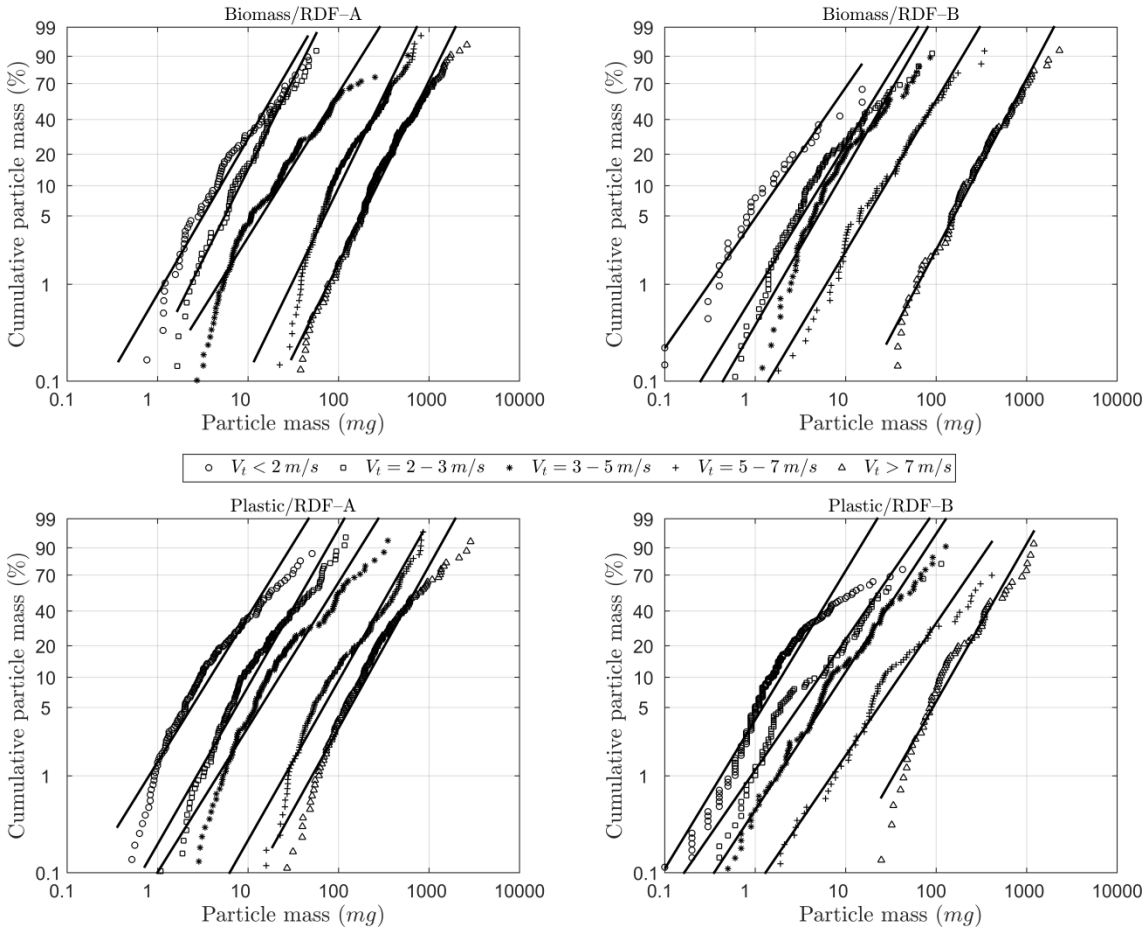

Figure 7-5: Mass distribution fitted to Rosin-Rammler distribution of the plastic and biomass fractions of RDF-A and RDF-B.

It is observed from the data that the particle mass increases with the terminal velocity. The parameter m_{RR} (63rd percentile) increases through the groups with higher terminal velocity. The spread parameter n_{RR} also appears to increase slightly with the terminal velocity, but this trend is less clear and noisier. Furthermore, it is observed that sample A is generally slightly heavier than sample B, for both the

plastic and biomass fractions. This may be explained by RDF-A having a slightly lower particle sphericity, i.e. it is flatter, as discussed in the following chapter.

Table 7-3: Parameters for the Rosin-Rammler distribution of RDF-A and RDF-B samples.

	Biomass RDF-A		Biomass RDF-B		Plastic RDF-A		Plastic RDF-B	
Velocity Range (m/s)	m_{RR} (mg)	n_{RR}	m_{RR} (mg)	n_{RR}	m_{RR} (mg)	n_{RR}	m_{RR} (mg)	n_{RR}
<2	20.2	1.61	9.3	1.35	16.9	1.51	8.3	1.54
2-3	27.1	1.87	23.1	1.52	45.4	1.63	27.1	1.35
3-5	102.4	1.50	31.3	1.62	99.3	1.50	44.2	1.43
5-7	330.5	1.92	114.3	1.57	410.7	1.65	201.9	1.37
>7	874.9	1.89	844.1	1.77	785.8	1.68	565.8	1.63

7.5 Particle Shape Determination by Imaging

The shape of particles also have a significant effect on their combustion time [86,175]. The larger the surface area of a particle, the faster heat and oxygen can be transferred to the particle. In addition, the shape of particles also influence their flow and terminal velocity [162].

A camera setup was developed to take pictures of single particles of SRF, to describe their size and shape. The camera setup is shown in Figure 7-6. It consists of a back lit platform where particles are placed on. Images are taken by two cameras placed above and in front of the particle.

Figure 7-6: Camera setup with two cameras to determine particle size and shape.

The particle mass was determined by weighing the particles as explained in chapter 7.4. Based on the particle mass, the particle volume, V_p, is calculated assuming a density of 650 kg/m^3 [176] for biomass and 950 kg/m^3 [177] for plastics. Assuming that the particles are cuboids, the thickness of the particle can be determined by:

$$t_p = V_p / A_p \qquad \text{E 7.2}$$

The particle projected area, A_p, is derived from the top image taken in the camera setup. With the volume and surface area, the particle sphericity can be calculated:

$$\varphi_p = \frac{\pi \left(\frac{6V_p}{\pi}\right)^{2/3}}{2A_p + 4t_p A_p^{1/2}} \qquad \text{E 7.3}$$

The sphericity of the biomass and plastic samples of RDF-A and RDF-B are shown in Figure 7-7, and the mass- weighted average values are presented in Table 7-4. It is observed that the sphericity of the plastic particles is generally slightly lower than for the biomass particles. The sphericity generally increases with the terminal velocity, i.e. the particles are flatter and more sheet like at low terminal velocity. In each group there is a slight trend that increasing mass results in a lower sphericity. This is most visible for the fraction 5-7 m/s. This is reasonable as a heavy and a light particle can have the same terminal velocity, if the heavy particle has a larger projected area, i.e. it is flatter and has lower sphericity. RDF-A has a slightly lower sphericity than RDF-B. This is also consistent with a slightly higher mass for RDF-A in each of the terminal velocity ranges.

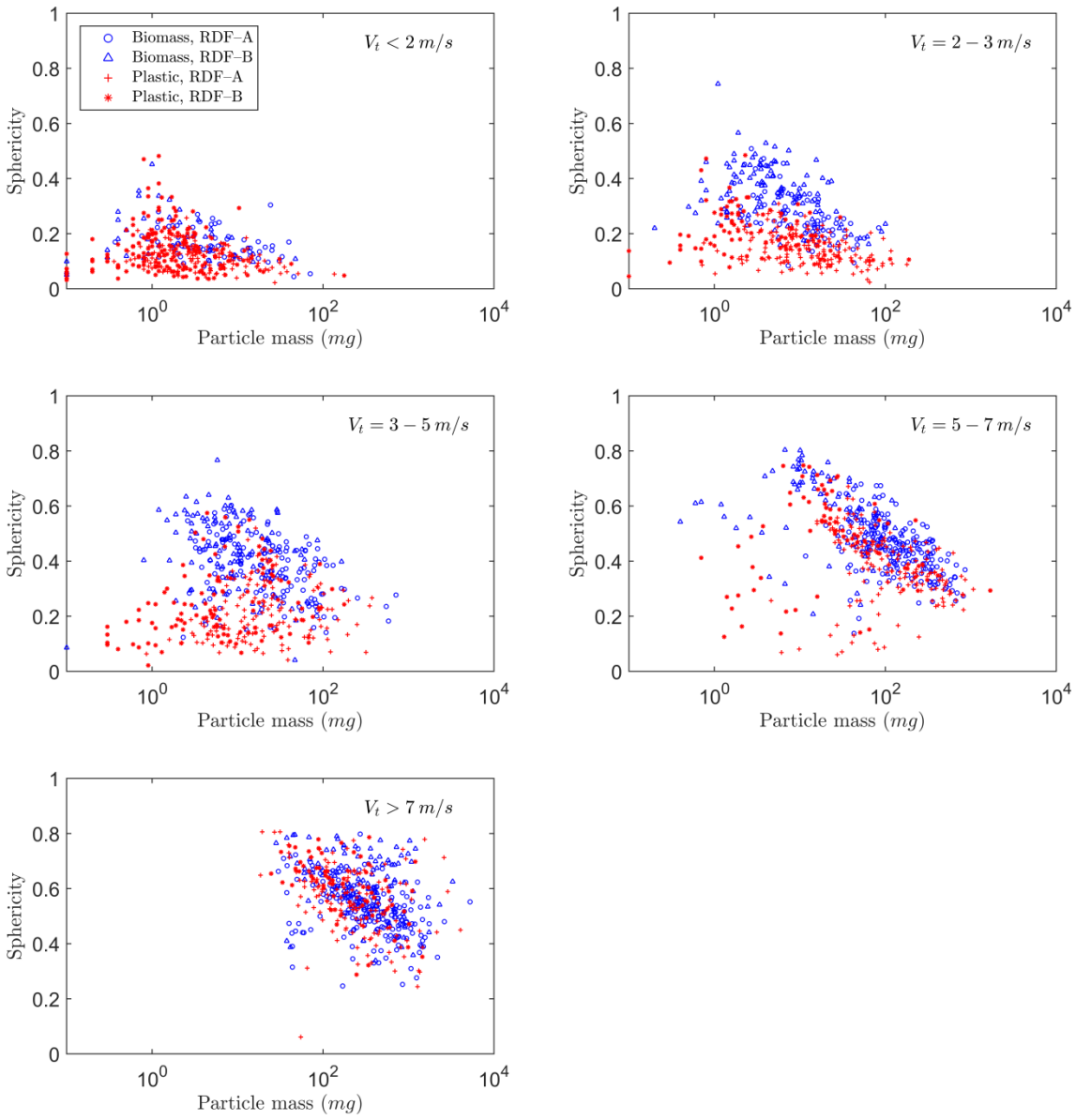

Figure 7-7: Sphericity of biomass and plastic of RDF-A and RDF-B in relation to the particle mass.

Table 7-4: Mass weighted average sphericity for biomass and plastics fractions of RDF-A and RDF-B.

Velocity Range (m/s)	Biomass RDF-A	Biomass RDF-B	Plastic RDF-A	Plastic RDF-B
<2	0.14	0.15	0.09	0.10
2-3	0.23	0.28	0.12	0.15
3-5	0.31	0.39	0.21	0.26
5-7	0.41	0.49	0.33	0.39
>7	0.50	0.60	0.52	0.55

7.6 Conclusions

A wind sieve setup was used to characterize the size of different refuse derived fuels from three different cement plants. A clear distinction can be made between fine, medium, and coarse fuels. Fuels used in the kiln are lighter than fuels used in the calciner. The current data is limited, but it is suggested that SRF for use in a cement kiln should have at least 20, 60, and 80 wt% light fraction tested at 3, 5 m/s, and 7 m/s, respectively.

Two samples were selected from the wind sieve and a more in-depth analysis was made. Plastics and biomass in SRF behave very differently during combustion. Thus, the plastic and biomass content of the SRF was determined. Plastic particles tend to accumulate in the low terminal velocity ranges, while biomass is more prevalent in the high terminal velocity ranges. This indicates that plastic particles are flatter, which is also reflected in the determination of the particle sphericity.

The mass of individual particles of biomass and plastic was determined, and the mass distribution was fitted to a Rosin-Rammler distribution. The average particle mass increased with the wind sieve terminal velocity range. It was also found that particle sphericity increased with the terminal velocity. Furthermore, heavy particles in the same wind sieve fraction tended to have a lower sphericity. This confirms that the wind sieve separation accounts for both particle mass and shape. Both factors are important for the particle combustion. The combustion time will generally be shorter for low mass particles with a low sphericity, which can be found in the low terminal velocity ranges of the wind sieve.

The knowledge of SRF composition, particle size distribution, and shape factors can be used as input to detailed models for the combustion in the kiln, such as CFD simulations. The data derived in this chapter will be used as input for modeling the combustion of SRF described in chapter 9.

8 Cement Kiln Model Development

The purpose of this chapter is to present a simplified model for the cement kiln. The model will be used to calculate temperature profiles in the gas phase and clinker bed. This is coupled to a simplified model of the formation of clinker minerals, to determine free lime or alite content in the clinker. The model takes into consideration fuel properties, burner settings, and other process parameters and can thus be used to estimate how these factors influence kiln temperature and clinker composition. Consequently, it can also be used to propose changes that compensates for the negative effects of alternative fuels co-firing.

It is a 1-D model to describe changes in the axial direction of the kiln. This approach has been chosen over Computational Fluid Dynamics (CFD) simulations. It is believed that a 1-D model will be adequate to capture the main differences in temperature caused by variations in fuel quality. In addition, this model is faster to converge, less complex, and easier to use.

The first part of this chapter provides an overview of the various models found in the literature, as well as the major findings and conclusions of these studies. In later parts of this chapter the main processes in the cement kiln will be described, and simplified models are presented. These sub-models, for e.g. clinker flow, heat transfer, and reactions, are combined in the final kiln model. The kiln model is

validated using literature results and used to investigate the impacts of SRF co-firing in chapter 9.

8.1 Cement Kiln Modeling in Literature

The literature is quite rich in models attempting to describe the various processes taking place in the cement kiln. Several models have been developed since the 1970's based on engineering principles to understand and optimize the cement kiln. Within the last 10-20 years advanced models aided by Computational Fluid Dynamics (CFD) have also appeared. However, only a few recent studies have dealt with alternative fuels firing in the cement kiln.

8.1.1 Engineering Models

Some of the first attempts to model the heat transfer in rotary kilns were made by Imber and Paschkis in the early 60's [178]. In their work two extreme cases were considered for the kiln charge temperature, a well-mixed and non-mixed case. In the well mixed case the bed was assumed to have a uniform temperature in the radial direction and in the non-mixed case a non-uniform temperature was assumed. A number of simplifying assumptions were made in their analysis, and a lack of correlations for the heat transfer coefficient made the model of limited use.

A group of researchers from the University of British Columbia made a detailed study of the heat transfer in the cement kilns publishing a number of articles in this area, first by Brimacombe and Watkinson [179,180], Gorog et al. [181–183], and later by Barr et al. [184,185].

They used a gas fired pilot scale rotary kiln of 0.406 m diameter and 5.5 m length to experimentally study the heat transfer mechanics and later compare with modeling results. The kiln was equipped with numerous thermocouples to measure temperatures in the bed, gas, and wall, which allowed determination of the various heat transfer mechanics in the rotary kiln. Using the kiln, it was possible to study the effect on heat transfer of a long range of operating parameters such as rotation speed, degree of fill, and firing rate [179].

Watkinson and Brimacombe [180] used the pilot rotary kiln to study the heat transfer from the gas phase to kiln wall and bed. They determined that motion of the bed has a great influence on the heat transfer. At high bed feed rates and rotation,

the bed motion changed from slumping to rolling, which increased the heat transfer rate. This could result in the gas to bed heat flux being up to ten times higher than the gas to wall heat flux. It was found that radiation only contributed some 30 percent of the heat flow. The temperature in the pilot experiments was around 1000 K. In a real cement kiln, gas temperatures are much higher, and radiation becomes more important. It must be expected that radiation in an industrial kiln contributes more than the 30 percent found in the pilot kiln.

Gorog et al. made a thorough contribution to model the different mechanisms of heat transfer in the rotary kiln. The work describes radiation [181] and regenerative heat transfer (heat transfer between covered wall and bed) [182]. In later work [183] the radiative heat transfer from a flame was modeled to calculate an axial temperature profile of the flame and wall. It was assumed that the flame was cylindrical in shape and moved in plug flow through the kiln. The length of the flame and the entrainment of secondary air were calculated by empirical relations from Beér and Chigier [186] and Ricou and Spalding [187]. The temperature profile was calculated for fuel oil, natural gas, and producer gas for different levels of firing rate, secondary air temperature, primary air fraction, and oxygen enrichment. Gorog and Adams used the developed model as a basis to optimize the design and performance of a rotary lime kiln in a number of papers [188–192].

Barr et al. [184,185] refurbished the pilot kiln used by Watkinson and Brimacombe, which was described above. This allowed for additional measurements and accuracy of the heat transfer modes. In addition, heat transfer to limestone, a reactive bed, was studied. The heat transfer models from the previous work of Gorog et al. were combined to yield a detailed model of the cross-sectional heat flow, which covered all the modes of heat transfer in the kiln.

Spang [193] developed a dynamic model for the axial temperature profile of the cement kiln based on heat and mass balances. The study included a simplified approach to model the kiln reactions by Arrhenius type expressions. The fuel combustion was implemented by assuming an exothermic reaction that releases the energy directly to the gas phase. The reaction rate was controlled by diffusion of oxygen from the gas to the particle surface, which was assumed adequate for coal and oil flames. The model was used to investigate the response to changes in e.g. gas and solids flow.

Locher proposed models for the entire pyro-processing line of a cement plant including the preheater, calciner, bypass, rotary kiln, and grate cooler in a series of publications [194–196]. The kiln is modeled by dividing it into 20-50 sections in the axial direction. In each section the mass and energy exchange are calculated. Heat transfer accounts for gas-wall, gas-bed, and wall-bed interactions through radiation, convection, and conduction. Compared to the other models described in this chapter, Locher's model also considers entrainment of dust, although the complete details of the calculation method are not stated. Chemical reactions of the clinker are also considered.

A rather recent model has been developed by Mujamdar and Ranade [197]. The model accounts for the solids flow with a non-uniform bed height and the chemical reactions in the bed. The gas temperature was assumed to follow a fixed profile, which was derived from CFD-calculations, previously performed by the authors. In later work [198], coal combustion was added to the model. The conversion of coal was assumed to follow three steps: heating, devolatilization, and char combustion.

The investigation of alternative fuels combustion on the cement kiln is relatively limited for 1-dimensional models, but was attempted by Haas and Weber [199]. Initially they assumed a simplified ideal kiln consisting of a well stirred reactor and showed that co-firing of RDF would lower the adiabatic flame temperature, due to the lower calorific value of the RDF compared to coal. To maintain the same heat transfer to the bed when the adiabatic flame temperature drops, it is necessary to increase the energy input to the kiln. The authors went on to model the kiln as a series of well stirred reactors. The combustion of RDF was modeled considering only the solid conversion controlled by oxygen diffusion and surface reaction. This is a serious simplification, due to the high volatile content of the RDF. The RDF reaction kinetics were assumed similar to that of coal. Thus, the differences in the reaction rates are related to the large size difference between coal and RDF particles, which was characterized by a specific surface area. The effect of different co-firing rates of RDF were then studied, assuming that the total heat transfer to the clinker should be constant. The effect of increased RDF was a lower peak gas temperature and a longer flame zone. If the RDF particle size is assumed similar to that of coal, the flame becomes shorter and the peak temperature is boosted, although the coal will still burn at higher peak temperature.

The effects of alternative fuels on kiln temperatures (with no clinker bed) have been investigated by Nørskov [31]. In this work it was also attempted to account for the influence of burner settings by describing the entrainment of secondary air into the primary air and fuel jet. It was concluded that co-firing with sewage sludge or RDF would shift the peak flame temperatures further away from the burner due to the larger particle size and slower combustion. Flame temperatures would also be reduced.

8.1.2 Computational Fluid Dynamic Models

During the last 10-15 years, the use of computational fluid dynamics (CFD) for numerical models of the cement kiln has increased significantly. The increasing computing power makes it possible to solve detailed three-dimensional models of flow, temperature, and combustion.

Some of the first work using computer aided numerical models for cement kilns was done by Lockwood [200] in the 1990's. In this work, they compared predictions of the k-ε and Reynolds stress model for turbulence for a coal fired flame. The modeling results were also compared with experimental results obtained at the pilot scale burner of the International Flame Research Foundation. Since then, numerous studies have been made where CFD is used to model coal fired flames, such as [201–203].

The amount of literature dealing with the combustion of alternative fuels in the cement kiln is limited. However, the CFD modeling attempts emphasize some of the challenges outlined in chapter 3.5.

Ariyaratne et al. [83] used CFD to compare the combustion of coal and meat and bone meal (MBM). The main finding was that MBM burns at 300 K lower temperatures than coal due to a higher air demand, higher ash and moisture content, and poor char burnout.

Liedmann et al. [163] simulated the co-firing of lignite and RDF in a cement kiln. An example of their results is shown in Figure 8-1. Introducing RDF (Figure 8-1b) results in a shorter and colder flame, caused by the increased conversion time of the larger particles. Some of the RDF lands unconverted in the bed around 20 meters from the burner, which creates a high temperature zone. The unburnt particles are primarily textiles, paper and cardboard, and 3D plastics owing to their large size.

Thus, an optimized RDF where textiles were removed, and the size was reduced, was also modeled (in Figure 8-1c). This resulted in a higher temperature flame and less material burning in the bed.

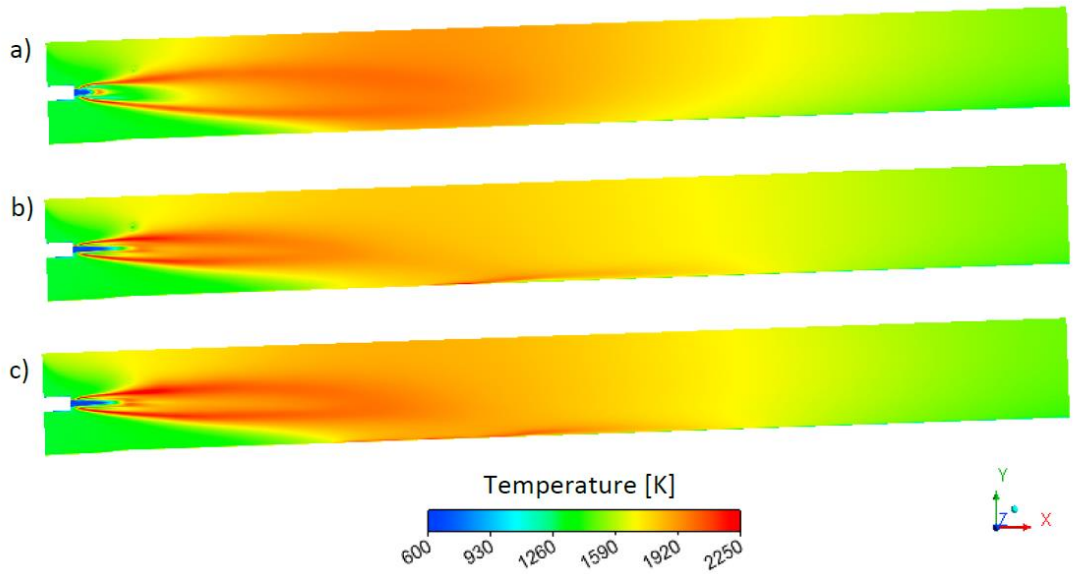

Figure 8-1: CFD simulations showing temperature profiles in the cement kiln for different co-firing scenarios of a) lignite, b) 50 % SRF, and c) 50 % optimized SRF [163]. Notice the high temperatures at the lower kiln wall halfway through the kiln for case b and c.

Another paper by Liedmann et al. [143] studied the effect of different operating conditions on a co-fired kiln flame. It was found that an increased axial momentum would increase peak temperatures near the burner, but slightly reduce SRF burnout due to a lowered residence time. An increased swirl resulted in a wider flame with lower peak temperatures. Light SRF particles were also whirled out of the flame, causing more material to burn on the walls and in the clinker. An increased secondary air temperature caused increased flame temperatures, which resulted in faster ignition and higher burnout of SRF.

Isaac et al. [204] investigated the effect of the moisture content of SRF particles on a co-fired cement kiln flame. A higher moisture content caused delays in flame ignition, lower flame temperatures, and decreased burnout of the fuel.

Examples of alternative fuels combustion CFD modeling in the calciner can also be found [205,206].

8.1.3 Conclusions and Next Steps

The literature survey has revealed different approaches to model the combustion in cement kilns. The CFD models yield detailed information of the gas flow coupled with the combustion reactions. However, their downside is typical significant computational requirements and software that requires considerable experience. It is believed that a 1-D model will be adequate to describe the main differences between fuel types. relating to conversion time and combustion temperatures. Thus a 1-D model will be developed here.

The models present in the literature form a good foundation for understanding the key processes in the cement kiln e.g. combustion, heat transfer and clinker reactions. Most 1-D models in the literature only deal with fossil fuels combustion. Thus, a further development of these models to investigate the effects of alternative fuels co-firing is performed in this thesis. The model will couple the gas phase temperature to the bed temperature to determine the clinker phase composition. This has been done before, but it has not been coupled with models for alternative fuel combustion. The effect of burner settings has only been investigated in one CFD study and the study by Nørskov [31]. It is deemed relevant to incorporate a model for the mixing of secondary and primary air, to also investigate the effect of burner settings on the kiln temperature.

8.2 Modeling of Processes in the Cement Rotary Kiln

Although the cement rotary kiln in itself is fairly simple, it is essentially a giant rotating cylinder, many complex phenomena occur inside the kiln at the same time. Hot calcined meal enters at one end and undergoes several different reactions to form the cement clinker. In addition to the 4 main oxides, (CaO, SiO_2, Fe_2O_3, Al_2O_3) other components are also present in the kiln, e.g. MgO, SO_3, K_2O, Na_2O, Cl (using oxide notation). These combine in different ways forming numerous different mineral phases. The counterflowing gas has a complex flow pattern with complicated combustion reactions taking place. In addition, there is heat and mass transfer between the different phases. It is possible to write an entire PhD thesis on any of these subjects, such as clinker phase chemistry and kinetics [207], recirculation of volatiles in the kiln [112], or heat transfer in the kiln [208].

Consequently, it will be necessary to make several simplifying assumptions in a model that encompasses several different mechanisms.

A brief introduction to the clinker reactions and the kiln was given in chapter 2.3 and 2.6. The purpose of the following subchapters is to present a more detailed description of the processes occurring in the kiln. A focus point is the mathematical equations that describe these processes, and to propose simplified models for each of these sub-processes. The different models are then combined into a global model for the cement kiln.

8.3 Model Overview

A sketch of the proposed 1-D kiln model is shown in Figure 8-2, which illustrates the major mechanisms in the cement kiln, which are accounted for by the model.

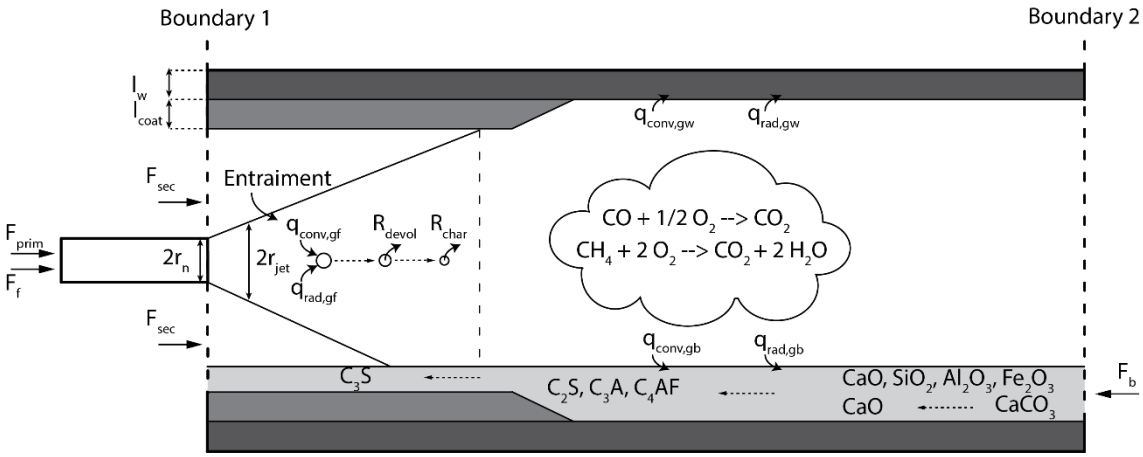

Figure 8-2: Sketch of the kiln model showing the main processes accounted for in the model.

At one end, Boundary 1, of the kiln primary air and fuel is admitted through the kiln burner with secondary air admitted around the burner. The secondary air will be entrained into the primary air jet, which causes it to expand, until it fills the entire kiln cross section. Meanwhile the fuel is heated and will undergo drying, devolatilization and char combustion. The released gasses, assumed to be CO and CH_4, will then combust in the gas phase.

From the opposite end of the kiln, Boundary 2, the preheated and calcined meal is admitted, which will flow through the kiln counter current to the gas. The kiln charge (bed) is heated by the hot gasses, which will initiate and accelerate the clinker reactions.

It is assumed that fossil fuels will follow the gas flow and stay in suspension in the kiln, as indicated in the sketch. Larger alternative fuels can drop out of the flame and burn in the bed. This is not indicated in the sketch.

8.4 Solids Movement in Kiln

The movement of the solids in the rotary kiln can be divided into an axial direction, which determines the residence time, and a transverse motion, which primarily governs mixing and heat transfer of the bed.

The transverse motion in a cylinder depends largely on the rotational speed. At low speeds the motion is characterized as slipping, where the bed slips along the wall. At very high rotational speeds the material may be centrifuged towards the wall. In a cement kiln the flow is normally characterized as rolling motion, where there is a steady discharge from the top of the bed to the lower parts of the kiln [27]. This forms an active surface layer, where renewal continually occurs, and a passive layer below the surface. In the passive layer the material is closely packed and rotates with the kiln. Most of the mixing occurs in the active layer, and mixing is thus increased by a larger active layer, which can be promoted by e.g. an increased kiln speed [209].

The regime of bed motion can be estimated based on the rotational Froude number [27]:

$$Fr = \frac{\omega^2 r_k}{g} \qquad \text{E 8.1}$$

Here ω is the rotational speed [rad/s], r_k the kiln diameter, and g the acceleration due to gravity. Rolling motion has a rotational Froude number between $0.5*10^{-3}$ and $0.2*10^{-1}$.

The typical geometry of the bed is sketched in Figure 8-3. Normally the angle of repose, ξ, is between 30-50°, but it increases with rotational speed and is lowered with increased particle size [14].

The axial motion of material in the kiln is dependent on the slope of the kiln, typically 1-3° [2], and the forward angle caused by the transverse flow, which is induced by the rotation of the kiln. By assuming a uniform bed height across the kiln the average residence time can be calculated by [210]:

$$t_{res} = \frac{L_K \sin \xi}{2\pi r_k n \psi} \qquad \text{E 8.2}$$

In the equation, L_K is the kiln length, n is the rotational speed [rot/s], ξ the bed angle of repose [rad], ψ the kiln slope [rad], θ is the angle between the bed and cylinder center [rad], and r_k is the kiln radius.

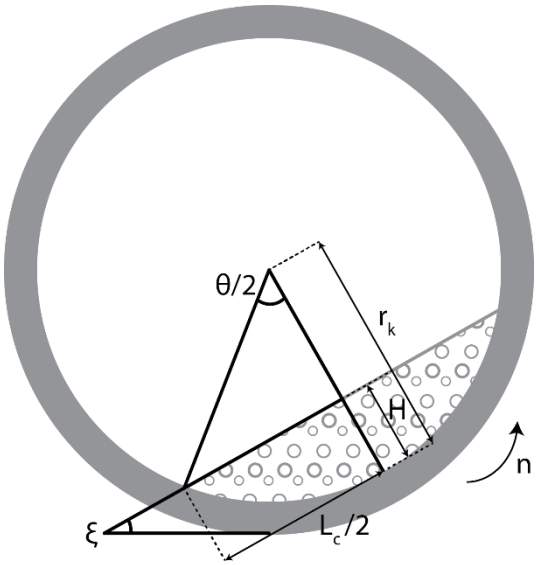

Figure 8-3: Geometry of a rolling bed indicating the applied nomenclature.

8.5 Clinker Reactions

The study of the chemical kinetics of the cement clinker reactions is a complex task due to the many species and various reaction pathways in the cement kiln [4]. It will only be attempted to describe the 5 main reactions, as also described in chapter 2.3. The equations to describe the extent of clinker reactions will be reviewed in chapter 8.5.1. A simplified approach used in kiln model will be presented in chapter 8.5.2. The approach for determining appropriate kinetics is presented in chapter 8.5.3.

8.5.1 Equations for the Extent of Clinker Reactions

The decomposition reaction of $CaCO_3$ mainly takes place in the calciner, but the residual $CaCO_3$ normally constitutes 5-8 % [18]. The remaining decomposition will occur in the cement kiln. The rate of $CaCO_3$ decomposition is dependent on several factors, amongst others it is highly dependent on both the temperature and the partial pressure of CO_2 [4].

The decomposition of $CaCO_3$ can, according to Imlach [211], best be described by a contracting geometry equation, valid for reaction control in cylinders [212]:

$$\mathbf{1 - (1 - X)^{\frac{1}{2}} = \frac{k}{r_p} t} \qquad \textbf{E 8.3}$$

Here X is the fraction of the limestone decomposed at time t, k is the rate constant given by an Arrhenius expression, and r_p is the particle radius.

The solid-state reactions in the cement rotary kiln are primarily governed by diffusion. The reaction occurs at the interphase between the crystals, where e.g. CaO diffuses into SiO_2. The rate of formation decreases as the thickness of the product layer increases [212]. The diffusion reaction can be described by the Jander equation [212,213]:

$$\mathbf{\left(1 - (1 - X)^{\frac{1}{3}}\right)^2 = \frac{k}{r_p^2} t} \qquad \textbf{E 8.4}$$

The equation performs rather well for the initial and intermediate stages of the decomposition, but fails to accurately describe the later stages, due to the formation of reaction product around the unreacted core, which inhibits further reaction [4,212]. The equation by Ginstling and Brounshtein may describe the latter stages better than the Jander equation [212,214]:

$$\mathbf{\left(1 - \frac{2}{3} X\right) - (1 - X)^{\frac{2}{3}} = \frac{k}{r_p^2} t} \qquad \textbf{E 8.5}$$

According to the notation used by Levenspiel [215] this is equivalent to the spherical shrinking core model for an ash diffusion controlled reaction.

Imlach [211] presents some numbers for activation energy that can be used to calculate the rate constants of the above equations. Telschow [207] used the Jander equation to calculate the extent of alite formation and compared model results with experiments performed in a lab-scale rotary kiln. The deviation to experimental results was on average around 5 %, but at low heating rates the model overestimates the alite formation. Chromy [216] has presented kinetic results for the formation of alite and belite based on isothermal experiments.

8.5.2 Simplified Equations of Clinker Reactions

A somewhat simpler approach to the modeling of clinker reactions will be used here. The approach was used by Mastorakos et al. [201] who suggested to model limestone decomposition as well as the four clinker reactions given in Table 8-1. The kinetics of the four clinker reactions were estimated by trial and error, until the computational model results matched the composition at the kiln exit. Mujumdar et al. [197,198] also used these kinetics and showed that the results compared well to clinker compositional data from industrial kilns.

Table 8-1: Reactions and kinetics for the model by Mastorakos et al. [201].

	Reaction	A	Unit of A	Ea (kJ/mol)
1	$CaCO_3 \rightarrow CaO + CO_2$	10^8	$\frac{1}{s}$	176
2	$CaO + 2SiO_2 \rightarrow C_2S$	10^7	$\frac{m^3}{kg * s}$	240
3	$CaO + C_2S \rightarrow C_3S$	10^9	$\frac{m^3}{kg * s}$	420
4	$3CaO + Al_2O_3 \rightarrow C_3A$	10^8	$\frac{m^3}{kg * s}$	310
5	$3CaO + Al_2O_3 + Fe_2O_3 \rightarrow C_4AF$	10^8	$\frac{m^6}{kg^2 * s}$	330

The kinetics of reaction are given by a pseudo-liquid rate. Instead of considering the diffusion limitations as discussed in chapter 8.5.1, the reactions rates will be assumed to depend on the concentration of each clinker mineral or phase.

$$\boldsymbol{R_1 = k_1 * Y_{CaCO3} * \rho_b} \quad \text{E 8.6}$$

$$\boldsymbol{R_2 = k_2 * Y_{CaO} * Y_{SiO2} * \rho_b^2} \quad \text{E 8.7}$$

$$\boldsymbol{R_3 = k_3 * Y_{CaO} * Y_{C2S} * \rho_b^2} \quad \text{E 8.8}$$

$$\boldsymbol{R_4 = k_4 * Y_{CaO} * Y_{Al2O3} * \rho_b^2} \quad \text{E 8.9}$$

$$\boldsymbol{R_5 = k_5 * Y_{CaO} * Y_{Al2O3} * Y_{Fe2O3} * \rho_b^3} \quad \text{E 8.10}$$

In the equations R is the reaction rate [kg/m^3 s], k is the rate constant, which is determined by a standard Arrhenius expression, Y is the mass fraction of the phase, and ρ_b is the bulk bed density.

8.5.3 Kinetics of Clinker Reactions

The kinetics proposed by Mastorakos [201] that are presented in Table 8-1 are used as the basis for the reaction kinetics. However, some modifications are made to better fit the modeling used here.

The kinetics are adjusted so that the limestone calcination (Reaction 1) mainly occurs at around 850-900 °C. The kinetics for the formation of belite, aluminate and ferrite (Reactions 2, 4, and 5) are adjusted so the reactions mainly take place in the temperature interval 900-1200 °C.

The formation of alite is the most important to adequately model, since alite is the main phase of interest in the cement clinker. The kinetics are adjusted based on experimental measurements performed in the laboratory. Two sets of kinetics are found for the reaction, one relatively fast set that mimics an easy to burn clinker, and a slower set, which mimics a hard to burn clinker. The details of the derivations can be found in Appendix B. The final kinetics that are used in the kiln model are given in Table 8-2.

Table 8-2: Preexponential factors and activation energies to determine rate constants for the clinker reactions.

	k_1	k_2	$k_{3,1}$ **easy burnability**	$k_{3,1}$ **hard burnability**	$k_{3,2}$	k_4	k_5
A	10^5	10^5	$3.32*10^8$	$1.1*10^8$	$2.86*10^{57}$	10^7	10^7
Unit of A	$\frac{1}{s}$	$\frac{m^3}{kg*s}$	$\frac{m^3}{kg*s}$	$\frac{m^3}{kg*s}$	$\frac{m^3}{kg*s}$	$\frac{m^3}{kg*s}$	$\frac{m^6}{kg^2*s}$
Ea (kJ/mol)	175	260	440	440	187	310	330

In the kiln, alite formation starts to occur as a melt phase is formed above 1200 °C. In order to limit the reaction of alite formation, so that it mainly occurs above 1200 °C, an effective rate constant is used for reaction 3 as shown in E 8.11. The values to determine $k_{3,2}$ are selected to be highly dependent on temperature. This gives the result that it will severely hinder reactions below 1200 °C, but have negligible effect when the temperature is above 1200 °C.

$$k_{3,eff} = \left(\frac{1}{k_{3,1}} + \frac{1}{k_{3,2}} \right)^{-1} \qquad \text{E 8.11}$$

It should be mentioned that there are some implications with this simplified approach that should be considered when analyzing the results.

Due to the way the mathematical model is formulated it is possible for the clinker to react fully, i.e. obtaining a free lime content of zero. This will not be possible in an industrial kiln, where the presence of large particles of silica and lime will impose diffusion limitations to the extent of reaction [25].

In the clinker model, only the main oxides and clinker phases are considered. Minor components such as MgO, Na_2O, and K_2O are assumed to be inerts, which do not affect the clinker composition. The model will thus predict the Bogue composition [24] at full conversion, which does not necessarily represent the clinker composition from industrial kilns.

The kinetics of the alite reactions are derived from laboratory experiments where model clinker is burned at up to 1500 °C for 30 minutes. In an industrial kiln the residence time at such high temperatures will be much shorter. However, it is possible to obtain a similar free lime content as in the laboratory. The slower rate of reaction in the laboratory compared to an industrial kiln is mainly caused by a higher porosity in the laboratory clinker [207], and a significant mixing effect in the industrial kiln.

8.5.4 Enthalpy of Clinker Reactions and Melting

The energy consumed and released as the clinker is formed can have a significant impact on the heat balance in the cement kiln. Most notably the calcination reaction is very endothermic, while the formation of alite is exothermic. In addition, the melting of clinker also requires energy. The enthalpies employed in the model are given in Table 8-3.

Furthermore, evaporation of volatile species such as SO_2 and KCl from the clinker also requires energy, but these effects are not included in the model.

Table 8-3: Enthalpy of the clinker reactions and the melting of clinker [217].

	Reaction	ΔH	Unit of ΔH
1	$CaCO_3 \rightarrow CaO + CO_2$	1780	$\frac{\text{kJ}}{kg\ CaCO_3}$
2	$CaO + 2SiO_2 \rightarrow C_2S$	-732	$\frac{\text{kJ}}{kg\ C_2S}$
3	$CaO + C_2S \rightarrow C_3S$	59	$\frac{\text{kJ}}{kg\ C_3S}$
4	$3CaO + Al_2O_3 \rightarrow C_3A$	-33.5	$\frac{\text{kJ}}{kg\ C_3A}$
5	$3CaO + Al_2O_3 + Fe_2O_3 \rightarrow C_4AF$	-33.8	$\frac{\text{kJ}}{kg\ C_4AF}$
	Clinker Melting	600	$\frac{\text{kJ}}{kg\ clinker}$

8.6 Burner Air Flow

As discussed in chapter 2.8 and 2.9, the distribution of axial air and swirl air is one of the main ways to control the flame in the cement kiln. One of the main design parameters of the cement kiln burner is the burner momentum, *I*, calculated as the mass flow of primary air multiplied by the axial velocity. The momentum is often normalized, *I'*, by the thermal power, P_{burner}, of the burner and reported in units of [N/MW].

$$\boldsymbol{I' = \frac{I}{P_{burner}} = \frac{u_{prim} * \dot{m}_{prim}}{P_{burner}}} \qquad \textbf{E 8.12}$$

The burner primary air is what controls the flame shape and intensity. The primary air creates a high velocity in front of the burner, which together with the recirculation zones, define the mixing rate with secondary air. The faster the secondary air is entrained into the fuel stream, the faster the fuel will heat up and ignite. For conventional fossil fuels, it is normally the mixing rate of oxygen that is the limiting factor for combustion, rather than chemical kinetics [136]. Therefore, a more intense mixing of oxygen creates a more efficient combustion process. In this chapter the theory of the mixing process will be described in further detail.

8.6.1 Jet Expansion

When a fluid is injected from a nozzle into a larger body filled with a fluid, either stagnant or co-flowing, the jet mixes with the surrounding fluid, creating turbulence, while the jet grows outwards. Figure 8-4 shows the principle of the mixing in co-flow through different regions. Close to the nozzle, in the flow development region (region 1), the turbulence will grow towards the central axis and a wedge is formed where the velocity is undiminished at the jet injection velocity. This wedge is called the potential core. The flow enters the fully developed region (region 2) when the turbulence has fully penetrated to the central axis and the core disappears. In the fully developed flow region, the axial velocity obtains a profile as indicated in Figure 8-4, with the highest velocity u_m along the center and the co-flowing velocity close to the walls. By the end of region 2, the secondary flow is completely entrained into the primary jet flow. Under certain conditions a recirculating zone may form in region 3. In region 4 the flow is fully developed pipe flow [218].

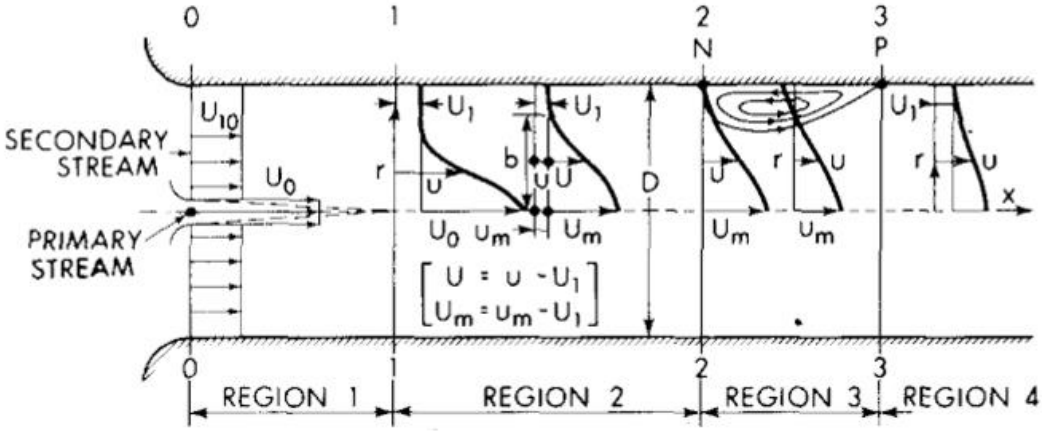

Figure 8-4: Sketch of the development of a turbulent jet in a pipe through different regions [218]. Region 1: The flow development region, Region 2: Fully developed region, Region 3: Possible formation of recirculation zones. Region 4: Fully developed pipe flow. In this figure only, U_1 denotes co-flow velocity, U velocity difference ($u-U_1$), D diameter, b the jet radius. Subscripts 1 denote co-flowing stream, and m the center value. r, x, and u denote radius, axial distance, and axial velocity (as used in the remainder of the thesis).

Ricou and Spalding [187] investigated the entrainment into free-flowing jets. They injected air into a chamber with stagnant air and found that the entrainment could be described by the equation:

$$\frac{\dot{m}}{\dot{m}_1} = K_{ent}\frac{x}{d_n}\left(\frac{\rho_{sec}}{\rho_{prim}}\right)^{\frac{1}{2}} \qquad \text{E 8.13}$$

They suggested a value of 0.32 for the entrainment constant, K_{ent}, for air mixing with air. The equation should hold for free jets up to values of 400 for x/d_n.

Under combustion conditions the entrainment will be influenced by the change in temperature and density. It has been suggested to take this into account by adjusting by the flame density:

$$\frac{\dot{m}}{\dot{m}_1} = K_{ent}\frac{x}{d_n}\left(\frac{\rho_{sec}}{\rho_{prim}}\right)^{\frac{1}{2}}\left(\frac{\rho_{fl}}{\rho_{prim}}\right)^{\frac{1}{2}} \qquad \text{E 8.14}$$

Here, $\dot{m}$ denotes the mass flow of the jet. K_{ent} is the entrainment constant, x the distance from the burner, d_n the burner nozzle diameter, and ρ the density. The subscripts *prim*, *sec*, and *fl* denotes primary flow, secondary flow, and flame, respectively.

Other effects in combustion may also influence the entrainment, e.g. buoyancy [187].

8.6.2 External Recirculation and the Craya-Curtet Parameter

In a cement kiln the jet is confined by the kiln walls. This may influence mixing by setting up an external recirculation zone, as sketched in Figure 8-4. A confined jet will otherwise behave as a free jet up to the point where recirculation occurs [219].

To determine if external recirculation takes place in the kiln the Craya-Curtet number can be calculated. The parameter describes when recirculation takes place for confined jets, normally when lower than the range 0.75-0.98 [218]. This also influences the flame in the cement kiln. When Ct <0.7, short and intense flames are encountered and when Ct > 1, the flame is long and lazy [27].

The number is defined as [219]:

$$Ct = \frac{u_k}{\sqrt{u_d^2 - \frac{1}{2}u_k^2}} \qquad \text{E 8.15}$$

With u_k being the kinematic mean velocity and u_d the dynamic mean velocity:

$$u_k = \frac{u_1 r_1^2 + u_2(r_2^2 - r_1^2)}{r_2^2} \qquad \text{E 8.16}$$

$$u_d = \frac{u_1^2 r_1^2 + u_2^2 (r_2^2 - r_1^2)}{r_2^2} + \frac{1}{2} u_2^2 \qquad \text{E 8.17}$$

Here, u_1 and u_2 are the velocities at the nozzle/burner (primary air) and of the surrounding stream (secondary air), respectively. Likewise, r_1 denotes the radius of the nozzle/burner and r_2 that of the enclosure. The kinematic velocity is the velocity that would be obtained if primary and secondary streams were fed uniformly, i.e. an average velocity. The dynamic velocity is the velocity that the streams would have if they were mixed to the same momentum, minus the static pressure head of the secondary stream.

Under combustion conditions, the density of the primary and secondary air streams will be different due to temperature differences, and the Craya-Curtet parameter must be adapted to take this into account [219].

8.6.3 Swirling Flows

The above analysis only considers axial flow, but cement kiln burners typically take advantage of swirl air to improve the flame characteristics. Swirl is induced by injecting air in a tangential manner, which causes a rotating motion. Swirl can have a large impact on the flow field, jet expansion, flame size and stability, etc. [144,148].

The intensity of swirl can be characterized by the swirl number [27,135]:

$$S = \frac{2 G_X}{G_Y 2 r_n} \qquad \text{E 8.18}$$

The flux of angular momentum is defined as:

$$G_Y = 2\pi \int_0^{r_n} (\rho u w) r^2 \, dr \qquad \text{E 8.19}$$

The axial thrust is defined as:

$$G_X = 2\pi \int_0^{r_n} (p + \rho u^2) r \, dr \qquad \text{E 8.20}$$

In the equations r_n is the radius of the nozzle/burner, p is the static pressure, u and w are axial and tangential velocities. In practice it may be difficult to measure the velocity and pressures needed to calculate the swirl number [144]. Thus, Gupta [148] proposes an approximation of the swirl flow, which is simpler to compute. It

is calculated based on the maximum axial and tangential velocities at exit of the burner nozzles:

$$S_{approx} = \frac{\frac{1}{2}\frac{w_{ex}}{u_{ex}}}{1 - \frac{1}{2}\frac{w_{ex}}{u_{ex}}} \qquad \text{E 8.21}$$

At low swirl intensities (S < ~0.4) the main effect of adding swirl is that the primary jet expands faster due to increased entrainment. At higher degrees of swirl (S > ~0.6), strong axial and radial pressure gradients are set up near the burner. This creates a zone of internal recirculation in front of the burner, which quickly expands the jet, but also slows it. Other effects that may affect the recirculation zone is the design of nozzles and enclosure size [148]. The recirculation zone mixes hot combustion gasses back to fresh fuel, which heats it up leading to earlier ignition. It also slows down the forward movement of fuel, which keeps the flame stabilized close to the burner. Both factors contribute to reduce flame length and increase intensity. The swirl can thus be used to influence the temperature and gas composition, which also affects the formation of pollutants, e.g. NOx [148].

According to Nørskov [31] the entrainment constant for swirling flows can be described as:

$$K_{ent} = 0.32 + 0.8S \qquad \text{E 8.22}$$

Analyzing the results published by Park and Shin [220] (regression of their published data) the entrainment rate can be determined as:

$$K_{ent} = 0.22 + 0.38S \qquad \text{E 8.23}$$

8.6.4 Air Flow in the Cement Kiln

It is inherently difficult to measure inside a large scale industrial rotary kiln as already outlined in chapter 4. Traditionally, the mixing in the cement kiln has been studied using down-scaled cold models. This can be compared to large scale operation, if the model is scaled appropriately to e.g. keep Reynolds number equal. It is not straightforward to translate the model results to information of the full scale system, since e.g. density differences are introduced by the combustion [221,222]. More recently advanced CFD models are used to a higher degree. Some interesting studies on the mixing in cement kilns are outlined in this section.

Moles et al. [136] made a study of a number of wet kilns to determine typical ranges of excess air, gas velocities and the Craya-Curtet number. They proceeded to study the flow in a scaled down kiln model using water and air flow. In addition, large scale measurements were attempted to validate the flow models. It was found that the gas flow through the cooler and cooler hood had an impact on the gas flow in the kiln, which creates a vortex under the burner and tends to push the flame downwards.

Ruhland [223] used acid-alkali modeling to study the flame in a cement kiln model, as shown in Figure 8-5. An alkaline solution containing a colored indicator is injected as primary air into a kiln filled with acid that acts as secondary air. When the two liquids mix, the pH is neutralized, and the color removed. This gives an estimate of the mixing length in the model. Ruhland found a formula for describing the mixing length produced by a smooth non-swirled nozzle. The mixing length is equivalent to the flame length for fossil fuels, where the combustion is mainly limited by the oxygen availability.

$$\frac{L_{fl}}{d_n} = \sqrt{K}\left[3.21\left(\frac{2}{3}+B_p\right)+3.862\left(\frac{1}{B_{p,exc}-1}\right)^{0.442} * exp(a+b)\right] \quad \text{E 8.24}$$

With the following definitions used:

$$K = \frac{\dot{m}_{prim}+\dot{m}_{sec}}{\left(\frac{\dot{m}_{prim}}{\rho_{prim}}+\frac{\dot{m}_{sec}}{\rho_{sec}}\right)\rho_{fl}} \quad \text{E 8.25}$$

$$a = 2.12\frac{\dot{m}_{sec}}{\dot{m}_{prim}}\left(\frac{d_n}{d_k-d_n}\right)^{1.245} \quad \text{E 8.26}$$

$$b = 0.1052\frac{d_k-d_n}{d_n} \quad \text{E 8.27}$$

In the equations, the following definitions are used: L_{fl} flame length, d_n nozzle diameter, B_p secondary air requirement for fuel combustion [kg/kg fuel], $B_{p,exc}$ excess air ratio for the secondary air, $\dot{m}$ mass flow, ρ density, d_k kiln diameter. The subscripts *prim*, *sec*, and *fl*, indicate primary air, secondary air, and flame, respectively.

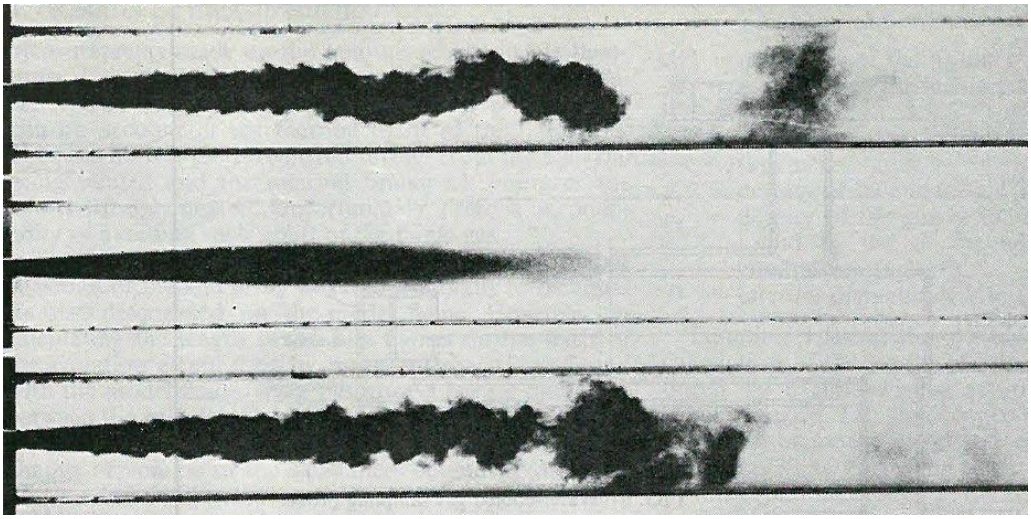

Figure 8-5: Examples of acid-alkali mixing used to investigate the kiln flame. The dark plume (alkali) represents the cement kiln flame. The dark color dissipates as the alkali is mixed with acid, representing the secondary air. Top and bottom images are single frames and middle picture is averaged over 60 seconds [223].

Bhad [224] modeled a coal fired cement kiln using CFD. The study focused on different levels of swirl. With a high swirl the flame length reduces and ignites earlier. The flame also becomes wider, which can overheat the refractory.

Orfanoudakis [225] studied a scaled down rotary kiln burner in the laboratory. The effect of swirl was studied for coal and gas fired flames with both experiments and CFD. The results showed that an internal recirculation zone was formed at swirl numbers above 0.65. Increasing the swirl number further also increased the width of the recirculation zone. Especially at high swirl numbers, coal particles can be centrifuged out of the internal recirculation zone (IRZ), which may increase NO_X emissions.

8.6.5 Model for the Secondary Air Entrainment

In order to formulate some simple rules for the mixing of secondary and primary air that can be used in the 1-D model, a number of CFD simulations were performed. These simulations have been carried out by David Jayanth Isaac of FLSmidth. The simulations are made on a petcoke flame from the FLSmidth Jetflex burner in a full-scale cement plant. The burner with a diameter of 0.64 m and the kiln with a diameter of 5 m. A thorough description of similar simulations for co-firing petcoke and SRF using the same kiln geometry and burner can be found in [204].

Six different simulations with varying swirl and axial momentum were made according to Table 8-4. The axial momentum and swirl number are increased by increasing the flow rate of axial and swirl air. The swirl air flow rate is set at two levels 50 and 100 %, which results in swirl numbers of ~0.2 and ~0.35. The swirl number and the simplified approximate swirl number were calculated using equations E 8.18 and E 8.21.

Table 8-4: Momentum and swirl number in CFD simulations, performed by David Jayanth Isaac, used to determine secondary air entrainment.

Momentum (N/MW)	Swirl Level (%)	Swirl Number (E 8.18)	Approximated Swirl Number (E 8.21)	$K_{ent,jet}$	$K_{ent,jet}$ by E 8.30
5.3	50	0.18	0.25	0.186	0.188
6.0	100	0.35	0.48	0.237	0.235
7.0	50	0.20	0.26	0.203	0.200
8.0	100	0.36	0.47	0.243	0.247
9.0	50	0.20	0.25	0.208	0.209
10.0	100	0.35	0.45	0.255	0.254

The jet radius was found in the simulations as the radial distance where the axial velocity of the jet becomes equal to the inlet secondary air velocity. The jet radius is plotted for the 6 simulation cases in Figure 8-6.

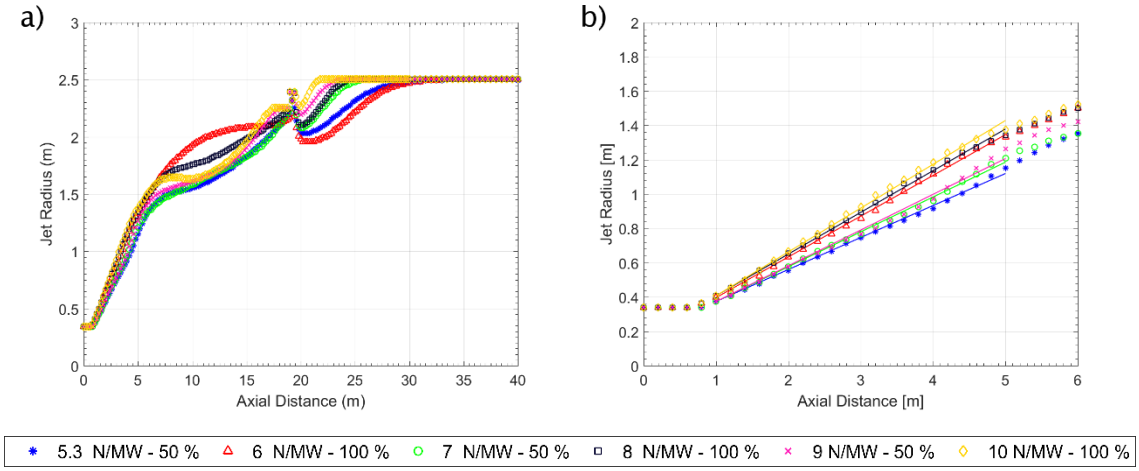

Figure 8-6: a) The jet radius as function of axial distance from burner with different burner axial momentum and swirl. b) Zoomed version of a, with regression lines. Data derived from CFD simulations of a petcoke flame performed by David Isaac.

The jet in Figure 8-6 is seen to initially, between 1 and 5 meters, expand linearly. The rate at which this occurs is increased by both axial momentum and swirl. At around 7 meters the location of an external recirculation zone inhibits the further

expansion of the jet. At a distance of 20 meters, the kiln diameter is expanded, which explains the odd shape of the curves around this point. The kiln diameter is constricted near the burner, since it has been assumed that a kiln coating is present.

For the model developed in this study, it will be assumed that the jet expands linearly as seen in Figure 8-6b. No recirculating zone is assumed to be present, thus the jet will expand until it reaches the kiln wall following the equation:

$$\boldsymbol{r_{jet} = r_n + K_{ent,jet} * x} \qquad \textbf{E 8.28}$$

And the mass fraction of secondary air entrained into the primary air jet will be proportional to the jet radius:

$$\boldsymbol{Y_{ent,sec} = \frac{r_{jet} - r_n}{r_k - r_n}} \qquad \textbf{E 8.29}$$

The entrainment constant, $K_{ent,jet}$, is found based on the jet expansion rate found in Figure 8-6b. The slope of each data set is found between 1-5 m, where the graphs are linear. The slopes, i.e. entrainment constants, for the six different simulation cases can be found in Table 8-4. A multilinear regression is then employed to determine the relationship between burner momentum, swirl, and the entrainment constant:

$$\boldsymbol{K_{ent,jet} = 0.116 + 4.69 * 10^{-3} * I' + 0.259 * S} \qquad \textbf{E 8.30}$$

Here I'[N/MW] is the burner momentum and S is the swirl number. Both swirl and axial momentum is according to this regression model serving to increase the entrainment of secondary air into the jet, which expands the jet radius. The numbers of the entrainment constant calculated using this equation can be found in Table 8-4.

8.7 Heat Transfer in the Cement Kiln

The heat transfer in the cement kiln is of very high importance as the main goal of the kiln is to heat the cement raw materials to a sufficiently high temperature for the clinker reactions to occur. Some attempts to model the heat transfer was already highlighted in chapter 8.1, but a more thorough evaluation of the different mechanisms will be covered here.

In the cement kiln, several modes of heat transfer occur, as sketched in Figure 8-7. The hot gasses exchange heat with the clinker bed and exposed wall through radiation and convection. The wall radiates heat to the bed, and where the wall is in

direct contact with the clinker bed, conduction also occurs [196]. In addition, there is a heat loss to the surroundings by conduction through the kiln wall. The exact loss is difficult to estimate due to the buildup of the kiln coating of varying thickness on the inside of the kiln [31]. Finally there is also heat transfer within the clinker bed itself [27], governed by both conduction, radiation and gas convection between the particles and motion of the particle bed [185], where the particle motion will typically dominate the heat transfer [27]. There are indications that the bed may be close to isothermal (at least in pilot scale) due to the good mixing of the bed [185]. Lehmberg et al. [226] report that mixing is typically complete within 4 rotations. If segregation occurs in the bed, due to significant differences in particle sizes. Boateng and Barr [227] modeled the bed core to be around 200 °C colder than the bed surface (with freeboard temperatures of 800 °C). Under the same operating conditions, the bed was largely isothermal for a more homogenous particle size distribution.

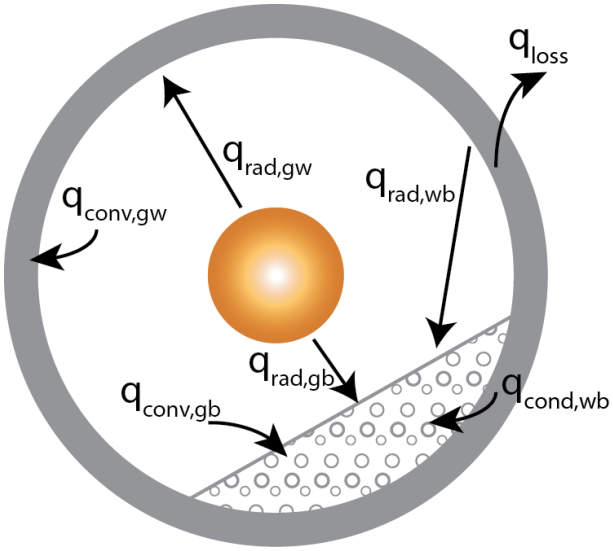

Figure 8-7: Paths of heat transfer in the cement rotary kiln.

In a cement rotary kiln two main heat transfer zones are present; the flame zone near the burner flame and the non-flame zone further downstream in the kiln. In the flame zone the radiating gases are confined to the visible flame at high temperatures, while they further downstream expand to occupy the entire freeboard, but also cools down. Thus, in the flame region, heat is primarily transferred by radiation from the flame, while convection plays a minor role. In the non-flame zone convection plays a larger role [183]. Due to the high temperatures in the kiln, radiative heat transfer is the dominating form of heat transfer [181,196], constituting around 90 % of the total heat transferred from the gas to bed [27]. Heat transfer in the radial

direction is predominant, while radiation in the axial direction of the kiln is negligible, even though large temperature differences can occur [181,183,185]. This is caused by a low transparency of the gas to its own radiation.

8.7.1 Convective Heat Transfer

The convective heat transfer between the gas and the bed or the wall can be described by the following relation:

$$\boldsymbol{q_{conv,ij} = h_{conv,ij} * (T_i - T_j)} \qquad \textbf{E 8.31}$$

Here the convective heat transfer coefficient between gas and bed can be described by an empirical relation found by Tscheng and Watkinson, based on experiments in a pilot scale rotary kiln [228]:

$$\boldsymbol{h_{conv,gb} = \frac{\lambda_g}{d_e} * Nu_{conv,gb} = \frac{\lambda_g}{d_e} * 0.46 * Re^{0.535} * Re_{\omega}^{0.104} * \eta^{-0.341}} \qquad \textbf{E 8.32}$$

Here the Reynolds number and the rotational Reynolds number are defined as:

$$\boldsymbol{Re = \frac{u_g * d_e}{\nu_g}} \qquad \textbf{E 8.33}$$

$$\boldsymbol{Re_{\omega} = \frac{d_e^2 * \omega}{\nu_g}} \qquad \textbf{E 8.34}$$

u_g is the axial velocity of gas, ω is the kiln angular velocity [rad/s], ν_g is the kinematic viscosity of gas, λ_g is the gas thermal conductivity, and η is the kiln fill degree. d_e is the equivalent diameter determined as [228]:

$$\boldsymbol{d_e = r_k * \frac{2 * \pi - \theta * sin\,\theta}{\pi - \frac{\theta}{2} + sin\frac{\theta}{2}}} \qquad \textbf{E 8.35}$$

With r_k being the kiln radius and θ the central angle subtended by the kiln bed (see Figure 8-3).

The convective heat transfer coefficient between the gas and exposed walls is determined by [228]:

$$\boldsymbol{h_{conv,gw} = \frac{\lambda_g}{D_e} Nu_{conv,gw} = \frac{\lambda_g}{D_e} * 1.54 * Re^{0.575} * Re_{\omega}^{-0.292}} \qquad \textbf{E 8.36}$$

The porous layer of rolling particles at the bed surface is commonly believed to increase the convective heat transfer to the bed over that of the exposed wall.

However, in one study the effect was not very pronounced, and the convective heat transfer coefficients from gas to bed were in the range 1-2 times the value from gas to exposed wall [184].

8.7.2 Conductive Heat Transfer

Where there is contact between the kiln bed and the wall, heat is transferred through conduction according to:

$$\boldsymbol{q_{conv,wb} = h_{cond,wb} * (T_w - T_b)} \qquad \textbf{E 8.37}$$

The heat transfer coefficient for conduction has also been investigated by Tscheng and Watkinson [228] and can be determined by:

$$\boldsymbol{h_{cond,wb} = 11.6 * \frac{\lambda_b}{l_{wb}} * \left(n * r_k^2 * \theta * \frac{\rho_b * Cp_b}{\lambda_b}\right)^{0.3}} \qquad \textbf{E 8.38}$$

Here n is the kiln rotational speed [revolutions/s], l_{wb} is the covered wall circumference [m] where the bed touches the wall. λ, Cp, and ρ are the heat conductivity, heat capacity, and density, respectively.

Pilot scale measurements in a gas fired rotary kiln have shown that the regenerative heat transfer from the covered wall to the bed can account for up to 50 % of the net energy to the bed, although it normally is lower (around 10-20 %) [184]. The amount is dependent on the location in the kiln and tends to be highest near the material inlet. In the flame zone a larger part of the energy is transferred from the flame to the exposed kiln bed, and there tends to be a net heat transfer from the bed to the covered wall.

8.7.3 Radiative Heat Transfer

It will be assumed that the radiative heat transfer takes place between the three surfaces of flame jet, kiln bed, and kiln walls and only occurs in the radial direction. This assumption significantly simplifies the model calculations, since the local heat transfer will not be dependent on upstream or downstream conditions. The radiation in the axial direction is only around 10-20 % of the radiation in radial direction in the hottest part of the flame [31,183].

For radiation between N diffuse grey surfaces the radiation exchange can be written as N equations of the form [229]:

$$\sum_{j=1}^{N}\left(\frac{\delta_{ij}}{\epsilon_j}-\Omega_{kj}*\frac{1-\epsilon_j}{\epsilon_j}\right)q_j=\sum_{j=1}^{N}\left(\delta_{ij}-\Omega_{ij}\right)*\sigma T_j^4 = \sum_{j=1}^{N}\Omega_{kj}\sigma*(T_i^4-T_j^4) \quad \text{E 8.39}$$

In the equation δ_{ij} is the Kronecker delta, ε the emissivity, q the heat transfer flux, T the temperature, σ the Stefan-Boltzmann constant, and Ω is the view factor between two surfaces.

The view factor for radiation can be determined by Hottel's crossed strings method [229] described in Appendix C. In addition, there will be radiative heat transfer to the fuel, which will be described in chapter 8.8.1.

8.7.4 Heat Loss

In the kiln there will be a significant heat loss of typically 10-20 % of the total energy input. Heat is transferred through the kiln walls and to the colder ambient environment outside the kiln. To minimize the heat loss, the kiln is lined with refractory bricks. A kiln coating, formed of molten and then solidified clinker, is also typically present in the clinker burning zone, which further limits the heat loss. The thickness of the coating will have a great effect on the heat loss but it is difficult to determine the exact thickness [31]. The outside temperature of the kiln shell is typically monitored by a kiln scanner, as discussed in chapter 4.6 [133].

For model purposes it will be assumed that a kiln coating is present near the burner end of the kiln. The thickness and extent of the coating can be adjusted in the model. The default values are a thickness of 25 cm, during the first 15 meters of the kiln (measured from the burner end), which afterwards linearly decreases to 0 cm for the next 5 meters.

For the model it will be assumed that there is thermal equilibrium between the heat transferred to the wall and the heat transferred through the wall as a loss:

$$q_{loss}=\sum_{i}^{N_{ht}}q_i=q_{rad,gw}+q_{rad,bw}+q_{conv,gw}+q_{cond,bw} \quad \text{E 8.40}$$

The heat transfer to the wall is given by radiation from the gas and bed, convection from the gas, and conduction from the bed.

It will be assumed that heat is first transferred through the coating (if it is present), then the kiln refractory, and at the outer surface it is transferred to the surroundings due to convection and radiation. The heat conduction through the kiln steel shell will be neglected here, since the resistance will likely be small compared to that of the thicker kiln coating and refractory.

The heat conduction through the coating:

$$\boldsymbol{Q_{coat} = \lambda_{coat}\left(\frac{T_w - T_{coat}}{ln\left(\frac{r_{k,i}}{r_{k,i} - l_{coat}}\right)}\right) * 2\pi\Delta x} \qquad \text{E 8.41}$$

The heat conduction through the kiln refractory:

$$\boldsymbol{Q_w = \lambda_w\left(\frac{T_{coat} - T_{sh}}{ln\left(\frac{r_{k,o}}{r_{k,i}}\right)}\right) * 2\pi\Delta x} \qquad \text{E 8.42}$$

And at the kiln shell surface energy is lost by convection and radiation:

$$\boldsymbol{Q_{sh} = \left(q_{rad,loss} + q_{conv,loss}\right) * 2\pi r_{k,o}\Delta x} \qquad \text{E 8.43}$$

The radiative loss and convective losses are given as:

$$\boldsymbol{q_{rad,loss} = \sigma\epsilon_{sh} * \left(T_{sh}^4 - T_{amb}^4\right)} \qquad \text{E 8.44}$$

$$\boldsymbol{q_{conv,loss} = h_{conv,sh} * \left(T_{sh} - T_{amb}\right)} \qquad \text{E 8.45}$$

It is possible to determine the convective heat transfer coefficient based on the Nusselt number and the outer kiln diameter:

$$\boldsymbol{h_{conv,sh} = Nu_{conv,sh} * \frac{d_{k,o}}{\lambda_{amb}}} \qquad \text{E 8.46}$$

Where the Nusselt number is determined based on the rotational Reynolds number, the Grashof number, and the Prandtl number as shown in E 8.47 [230]. The equation is valid in quiescent media, while the potential effect of wind speed was neglected.

$$\boldsymbol{Nu_{conv,sh} = 0.11 * \left((0.5 * Re_w^2 + Gr) * Pr\right)^{0.35}} \qquad \text{E 8.47}$$

With the following definitions of the dimensionless numbers:

$$\boldsymbol{Re_w = d_{k,o}^2 \frac{\omega}{2\nu_{g,amb}}} \qquad \text{E 8.48}$$

$$Gr = g * d_{k,o}^3 * \frac{1}{T_{amb}} * (T_{sh} - T_{amb}) * \frac{1}{\nu_{g,amb}^2} \quad \text{E 8.49}$$

$$Pr = \frac{\mu_{g,amb} Cp_{g,amb}}{\lambda_{g,amb}} \quad \text{E 8.50}$$

In the calculation of the Grashof number it has been assumed that the coefficient of thermal expansion is equal to $1/T_{amb}$, which is true for ideal gasses.

Since the heat transfer through the coating and refractory must be equal, it is possible to eliminate the unknown temperature T_{coat} from the equations E 8.41 and E 8.42, eventually yielding:

$$T_w = \left(\frac{1}{2\pi} * \left(\frac{ln\left(\frac{r_{k,i}}{r_{k,i} - l_{coat}}\right)}{\lambda_{coat}} + \frac{ln\left(\frac{r_{k,o}}{r_{k,i}}\right)}{\lambda_w} \right) * \sum_i^{N_{ht}} q_i * l_i \right) + T_{sh} \quad \text{E 8.51}$$

The shell temperature, T_{sh}, can be eliminated from the equation by use of the equations E 8.43-E 8.45. This is not trivial to solve due to the 4th power exponent in the radiation term, but it can be done numerically.

8.8 Combustion of Solid Fuels

Combustion of solid fuels conceptually follow the four steps heating, drying, devolatilization, and char oxidation. Subsequently the gasses released during the devolatilization will burn in the gas phase. A brief review of the different mechanisms will be presented along with the equations applied in the model.

8.8.1 Heating

When the fuel particles are injected into the kiln, they are heated as they are exposed to the hot secondary air and radiation from the environment. Small particles such as pulverized petcoke or coal, which generally have a particle diameter below 200 μm, can normally be considered isothermal. In larger particles, such as from alternative fuels with particle sizes in the range 1-10 mm, heat transfer inside the particle may be lower than the heat transfer to the particle, which creates significant temperature gradients inside the particle. To evaluate if the particle can be considered isothermal, the Biot number can be evaluated [231]. This number is the ratio between external heat transfer and internal heat transfer in the fuel particle.

$$\boldsymbol{Bi} = \frac{\boldsymbol{h_{ext} * r_p}}{\boldsymbol{\lambda_p}} \qquad \text{E 8.52}$$

In the equation, h_{ext} is the external heat transfer coefficient, r_p the particle radius, and λ_p is the particle heat conductivity. Biot numbers lower than 0.2 indicates that the particle can be assumed isothermal [231].

The particle temperature for small isothermal particles can be determined by the following equation:

$$\frac{\boldsymbol{dT_p}}{\boldsymbol{dt}} = \frac{\boldsymbol{1}}{\boldsymbol{m_p}} * \frac{\boldsymbol{1}}{\boldsymbol{Cp_p}} \left(\frac{\boldsymbol{1}}{\boldsymbol{\varphi_p}} \boldsymbol{A_p} * \boldsymbol{q_{ext}} - \boldsymbol{m_{p,0}} * \boldsymbol{Y_{H2O,0}} * \boldsymbol{\Delta H_{evap}} \frac{\boldsymbol{dX_{dry}}}{\boldsymbol{dt}} \right) \qquad \text{E 8.53}$$

The first term on the right-hand side of the equations accounts for the heat transfer to the particle, while the second term accounts for the loss of energy due to evaporation of water from the particle. It is assumed that the devolatilization has a net energy consumption of 0, and thus does not contribute to the particle heating. Furthermore, it is assumed that any energy released during volatile and char combustion is released solely to the gas phase.

For plastic particles, which are present in SRF, it is assumed that melting and decomposition of the polymer requires some energy, as proposed by Nakhaei et al. [232], which is added to the temperature equation.

$$\frac{\boldsymbol{dT_p}}{\boldsymbol{dt}} = \frac{\boldsymbol{1}}{\boldsymbol{m_p}} * \frac{\boldsymbol{1}}{\boldsymbol{Cp_p}} \left(\frac{\boldsymbol{1}}{\boldsymbol{\varphi_p}} \boldsymbol{A_p} * \boldsymbol{q_{ext}} - \boldsymbol{m_{p,0}} * \left(\boldsymbol{Y_{H2O,0}} * \boldsymbol{\Delta H_{evap}} \frac{\boldsymbol{dX_{dry}}}{\boldsymbol{dt}} + \boldsymbol{Y_{vol,0}} * \boldsymbol{\Delta H_{decomp}} \frac{\boldsymbol{dX_{devol}}}{\boldsymbol{dt}} + \boldsymbol{\Delta H_{melt}} \frac{\boldsymbol{dX_{melt}}}{\boldsymbol{dt}} \right) \right) \qquad \text{E 8.54}$$

According to calculations performed by Nakhaei et al. [232], an isothermal model for polyethylene predicts devolatilization times within a 20 % error compared to a more rigorous 1D-model. Since the polymer evaporates as a droplet, temperature gradients in the particle are limited. Thus, the isothermal particle model will be used here.

For other particle types, that form a char, non-isothermal effects are more important. For non-isothermal particles, a 1-D model will be applied to take into consideration the temperature gradients [233]:

$$\frac{\partial T_p}{\partial t} = \frac{\lambda_p}{\rho_p * Cp_p}\frac{1}{\varphi_p}\left(\frac{2}{r}\frac{\partial T_p}{\partial r} + \frac{\partial^2 T_p}{\partial r^2}\right) - \frac{\rho_{p,0}}{\rho_p}\frac{\Delta H_{evap} * Y_{H2O,0}}{Cp_p}\frac{\partial X_{dry}}{\partial t} \quad \text{E 8.55}$$

The boundary conditions for the partial differential equation for heat transfer in large particles are given in E 8.56 and E 8.57. They indicate the heat transfer to the particle and that the temperature gradient at the center is 0, due to symmetry.

$$\lambda_p \frac{\partial T_p(t, r = r_p)}{\partial r} = q_{ext} \quad \text{E 8.56}$$

$$\frac{\partial T_p(t, r = 0)}{\partial r} = 0 \quad \text{E 8.57}$$

The partial differential equation is solved by discretizing into a number of coupled ordinary differential equations using the Method of Lines [234].

The external heat transfer to the particles is divided into convection and radiation. The convective heat transfer between gas and particle is given by [235]:

$$q_{conv,gp} = h_{conv,gp} * (T_g - T_{p,s}) \quad \text{E 8.58}$$

The heat transfer coefficient is determined based on the Nusselt number which is found using the Ranz Marshall correlation [235]:

$$Nu = \frac{h_{conv,gp} * 2r_p}{\lambda_g} = 2 + 0.6Re^{\frac{1}{2}}Pr^{\frac{1}{3}} \quad \text{E 8.59}$$

The radiative heat transfer to the particle from the gas is determined by the equation [31]:

$$q_{rad,gf} = \sigma\frac{\epsilon_p + 1}{2}(\epsilon_g T_g^4 - \alpha_g T_{p,s}^4) \quad \text{E 8.60}$$

In the equation, σ is the Stefan-Boltzmann constant, ε the emissivity, α the absorptivity, and, T the temperature.

It is also assumed that there is radiation between the bed and the fuel particles according to:

$$q_{rad,bf} = \frac{1}{K_{rad}} * \tau_g \sigma(\epsilon_f T_f^4 - \epsilon_b T_b^4) \quad \text{E 8.61}$$

The radiative exchange is limited by the factor τ_g, which is the transmissivity of the gas phase. Furthermore, the factor K_{rad} limits radiation to the fuel particles. Since radiation will only occur to the fuel particles at the surface of the flame, it was found

to be necessary to further limit the radiation. A factor of 2 was found to be appropriate for the model validation in pilot scale, while a factor 100 was used for the industrial kiln as described in chapter 9. In the industrial kiln the fuel mass flow is larger relative to the kiln cross section, which leaves less particles exposed, justifying the larger correction factor.

8.8.2 Drying

When the fuel particle approaches a temperature around 100 °C moisture in the particle will begin to evaporate. Evaporation of water requires a lot of energy [236], and the fuel heating and ignition can thus be delayed by a high moisture content. This is especially of interest in alternative fuels where e.g. the moisture content in SRF can range from 10-40 % (see Table 3-3). In the cement industry pulverized fossil fuel normally has a low moisture content, since the fuel is dried during milling. This makes the drying step less important in the combustion sequence for fossil fuels.

Different models are used in the literature to model the evaporation of water in combustion [237]. Here a simple kinetic model based on a first order Arrhenius expression will be used for the evaporation [236]:

$$\frac{dX_{dry}}{dt} = A_{dry} * exp\left(\frac{-E_{A,dry}}{R_{gas}T_P}\right)(1 - X_{dry}) \qquad \text{E 8.62}$$

The conversion, X_{dry}, is the mass-based fraction of initial water content that has evaporated. Thus, X_{dry} is 0 when the particle is wet and 1 when it is dry. A_{dry} is the pre-exponential factor for drying, $E_{a,dry}$ the activation energy, R_{gas} the ideal gas constant and T_p the particle temperature.

8.8.3 Devolatilization

As the fuel is heated further to temperatures exceeding 200 °C, the solid begins to decompose into smaller volatile molecules that leave the solid matrix. For coal the process is divided into three stages. Loosely bound H_2O and CO_2 is released below 350 °C. Primary devolatilization takes place due to rupture of chemical bonds in the temperature region 350-550 °C. Secondary devolatilization occurs in the temperature range 600-800 °C, breaking the strongest covalent bonds, forming primarily H_2 and CH_4 [31,238]. Biomass primarily devolatilizes at temperatures

around 200-500 °C, depending on the content of cellulose, hemicellulose, and lignin [239]. For SRF the paper fractions primarily behaves as biomass and devolatilizes at 300-400 °C, and plastics at 400-500 °C [164].

The products formed from the devolatilization are normally divided into 3 groups being gasses, tars (i.e. condensable species), and char [85]. A major difference in the combustion behavior of fossil fuels and SRF is the amount of volatiles formed (see Table 3-4). SRF for instance has a volatile content around 70 %, while coal has a volatile content of approximately half that, and petcoke has an even lower volatile content. In SRF, plastics, e.g. polyethylene and polypropylene, are almost fully volatile, while the biomass fraction, e.g. paper and cardboard, has a volatile content around 80 %.

In addition to the type of fuel and its chemical composition, physical conditions during the devolatilization also has an impact. The rate of devolatilization and the products formed during it, depend on e.g. temperature, heating rate, particle size, and catalytic activity of ash components [85,238].

In this work a single global first order reaction will be assumed to account for the devolatilization of the fuel.

$$\frac{dX_{devol}}{dt} = A_{devol} * exp\left(\frac{-E_{A,devol}}{R_{gas}T_P}\right)(1 - X_{devol}) \qquad \text{E 8.63}$$

More advanced models can be found in the literature as e.g. discussed in [237,239].

8.8.3.1 Products of Devolatilization

The major products from biomass and coal devolatilization are CO_2, CO, and CH_4, while smaller quantities of H_2 and C_2 hydrocarbons can also be formed [85,240]. As a simplification, here it will be assumed that CO and CH_4 are the only products of devolatilization. This approach involves less species in the model, while it is still possible to adjust the heating value of the volatiles by adjusting the ratio between formed CO and CH_4.

The split of the two are found based on a mass and energy balance based on the proximate analysis and the heating value of the fuel. The proximate analysis of a fuel states the moisture, ash, fixed carbon (char), and volatile content. Thus, the mass fractions sum to 1:

$$Y_{H2O} + Y_{ash} + Y_{char} + Y_{vol} = 1 \quad \text{E 8.64}$$

It is assumed that the fuel char content from the proximate analysis (fixed carbon) is pure carbon and has an energy content of $\Delta H_{char} = 32.8$ MJ/kg [241], which is the reaction enthalpy for forming CO_2 from C. The energy content of the volatiles can then be calculated based on the fuel heating value subtracted the char energy:

$$\Delta H_{vol} = LHV - Y_{char} * \Delta H_{char} \quad \text{E 8.65}$$

The fraction of CH_4 and CO formed from the volatiles can then be calculated as:

$$Y_{vol,CH4} = \frac{\frac{\Delta H_{vol}}{Y_{vol}} - \Delta H_{CO}}{\Delta H_{CH4} - \Delta H_{CO}} \quad \text{E 8.66}$$

$$Y_{vol,CO} = 1 - Y_{vol,CH4} \quad \text{E 8.67}$$

While this assumption fulfills the mass and energy balance for the fuel, the elemental composition (on C, O, H) may not balance, since the ultimate analysis of the fuel is disregarded. This can lead to some issues when calculating the oxygen requirement of the combustion. To account for possible differences, additional nitrogen can be added to the secondary air, to keep a realistic air consumption. Some example calculations illustrating the difference are presented in Appendix D.

8.8.4 Char Oxidation

After the volatile species have been driven off, a solid residue called char remains. It mostly consists of carbon, potentially with some ashes and minor amounts of hydrogen, oxygen, nitrogen, and sulfur [242]. The amount and composition of the formed char depends on parameters such as fuel type, temperature, and heating rate during the devolatilization [85,242].

The solid char can be oxidized forming CO or CO_2, or it can be gasified by water or CO_2 [85,242] according to the overall reactions:

$$C + O_2 \rightarrow CO_2 \quad \text{R 8.1}$$

$$C + \frac{1}{2}O_2 \rightarrow CO \quad \text{R 8.2}$$

$$C + H_2O \rightarrow CO + H_2 \quad \text{R 8.3}$$

$$C + CO_2 \rightarrow 2CO \quad \text{R 8.4}$$

The rate of each reaction is governed by the gas phase composition, but also highly dependent on temperature. Under combustion conditions the oxidation reaction normally dominates [242] and the formation of CO is favored over that of CO_2 [242]. The rate of steam gasification is 2-5 times higher than that of the CO_2 gasification for wood chars [85].

Char burnout is normally slower than the devolatilization. In pulverized coal flames, the devolatilization process is completed within 0.1 s, whereas char burnout takes around 1 s [243]. For alternative fuels such as biomass [31,86,87] or sewage sludge [31], the char oxidation also tends to take longer, although only by a factor 2-3. This is caused by a higher volatile and lower char content in most alternative fuels compared to coal.

The char reactions are governed by several different steps [85]:

1. Film diffusion of oxidizing/gasifying agent to char surface
2. Diffusion through ash layer and particle
3. Adsorption onto the reaction site
4. Chemical reaction
5. Desorption of gaseous products
6. Diffusion of products through particle and ash layer
7. Film diffusion into the ambient gas.

Thus, it is evident that the char reaction rate will be dependent on several factors relating to both the chemical and physical properties of the char. The chemical structure of the char determines the chemical reaction rate. Meanwhile, the pore structure of the char affects the total surface area and the diffusion rate in the char and presence of inorganic constituents may catalyze the reaction [242]. Factors relating to the devolatilization may also affect the char reactivity. For example high heating rates during devolatilization will typically result in a more reactive char [85].

The combustion can be divided into three regimes depending mainly on particle size and temperature and the gaseous diffusion rates [85]:

1. Chemical control: At low temperatures and for small particles, the diffusion rate is high compared to the reaction rate. The oxidizing/gasifying agents can

penetrate far into the particle and the conversion occurs throughout the particle

2. Intra-particle diffusion control: For larger particle sizes or higher temperatures, the diffusion into the particle is low, and most of the reaction occurs in a thin layer close to the particle surface
3. External diffusion control: At high temperatures the reactions will be fast and the diffusion of the oxidizing/gasifying agent through the film layer is limiting and the reaction occurs at the particle surface

For alternative fuels, such as SRF, external diffusion is the main limitation at temperatures above 1000 °C. For the less reactive and smaller particles of coal and petcoke, chemical kinetics is limiting when the temperature does not exceed 2000 °C [31].

For modeling of the char oxidation, a shrinking core model [215,242] will be employed here. It is thus assumed that the char oxidation takes place at the particle surface. Diffusion to the particle surface as well as reaction kinetics will be considered, and no ash layer is assumed. It is assumed that the char can react with either O_2 or H_2O according to R 8.2 and R 8.3. Since the gasification with CO_2 is slower than H_2O gasification, CO_2 will be neglected.

$$\frac{dX_{char}}{dt} = \frac{3}{\varphi_p} * \frac{(1 - X_{char})^{\frac{2}{3}}}{r_p} * \frac{M_{char}}{\rho_{char}} * \left(\frac{1}{\phi_{O2}} * \frac{C_{O2,bu}}{\frac{1}{k_{eff,O2}}} + \frac{1}{\phi_{H2O}} \frac{C_{H2O,bu}}{\frac{1}{k_{eff,H2O}}} \right) \quad \text{E 8.68}$$

In the equation, X_{char} is the conversion with respect to char, φ_p the particle sphericity, M_{char} and ρ_{char} are the molecular mass and density of the char, C_{bu} is the bulk concentration, and ϕ is the stoichiometry for the reaction [mol O_2 or H_2O/mol fuel]. The effective rate of the char reaction, k_{eff} is combined by the rate of reaction, k_{char}, and the rate of film diffusion, k_{film}:

$$\frac{1}{k_{eff,i}} = \frac{1}{k_{char,i}} + \frac{1}{k_{film,i}} \quad \text{E 8.69}$$

The rate constant for the chemical reaction is found based on an Arrhenius expression:

$$k_{char} = A_{char} * exp\left(\frac{-E_{A,char}}{R_{gas}T}\right) \quad \text{E 8.70}$$

The rate of film diffusion is determined based on the diffusivity of oxygen or water:

$$k_{film,i} = \frac{D_i * Sh}{2r_p} \quad \text{E 8.71}$$

The Sherwood number is determined based on the Reynolds and Schmidt numbers [215]:

$$Sh = 2 + 0.6 * Re^{\frac{1}{2}} * Sc^{\frac{1}{3}} \quad \text{E 8.72}$$

8.8.5 Fuel Combustion in the Clinker Bed

It is evident from the performed industrial tests and camera measurements that a substantial part of the SRF does not fully combust while it is in suspension in the cement kiln. Large fractions of the fuel may only be combusted as it drops out of the flame and into the clinker bed. This is consistent with the literature modeling results described previously [143,163,204]. Thus, it will be necessary to account for fuel combustion in the bed.

8.8.5.1 Fuel Trajectories

It will be assumed that fossil fuel particles are small enough to be carried with the gas stream and not drop out of the flame. Only the larger alternative fuel particles can drop out of the flame.

Approximate fuel trajectories can be calculated based on some simple force balances. In the vertical direction the fuel is impacted by gravity as well as drag, from an assumed quiescent gas:

$$F_y = \frac{1}{2}A_p\rho_g C_D * \left(v_{p,y}\right)^2 - g * m_p \quad \text{E 8.73}$$

In the axial direction the particle will be slowed by drag from the slower flowing air.

$$F_x = -\frac{1}{2}A_p\rho_g C_D * \left(u_{p,x} - u_g\right)^2 \quad \text{E 8.74}$$

For simplicity, the gas can be assumed to flow at a velocity equal to the inlet velocity of the secondary air, and the gas properties can also be evaluated at the secondary air temperature. This eliminates the effect of changing velocity due to an expanding

jet and temperature differences. The drag coefficient, C_D, may be assumed a value of 0.44. Example trajectories are shown in Figure 8-8. The larger the particle is, the further it can travel inside the kiln, as it is less influenced by drag. However, it may also have a lower residence time since it drops faster.

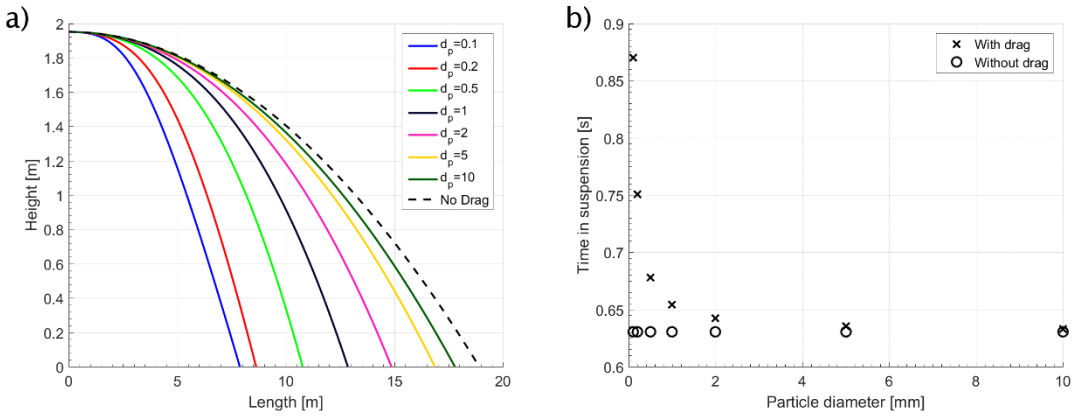

Figure 8-8: Trajectories (a) and time in suspension (b) for particles with diameter 0.1-10 mm injected in kiln. $u_{p0} = 30$ m/s, $\rho_p = 1000$ kg/m³, $u_g = 5.8$ m/s, $T_g = 750$ °C, $r_k = 1.95$ m.

It will be assumed that particles on average travel as far as calculated by this simple approach. The landing spot will be calculated as the location where the particles hit the wall, i.e. have travelled a vertical distance equal to the kiln radius. A normal distribution around the landing spot will be assumed for each particle size. The fuel trajectories are based on constant parameters, but in reality they will be influenced by changing conditions as e.g. the kiln gas is heated.

8.8.5.2 Fuel Conversion

When the particles hit the bed or kiln wall it will be assumed that they are converted instantly. As the particles hit the bed, they are likely to be heated very fast, which will quickly release the volatiles to the gas phase. The volatile content may also increase (char yield reduced) due to the higher heating rate. On the other hand, if the particles are covered in the bed, oxygen diffusion to the particles will be severely hindered and char oxidation will be slow. Consequently, this simplification will be more accurate for fuels with a relatively low char content, which is the case for many alternative fuels

Since it is assumed particles drop around the landing spot, with a normal distribution, and the particles are instantly converted, the conversion can be described by the probability density of the normal distribution:

$$\frac{dX}{dx} = \frac{1}{\sigma_{f,drop}\sqrt{2\pi}} * exp\left(-\frac{\left(x - l_{f,drop}\right)^2}{2\sigma_{f,drop}^2}\right) \qquad \text{E 8.75}$$

The normal distribution will integrate to 1, which is convenient as the conversion is bounded between 0 and 1. This equation will be applied both for drying, devolatilization, and char oxidation when fuels enter the bed.

It is assumed that particles drop within a distance of $l_{f,drop2}$ of the average drop spot $l_{f,drop}$. Then the standard deviation can be calculated by E 8.76, and 99.7 % of particles will drop within the interval $[l_{f,drop} - l_{f,drop2};\ l_{f,drop} + l_{f,drop2}]$

$$\sigma_{f,drop} = \frac{l_{f,drop2}}{3} \qquad \text{E 8.76}$$

Using these assumptions, the fuel landing and conversion in the bed can be sketched as shown in Figure 8-9. The probability density function indicates the area around the landing spot, $l_{f,drop}$, where the fuel falls into the bed. The cumulative distribution function describes the fuel conversion, assuming it is instant when fuel enters the bed.

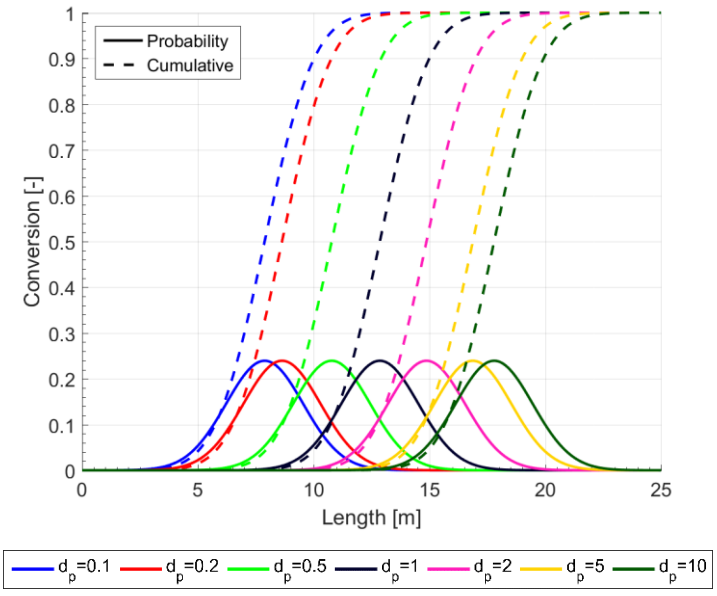

Figure 8-9: Sketch of the landing spot and particle conversion using normal distributions for particles with diameter 0.1-10 mm. Parameters are similar to Figure 8-8.

8.8.6 Gas Phase Reactions

During the devolatilization of the fuel and the char oxidation combustible gasses are released to the gas phase. The combustible volatiles in the model are assumed to be CO and CH_4, which react according to:

$$CO + \frac{1}{2}O_2 \rightarrow CO_2 \qquad \text{R 8.5}$$

$$CH_4 + 2O_2 \rightarrow CO_2 + 2H_2O \qquad \text{R 8.6}$$

As the temperature in the kiln is high, the gas phase reactions are primarily limited by turbulent mixing of the fuel and oxygen eddies. Accordingly, the eddy dissipation concept proposed by Magnussen and Hjertager [244] will be used to describe the combustion.

The model assumes that the combustion rate can be limited by either oxygen availability or fuel availability. The rate of fuel limited combustion is given by:

$$R_{comb,1,i} = K_1 C_i M_i \frac{\epsilon}{k} \qquad \text{E 8.77}$$

Here i indicates the species that can be either CO or CH_4. C_i is the gas concentration, M_i is the molar mass, and the ratio ε/k is the turbulent eddy dissipation rate.

If oxygen availability is limiting the reaction, then the rate is given as:

$$R_{\mathrm{comb},2,i} = K_1 \frac{C_{O2} M_{O2}}{\phi_{m,O2,i}} \frac{\epsilon}{k} * \left(\frac{C_i M_i * \phi_{m,O2,i}}{\sum_{j=1}^{Nreactants} C_j M_j * \phi_{m,O2,j}} \right) \qquad \text{E 8.78}$$

The reaction rates are expressed in units [kg/(m^3s)]. K_1 is a constant with an assumed value of 4 and ϕ_m is the stoichiometric coefficient for the reaction [kg oxygen/kg fuel].

The reaction rate of fuel combustion is determined by the lowest of the above rates:

$$R_{comb,i} = min(R_{comb,1,i}, R_{comb,2,i}) \qquad \text{E 8.79}$$

8.8.6.1 The Eddy Dissipation Rate

The turbulent dissipation rate is determined based on the CFD simulations of the full-scale rotary kiln, which were also used to derive parameters for the jet expansion (see chapter 8.6.5). The average eddy dissipation rate inside the jet is calculated and shown in Figure 8-10. The rate is very high close to the burner where

the gas velocities are high, while it decreases further from the burner as the gas velocities are decreased.

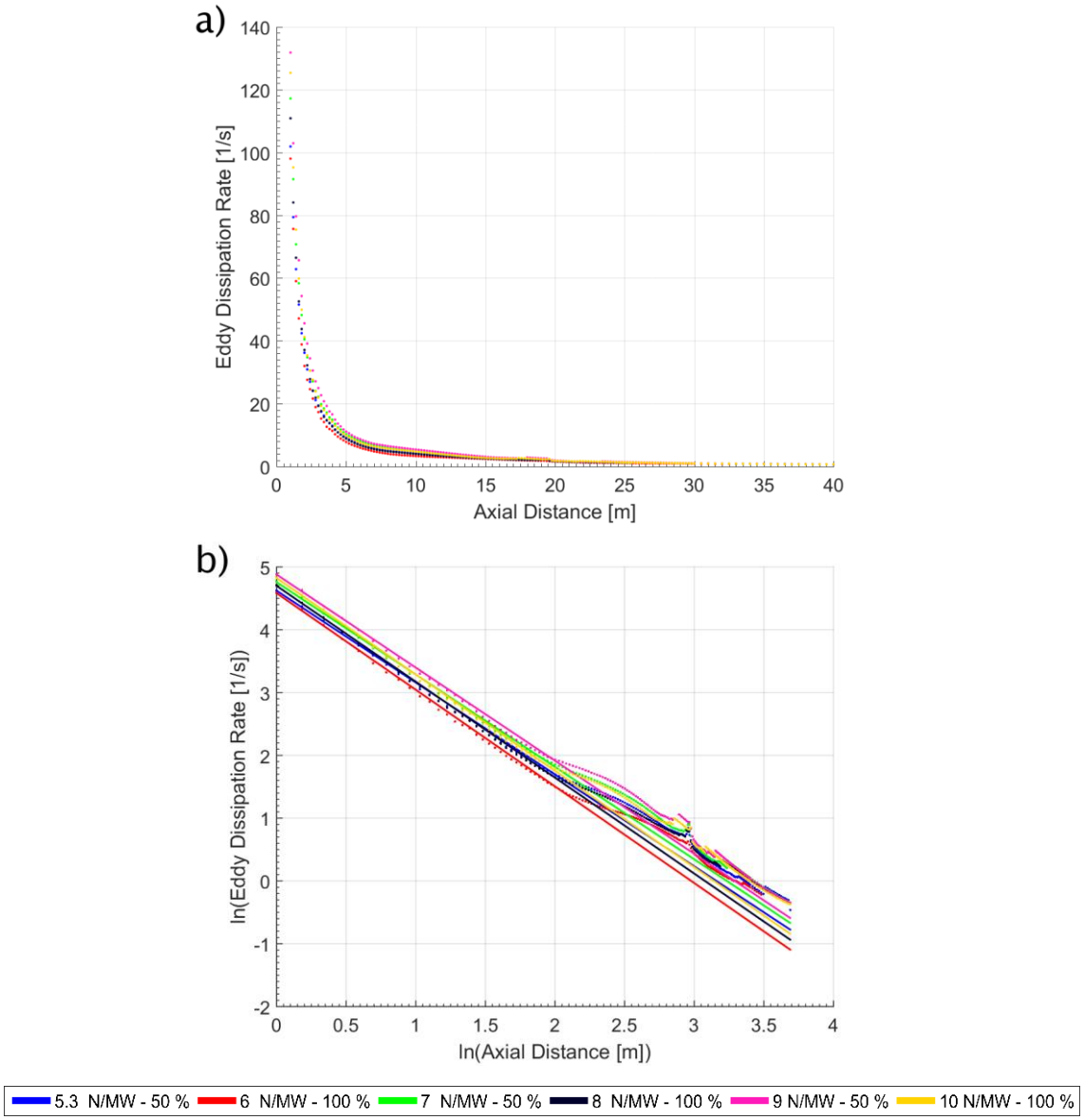

Figure 8-10: The eddy dissipation rate as function of distance from the burner in the kiln. a) Normal data, b) log transformed data. Data derived from CFD simulations of a petcoke flame performed by David Isaac.

In a log-log plot, Figure 8-10b, the data are approximately linear as long as the jet spreads linearly (compare with Figure 8-6), up to around 7 m. Thus, the eddy dissipation rate can be described as:

$$\frac{\epsilon}{k} = K_{edr,1} * x^{K_{edr,2}} \qquad \text{E 8.80}$$

The values of $K_{edr,1}$ and $K_{edr,2}$ can be found in Table 8-5. It is seen that the eddy dissipation rate increases with the axial momentum of the burner and decreases when the swirl is increased. This is likely caused by a lower axial velocity for the higher level of swirl.

Table 8-5: Momentum and swirl number in CFD simulations and corresponding values of $K_{edr,1}$ and $K_{edr,2}$.

Momentum (N/MW)	Swirl Level (%)	Swirl Number	$K_{edr,1}$	$K_{edr,2}$	$K_{edr,1}$ by E 8.81	$K_{edr,2}$ by E 8.82
5.3	50	0.18	102	-1.46	104	-1.47
6	100	0.35	97.7	-1.54	96.2	-1.53
7	50	0.20	116	-1.47	115	-1.47
8	100	0.36	110	-1.53	110	-1.54
9	50	0.20	131	-1.48	130	-1.48
10	100	0.35	124	-1.54	126	-1.54

The values of the constants $K_{edr,1}$ and $K_{edr,2}$ can be determined by a multilinear regression based on the axial momentum and the swirl number:

$$K_{edr,1} = 78.9 + 7.39 * I' - 77.1 * S \qquad \text{E 8.81}$$

$$K_{edr,2} = -1.39 - 1.46 * 10^{-3} * I' - 0.372 * S \qquad \text{E 8.82}$$

According to this regression model the eddy dissipation rate, $K_{edr,1}$, increases with the axial momentum and decreases with the swirl number. The rate at which the eddy dissipation decreases further from the burner, $K_{edr,2}$, is decreased by both momentum and swirl. The values of the two constants calculated using E 8.81 and E 8.82 are shown in Table 8-5.

8.8.7 Combustion Model Approach

Solid fossil fuels such as coal or petcoke are fairly homogenous. Thus, in the model the only difference between two coal particles will be the size difference. The model is equipped to handle different particle sizes, which can be designated as a discrete distribution. This has been done based on a Rosin-Rammler distribution [172,173], divided into 10 discrete particle sizes.

In comparison SRF is highly heterogenous, consisting of different materials, as outlined in chapter 3.4.1. The main parts of the combustible fractions can be derived into biomass, paper & cardboard, plastics, and textiles (see Figure 3-3).

In the experimental section, covered in chapter 7, it was discussed how accounting for only biomass and plastic combustion is sufficient to describe the combustion of SRF. A detailed physical characterization was made of two SRF samples, where the size distribution of biomass and plastics have been determined. These data will be used as input to the model for the size characterization of the SRF.

For the combustion reactions the plastic will be assumed to behave as polyethylene and the model proposed recently by Nakhaei et al. [232] will be implemented here. For the polyethylene an isothermal model predicts devolatilization times within a 20 % error compared to a more rigorous 1D-model. Thus, the isothermal particle model will be used here.

The model for the biomass combustion is as described in the previous subchapters 8.8. The model is validated against experimental data collected from the literature in Appendix E. The results indicate that the same conversion kinetics can be used for a large range of different wood types and sewage sludge. The reason being that heat transfer and oxygen diffusion limits the devolatilization and char oxidation, rather than kinetics. As long as particles have diameter in the range of millimeters, it seems justified to apply the same kinetics to different alternative fuels, as long as they follow the general steps of drying, devolatilization, and char oxidation.

A comparison of using an isothermal and a 1-D model for predicting biomass devolatilization times of particles in the range 0.1-20 mm can be found in Appendix F. Significant errors can be made by assuming isothermal particles. The difference between the models increases as the particle diameter and the gas phase temperature surrounding the particle is increased. For particle above 10 mm, the isothermal devolatilization time may be only 10 % of the non-isothermal time. Nevertheless, for the kiln model it was found that an isothermal model could be applied without significant error. It is assumed that alternative fuels can drop into the bed and burn there (see chapter 8.8.5). The largest particles will mainly burn in the bed rather than in suspension, making the heating rate negligible. Accounting for non-isothermal particles increases model convergence time by approximately a factor of three and does not change the results significantly. Consequently, isothermal particles were assumed in the model results presented later in chapter 9.

The effects of particle shape are included by accounting for the sphericity in the particle temperature (E 8.53-E 8.55) and char oxidation equations (E 8.68). The equations have been derived for spherical particles. In the case where the particles are not spherical, the particle equivalent diameter is used instead of the actual diameter. The inclusion of sphericity in the heat transfer and char oxidation equations accounts for the higher surface area of non-spherical particles compared to their spherical counterparts. The result is that the effective particle surface area for heat transfer and char oxidation is increased by a factor $1/\varphi$.

8.9 Gas Properties in the Kiln Model

The estimation of physical properties is an important part of the model. They e.g. influence the convective heat transfer in the kiln as outlined in chapter 8.7.1 . This is especially true for the gas phase where large differences in temperature and composition are expected.

The heat capacity of the gas will change both according to temperature and the gas composition. However, it has been elected to keep it constant for simplicity. The value applied in the model will be assumed equal to that of the initial heat capacity of the secondary air. The initial heat capacity will be calculated based on data from the National Institute of Standards and Technology [241], using the following correlation:

$$Cp_g = \frac{1}{M_g}\sum_{i=1}^{N} y_i\left(K_{1,i} + K_{2,i} * \frac{T_g}{1000} + K_{3,i} * \left(\frac{T_g}{1000}\right)^2 + K_{4,i} * \left(\frac{T_g}{1000}\right)^2 + K_{5,i} * \left(\frac{T_g}{1000}\right)^{-2}\right) \quad \text{E 8.83}$$

The density will be calculated based on the ideal gas law:

$$\rho_g = \frac{p}{RT_g}\sum_{1}^{N_g} M_i * y_i \quad \text{E 8.84}$$

The viscosity is determined based on the following expression used by Guo et al. [245].

$$\mu_g = 0.1672 * 10^{-5} * \sqrt{T_g} - 1.058 * 10^{-5} \quad \text{E 8.85}$$

The thermal conductivity is based on the following polynomial proposed by Thunman and Leckner [246]. The data are valid for atmospheric air in the range 250-3000 K.

$$\lambda_g = -7.494 * 10^{-3} + 1.709 * 10^{-4} * T_g - 2.377 * 10^{-7} * T_g^2 + 2.202 * 10^{-10} * T_g^3 - 9.463 * 10^{-14} * T_g^4 + 1.581 * 10^{-17} * T_g^5 \quad \text{E 8.86}$$

For the char oxidation it is important to determine the diffusivity of oxygen and water (see E 8.71). The constants can be calculated by the Fuller-Schettler-Giddings approach based on diffusion volumes [247]:

$$D_i = 1 * 10^{-7} * T_g^{1.75} * \frac{\sqrt{\left(\frac{1}{M_i * 1000} + \frac{1}{M_{air} * 1000}\right)}}{\left(\frac{p}{1.01325 * 10^5} * V_{diff,i}^{1/3} * V_{diff,air}^{1/3}\right)^2} \quad \text{E 8.87}$$

D is the diffusion coefficient [m²/s], T_g is the gas temperature, M the molar mass, p the pressure, and V_{diff} is the diffusion volume [cm³/mol]. The coefficients on the molar mass and the pressure are to recalculate into [g/mol] and [atm] units, which are the units used by Fuller, Schettler, and Giddings [247].

The values of viscosity, heat conductivity, and diffusion coefficients are determined for air. Some error can thus be expected, since the gas composition in the kiln is different following combustion.

The emissivity of the gas for radiation is determined by the Weighted Sum of Grey Gasses (WSGG) model. The method described by Johansson et al. [248] will be used here. It is assumed that only H_2O and CO_2 contribute to the emissivity of the gas.

$$\epsilon_g = \sum_{j=0}^{N_{gas}} a_j (1 - exp\left(-\kappa_j l_m (p * 10^{-5})(y_{H_2O} + y_{CO2})\right) \quad \text{E 8.88}$$

$N_{gas} = 4$ components are used here. In the equation a is a weighting factor in the WSGG model and κ is an absorption coefficient, p is the pressure. Details of how these are calculated will not be presented here, but can be looked up in the source [248]. l_m is the total path length for radiation. It will be assumed that the value for an infinite cylinder can be used here [229]:

$$l_m = 0.95 d_k \quad \text{E 8.89}$$

For the radiation model proposed in chapter 8.7.3 it will be assumed that the secondary air does not absorb radiation, since it does not contain H_2O or CO_2. However, it will contain entrained clinker dust that could affect radiation [196], but this effect will be neglected here.

8.10 Energy and Mass Balances in Kiln

The following chapter will describe the final equations to determine gas and bed temperatures in the kiln, based on energy and mass balance considerations. The equations are derived for changes in the axial direction of the kiln. Detailed derivations can be found in Appendix G.

8.10.1 Temperature in Clinker Bed

A sketch of the different heat sources to a section of the bed is shown in Figure 8-11. This approach is used to derive the energy balance and the temperature equation for the bed. At the left boundary, clinker enters at one temperature and a given fraction of melt, and it exits at the right boundary at a second temperature and melt fraction. Inside the section, energy is lost as CO_2 leaves the bed (1), heat is released or consumed by the clinker reactions (2), and heat is transferred to or from the bed (3).

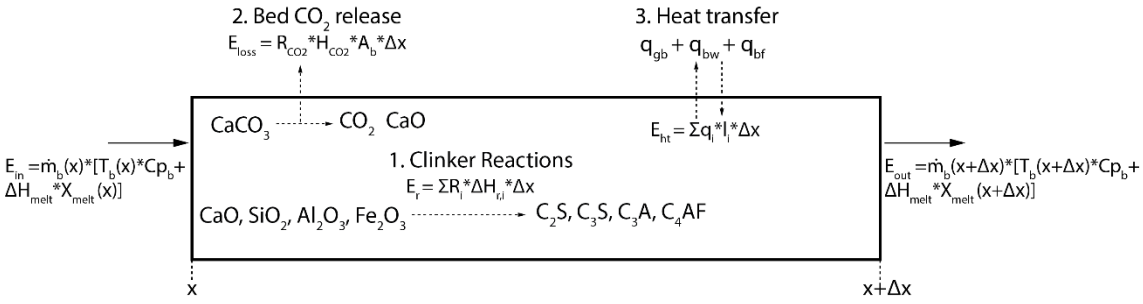

Figure 8-11: The energy sources in a section of the bed used to derive the temperature equation for the bed.

In Figure 8-11 and E 8.90 E is energy, T_b is the bed temperature, x is the axial distance in the kiln, Cp_b the bed heat capacity, $\dot{m}_b$ the mass flow of clinker, R the reaction rate of the i'th reaction [kg/m^{3}s], ΔH the enthalpy for reactions or melting, A_b the cross sectional area of the bed, q the heat flux to the bed, I the contact area of the bed (e.g. between gas and bed), and M is the molar mass.

The temperature in the bed can be described by the following equation:

$$\frac{d}{dx}T_b = \frac{1}{\left(Cp_b + \frac{\Delta H_{melt} * X_{melt,max}}{T_{melt,2} - T_{melt,1}}\right)} \frac{1}{\dot{m}_b} \left(\underbrace{\sum_i^{N_r} R_i * \Delta H_{r,i} * A_b}_{1} + \underbrace{(\Delta H_{melt} * X_{melt}) * R_1 * \frac{M_{CO2}}{M_{CaCO3}} A_b}_{2} + \underbrace{\sum_i^{N_{ht}} q_i * l_i}_{3} \right) \quad \text{E 8.90}$$

On the right-hand side of the equation term 1 describes the heat from the endothermic and exothermic clinker reactions. Term 2 accounts for enthalpy changes of melting where CO_2 leaves the bed, and term 3 describes the heat transfer to the bed.

It is assumed that the bed will begin to melt as it reaches a certain temperature, $T_{melt,1} = 1280$ °C [217]. Upon further heating the bed will continue to melt, with the melt fraction increasing linearly to an upper temperature, $T_{melt,2} = 1450$ °C.

$$X_{melt} = X_{melt,max} * \frac{T_b - T_{melt,1}}{T_{melt,2} - T_{melt,1}} \quad \text{E 8.91}$$

The C_3A and C_4AF phases form most of the melt phase in the kiln. Typically, around 20 % of the clinker will melt in the kiln [249]. For bed temperature above $T_{melt,2}$ the melt fraction is capped to the value of $X_{melt,max}$.

8.10.2 Temperature in Gas Phase

A section of the gas phase is shown in Figure 8-12. The sketch shows the different energy source terms used to derive the heat balance in the gas phase. In the gas phase, energy is entrained with the secondary air (1), CO_2 is released from the bed (2), gasses are released from the fuel (3), heat is transferred to and from the gas (4), and heat is released from the combustion reactions (5).

In Figure 8-12 and E 8.92 E is energy, T_g is the gas temperature, x is the axial distance in the kiln, Cp_g the gas heat capacity, $\dot{m}_g$ the mass flow of gas, and R [kg/m^{3}s] denotes rate of entrainment, CO_2 release, gas release from the fuel, and reactions. H indicates enthalpy and ΔH the enthalpy for reactions, A_g and A_b the cross sectional area of the gas and bed, q the heat flux to the gas, and l the contact area of the gas (e.g. between gas and bed).

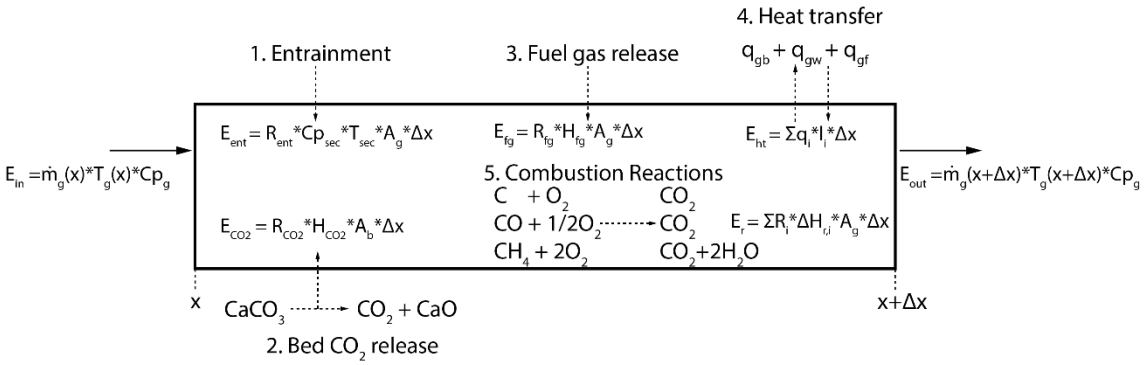

Figure 8-12: The energy sources in a section of the gas phase used to derive the temperature equation for the gas phase.

The gas phase temperature is determined based on the following equation.

$$\frac{d}{dx}T_g = \frac{1}{\dot{m}_g * Cp_g}\left[\underbrace{R_{ent} * H_{sec} * A_g}_{1} + \underbrace{R_{CO2} * H_{CO2} * A_b}_{2} + \underbrace{R_{fg} * H_{fg} * A_g}_{3} + \underbrace{\sum_i^{N_{ht}} q_i * l_i}_{4} + \underbrace{\sum_i^{N_r} R_i * \Delta H_{r,i} * A_g}_{5} - \underbrace{\frac{d}{dx}(\dot{m}_g)Cp_g * T_g}_{6}\right] \quad \text{E 8.92}$$

On the right-hand side of the equation term 1 describes the energy obtained as secondary air is entrained into the jet, term 2 as CO_2 is released from the bed to the gas phase. Term 3 accounts for the release of gasses from the fuel. Term 4 describes the heat transfer to and from the gas and term 5 the heat released in the combustion reactions. Term 6 account for changes in the energy as the mass flow rate is changed.

8.10.3 Mass Flow in Clinker Bed

It will be assumed that the mass flow of clinker is constant throughout the kiln, except for the mass loss due to calcination. This loss is given as:

$$\frac{d\dot{m}_b}{dx} = v_b \frac{d\rho_b}{dx} * A_b = -R_1 * \frac{M_{CO2}}{M_{CaCO3}} * A_b \quad \text{E 8.93}$$

8.10.4 Mass Flow in Gas Phase

The mass flow in the gas phase changes due to entrainment of secondary air, release of volatiles during drying, devolatilization, and char oxidation, and release of CO_2 as residual limestone in the clinker is calcined. The overall balance can be written as:

$$\frac{d\dot{m}_g}{dx} = A_g\left(R_{ent} + R_{dry} + R_{devol} + R_{char} + R_1 * \frac{M_{CO2}}{M_{CaCO3}} * \frac{A_b}{A_g}\right) \qquad \text{E 8.94}$$

In addition to the overall mass balance, the gas components N_2, O_2, CO_2, H_2O, CO, and CH_4 will be tracked in the kiln. The combustion air is assumed to be atmospheric air consisting of N_2 and O_2. During combustion, O_2 will be consumed while the different combustion products are released. Minor species in the fuel and gas phase such as N, S, and Cl, will not be tracked. The following balances are written on a molar basis.

The N_2 flow in the primary jet is changed due to entrainment of secondary air:

$$\frac{d\dot{n}_{N2}}{dx} = A_g * R'_{ent} * y_{N2,sec} \qquad \text{E 8.95}$$

Oxygen is entrained into the flame and used up during combustion of char, CO, and CH_4:

$$\frac{d\dot{n}_{O2}}{dx} = A_g * \left(R'_{ent} * y_{O2,sec} - R'_{char,ox}\phi_{char} - R'_{CO,ox}\phi_{CO} - R'_{CH4,ox}\phi_{CH4}\right) \qquad \text{E 8.96}$$

CO_2 is formed from the oxidation of CO and CH_4, but can also be released from the clinker during calcination:

$$\frac{d\dot{n}_{CO2}}{dx} = A_g * \left(R'_{CO,ox} + R'_{CH4,ox} + R_1 * \frac{1}{M_{CaCO2}}\frac{A_b}{A_g}\right) \qquad \text{E 8.97}$$

H_2O is released during the drying of the fuel and the combustion of CH_4:

$$\frac{d\dot{n}_{H2O}}{dx} = A_g * \left(\frac{R_{dry}}{M_{H2O}} + 2R'_{CH4,ox}\right) \qquad \text{E 8.98}$$

CH_4 is released during devolatilization and removed through combustion:

$$\frac{d\dot{n}_{CH4}}{dx} = A_g * \left(\frac{Y_{\text{vol},CH4}}{M_{CH4}}R_{devol} - R'_{CH4,ox}\right) \qquad \text{E 8.99}$$

CO is released during devolatilization and char oxidation, and then removed as it is oxidized into CO_2 in the gas phase reactions.

$$\frac{d\dot{n}_{CO}}{dx} = A_g * \left(\frac{Y_{vol,CO}}{M_{CO}} R_{devol} + R'_{char,ox} - R'_{CO,ox}\right) \quad \text{E 8.100}$$

In the above equations reaction rates denoted R are on a mass basis [kg/m^3/s] and rates denoted R' are on a molar basis [mol/m^3/s]. ϕ is the stoichiometry for the combustion reactions [mol O_2/mol fuel]. Y is mass fraction, y is mole fraction, A_g and A_b are the cross-sectional area of the gas and bed, M is molar mass, $\dot{m}$ is mass flow, and $\dot{n}$ is molar flow.

8.11 Model Solution Procedure

The model is solved using Matlab R2015b, where the differential equations are solved using the stiff ODE solver ode15s [250].

Due to the counter current flow of the gas and bed, the model is divided into two parts one for the gas phase and one for the bed phase. This is necessary since it is not feasible to calculate the extent of clinker reactions backwards with respect to time. The model for the gas phase includes the equations for the primary air, secondary air, fuel, and shell and wall temperatures. The model for the bed phase includes bed temperatures and clinker reactions.

Initially, the model part for the gas phase is solved assuming no reactions in the bed phase. The initial conditions, e.g. air and fuel flow rates and temperatures, are known at the burner end (kiln clinker outlet), while the temperature of the pre-calcined raw meal is known at the other end of the kiln (raw material inlet). Thus, initially an outlet temperature of the clinker is guessed, and a number of iterations are performed until the inlet temperature matches the initial condition. This is done by utilizing the shooting method [251].

An example is shown in Figure 8-13. In this case the inlet raw material temperature is known to be 830 °C, and the clinker outlet temperature is guessed to be 1327 °C. This temperature, however, results in an inlet temperature of 769 °C, which is lower than the actual temperature of 830 °C. In the second iteration the guess on the outlet temperature is increased. This then results in an inlet temperature that is too high. Additional iterations are performed until the guessed clinker outlet temperature yields an appropriate raw meal inlet temperature, within 10 °C of the actual inlet value.

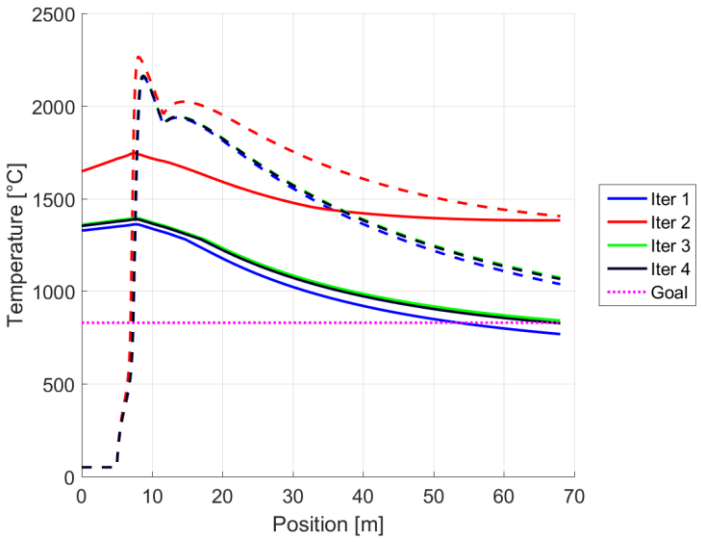

Figure 8-13: Example of the iterative procedure (shooting method) to find initial solution of the gas and bed temperature. Solid line indicates bed temperature and dashed line indicates gas temperature.

After the initial temperature profiles have been found, the clinker reactions are added to the bed. This changes the bed temperature due to heat release and consumption in the clinker reactions. This also has an effect on the gas temperature, since the heat transfer is dependent on the bed temperature. Furthermore, the calcination of residual limestone can change the gas flow, as CO_2 is released from the bed into the gas phase.

The solution is performed in an iterative procedure, where the coupling between the bed and gas phase is handled by successively solving the model for the gas phase followed by the model for bed phase. The iterations are assumed to have reached convergence after a minimum of 4 iterations and when the average gas and bed temperature changes less than 3 K upon successive iterations.

An example of the different solutions is shown in Figure 8-14. The initial gas temperature is found assuming no reactions in the clinker phase. When clinker reactions are added (dashed blue line), the temperature of the bed rapidly increases around 30 meters as belite (C_2S) is formed. As the bed temperature is now higher, the heat transfer between gas and bed is changed, and the gas temperature also becomes higher, which in turn affects the bed temperature, etc. After convergence the temperatures stabilize at levels that are slightly higher than the initial temperatures.

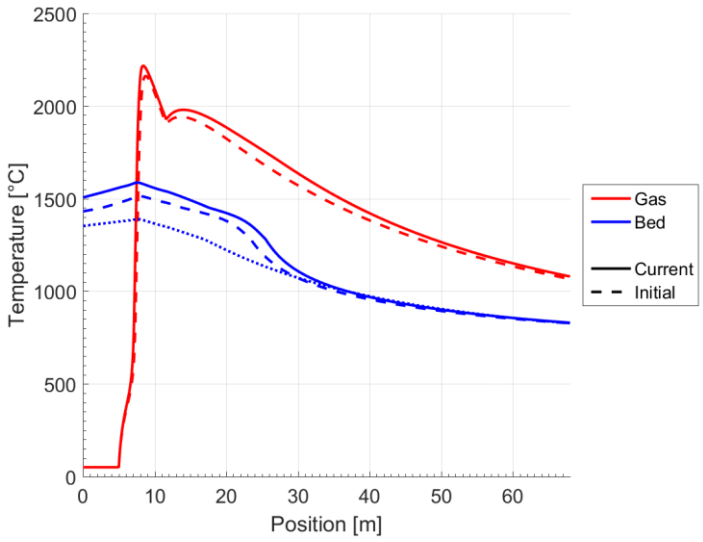

Figure 8-14: The temperature profiles in the gas and bed phase before (dashed lines) and after convergence (solid lines) has been reached. Bed temperature without clinker reactions (dotted line) is also shown.

8.12 Summary and Conclusions

The review of the literature revealed that many research groups have made a concerted effort to model the different processes in the cement kiln. However, only a few works have dealt with the combustion of alternative fuels in the cement kiln, and none of this work has attempted to couple the combustion models to the clinker chemistry and quality. Consequently, the kiln model developed here includes a simple model for the clinker formation. The burner settings may also have a significant impact on the kiln flame, which was also accounted for in the model.

Many processes occur in the cement rotary kiln at the same time, these include: solid movement, clinker reactions, air flow and mixing, heat transfer, and combustion. A brief review of these mechanisms has been given, and simplified models have been proposed to account for the different processes. These sub-models were combined to yield a model for the cement kiln. The kiln model is able to calculate temperature profiles in the kiln and estimate the clinker phase composition. The model will be validated and tested in chapter 9.

9 Model Validation and SRF Co-Firing

The purpose of this chapter is to present model simulation results and behavior and to test the developed model. The model will be validated against literature results obtained in a pilot scale kiln as well as results obtained in an industrial kiln. Afterwards, the model will be used to investigate the impact of co-firing SRF.

9.1 Model Validation – Pilot Scale

The model is first validated against measurements from the Cemflame 3 experiments carried out at the IFRF (International Flame Research Foundation), which were also briefly described in chapter 3.5.1. These are to the author's knowledge the most detailed measurements available in a pilot-scale rotary kiln. While the pilot scale measurements do not include a clinker bed, they contain more detailed measurements of gas phase temperatures and composition, than what can be obtained in a full-scale plant. Thus, they provide a basis for validating the combustion part of the kiln model.

9.1.1 The Cemflame 3 Experiments

The Cemflame 3 experiments are described by Haas et al. [80]. The goal was to evaluate the effect of co-firing coal with different alternative fuels, such as sewage sludge and plastic waste. The 4 main objectives were detailed as follows:

1. To assess different co-firing fuel types for use in cement and lime kilns and to give recommendations for their optimum application.
2. To maximize the co-firing ratio of alternative fuels in a kiln whilst maintaining acceptable combustion (heat transfer) performance.
3. To identify flame characteristics for cement kiln flames when co-firing alternative fuels.
4. To evaluate the effect of oxygen boosting in a cement kiln.

9.1.2 Experimental Facilities

Experiments were made in a pilot scale cement kiln simulator of 9 m length and 0.78 m in diameter. The kiln was refractory lined to maintain high temperatures and was equipped with a burner with a thermal input of 2 MW. A pre-combustor unit supplied hot combustion air (900 °C) as secondary air to the kiln.

A series of detailed measurements were made on a coal flame as reference, while the measurements on alternative fuels co-firing are less detailed. For the coal flame, temperatures, gas composition, and burnout were measured along the centerline of the flame, and at various cross sections.

The kiln does not contain a clinker bed, and the experiments can thus only be used to validate the temperature and reactions in the suspended gas phase. The kiln model is thus slightly adjusted to not contain the bed.

9.1.3 Experimental Results

Selected results of the coal flame measurements are shown in Figure 9-1 and Figure 9-2. Figure 9-1 shows measurements in the gas phase taken along the axial centerline of the flame, while Figure 9-2 shows wall temperatures for the baseline coal flame as well as several co-firing scenarios with varying amounts of plastic foils. The wall temperature derived from Figure 9-2 is used as input to the model, instead of calculating the wall temperature based on a heat balance through the wall.

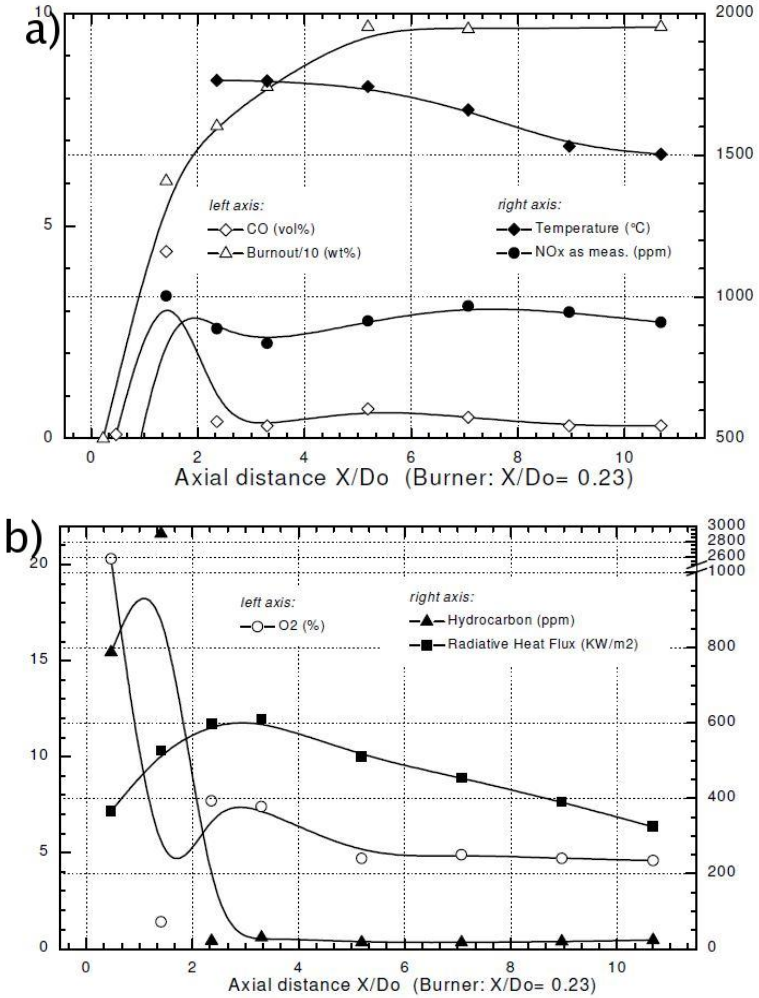

Figure 9-1: Measurements along the axial centerline of the kiln flame. a) CO concentration, burnout, gas temperature and NOx concentration. b) oxygen concentration, hydrocarbon concentration, and radiative heat flux upon the kiln walls [80].

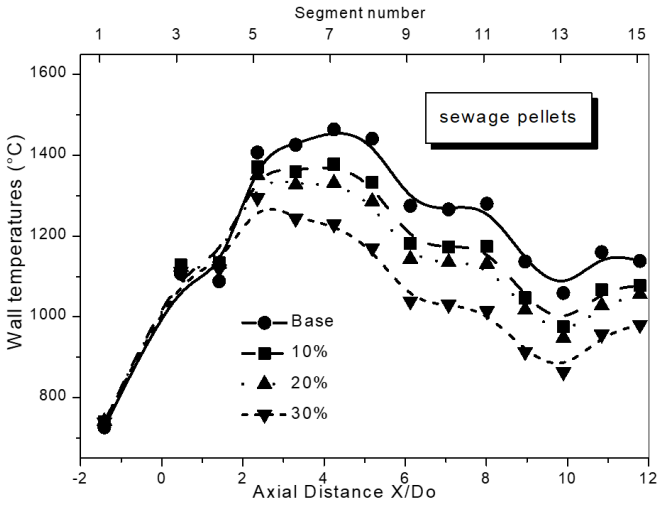

Figure 9-2: Kiln wall temperatures of baseline coal flame experiments and co-firing with different amounts of plastic foils in % of the energy input [80].

The size of the fuel is detailed in Figure 9-3a. The data for the fetnuss coal was extracted from the figure and fitted to a Rosin-Rammler plot in Figure 9-3b.

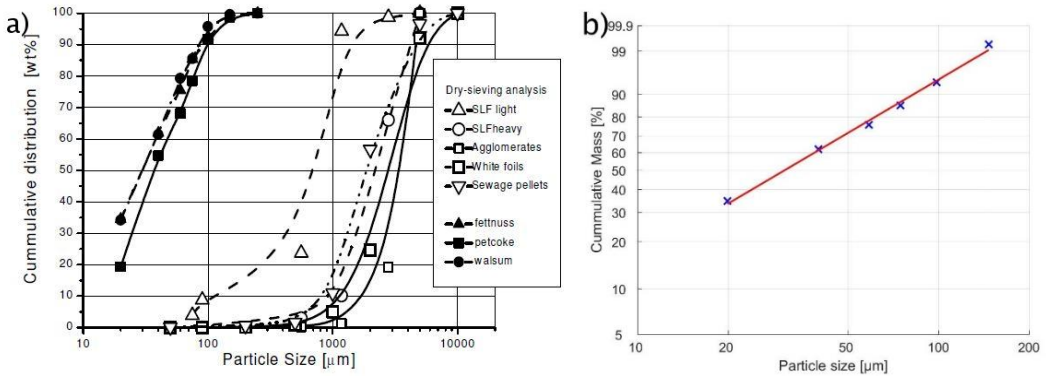

Figure 9-3: a) Size distribution of fuel as reported in the Cemflame experiments [80]. b) Rosin Rammler plot of the fetnuss coal size distribution.

The Rosin Rammler distribution is given in equation E 9.1. The cumulative mass, Cm_{RR}, for a given particle size, d_p, can be described by the 63rd percentile, d_{RR}, and the spread, n_{RR}. The parameters for the size distribution were fitted as $d_{RR} = 41.6$ µm and $n_{RR} = 1.22$. In the model 10 discrete particle sizes will be used, based on the fitted distribution.

$$\boldsymbol{Cm_{RR}(d_p) = 100 - \left(100 * exp\left(-\left(\frac{d_p}{d_{RR}}\right)^{n_{RR}}\right)\right)} \qquad \textbf{E 9.1}$$

9.1.4 Model Input Parameters

The operating parameters that are used to model the Cemflame coal flame are listed in Table 9-1. The coal flame measurements are based on a medium volatile fetnuss coal with the proximate composition as stated in Table 9-1. Additional 0.06 MW of natural gas is used to support the flame, but this will be neglected in the model, as the energy input is very low.

Not all necessary model input parameters are stated in the Cemflame report. Thus, Table 9-2 defines some additional parameters that are used in the model. These numbers are estimated based on information available in the Cemflame report, or taken from elsewhere, if necessary. They include for instance the kinetics of drying and devolatilization of the coal. In addition, some assumptions are made on inlet primary air and fuel temperatures, which are not stated in the Cemflame report.

Table 9-1: Model parameters used to model the Cemflame experiments.

	Unit	Value
Fuel Composition		
Volatiles	wt% dry	24.25
Char	wt% dry	72.84
Ash	wt% dry	2.79
Moisture	wt% a.r.	0.64
Fuel Properties		
Density	kg/m^3	1336
Lower Heating Value	MJ/kg dry	33.97
Preexponential factor for char oxidation	$kg/(m^2\ s\ Pa)$	0.01
Activation energy for char oxidation	J/mol	$105*10^3$
Kiln Parameters		
Inner Diameter	m	0.78
Length	m	9
Burner Diameter	m	0.22
Secondary air flow	kg/h	2720
Secondary air temperature	°C	900
Initial oxygen concentration of gas	mol%	20.9
Burner Firing and Air		
Energy Input	MW	1.94
Coal Feed	kg/h	210
Axial Air	kg/h	62.5
Swirl Air	kg/h	62.5
Transport Air	kg/h	75

It is stated in the report that the simulated secondary air is generated by combustion of natural gas in a pre-combustion chamber. The oxygen content is then adjusted to 20.9 mol%. The remaining composition is not stated, and it will be assumed in the simulations that the remaining gas is nitrogen. In reality, significant amounts of CO_2 and H_2O will be present in the gas due to the combustion in the pre-combustion chamber.

The burner momentum and swirl number during the baseline experiments are not stated. Elsewhere in the report it is stated that experiments were performed at 3.1 N/MW (low momentum) and 4.1 N/MW (high momentum) and swirl numbers up to 0.55. It will be assumed that the momentum was 3.1 N/MW and the swirl number 0.24. For the sake of simplicity, the heat capacity of the two gas phases were assumed constant in the calculations. The heat capacity in Table 9-2 for the secondary air is calculated for air at 900 °C, while the value for the primary air was evaluated as the average heat capacity of air and flue gas at 1500 °C.

Table 9-2: Estimated input parameters for to model the Cemflame experiments. Parameters marked by * have been assumed.

Parameter	Unit	Value	Reference
Fuel parameters			
Fuel particle emissivity	-	0.9	[31]
Fuel heat capacity	J/kg/K	1400	[31]
Initial temperature of fuel	°C	50	*
Preexponential factor for drying of coal	1/s	$5.13*10^6$	[31]
Activation energy for drying of coal	J/mol	$87.9*10^3$	[31]
Preexponential factor for devolatilization of coal	1/s	$9.59*10^4$	[31]
Activation energy for devolatilization of coal	J/mol	$82.6*10^3$	[31]
Primary and secondary air parameters			
Temperature of primary air	°C	50	*
Initial nitrogen concentration of gas	mol %	79.1	*
Heat capacity of primary air	J/kg/k	1290	*
Heat capacity of secondary air	J/kg/k	1179	*
Burner Momentum	N/MW	3.1	*
Burner Swirl Number	-	0.24	*
Other parameters			
Wall Emissivity	-	0.8	[31]

9.1.5 Model Results

The model and experimental results from the Cemflame 3 experiments are compared in Figure 9-4 and Figure 9-5. It should be noted that the experimental points have been shifted by $x/d_k = 0.23$, to set the burner tip at $x/d_k = 0$ (compared to Figure 9-1 and Figure 9-2). As input to the model the wall temperature was derived from Figure 9-2. The experimental data were smoothed using a moving average filter with a window size of 10 and local regression using a 2nd degree polynomial (Matlab function 'smooth' with method 'loess'). This significantly reduces the data scatter giving the red line in Figure 9-4a.

Figure 9-4a shows the temperatures of the gas and wall. Figure 9-4a shows 'peak' temperatures, which are measured at the axial centerline of the flame, while the 'average' temperatures are arithmetic means based on traverses through the flame. The model shows a rapid increase in the flame temperature as secondary air is entrained into the primary air jet and as the volatiles are burned. This gives a peak temperature of close to 2100 °C, which is somewhat above the measured values. As combustion takes place the flame temperature exceeds that of the secondary air, and the flame will be cooled as the remaining secondary air is entrained into the flame.

At $x/d_k = 2$, the secondary air is fully entrained, which gives a bend in the temperature profile, where it starts to increase again as combustion of the char takes place. From $x/d_k = 2.5$, most of the combustion has already occurred and the temperature begins to decrease as heat is lost to the wall. The temperature predicted by the model decreases slightly faster than what has been measured, but the temperature is generally in the correct range.

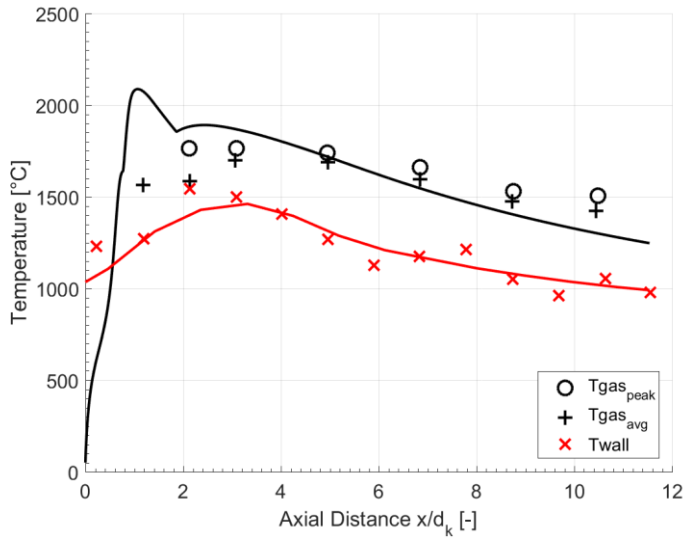

Figure 9-4: Comparison of measurements and model predictions of the gas temperature through the kiln simulator of the Cemflame experiments [80]. Lines are model and markers are experimental points. The peak temperatures are measured at the axial centerline of the flame. The average temperatures are the mean based on traverses in radial direction through the flame.

Figure 9-5 shows the measurements and model predictions of selected gas phase components and the fuel burnout. In the model the only hydrocarbon is CH_4, while others (although not specifically stated) are measured in the Cemflame experiments. The fuel burnout is in the model defined as the total conversion, which is the weighted average of drying, devolatilization, and char oxidation:

$$X_{tot} = \frac{Y_{H2O} * X_{dry} + Y_{vol} * X_{devol} + Y_{char} * X_{char}}{Y_{H2O} + Y_{vol} + Y_{char}} \qquad \text{E 9.2}$$

The total conversion is calculated for each particle size and averaged over the 10 different particle sizes used in the model to give the burnout plotted in Figure 9-5a. The conversion of the individual particles is shown in Figure 9-5b.

Based on the model it can be seen that volatiles are released, and small particles undergo char oxidation within 1-2 kiln diameters. This results in a rapid consumption of oxygen, resulting in a low oxygen content at $x/d_k = 1$. A small peak in CO and CH_4 concentration is also observed. In the experiments a higher CO peak and lower oxygen concentrations were measured, than what the model predicts. This may be because concentrations are measured at the center of the flame, where oxygen depletion can occur, while the model predicts an average for the cross section. The oxygen concentration increases and the CO and CH_4 is converted as the remaining secondary air is entrained into the flame. The model mixing is predicted to $x/d_k \sim 2$, which corresponds well to the measured local maximum in oxygen concentration. The oxygen concentration then decreases through the rest of the kiln as char oxidation of the larger coal particles take place.

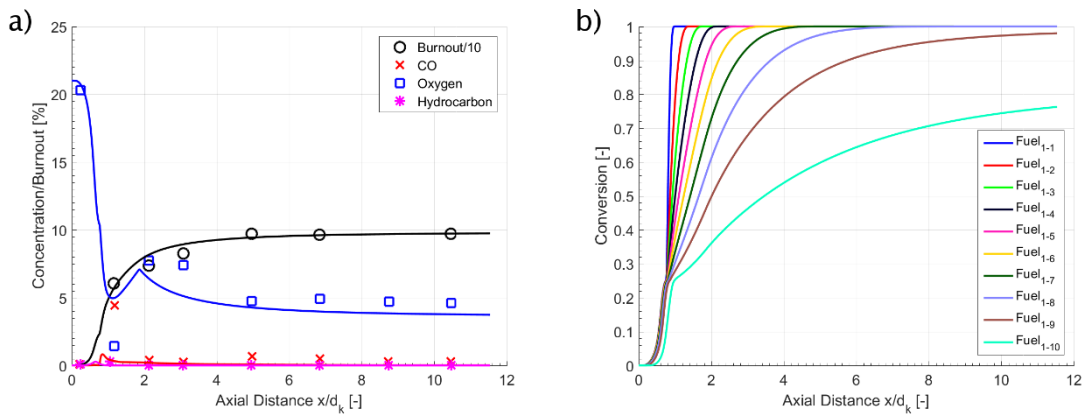

Figure 9-5: a) Comparison of measurements and model predictions of gas concentration of CO, oxygen, and hydrocarbons (CH_4) and average fuel burnout of the Cemflame experiments [80]. Lines are model and markers are experimental points. b) Conversion of the 10 discrete fuel sizes according to model.

The model predicts an average burnout that appears to match the experimental trend well as seen in Figure 9-5a. The 10 discrete fuel particle sizes show that the size does not influence drying and devolatilization particularly, which is completed within 1 kiln diameter yielding a conversion of 0.25. For the larger particle char oxidation takes much longer, and the two largest particle size groups ($d_p = 70$ and 110 µm) are not completely converted within the kiln as seen in Figure 9-5b.

It should be noted that the measurements are taken along the axial centerline of the flame. In comparison, the model calculates average temperatures and concentrations in the cross section of the jet. This means that the local

measurements in the center of the flame could be significantly different than what the model predicts, if large radial gradients are present during the experiments. Radial traverses of the gas temperature and CO concentrations indicate that this might be the case, especially close to the burner, as shown in Figure 9-6. For instance, it is seen that the gas temperature is at least 100 °C higher in the center of the kiln than close to the walls. The gas temperature could thus be somewhat underestimated by the model compared to the measurements.

The CO concentration is also highly dependent on the radial position. Thus, the very high peak CO concentration and low oxygen seen in Figure 9-5 may be due to oxygen depletion in the center of the flame.

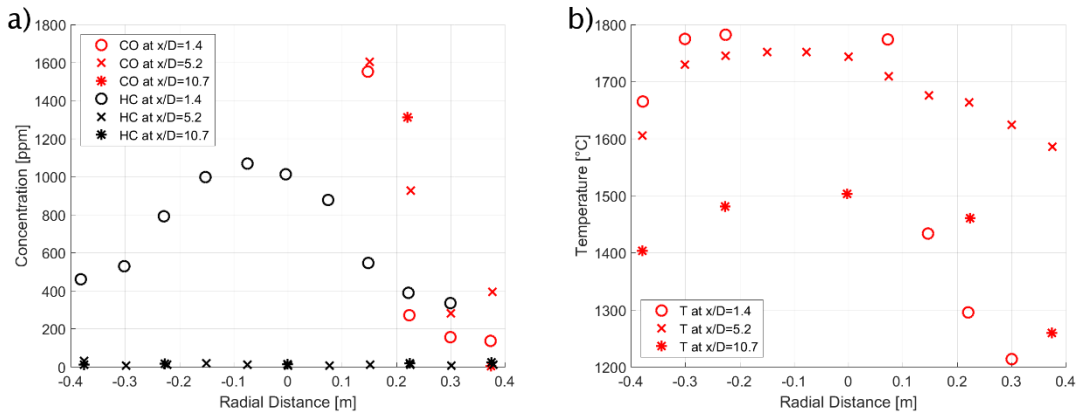

Figure 9-6: Radial traverses of a) CO and hydrocarbon (HC) concentrations and b) gas temperatures in the Cemflame experiments [80].

9.2 Model Validation – Industrial Scale

The validation of the model in industrial scale will be performed against measurements described by Ariyaratne et al. Two sets of industrial tests were performed to investigate the effect of co-firing rate on the clinker quality. The first set of tests investigated the effect of co-firing meat and bone meal (MBM) with coal [81] and the second set of tests dealt with solid hazardous waste (SHW) [82]. Results of the tests were already briefly discussed in chapter 3.5.1. Additional details of the kiln system, such as amount of primary air and secondary air, can be found in subsequent papers, where the same kiln system was modeled [83,84].

9.2.1 The Industrial Tests

The industrial tests were made at a Norwegian cement plant. The kiln system consisted of a 4-stage, 2-string preheater with calciner, with a kiln length of 68 m and diameter of 4.4 m. The kiln had a production capacity of 3,400 ton clinker per day.

Tests were performed with coal as the baseline fuel, and the feed rate of MBM or SHW was incremented in steps lasting two hours (as previously shown in Figure 3-5). The coal firing rate was adjusted to keep the heat input constant. The clinker quality was reported by measuring the free lime content. Details of the tests can be found in Table 9-3 and Table 9-4. During the SHW tests, 1.5 t/h liquid hazardous waste was also co-fired in the kiln. To simplify the calculations, this was replaced by 0.7 t/h of coal, which has the same energy content.

Table 9-3: Details of the meat and bone meal (MBM) co-firing tests [81].

Test Number	Coal feed rate	MBM feed rate	Raw meal feed rate	Clinker free lime	Specific Energy Input
	ton/h	ton/h	ton/h	wt%	MJ/kg clinker
1-1	7.8	0.0	220	1.27	1.55
1-2	6.5	2.0	220	1.69	1.56
1-3	5.3	4.0	220	1.42	1.57
1-4	4.5	5.0	220	1.51	1.55
1-5	3.9	6.0	220	2.29	1.56
1-6	3.2	7.0	220	3.03	1.56
1-7	3.2	7.0	210	2.92	1.63

Table 9-4: Details of the solid hazardous waste (SHW) co-firing tests [82].

Test Number	Coal feed rate	SHW feed rate	Raw meal feed rate	Clinker free lime	Specific Energy Input
	ton/h	ton/h	ton/h	wt%	MJ/kg clinker
2-1	7.6	0.0	218	0.99	1.48
2-2	7.0	0.5	227	1.68	1.36
2-3	6.7	1.0	226	2.30	1.36
2-4	6.4	1.5	226	1.99	1.35
2-5	5.7	2.0	226	2.49	1.27
2-6	5.6	2.5	223	3.19	1.33
2-7	5.9	2.5	216	2.23	1.43
2-8	5.9	2.5	221	1.91	1.40
2-9	5.7	3.0	221	1.83	1.41
2-10	7.4	0.0	220	1.05	1.43

The raw meal feed rate was also reported. This was converted to a clinker production rate by using a factor 0.64. The assumption is that an average raw meal

feed rate of 220 t/h (5,280 t/day) results in 3,400 ton clinker per day. The standard deviation on the free lime measurements were on average 0.16 wt%. This was determined based on the steps in the MBM feed rate where two measurements of free lime were performed [81].

The data from the tests indicate that an increased co-firing rate increases the free lime content of the cement clinker. This is most likely caused by reduced flame temperatures in the kiln as discussed in chapter 3.5.1.

Details of the fuels can be found in Table 9-5. Parameters for the Rosin-Rammler particle size distribution were derived from the data presented in the articles. The shape of the fuel particles has not been detailed in the articles. Thus, all particles have been assumed spherical. This is perhaps a fair assumption for the coal and MBM, but the wood chips from the SHW are more irregularly shaped. This affects the sieving analysis of size, and the combustion characteristics of the fuel.

Additional details of parameters used in the model can be found in Appendix H.

Table 9-5: Details of the fuels used in the industrial tests.

Property	Unit	Coal for MBM tests	MBM	Coal for SHW tests	SHW
Moisture	wt. %	1.0	4.0	17.6	30.0
Volatiles	wt. %	23.0	60.9	27.5	51.4
Char	wt. %	62.4	8.0	51.4	1.0
Ash	wt. %	13.6	27.1	19.4	17.6
LHV	MJ/kg	28.0	18.5	27.1	15.0
Density	kg/m^3	1287	1354	1336	640
d_{RR}	µm	42.2	726.4	40.7	2663.1
n_{RR}	-	0.88	1.00	0.90	1.61

9.2.2 Model Results MBM Tests

The focus of this chapter will be on the differences between the free lime content measured in the experiments of Ariyaratne et al. and the predictions of the developed model. Example temperature profiles of the gas and bed are shown to further understand the differences in the model predictions. In Appendix I results of the coal case simulation are discussed in further detail. Temperatures and fuel conversion through the kiln are presented in this appendix, among other things.

A comparison of the experimental and model results of free lime content in the clinker during the MBM tests is shown in Figure 9-7. According to the experiments

the co-firing with MBM does not influence the free lime content significantly through Tests 1-1 to 1-4 where the MBM feed rate is 5 t/h. It is only when the feed rate is increased to 6 t/h and above during Test 1-5 to 1-7 that the free lime content significantly increases. In comparison the model predictions show a steady increase in free lime content as the MBM feed rate is increased through Tests 1-1 to 1-6. In Test 1-7, the model predicts a sharp decrease in the free lime content as the raw meal feed rate is decreased from 220 to 210 ton/h, while the experiments only show a minor decrease.

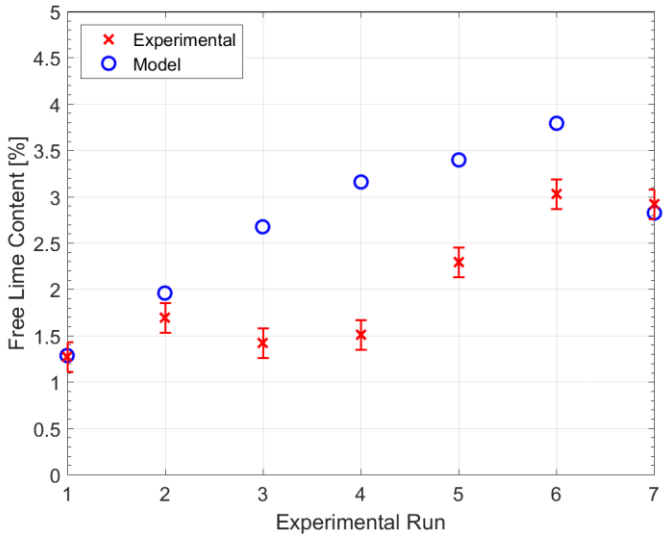

Figure 9-7: Comparison of clinker free lime content measured in experimental tests by Ariyaratne [81] and corresponding model calculations during MBM tests. Error bars indicate standard deviation in measurements.

The model generally overpredicts the effect of co-firing MBM on the free lime content. The mean absolute deviation is 40 % (RMSE = 0.94 wt%). Especially the values of Test 1-3 and 1-4 are overpredicted by close to 100 %. The model predicts a much larger effect of reducing the raw meal feed rate from 220 to 210 t/h during Test 1-7, than measured in the experiments. During experiments, the lower feed rate was only upheld for 1 hour, which may be too little time to see the full effects on the free lime content.

The MBM contains 27 % ash with close to 50 % of the ash being calcium and the other 50 % phosphorous [81]. The calcium introduced with the fuel may not have sufficient time to combine with the clinker, which would increase the free lime content, and the clinker. Moreover, phosphorous can stabilize belite and lower alite

formation and thus increase the free lime content [81,88]. According to Taylor [13] higher contents than 0.2 % P_2O_5 decrease alite, and during Test 2-6 the clinker phosphorous content is 0.5 wt% (see Figure 3-5). Neither of these effects are included in the model. If they were to be included, they would increase the free lime content, further increasing the overprediction of the free lime content.

Examples of the calculated gas and bed temperature profiles in the kiln are shown in Figure 9-8. Observing the temperature profile for the coal case, Test 1-1, the gas temperature is quickly increased as entrainment of the secondary air heats the primary air and the fuel. This causes the coal to rapidly devolatilize, and the volatiles are combusted to increase the temperature. The maximum temperature is reached at around 8 m from the kiln clinker exit (3 m from the burner). The flame core is now hotter than the surrounding secondary air, and entrainment of the remaining secondary air cools the flame. The coal char is combusted, which for a while keeps the gas temperature around 1900-2000 °C and results in a second temperature peak at around 15 m. Afterwards the gas temperature gradually decreases as most of the coal has been converted and heat is transferred to the bed. Further details of the temperature profile for the coal case can be found in Appendix I.

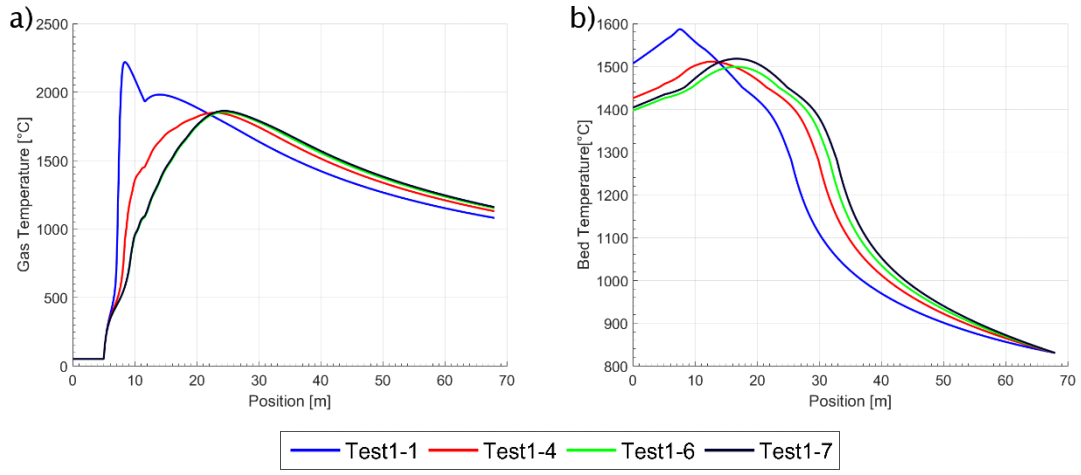

Figure 9-8: Model simulation results of gas temperatures (a) and bed temperatures (b) through the kiln for different co-firing scenarios with MBM.

As more MBM is added to flame, the gas temperature increases less rapidly. The amount of coal is reduced, and the larger MBM particles take longer to heat and devolatilize. Furthermore, the amount of combustion air is increased. The peak gas temperature of 1850 °C is reached at around 23-25 m, which is where the largest MBM particles drop into the bed. In comparison, the peak temperature in the coal

case is 2200 °C. The major difference is caused by a much lower adiabatic temperature, caused by a higher air consumption of the MBM (see Appendix D). For the remaining length of the kiln, the temperatures during MBM co-firing are generally higher than for the coal case. This also leads to higher gas temperatures at the raw meal inlet.

The bed temperatures initially increase slowly from the raw meal inlet side. The higher gas temperatures at the raw meal inlet in the co-firing cases contribute to heating the bed faster. Around 30-40 m from the clinker outlet, the temperature increases rapidly. This is caused by the exothermal formation of belite (C2S). As this reaction is complete at around 20-30 m, the temperature increase of the bed flattens out. At this point the bed temperatures are higher for the co-fired cases, due to the late combustion of MBM. However, as the clinker continues through the kiln, the high peak temperatures of the coal combustion, results in significant increases to the bed temperature, which accelerates the formation of alite and lowers free lime (see Figure 9-7). As the clinker moves to the exit of the kiln, it is cooled by the incoming secondary air and heat loss to the surroundings.

Comparing the cases Test 1-6 and 1-7, it is seen how the gas temperatures are almost the same. However, the bed temperature increases faster during Test 1-7. The lower flow of raw meal and clinker is easier to heat and the bed peak temperature is raised by approximately 20 °C.

The outlet temperature of the clinker is lowered from 1500 °C in the coal case to 1400 °C when co-firing in Test 1-6 and 1-7. This lower discharge temperature of the clinker, will result in lower temperatures in the clinker cooler, which will also reduce the secondary air temperatures [252]. A simple model was formulated for the clinker cooler in order to describe the effect of the clinker outlet temperature on the secondary air temperature. The model is described in Appendix J. The result is that the secondary air temperature is decreased from 750 °C in the coal case to 640 °C in Test 1-6 and 7. The lower secondary air temperature also contributes to decreased combustion temperatures, and thus bed temperatures, during MBM co-firing.

9.2.3 Model Results SHW Tests

A comparison of the experimental and model results of free lime content in the clinker during the SHW tests is shown in Figure 9-9.

The free lime content in the coal firing scenario Test 2-1, is well described by the model. The specific energy input during Test 2-1 is 1.48 MJ/kg clinker, compared to 1.55 MJ/kg clinker, during Test 1-1. However, the free lime content during Test 2-1 is lower at 0.99 wt% compared to 1.27 wt%. The kiln model accurately predicts a free lime content of 0.98 wt% and 1.29 wt% for the two cases. The main difference between the cases appears to be a difference in the clinker composition shown in Table 9-6. The Lime Saturation Factor (LSF) is lower during the SHW tests, which suggests, that a lower free lime content can be expected during the SHW tests. The calculated C_3S content by the Bogue formula, shows a higher C_3S content can be expected during the MBM tests. The model predicts a C_3S content of 55.3 and 57.6 wt% during the SHW and MBM tests, respectively, which is similar to the Bogue calculations, if corrected for the clinker free lime.

As seen in Table 9-5 there is also a slight difference in the composition and heating value of the used coal. However, this difference is not sufficient to describe the differences in the free lime content. All other model parameters related to the kiln were kept constant in the two model cases.

Table 9-6: Average clinker oxide composition and calculated LSF, SR, AR, and Bogue C_3S (not corrected and corrected for free lime) during the MBM and SHW industrial tests of Ariyaratne et al. [81,82].

	CaO	**SiO_2**	**Al_2O_3**	**Fe_2O_3**	**Inerts**	**LSF**	**SR**	**AR**	**Bogue C_3S**	**Bogue C_3S**
	wt%	wt%	wt%	wt%	wt%	-	-	-	wt%	wt%
MBM Test	63.53	20.37	5.37	3.45	7.28	0.97	2.31	1.56	62.8	57.6
SHW Tests	63.63	21.00	5.24	3.48	6.65	0.94	2.41	1.51	59.2	55.2

In Figure 9-9, the experiments show a steady increase in the free lime content during Test 2-2 to 2-6, where the SHW is added to the flame in increments of 0.5 ton/h. In Test 2-7 and 2-8 the SHW feed rate is kept constant at 2.5 ton/h, similar to Test 2-6. The decrease in the free lime content compared to Test 2-6 is caused by an increase of the coal feed by 0.3 ton/h and a reduction of the raw meal feed rate to 216 ton/h

in Test 2-7 and 221 ton/h in Test 2-8, compared to 223 ton/h in Test 2-6. In Test 2-9 the SHW feed rate is increased to 3 ton/h, and a slight reduction is seen in the experimentally determined free lime content. In Test 2-10 the SHW co-firing is switched off, and a reduction in free lime content is seen. The free lime content is at 1.05 wt% slightly higher than the 0.99 wt% in Test 2-1, presumably caused by a lower specific energy input.

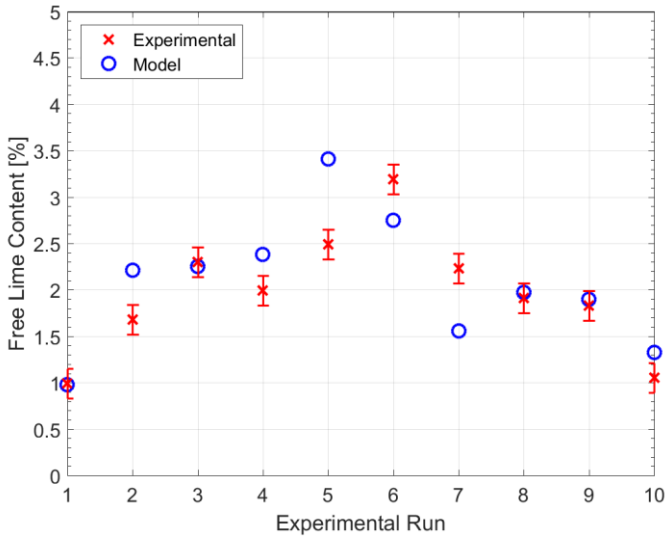

Figure 9-9: Comparison of clinker free lime content measured in experimental tests by Ariyaratne [82] and corresponding model calculations during SHW tests. Error bars indicate standard deviation in measurements.

The overall trend of the model results follows the experimental results well. On average the absolute deviation between model and experimental free lime is 17 % (RMSE = 0.45 wt%).

The largest deviation is seen for Test 2-5 and Test 2-7. The model predicts the largest free lime content for Test 2-5, where the specific energy input is the lowest at just 1.27 MJ/kg clinker, compared to 1.32 MJ/kg during Test 2-6. In Test 2-7 the raw meal feed rate is decreased to just 216 ton/h, which has a greater effect on modeled free lime content, than the experimentally determined. In the MBM tests it was also experienced that the model was more sensitive to changes in the raw meal feed rate than the experiments.

In fact, there seems to be some transient effects on the experimental free lime content. When settings are changed it will take some time for an industrial size kiln to stabilize around new settings. For instance, the clinker residence time in the kiln

is typically around 30 minutes, which gives a considerable time lag for changes in the raw meal feed rate. There may also be some thermal inertia in the kiln when fuels are changed and the temperature profile shifts. This may be one of the reasons the model predicts a local minimum for the free lime content during Test 2-7, while the experiments show a steady decrease in the free lime content.

Model predictions for selected cases of the gas and bed temperature profiles through the kiln are shown in Figure 9-10. The trends of the curves are similar to that shown for the MBM cases. The peak gas temperature is lowered by adding SHW to the flame, while for Test 2-7 a second temperature peak between 20-25 m is created by the SHW dropping out of the flame and burning in the bed at this distance. The lower gas temperatures are also reflected in lower bed temperatures, which serve to decrease the free lime content. Test 2-7 has the lowest raw meal feed rate and it can be seen how the bed temperature is increased more readily. It is only in the last 15 m of the kiln that the bed temperature of the coal case becomes higher.

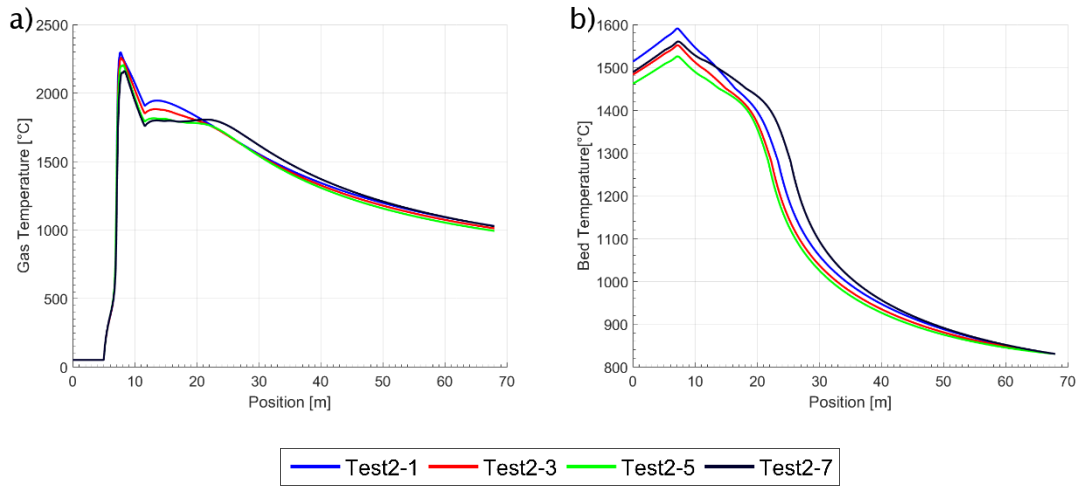

Figure 9-10: Model simulation results of gas temperatures (a) and bed temperatures (b) through the kiln for different co-firing scenarios with SHW.

Comparing the graphs in Figure 9-8 and Figure 9-10 the temperatures during SHW co-firing are les influenced than during MBM co-firing. This can be explained by the lower degree of co-firing. A maximum of 7 ton/h MBM is co-fired, while only 3 t/h SHW is co-fired, corresponding to 60 and 30 % of the energy input, respectively. Furthermore, the air consumption per MJ of fuel is higher for the MBM than for SHW, which increases the gas flow in the kiln, and reduces peak temperatures for MBM co-firing.

9.3 Discussion of Model Predictions

The model has been compared to experimental results obtained in both pilot and industrial scale. The ignition, entrainment, temperatures, and combustion rate of a coal flame are described adequately when compared to the measurements from the pilot scale kiln. The free lime content measured for the coal fired flame in the two industrial test scenarios is also well determined by the model. The model responds well to changes in fuel type when co-firing, energy input, and raw meal feed, although the model tends to be more sensitive to these changes than what was measured in the industrial tests. Overall, the model has shown good agreement with the validation cases.

Normally it is expected that gas temperatures in the kiln are a maximum of around 2000 °C, while the clinker experiences temperatures up to 1450-1500 °C [31]. The model predicts somewhat higher temperatures for both the gas phase and the bed, peaking at 2200-2300 °C and almost 1600 °C, respectively. This can be explained by some of the simplifications applied in the model

Sources in the literature determined that neglecting axial radiation would only lead to errors of around 10 % of the total heat transfer [31,183]. Based on this it was decided to neglect it in the model. If axial radiation was included it could serve to reduce peak flame temperatures and flatten the temperature profile as more heat would radiate away from the very hot areas.

As temperatures increase above 2000 °C the major combustion products CO_2 and H_2O may start to dissociate into smaller products, which absorbs heat [253]. If this occurs, it would lower the peak temperature, and release the heat later, when the temperature has been lowered enough that H_2O and CO_2 become stable. Some calculations were made separately from the model that indicate that the peak temperature during coal combustion could be reduced by approx. 250-300 °C due to dissociation.

It has been assumed that the gas phase of the kiln is dust free. In an industrial kiln significant amounts of dust are entrained from the clinker cooler and the kiln. Entrainment of around 0.03 kg dust per kg clinker, carried with the secondary air from the cooler to the kiln is not uncommon [196]. Close to the burner entrained

dust in the secondary air would decrease the radiation from the flame to the bed, and thus heat transfer and bed temperatures.

If the bed was to be assumed non-isothermal the surface could be much hotter than the interior, perhaps up to 200 °C or more [227]. This hot surface would decrease the temperature gradient between the gas and bed and lower heat transfer, resulting in lower bed temperatures on average.

Even though the bed temperatures may be overestimated to some extent, the effect of this is compensated by the relatively slow kinetics derived from laboratory experiments. The result is that the free lime content calculated by the model agrees well with industrial measurements.

9.4 Co-firing with SRF

SRF is one of the most commonly used alternative fuels in the cement industry. It was also the main alternative fuel used at the three cement plants studied in the large-scale experiments (see chapter 5 and 6). Therefore, it is desired to study the effect of co-firing SRF in further detail using the developed model. As seen when co-firing MBM or SHW, it is expected that co-firing with SRF will lower kiln temperatures and increase the clinker free lime content, which was also observed in the industrial tests of this PhD study. Consequently, it will also be investigated if the firing can be altered to minimize the negative consequences of co-firing SRF.

9.4.1 SRF Properties

Two samples of SRF were characterized in detail in chapter 7. The properties of SRF-B, will be used as input to the mathematical model.

The SRF sample has been divided into 5 size groups based on the wind sieve fractionation. In each of these groups the content of plastics, biomass, textiles, inerts, and fines was determined. For the model, the textiles will be assumed to be 50 % biomass and 50 % plastic. Furthermore, the fines will be collected in one group, assuming 30 % ash, 35 % biomass, and 35 % plastic content. It is expected that the fine fraction has a low heating value, since moisture and ash tends to accumulate amongst the smallest particles [72,100,162]. Thus, a high ash content is assumed in the fine fraction. The inerts from the five wind sieve fractions and the ash from the

fine fraction will be collected in one group as well. This creates a total of 13 different size groups for the model – 6 biomass, 6 plastic, and 1 inert group.

The fines were sieved to be < 2 mm, and it will be assumed that the average particle diameter is 1 mm. The particle mass distribution was determined for the remaining biomass and plastic fractions.

During the model validation (see Chapter 9.2) coal and alternative fuel was divided into 10 discrete particle size categories, based on the given particle size distribution. However, doing this for both the biomass and plastic fraction for each of the 5 wind sieve subgroups would result in a system of 2x5x10 equations for the particles, taking a considerable amount of time to solve. To reduce model calculation times, only the mean particle mass in each subgroup is used.

The mean particle mass is taken as the mass of the particle at which 50 % of the cumulative mass is achieved. This can be calculated based on the characteristic size of the Rosin-Rammler distribution:

$$\boldsymbol{Cm_{RR,50} = \left(-ln\left(\frac{100-50}{100}\right)\right)^{\frac{1}{n_{RR}}} * m_{RR}} \qquad \textbf{E 9.3}$$

The details of the composition and size of the SRF sample as implemented in the model is given in Table 9-7.

Table 9-7: Distribution of the SRF composition, particle mass and equivalent diameter, and sphericity used for simulating SRF co-firing.

Fraction	**Content (wt%)**		**Mean particle Mass (mg)**		**Mean equivalent diameter (mm)**		**Sphericity**	
(Terminal velocity (m/s))	Plastic	Biomass	Plastic	Biomass	Plastic	Biomass	Plastic	Biomass
1 (<2)	2.22	0.53	6.5	7.1	2.4	2.8	0.10	0.15
2 (2-3)	5.04	3.23	20.7	18.2	3.5	3.9	0.15	0.28
3 (3-5)	15.69	22.53	34.2	25.0	4.1	4.3	0.26	0.39
4 (5-7)	9.28	11.51	154.5	90.5	6.8	6.6	0.39	0.49
5 (>7)	3.35	8.40	451.9	686.2	9.7	13.0	0.55	0.60
Fines	4.69	4.69	0.5	0.3	1.0	1.0	0.10	0.15
Inerts	8.84	-	-	-	-	-	-	-

The SRF heating value and proximate analysis of the SRF sample has been determined and shown in Table 9-8. Factors such as heating rate and final

temperature has an influence on the char yield of biomass and SRF [254], thus the proximate analysis typically overestimates the char yield [96]. Here it will be assumed that the actual char yield is 70 % of that measured in the proximate analysis, and the volatile content is correspondingly greater.

It is assumed that the plastic and ash fractions have fixed properties, and the biomass properties are adjusted so the average composition matches that determined for the SRF. The plastic fraction is assumed to form no char and have a volatile content of 97.5 %, close to that of polyethylene [164] and an ash content of 2.5 %. The lower heating value is assumed as 35 MJ/kg, which is somewhat lower than for pure polyethylene [95]. Since polyethylene and other plastics used for packaging absorb only little water [177], it is assumed that the water stays on the particle surface and the content is small, at 5 %. Thus, most of the SRF water content is held by the biomass particles. The assumed dry and as fired composition is shown in Table 9-8.

Table 9-8: Composition of the SRF and the Plastic, Inert, and Biomass fractions used for modeling SRF co-firing.

		Dry Basis				Wet Basis			
Property	**Unit**	**SRF**	**Plastic**	**Inert**	**Biomass**	**SRF**	**Plastic**	**Inert**	**Biomass**
LHV	MJ/kg	20.2	35	0	12.0	15.4	33.3	0	7.3
Moisture	wt%	0	0	0	0	21.4	5.0	0	33.0
Ash	wt%	22.4	2.5	100	24.7	17.6	2.4	100	16.5
Volatiles	wt%	69.8	97.5	0	60.1	54.9	92.6	0	40.2
Fixed Carbon	wt%	7.8	0	0	15.2	6.1	0	0	10.2
Adj. Volatiles	wt%	72.2	97.5	0	64.7	56.7	92.6	0	43.3
Adj. Fixed Carbon	wt%	5.4	0	0	10.7	4.3	0	0	7.2
Amount in sample	wt%	-	40.3	8.8	50.9	-	33.3	7.0	59.7

9.4.2 Effect of Co-Firing Rate

The effects of co-firing SRF ranging from 0 % to 100 % of the energy input has been investigated using the developed kiln model. The employed coal, SRF, and raw meal feed rates are given in Table 9-9. The same conditions and model inputs employed during the MBM validation are used here. The only difference is the SRF fuel properties. The parameters used in the model calculations are detailed in Appendix H.

Table 9-9: The feed rate of coal, SRF, and raw meal used for simulating the effect of SRF co-firing.

SRF Energy Input [%]	Coal [t/h]	SRF [t/h]	Raw Meal [t/h]
0	7.80	0.00	220
10	7.02	1.42	220
20	6.24	2.84	220
30	5.46	4.26	220
40	4.68	5.68	220
50	3.90	7.10	220
60	3.12	8.52	220
70	2.34	9.94	220
80	1.56	11.4	220
90	0.78	12.8	220
100	0.00	14.2	220

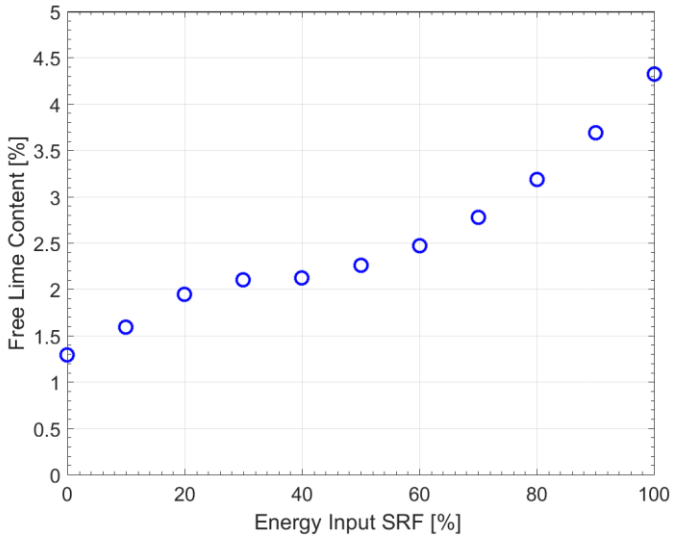

Figure 9-11: The clinker free lime content as the share of SRF energy input is increased.

The free lime content from the simulations is shown in Figure 9-11. The free lime content steadily increases as the SRF energy input is increased with a plateau present around an SRF energy input of 30-50 %. The upper limit for the free lime concentration is 2.5 % [81]. This limit is reached at 60 % SRF energy input. In addition to lowering the alite content and cement strength [2], excessive free lime may also cause concrete expansion [13]

Temperature profiles in the gas and bed for selected degrees of co-firing are shown in Figure 9-12. The temperature trends are similar to those explained for the MBM and SHW co-firing in chapters 9.2.2 and 9.2.3. As more SRF is added to the flame the

initial peak temperature around 10 m is lowered. This is caused by a lower flow rate of coal and a higher flow rate of air, since the SRF combustion requires more air per energy content (see Appendix D). Furthermore, the colder clinker leaving the kiln, results in reduced secondary air temperatures.

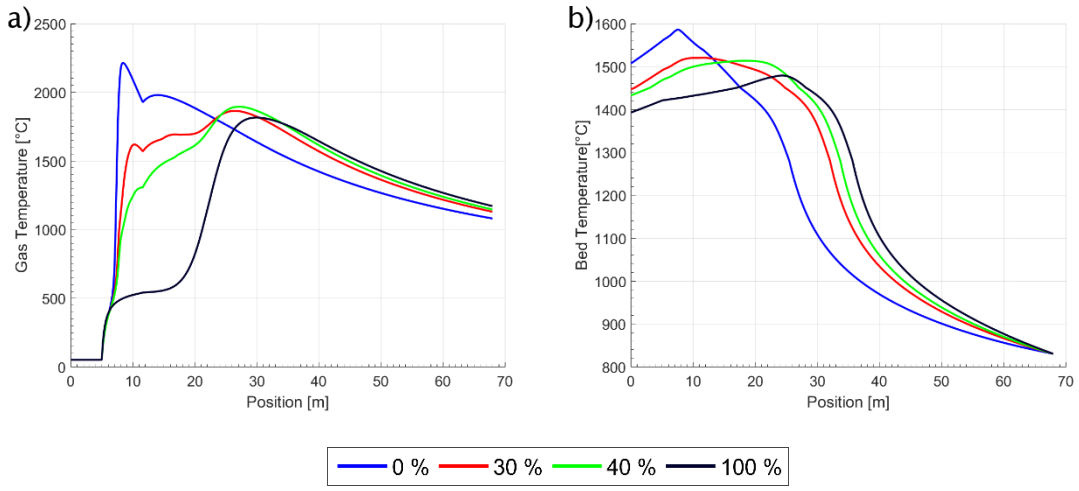

Figure 9-12: Model simulation results of gas temperatures (a) and bed temperatures (b) for different energy inputs of SRF.

The residence time in suspension for the SRF particles is around 1.5 seconds. This is only sufficient to devolatilize the smallest of the SRF particles, with a terminal velocity lower than 2 m/s (see additional details in Appendix I). The larger particles are only converted when they land in the bed at around 20 m. Thus, for co-firing, a second temperature peak in the gas is present around 25 m. This is especially clear for the case with 100 % SRF firing, where the temperature plateaus at around 500 °C until 18 m, where the SRF is converted as it enters the bed.

The lower gas temperature obtained during co-firing also influence the bed temperatures, which are significantly reduced, which serves to increase the free lime content. The peak bed temperature is also shifted further into the kiln, caused by the delayed combustion of SRF. This results in lower clinker temperatures at the kiln outlet, which cause lower secondary air temperatures.

According to the model, the free lime content does not change as the SRF co-firing rate is increased from 30 to 40 %. In Figure 9-12b it observed that the temperature profiles of the two cases are quite similar, with the same maximum temperature. The temperature for the 40 % co-firing scenario is just shifted further into the kiln.

The 30 % SRF firing case is discussed in further detail in Appendix I.

9.5 Possibilities to Increase SRF Co-Firing

It is evident that co-firing with SRF lowers the temperatures in the kiln, which has a negative impact on the free lime content. In the following chapters, it will be investigated if the impact of co-firing can be lessened, by changing the SRF quality or other process parameters. The 30 % co-firing case is selected as the base scenario to study improvements.

9.5.1 Effect of Moisture Content

The SRF contains 21.4 wt% water, a high amount compared to the 1.3 wt% of the coal. The moisture content in SRF may also vary considerably over time. Furthermore, it was determined during the industrial tests, that the moisture content would have a negative effect on the clinker alite content (see chapter 6.4.1). Consequently, investigating the effect of moisture content is relevant.

The moisture content of the SRF was set to vary between 0 and 30 wt%, while the energy input was kept constant. Accordingly, the SRF feed was increased from 3.3 to 4.9 ton/h, to compensate for the lower heating value, when the moisture content increased.

Figure 9-4 shows the free lime content in clinker caused by changes in the moisture content of SRF. The free lime content changes from 1.8 to 2.2 wt% when the SRF moisture content is increased from 0 to 30 wt%.

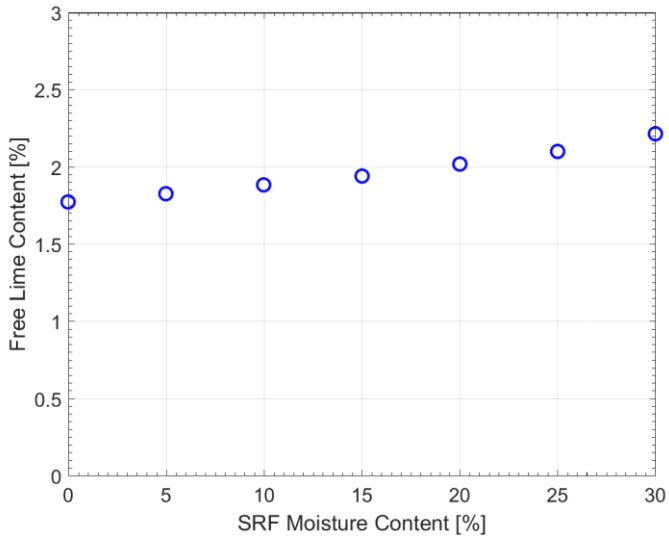

Figure 9-13: The clinker free lime content for different moisture content in the SRF. SRF energy input is 30 %.

Figure 9-14 shows the gas and bed temperature profiles through the kiln for moisture contents of 0, 10, 20, and 30 wt%. The gas temperatures are seen to be decreased by added moisture. The peak gas temperature at 26 m is decreased by approximately 40 °C when the moisture content is increased from 0 to 30 wt%. The added moisture increases the flue gas amount in the kiln for the same energy input and will lead to reduced flame temperatures. In addition, the devolatilization of the SRF will be delayed due to the energy intensive water evaporation. The lower gas temperatures also cause lower temperatures in the bed.

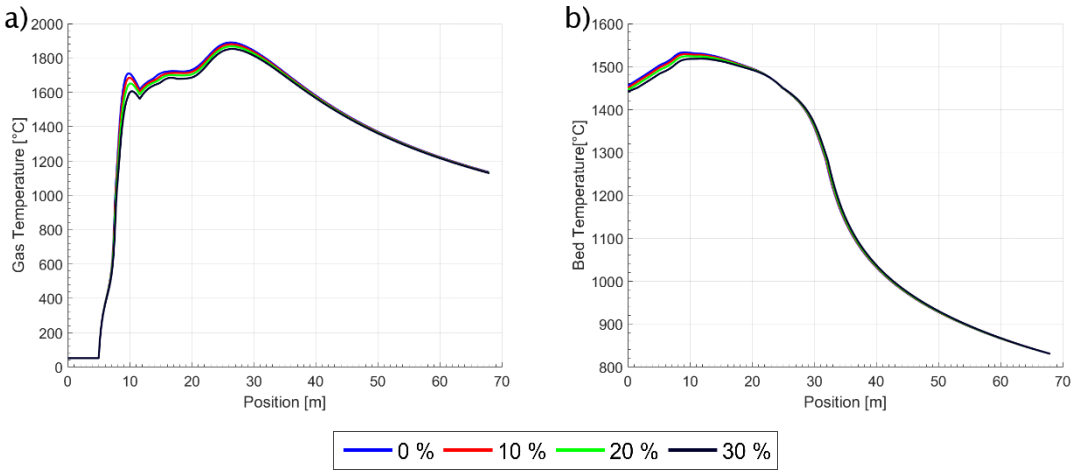

Figure 9-14: Model simulation results of gas temperatures (a) and bed temperatures (b) for different SRF moisture contents. SRF energy input is 30 %.

9.5.2 Effect of Particle Size

Another factor that contributes to lower combustion temperatures during co-firing with SRF is the large particle size. The largest coal particles in the simulations are 170 µm in diameter, while the SRF particle diameter ranges from 1 to 13 mm. This increases the heating time of the particles and delays their combustion.

To investigate the effect of particle size, a factor ranging from 0.1 to 1 is multiplied to the original particle diameter of the SRF, which decreases the particle size. Figure 9-15 shows the effect of lowering the SRF particle size. The free lime content decreases from 2.0 wt% in the base scenario to 1.3 wt% with SRF particles 1/10 the size of the base scenario. This is a free lime content that is comparable to the one obtained when firing only coal.

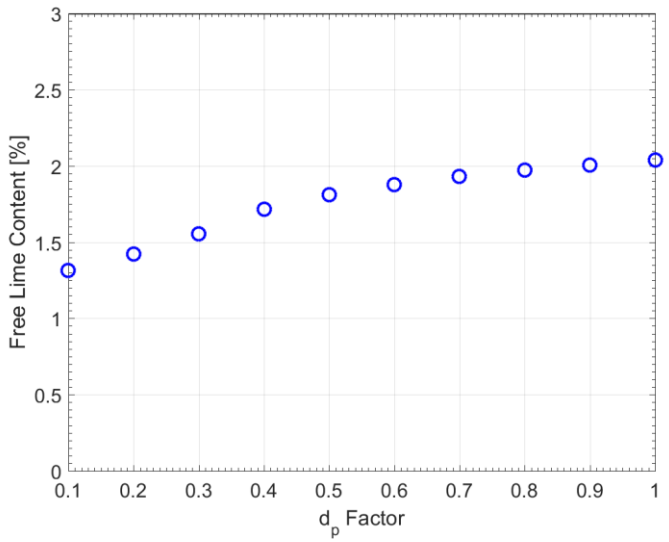

Figure 9-15: The clinker free lime content for different SRF particle sizes. The standard SRF particle diameter is multiplied by a factor in the range 0.1-1. SRF energy input is 30 %.

The temperature profiles in the gas and bed are shown in Figure 9-16 for select SRF particle sizes. As the particle diameter is reduced, the SRF particles will burn closer to the burner and the peak gas temperature is increased and moved closer to the burner. This also affects the bed with increased temperatures.

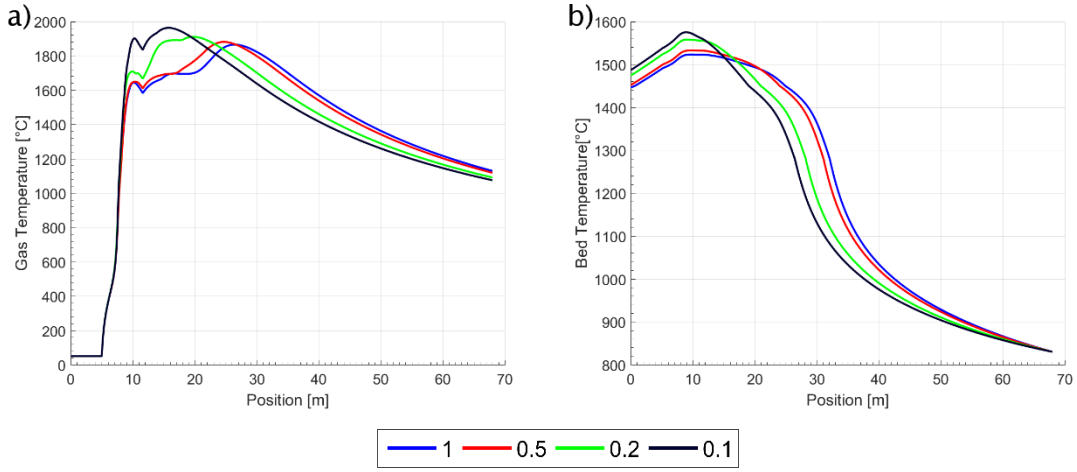

Figure 9-16: Model simulation results of gas temperatures (a) and bed temperatures (b) for different SRF particle sizes. The indicated factor is multiplied to the original particle diameter. SRF energy input is 30 %.

9.5.3 Effect of Increased Specific Energy Input

The specific energy input is as standard 1.55 MJ/kg clinker. To reduce the negative effects that co-firing of SRF has on the free lime content, the energy input to the kiln can be increased. Figure 9-17 shows the effects of increasing the specific energy input by up to 10 %. This is done in three different ways:

1. The coal and SRF feed rate is increased to keep the energy input of SRF at 30 % of the total.
2. The feed rate of SRF is increased to match the desired increase in specific energy input, while the coal input is kept constant.
3. The raw meal feed rate and thus clinker production rate is decreased.

All three methods can be used to lower the free lime content in the clinker during co-firing. Reducing the raw meal feed rate is more efficient than increasing the fuel input. Increasing both the coal and SRF feed rate is slightly more effective than only raising the SRF feed rate. To obtain a free lime content of 1.3 wt%, which is comparable to coal firing, the energy input should be increased by slightly more than 10 %, or the raw meal feed rate should be decreased by 5 %.

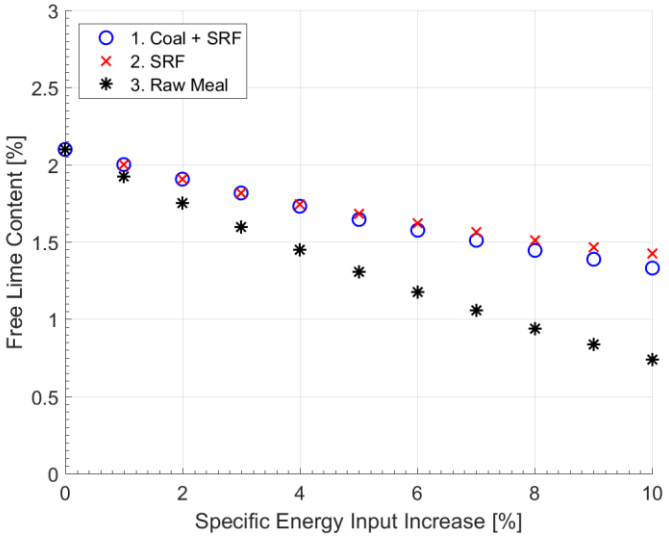

Figure 9-17: The clinker free lime content for increasing specific energy input by 1. Increasing coal and SRF feed rate, 2. Increasing SRF feed rate, 3. Decreasing the raw meal feed rate. SRF energy input is 30 % in case 1 and 3, but changes in case 2.

Changes to the temperature profiles of the gas and bed caused by increases in the specific energy input by reducing the raw meal feed is shown in Figure 9-18.

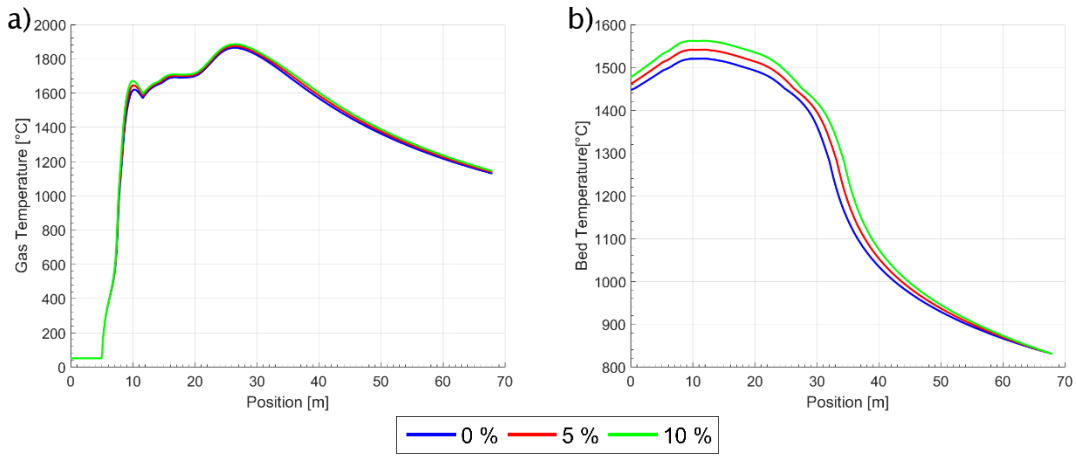

Figure 9-18: Model simulation results of gas temperatures (a) and bed temperatures (b) for different increases in specific energy consumption by reduction of raw meal feed. SRF energy input is 30 %.

The gas temperature is only increased slightly by lowering the raw meal feed. For instance, the peak gas temperature increased by 20 °C, when the specific energy input is increased by 10 %. The effects on the bed temperature are somewhat greater. The bed temperature increases more rapidly, and the peak temperature is increased by 40 °C.

9.5.4 Effect of Burner Settings

Based on the experimental results of the tests on the Jetflex burner (see chapter 6), it was concluded that the burner settings could be adjusted to increase the clinker quality when co-firing. Increased swirl and dispersion of SRF was found to be beneficial for co-firing SRF.

The model was developed with the goal that it should be able to help understand how burner settings can be used to increase the co-firing rate of alternative fuels. For this purpose, the mixing and eddy dissipation rates were derived based on CFD modeling, considering the burner axial momentum and swirl number (see chapters 8.6.5 and 8.8.6.1).

The burner settings were tested on the co-firing scenario using 30 % SRF. The axial momentum and swirl number were changed 50 % around their original values of 5.8 N/MW and 0.26, in four new cases as shown in Table 9-10. The corresponding effect on the entrainment rate of the jet and the turbulent eddy dissipation rate is also shown.

Table 9-10: Axial momentum and swirl number used to determine the effect of burner settings on clinker free lime and the corresponding values of $K_{ent,jet}$ and ε/k calculated at 10 and 25 m from the clinker exit.

	Case 1	Case 2	Case 3	Case 4	Case 5
Axial Momentum (N/MW)	5.8	8.7	8.7	2.9	2.9
Swirl Number	0.26	0.39	0.13	0.39	0.13
$K_{ent,jet}$	0.21	0.26	0.19	0.23	0.16
ε/k at 10 m (1/s)	9.2	9.4	12.9	5.9	8.9
ε/k at 25 m (1/s)	0.8	0.8	1.2	0.5	0.9

The model predicted free lime content for the five burner setting scenarios is shown in Figure 9-19. The free lime content is only decreased slightly in case 2 and 3 employing a 50 % higher axial momentum. Employing a 50 % lower axial momentum in case 4 and 5 has a more significant effect on increasing the free lime content. The swirl has less of an impact, but a higher swirl tends to increase the free lime.

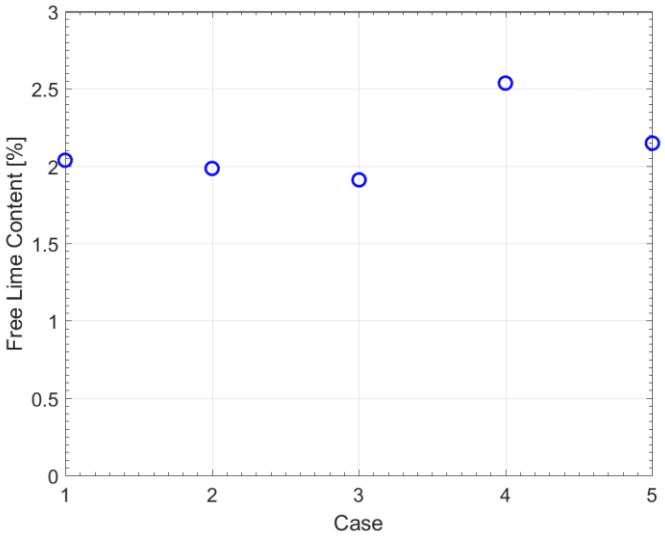

Figure 9-19: The clinker free lime content for different cases of burner settings. SRF energy input is 30 %.

Gas and bed temperature profiles through the kiln for the different burner setting cases are shown in Figure 9-20. The burner settings influence the peak gas temperatures around 10 and 25 m. Case 5 has the lowest entrainment rate, which results in the highest peak temperature during the coal devolatilization around 10 m. Case 2 and 4 have the highest entrainment rates and the lowest peak temperatures around 10 m.

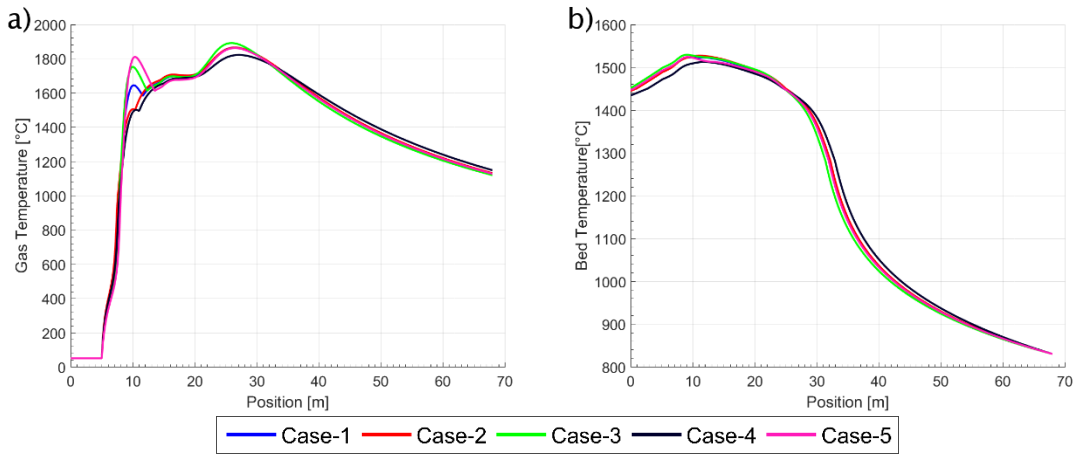

Figure 9-20: Model simulation results of gas temperatures (a) and bed temperatures (b) for different burner setting cases. SRF energy input is 30 %.

The highest peak temperature at 25 m is obtained by case 3 and the lowest by case 4. This difference is related to the eddy dissipation rate, which control the rate of volatile combustion. The higher rate of volatile combustion benefits the gas temperature and increases the bed temperature causing the lowest clinker free lime content for case 3. Conversely, case 4 settings result in the highest free lime content.

According to the model, both axial momentum and swirl influence the entrainment rate and the eddy dissipation rate. The gas temperatures are more sensitive to changes in the eddy dissipation rate, which control the volatile combustion. A high combustion rate is best achieved by increasing the axial momentum and lowering the swirl.

9.5.4.1 Effect of the Entrainment Rate

Changing the burner momentum and swirl influences both the entrainment rate and the volatile combustion rate. In the following it is desired to only change the entrainment rate. The standard value, of $K_{ent,jet} = 0.21$, is used and factors ranging from 0.5 to 1.5 are employed to vary the value of $K_{ent,jet}$ between 0.11 and 0.32.

Figure 9-21 shows the effect of changing the entrainment rate on the free lime content. Lower entrainment rates result in a higher free lime content. As standard the free lime content is 2.0 wt%, which can be increased to 2.5 wt% or decreased to 1.8 wt% by adjusting the entrainment rate.

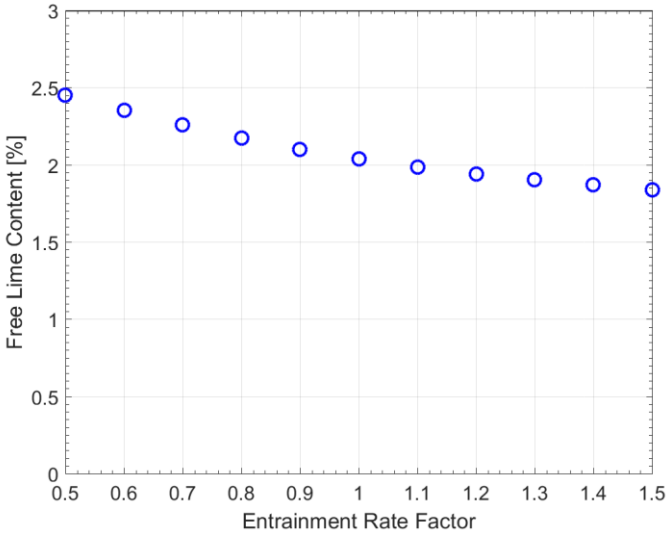

Figure 9-21: The clinker free lime content for different secondary air entrainment rates. The standard entrainment rate is multiplied by a factor in the range 0.5-1.5. SRF energy input is 30 %.

Figure 9-22 shows gas and bed temperature profiles in the kiln for the different values of the entrainment factor. With a low entrainment rate (factor 0.5), a gas peak temperature of 2050 °C is reached at 10 m. With a higher entrainment rate the gas temperature at this location is reduced to 1650 and 1500 °C, for a factor 1 and 1.5, respectively. The higher flow of gas caused by a fast entrainment of the secondary air reduces the peak temperature. However, after the mixing is complete, the case with the highest entrainment rate maintains the highest gas temperature. The higher entrainment initially also causes a higher heating rate of the primary gas, as the incoming secondary air heats and devolatilizes the coal.

Even though gas temperatures are significantly higher with a low entrainment rate, the heat transfer to the bed is impeded. The enveloping secondary air prevents the hot flame gasses from convective heat transfer to the bed. When the jet diameter expands faster, the larger surface area also increases the radiative heat transfer. Consequently, a higher entrainment rate is beneficial.

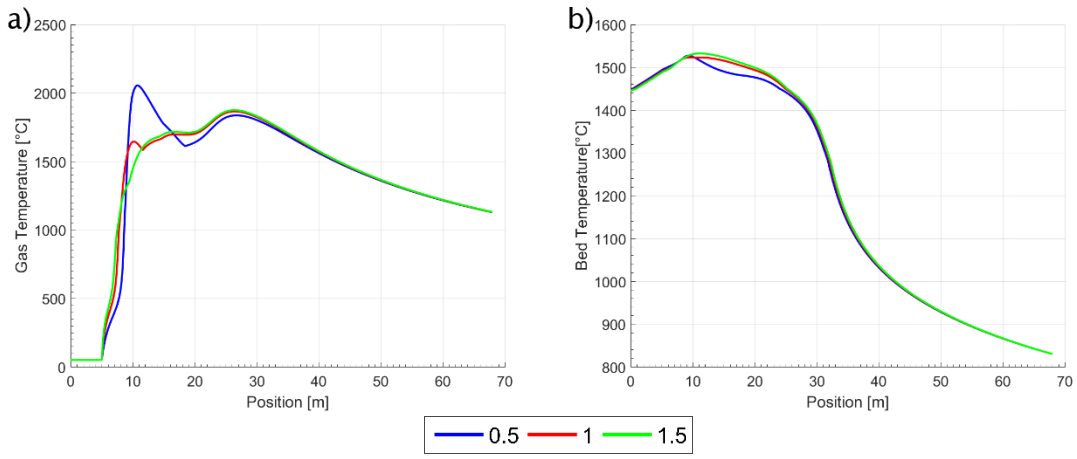

Figure 9-22: Model simulation results of gas temperatures (a) and bed temperatures (b) for different entrainment rates. The indicated factor is multiplied to the original entrainment rate. SRF energy input is 30 %.

9.5.4.2 Effect of Fuel Landing Place

In the model the SRF particles are assumed to be well dispersed in the primary air jet, until they drop into the bed, where they are instantly converted. The effect of burner settings on the particle trajectories have not been considered in the model. However, the industrial tests on the Jetflex burner (see chapter 6) showed that increased swirl was beneficial for the co-firing of SRF. The swirl particularly influenced the dispersion of SRF near the burner. The increased dispersion will also affect the distance at which the particles land in the bed. This has been confirmed by the CFD model study by Liedmann et al. [143], as discussed in chapter 8.1.2.

The effect of the particle landing was studied in the model by calculating the particle landing place, $I_{f,drop}$, as described in chapter 8.8.5. A factor between 0.5 and 1 was then multiplied to the calculated value, which forces the particles into the bed earlier. The effect of the landing place is shown in Figure 9-23. With the normally calculated value of the landing place (Fuel Landing Factor = 1), the free lime content is 2.0 %. As the particles drop into the bed earlier the free lime content is decreased, to a minimum value of 1.4 wt%, using a factor of 0.65. This is only 0.1 wt% higher than the coal fired case. Decreasing the factor further leads to a slight increase in the free lime content, which is 1.5 wt% using a factor of 0.5.

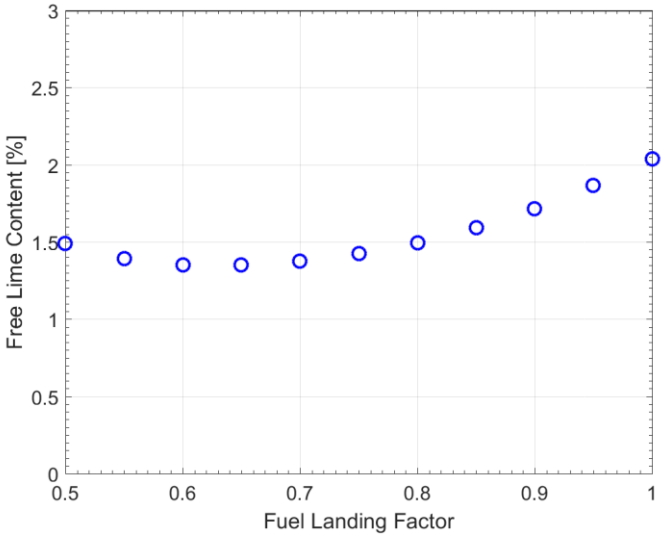

Figure 9-23: The clinker free lime content for different landing places of the SRF. The standard landing place is multiplied by a factor in the range 0.5-1. SRF energy input is 30 %.

The temperature profiles of the gas and bed of select cases are shown in Figure 9-24. The main effect of the particles dropping into the bed closer to the burner is a faster conversion and heat release from the fuel. This results in faster temperature increase in the gas phase and the peak related to SRF firing originally around 25 m is moved closer to the burner by 10 m and increased by 100 °C.

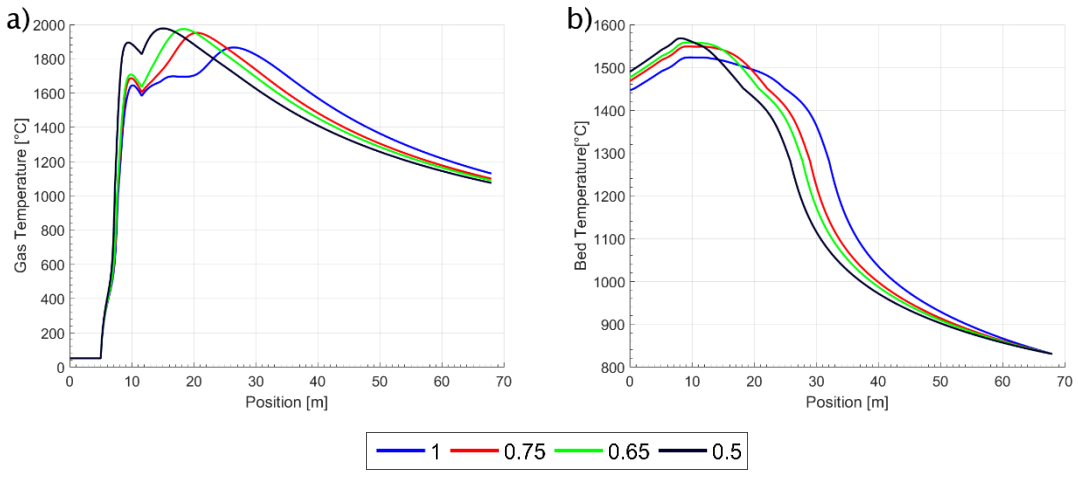

Figure 9-24: Model simulation results of gas temperatures (a) and bed temperatures (b) for different SRF particle landing factors. The indicated factor is multiplied to the original landing place. SRF energy input is 30 %.

The changes in the gas phase temperature also increase the bed temperature, resulting in higher peaks as the fuel burns closer to the burner. The free lime content

is lowest when the fuel landing factor is 0.65, even though higher bed temperatures are reached when it is 0.5. When the factor is 0.65, the bed is heated faster, and the maximum bed temperature is almost constant for 3-4 m, while for the factor 0.5, the bed temperature is more peaked. The heating rate of the bed is slower, which results in shorter residence time of the clinker at high temperature.

9.5.5 Discussion of Options to Increase Co-Firing

In the above sections different methods to limit the negative effects of co-firing have been reviewed. Based on the findings, some suggestions for increasing co-firing of SRF are proposed. The conclusions are likely also valid for other types of alternative fuels.

For the investigated simulation case it can be expected that 30-40 % SRF can be used in the kiln without making significant changes to the kiln operation. This results in an increase in the free lime content from 1.3 wt% when only firing coal to 2 wt% when co-firing 30 % energy SRF. The kiln system, ID fan etc., should however be able to cope with the increased amount of flue gas formed. At 30 % co-firing, the flue gas mass flow rate is increased by 4 %.

If the increase in free lime, and consequently lower alite content, cannot be tolerated, or higher SRF co-firing is desired, the first step should be to increase the specific energy consumption in the kiln by increasing the SRF feed rate. If SRF can be obtained cheaply at the cement plant, increased firing will not significantly increase the production costs of the cement. Lowering the production rate has been shown to be more effective on the free lime content, but it is likely to be a more expensive option.

The optimal burner settings for co-firing should also be investigated. The model shows that increased burner momentum, increased entrainment rate of secondary air, or increased dispersion of the SRF could help decrease the clinker free lime content when co-firing SRF. If the burner at the plant does not allow any significant flexibility, installing a new burner should be considered.

After the above possibilities have been exhausted, changes to the SRF can be considered. This approach will require new equipment for SRF drying and comminution. Drying of SRF could possibly be achieved by utilizing hot waste air

from the process. Drying of the SRF from 20 to 0 % moisture could decrease the clinker free lime content from 2.0 to 1.8 wt%, when utilizing 30 % SRF by energy.

A size reduction of the fuel can also be considered. A factor 10 reduction of the SRF particle size resulted in a decrease in free lime content from 2.0 to 1.3 wt%, when utilizing 30 % SRF by energy. However, comminution of SRF is difficult, and size reduction should be one of the last options to be pursued.

Other options to increase SRF co-firing that have not been investigated here are e.g. oxygen enrichment.

It should be emphasized that an increased clinker production may be pursued instead of alternative fuels firing, if there is enough margin on the free lime content. The choice comes down to a focus on maximizing production contra minimizing production costs, and the best choice for any given cement plant would depend on its market conditions.

9.6 Conclusions

A simplified 1-D model for calculating gas and bed temperatures in the kiln has been developed. The model couples the calculated temperature profiles to the clinker quality, measured as the free lime content. To the author's knowledge, this is the first model that attempts to describe the effects of co-firing alternative fuels by coupling the combustion process and temperatures to the clinker quality.

The model was validated against pilot experiments showing appropriate temperature profiles, gas species concentration, and fuel burnout, for a coal flame without any clinker. Industrial tests described in the literature examined the effect of co-firing meat and bone meal (MBM) and solid hazardous waste (SHW) on the clinker free lime content. The model adequately described the trends of co-firing and specific energy input on the free lime content.

The model was used to investigate co-firing of solid recovered fuel (SRF). Co-firing with SRF reduced gas and bed temperatures in the kiln and resulted in an increased clinker free lime content compared to pure coal firing. This is caused by lower combustion temperatures of the SRF due to a higher air requirement per energy content. The larger particle size and high moisture content of the SRF also lead to a slower combustion rate, which moves the peak temperatures further downstream

in the kiln. This results in reduced temperatures of the clinker that exits the kiln. Consequently, the secondary air temperature is lowered, which also contributes negatively to the temperatures in the kiln.

Different approaches to limit the negative impact of co-firing were investigated using the model. The most promising is to increase the specific energy input of the kiln, by increasing the feed rate of SRF. As an example, when co-firing 30 % SRF by energy, the clinker free lime content is increased from 1.3 to 2.0 wt%. Increasing the SRF feed rate by 10 %, reduces the free lime to 1.4 wt%. Another option is to optimize the burner operation. This may be done by increasing the entrainment rate of secondary air or increase the dispersion of SRF to cause it to burn closer to the burner. This generally increases the bed temperatures and lower clinker free lime. The industrial experiments conducted during this PhD study, confirmed that burner settings, especially increased dispersion of SRF, could increase the clinker quality when co-firing SRF.

10 Final Conclusions

Through the last 20-30 years the cement industry has increased the use of alternative fuels, substituting conventional fossil fuels such as coal and oil. The development has been driven by the possibility to lower operating costs and CO_2 emissions. Furthermore, the use of waste derived fuels in the cement industry reduces the need for landfilling. Alternative fuels can be introduced both in the cement calciner and rotary kiln. The focus of this thesis has been on co-firing in the kiln.

Tests were carried out at three different full-scale cement plants where fossil fired and solid recovered fuel (SRF) co-fired flames were compared, using a specially developed water cooled camera probe. The probe can be inserted into the cement kiln hood, which makes it possible to observe the flames in detail, investigating e.g. ignition point and fuel flow. It was found that co-firing between 30 and 70 % SRF by energy, would delay ignition by approximately 2 meters. The intensity and temperatures of the flames were also lowered. This is caused by the large particle size and high moisture content of the SRF, which takes longer to ignite than fossil fuel. A decrease in kiln drive power consumption was also observed, which further suggests lower temperatures in the kiln. The lower temperature may negatively affect the clinker quality by decreasing the formation of alite.

Furthermore, it was observed how some of the SRF drops out of the flame and burns in contact with the clinker bed. At two of the plants this led to problems with sulfur evaporation or reduced brown clinker. The last plant appeared to be more robust to

these issues related to local reducing conditions. The difference in robustness is not fully understood at the present, but it may be related to sulfur modulus or oxygen availability near the clinker bed.

Recently, FLSmidth A/S developed the Jetflex burner, which was specifically developed for burning alternative fuels. At one of the test plants, the burner was changed to the Jetflex burner. The main difference in burner design was a change from an annular axial air channel to axial air jets. In addition, a more powerful swirl channel was installed, which was placed inside the coal annular channel, thus being closer to the central alternative fuel channel. The design changes benefited the ignition of petcoke and made it possible to disperse SRF in the near burner zone. Measurements of the clinker quality showed a 4 % increase in the alite content when operating with the new burner, which was achieved with an 8 % higher use of SRF.

Additional tests were carried out with the Jetflex burner. The burner was designed with several different possibilities to influence the flame shape. In addition to the conventional changes to burner momentum and swirl intensity, it is also possible to change the direction of the axial air jets and mix pulverized fossil fuel and SRF in a common central channel. The effect of the different changes was studied using the kiln camera probe. For a petcoke flame the ignition point could be changed from approximately 5 to 3.5 meters by adjusting the swirl and axial air jets. SRF co-fired flames were more difficult to ignite, but dispersion of the SRF into the hot secondary air by a high swirl level was possible, which helped ignite the SRF particles.

A statistical analysis of collected operating data using partial least squares regression (PLSR) revealed that higher swirl and directing the axial air nozzles outwards, contribute to increase the clinker alite content when co-firing SRF. Firing petcoke through the central channel with SRF and retracting this channel was also found to have a positive effect. Overall these measures contribute to disperse the SRF near the burner, which presumably increases combustion temperatures in the near burner field during co-firing.

Different SRF samples were collected from cement plants and a physical characterization was performed to study the SRF composition, particle size and shape. The SRF samples were first classified into different terminal velocity ranges using a wind sieve setup. The setup may provide an improved distinction between particle sizes, compared to a normal sieving analysis, which may not be suited for

irregular shaped particles such as SRF. It was shown how light fuels, suited for use in the cement kiln, could be distinguished from heavier fuels, suited for use in the calciner. Based on the initial measurements it is recommended that SRF for use in the main burner should have at least 20 wt% of the sample with a terminal velocity lower than 3 m/s, 60 wt% lower than 5 m/s, and 80 wt% lower than 7 m/s.

Two SRF samples separated in the wind sieve were selected for further detailed analysis. The fraction of biomass and plastic in the samples was determined. Furthermore, the distribution of particle mass and the particle shape, defined as the sphericity, were determined. The average particle mass of samples with a terminal velocity below 2 m/s was around 10 mg, while the mass for particles with a terminal velocity greater than 7 m/s was 600 mg. This corresponds roughly to equivalent diameters of 3 and 12 mm. The shape was also found to change with the terminal velocity. Lighter particles had an average sphericity of 0.1, while the heavier particles had a sphericity of 0.5. With lower mass and higher surface area, it is expected that the particles with low terminal velocity burn significantly faster than those with high terminal velocity.

A one-dimensional model was developed to help understand the impact of co-firing on the temperatures in the kiln. The model describes temperature changes in the gas and clinker bed in the axial direction of the kiln. A simplified clinker model was developed to couple the bed temperature to a clinker quality, measured as the residual free lime content. The model was validated using results obtained from the literature. The coal flame model was validated against experiments performed in a pilot scale rotary kiln simulator, without clinker. Co-firing of meat and bone meal (MBM) and solid hazardous waste (SHW) were also tested with the model, with predictions of clinker free lime content agreeing well with results from industrial tests. The absolute deviation between the free lime content calculated by the model and the experiments was on average 40 % and 20 %, for the MBM and SHW cases, respectively.

Furthermore, the model was used to examine the effects of SRF co-firing on temperatures in the kiln and the clinker free lime content. It was found that co-firing reduced gas and bed temperatures in the kiln, while the peak temperatures were moved further away from the burner. The reduced temperatures resulted in an increased free lime content of the clinker, indicating a reduced clinker quality. The

lower combustion temperatures can be explained by a higher air consumption for the same energy input of SRF compared to coal. In addition, the large and wet SRF particles take longer to convert than coal particles, shifting the temperature peak further into the kiln. Much of the SRF was found to not be converted while in suspension, having a residence time around one second. Only particles with a terminal velocity lower than 2 m/s (as determined in the wind sieve), can be expected to be devolatilized while in suspension in the kiln. Thus, especially larger particles end up burning in the bed. The camera observations of the industrial co-fired flames confirm these findings.

Different methods to decrease the negative impacts of co-firing were investigated. Increasing the energy input of SRF may be the simplest method to mitigate the effects of reduced temperatures. As an example, co-firing of 30 % SRF by energy, was found to increase the clinker free lime to 2.1 wt% compared to 1.3 wt% when firing only coal. By increasing the specific fuel energy input to the kiln by 10 %, it was possible to reduce the free lime content to 1.4 wt%.

Alternatively, increased entrainment of secondary air and dispersion of SRF closer to the burner can also help increase clinker temperatures and decrease clinker free lime. This finding agrees with the conclusions of the performed industrial tests. Pretreatment of the SRF by drying and particle comminution can decrease the conversion time and reduce the clinker free lime content. However, this may be expensive options that require investments in new equipment.

10.1 Suggestions for Future Work

In the industrial tests it was experienced that SRF would burn in contact with the clinker at all three cement plants where tests were performed. At one plant this was found to be very severe, while it was less of an issue at the two other plants. The cause appears to be a difference in the sensitivity towards local reducing conditions, in the form of sulfur evaporation and brown cores in the clinker. A further understanding of what imposes these limitations and how they can be avoided, would serve to increase the possibility for alternative fuels firing.

The characterization of SRF using the wind sieve setup has shown that it is possible to separate particles with different particle size and shape. These factors heavily influence the combustion time. Only a limited number of samples have been

analyzed. A more rigorous analysis of samples from different cement plants, coupled with a knowledge of the limitations and specific challenges experienced at those plants, would be highly beneficial. This could serve as a basis to uncover the relationship between SRF quality and corresponding limitations to co-firing.

The developed model relies on many simplifying assumptions. However, its predictions are still reasonable. It may be hard to significantly increase the accuracy of the model, keeping the model one-dimensional. Especially, the flow of gas and effect of burner settings, which were derived from CFD simulations, and the fuel flow is difficult to resolve in a simple one-dimensional model. Thus, moving forward it is recommended to focus mainly on the use of 3-dimensional CFD simulations. However, the use of a more advanced model is only justified if it can be validated. In addition to the flame images provided here, measurements of temperatures and gas concentrations in a cement kiln, would be desirable.

11 REFERENCES

[1] K. L. Scrivener and R. J. Kirkpatrick, "Innovation in use and research on cementitious material," *Cement and Concrete Research*, vol. 38, no. 2, pp. 128–136, 2008.

[2] S. Telschow, F. Frandsen, K. Theisen, and K. Dam-Johansen, "Cement Formation—A Success Story in a Black Box: High Temperature Phase Formation of Portland Cement Clinker," *Industrial & Engineering Chemistry Research*, vol. 51, no. 34, pp. 10983–11004, 2012.

[3] R. R. Wertz, "Three Gorges Dam," 2011. [Online]. Available: http://www.ibiblio.org/chinesehistory/contents/07spe/specrep01.html. [Accessed: 18-Apr-2018].

[4] P. C. Hewlett, *Lea's Chemistry of Cement and Concrete*, 4th ed. Butterworth-Heinemann, 1998.

[5] J. M. Crow, "The concrete conundrum," *Chemistry World*, pp. 62–66, 2008.

[6] G. C. Bye, *Portland Cement*, 2nd ed. Thomas Telford, 1999.

[7] US Geological Survey, "Mineral Commodities Summaries 2018," Reston, Virginia, USA, 2018.

[8] K. A. Baumert, T. Herzog, and J. Pershing, "Navigating the numbers," World Resources Institute, Washington, DC, USA, 2005.

[9] International Energy Agency (IEA), "Energy Technology Transitions for industry," Paris, France, 2009.

[10] E. Mokrzycki and A. Uliasz- Bochenczyk, "Alternative fuels for the cement industry," *Applied Energy*, vol. 74, no. 1–2, pp. 95–100, 2003.

[11] F. Schorct, I. Kourti, B. M. Scalet, S. Roudier, and L. D. Sancho, "Best Available Techniques (BAT) Reference Document for the Production of Cement, Lime and Magnesium Oxide," Sevilla, Spain, 2013.

[12] International Energy Agency (IEA), *Energy Technology Perspectives: Scenarios & Strategies*

To 2050. Paris, France, 2010.

[13] H. F. W. Taylor, *Cement Chemistry*, 2nd ed. London, United Kingdom: Thomas Telford, 1997.

[14] A. R. Nielsen, "Combustion of Large Solid Fuels in Cement Rotary Kilns," PhD Thesis, Technical University of Denmark, 2012.

[15] O. Labahn and B. Kohlhaas, *Cement Engineers' Handbook*, 4th ed. Bauverlag GMBH, Wiesbaden, Germany, 1983.

[16] F. M. Miller, "Raw Mix Design Considerations," in *Innovations in Portland Cement Manufacturing*, 1st ed., J. I. Bhatty, F. M. Miller, S. H. Kosmatka, and R. P. Bohan, Eds. Skokie, Illinois, USA: Portland Cement Association, 2011, pp. 193–207.

[17] G. L. Young and F. M. Miller, "Kiln System Operations in Cement Manufacturing," in *Innovations in Portland Cement Manufacturing*, 1st ed., J. I. Bhatty, F. M. Miller, S. H. Kosmatka, and R. P. Bohan, Eds. Skokie, Illinois, USA: Portland Cement Association, 2011, pp. 311–342.

[18] FLSmidth A/S, "Preheater Calciner Systems," Copenhagen, Denmark, 2013.

[19] IEA, "Cement Technology Roadmap: Carbon Emissions Reductions up to 2050," Paris, France, 2009.

[20] CEN (European Committee for Standardization), "EN 197-1:2011; Cement – Part 1: Composition, specifications and conformity criteria for common cements." 2011.

[21] J. Thomas and H. Jennings, "Mineral and Oxide Composition of Portland Cement." [Online]. Available: http://iti.northwestern.edu/cement/monograph/Monograph3_6.html. [Accessed: 05-Apr-2018].

[22] K. Theisen, "The International Cement Production Seminar 2007, Volume II." FLSmidth A/S, Valby, Denmark, 2007.

[23] K. Theisen, E. Jøns, and B. Osbæck, "Cement Clinkering: Chemical and Physical Aspects," in *Innovations in Portland Cement Manufacturing*, 1st ed., J. I. Bhatty, F. M. Miller, S. H. Kosmatka, and R. P. Bohan, Eds. Skokie, Illinois, USA: Portland Cement Association, 2011, pp. 365–400.

[24] R. H. Bogue, "Calculation of the Compounds in Portland Cement," *Industrial and Engineering Chemistry Analytical Edition*, vol. 1, no. 4, pp. 192–197, 1929.

[25] I. F. Petersen and V. Johansen, "Burnability and clinker nodule formation from a statistical point of view," *Cement and Concrete Research*, vol. 9, no. 5, pp. 631–639, 1979.

[26] L. M. Hills, V. Johansen, and F. M. Miller, "Solving Raw Material Challenges," in *IEEE-IAS/PCA 44th Cement Industry Technical Conference*, 2002, pp. 139–151.

[27] A. A. Boateng, *Rotary Kilns Transport Phenomena and Transport Process*, 1st ed. Oxford, UK: Butterworth-Heinemann, 2008.

[28] M. B. Larsen, "Alternative Fuels in Cement Production," PhD Thesis, Technical University of Denmark, Kgs. Lyngby, Denmark, 2007.

[29] FLSmidth A/S, “ACC Wadi’s expanded plant sets world records,” 2011. .

[30] R. Wirthwein and B. Emberger, “Burners for alternative fuels utilisation - Optimization of kiln firing systems for advanced alternative fuel co-firing,” *Cement International*, vol. 8, no. 4, pp. 42–46, 2010.

[31] L. K. Nørskov, “Combustion of Solid Alternative Fuels in the Cement Kiln Burner,” PhD Thesis, Technical University of Denmark, 2012.

[32] P. J. Mullinger, “Burner design for coal fired cement kilns,” *World Cement*, pp. 348–353, Dec-1984.

[33] D. Moore, “Grate Coolers,” 2017. [Online]. Available: http://www.cementkilns.co.uk/cooler_grate.html. [Accessed: 01-Apr-2018].

[34] K. E. Peray and J. J. Waddell, *The Rotary Cement Kiln*. New York: Chemical Publishing Co., Inc., 1972.

[35] R. H. Nobis, “Latest rotary kiln burner technology: Possibilities and experiences,” *IEEE Transactions on Industry Applications*, vol. 27, no. 5, pp. 798–806, 1991.

[36] A. Wagner, “Aerodynamic features of a rotary kiln burner with multijet outflow of the primary air,” *Cement International*, vol. 2, pp. 88–97, 2004.

[37] A. Schall, “Burner operation and flame characteristics of kiln firing systems,” in *ECRA Seminar*, 2017.

[38] D. Moore, “Firing Systems,” 2014. [Online]. Available: http://www.cementkilns.co.uk/ck_firing.html. [Accessed: 01-Jun-2017].

[39] C. Greco, G. Picciotti, R. M. Greco, and G. M. Ferreira, “Fuel Selection and Use,” in *Innovations in Portland Cement Manufacturing*, 1st ed., J. I. Bhatty, F. M. Miller, S. H. Kosmatka, and R. P. Bohan, Eds. Skokie, Illinois, USA: Portland Cement Association, 2011, pp. 239–308.

[40] T. M. Lowes and L. P. Evans, “The effect of burner design and operating parameters on flame shape, heat transfer, NOx and SO3 cycles,” *Zement-Kalk-Gips*, no. 12, pp. 761–768, 1993.

[41] T. M. Lowes and L. P. Evans, “Optimisation of the design and operation of coal flames in cement kilns,” *Journal of the Institute of Energy,* pp. 220–228, Dec-1989.

[42] M. H. Vaccaro, “Low NOx rotary kiln burner technology: design principles & case study,” in *2002 IEEE Cement Industry Technical Conference*, 2002, pp. 265–270.

[43] P. B. Nielsen and O. L. Jepsen, “An overview of the formation of SOx and NOx in various pyroprocessing systems,” *IEEE Transactions on Industry Applications*, vol. 27, no. 3, pp. 431–439, 1991.

[44] S. Gajewski and V. Hoenig, “Influence of pulverized coal fineness on the formation of NOx in rotary kilns in the cement industry,” *ZKG International*, no. 1, pp. 44–53, 1999.

[45] M. Vaccaro, “Burning alternative fuels in rotary cement kilns,” in *2006 IEEE Cement Industry*

Technical Conference, 2006, pp. 127–136.

[46] B. Emberger and V. Hoenig, "Rotary kiln burner technology for alternative fuel co-firing," *Cement International*, vol. 9, no. 5, pp. 48–60, 2011.

[47] X. D'Hubert, "There's no such thing as a 'Perfect' burner," *Global Cement Magazine*, pp. 12–23, Feb-2017.

[48] X. D'Hubert, "Latest Burner Profiles," *Global Cement Magazine*, pp. 10–18, Mar-2017.

[49] O. A. Ahmed and K. R. Osman, "The Rise of Coal Mills in the Egyptian Cement Sector," *Global Cement Magazine*, pp. 61–63, Jul-2017.

[50] P. J. Mullinger and B. G. Jenkins, "Petroleum coke firing of rotary kilns," *World Cement*, no. 2, pp. 48–56, 1987.

[51] G. Roy, "Petcoke combustion characteristics," *World cement*, vol. 33, no. 4, 2002.

[52] J. Chen and X. Lu, "Progress of petroleum coke combusting in circulating fluidized bed boilers-A review and future perspectives," *Resources, Conservation and Recycling*, vol. 49, no. 3, pp. 203–216, 2007.

[53] A. R. Nielsen, M. B. Larsen, P. Glarborg, and K. Dam-Johansen, "Sulfur Release from Cement Raw Materials during Solid Fuel Combustion," *Energy & Fuels*, vol. 25, no. 9, pp. 3917–3924, 2011.

[54] M. D. M. Cortada Mut, L. K. Nørskov, P. Glarborg, and K. Dam-Johansen, "SO2 release as a consequence of alternative fuel combustion in cement rotary kiln inlets," *Energy and Fuels*, vol. 29, no. 4, pp. 2729–2737, 2015.

[55] ASTM International, "ASTM D396-16 Standard Specification for Fuel Oils," West Conshohocken, Pennsylvania, USA, 2016.

[56] A. A. Usón, A. M. López-Sabirón, G. Ferreira, and E. Llera Sastresa, "Uses of alternative fuels and raw materials in the cement industry as sustainable waste management options," *Renewable and Sustainable Energy Reviews*, vol. 23, pp. 242–260, 2013.

[57] A. Murray and L. Price, "Use of Alternative Fuels in Cement Manufacture: Analysis of Fuel Characteristics and Feasibility for Use in the Chinese Cement Sector," Berkeley, California, USA, 2008.

[58] J. Fellner and H. Rechberger, "Abundance of 14C in biomass fractions of wastes and solid recovered fuels," *Waste Management*, vol. 29, no. 5, pp. 1495–1503, 2009.

[59] G. Habert, C. Billard, P. Rossi, C. Chen, and N. Roussel, "Cement production technology improvement compared to factor 4 objectives," *Cement and Concrete Research*, vol. 40, no. 5, pp. 820–826, 2010.

[60] K. H. Karstensen, "Formation, release and control of dioxins in cement kilns," *Chemosphere*, vol. 70, no. 4, pp. 543–560, 2008.

[61] Cembureau, "Environmental Benefits of Using Alternative Fuels in Cement Production," Brussels, Belgium, 1999.

[62] WBCSD, "Getting the Numbers Right Database," 2015. [Online]. Available: https://www.wbcsdcement.org/GNR-2013/index.html. [Accessed: 01-Jun-2016].

[63] WBCSD, "Global Cement Database on CO2 and Energy Information," 2015. [Online]. Available: http://www.wbcsdcement.org/index.php/key-issues/climate-protection/GNR-database. [Accessed: 01-Jun-2016].

[64] European Parliament and Council, *Directive 2008/98/EC on Waste and Repealing Certain Directives*. 2008.

[65] European Parliament and Council, *Directive 2000/76/EC on the Incineration of Waste*. 2000.

[66] World Business Council for Sustainable Development (WBCSD), "Getting the Numbers Right: Cement Industry Energy and CO2 Performance," Geneva, Switzerland, 2011.

[67] Verein Deutscher Zementwerke (VDZ), "Environmental Data of the German Cement Industry 2015," Düsseldorf, 2016.

[68] G. Mauschitz, "Emissionen aus Anlagen der Österreichischen Zementindustrie 2015," Vienna, 2016.

[69] A. Gendebien, A. Leavens, K. Blackmore, *et al.*, "Refuse Derived Fuel, Current Practice and Perspectives," Swindon, UK, 2003.

[70] European Commission, *M/325 Mandate to CEN on Solid Recovered Fuels (SRF)*. Brussels, Belgium, 2002.

[71] CEN (European Committee for Standardization), "CEN/TC 343 - Solid Recovered Fuels," Brussels, Belgium, 2012.

[72] L. F. Diaz, G. M. Savage, and L. L. Eggerth, "Production of Refuse-Derived Fuel (RDF)," in *Solid Waste Management*, United Nations Environment Program (UNEP), 2005, pp. 295–302.

[73] C. A. Velis, P. J. Longhurst, G. H. Drew, R. Smith, and S. J. T. Pollard, "Production and quality assurance of solid recovered fuels using Mechanical- Biological Treatment (MBT) of waste: A comprehensive assessment," *Critical Reviews in Environmental Science and Technology*, vol. 40, no. 12, pp. 979–1105, 2010.

[74] B. Krüger, A. Mrotzek, and S. Wirtz, "Separation of harmful impurities from refuse derived fuels (RDF) by a fluidized bed," *Waste Management*, vol. 34, no. 2, pp. 390–401, 2014.

[75] R. Sarc and K. E. Lorber, "Production, quality and quality assurance of Refuse Derived Fuels (RDFs)," *Waste Management*, vol. 33, no. 9, pp. 1825–1834, 2013.

[76] V. S. Rotter, T. Kost, J. Winkler, and B. Bilitewski, "Material flow analysis of RDF-production processes," *Waste Management*, vol. 24, no. 10, pp. 1005–1021, 2004.

[77] P. Vainikka, D. Bankiewicz, A. Frantsi, *et al.*, "High temperature corrosion of boiler waterwalls

induced by chlorides and bromides. Part 1: Occurrence of the corrosive ash forming elements in a fluidised bed boiler co-firing solid recovered fuel," *Fuel*, vol. 90, no. 5, pp. 2055–2063, 2011.

[78] FLSmidth A/S, "Feedex overhead reclaimer," 2014. [Online]. Available: http://www.flsmidth.com/en-US/Industries/Categories/Operation/Alternative+fuels+solutions/Feedex+overhead+reclaimer. [Accessed: 01-Jan-2017].

[79] F. C. Lockwood and J. J. Ou, "Review: burning refuse derived fuel in a rotary cement kiln," *Proceedings of the Institution of Mechanical Engineers, Part A: Journal of Power and Energy*, vol. 207, pp. 65–70, 1993.

[80] J. Haas, A. Agostini, C. Martens, and E. Carrea, "The combustion of pulverized coal and alternative fuels in cement kilns. Results on the CEMFLAME-3 Experiments," IJmuiden, Netherlands, 1999.

[81] W. K. H. Ariyaratne, M. C. Melaaen, K. Eine, and L. a Tokheim, "Meat and Bone Meal as a Renewable Energy Source in Cement Kilns : Investigation of Optimum Feeding Rate," in *International Conference on Renewable Energies and Power Quality (ICREPQ'11)*, 2010.

[82] W. K. H. Ariyaratne, M. C. Melaaen, and L. A. Tokheim, "Optimum feeding rate of solid hazardous waste in a cement kiln burner," *International Journal of Energy and Environment*, vol. 4, no. 5, pp. 777–786, 2013.

[83] W. K. H. Ariyaratne, A. Malagalage, M. C. Melaaen, and L.-A. Tokheim, "CFD Modeling of Meat and Bone Meal Combustion in a Rotary Cement Kiln," *International Journal of Modeling and Optimization*, vol. 4, no. 4, pp. 263–272, 2014.

[84] W. K. H. Ariyaratne, E. V. P. J. Manjula, M. C. Melaaen, and L.-A. Tokheim, "Mathematical Model for Alternative Fuel Combustion in a Rotary Cement Kiln Burner," *International Journal of Modeling and Optimization*, vol. 4, no. 1, pp. 56–61, 2014.

[85] C. Di Blasi, "Combustion and gasification rates of lignocellulosic chars," *Progress in Energy and Combustion Science*, vol. 35, no. 2, pp. 121–140, 2009.

[86] M. Momeni, C. Yin, S. K. Kær, T. B. Hansen, P. A. Jensen, and P. Glarborg, "Experimental Study on Effects of Particle Shape and Operating Conditions on Combustion Characteristics of Single Biomass Particles," *Energy & Fuels*, vol. 27, no. 1, pp. 507–514, 2013.

[87] P. E. Mason, L. I. Darvell, J. M. Jones, M. Pourkashanian, and A. Williams, "Single particle flame-combustion studies on solid biomass fuels," *Fuel*, vol. 151, pp. 21–30, 2015.

[88] R. Klaska, S. Baetzner, H. Moller, M. Paul, and T. Roppelt, "Effects of secondary fuels on clinker mineralogy," *Cement International*, vol. 1, no. 4, pp. 88–98, 2003.

[89] S. Uda, E. Asakura, and M. Nagashima, "Influence of SO3 on the Phase Relationship in the System CaO-SiO2-Al2O3-Fe2O3," *Journal of the American Ceramic Society*, vol. 81, no. 3, pp.

725–729, 2005.

[90] H. E. Belkin, S. J. Tewalt, J. C. Hower, *et al.*, "Petrography and geochemistry of Oligocene bituminous coal from the Jiu Valley, Petrosani basin (southern Carpathian Mountains), Romania," *International Journal of Coal Geology*, vol. 82, no. 1–2, pp. 68–80, 2010.

[91] O. G. Duliu, O. A. Culicov, I. Rădulescu, C. Cristea, and T. Vasiu, "Major, trace, and natural radioactive elements in bituminous coal from Australia, Romania, Russia, South Africa and Ukraine: A comparative study," *Journal of Radioanalytical and Nuclear Chemistry*, vol. 264, no. 3, pp. 525–534, 2005.

[92] J. M. Commandré and S. Salvador, "Lack of correlation between the properties of a petroleum coke and its behaviour during combustion," *Fuel Processing Technology*, vol. 86, no. 7, pp. 795–808, 2005.

[93] M. Bläsing, K. Nazeri, and M. Müller, "Fate of sulfur, chlorine, alkali metal, and vanadium species during high-temperature gasification of Canadian tar sand products," *Energy and Fuels*, vol. 28, no. 10, pp. 6345–6350, 2014.

[94] D. Moore, "Oil Data," 2011. [Online]. Available: http://www.cementkilns.co.uk/data_oil.html. [Accessed: 01-Jan-2017].

[95] J. M. Heikkinen, J. C. Hordijk, W. De Jong, and H. Spliethoff, "Thermogravimetry as a tool to classify waste components to be used for energy generation," *Journal of Analytical and Applied Pyrolysis*, vol. 71, no. 2, pp. 883–900, 2004.

[96] A. Trubetskaya, P. A. Jensen, A. D. Jensen, A. D. Garcia Llamas, K. Umeki, and P. Glarborg, "Effect of fast pyrolysis conditions on biomass solid residues at high temperatures," *Fuel Processing Technology*, vol. 143, pp. 118–129, 2016.

[97] J. M. Lee, D. W. Kim, J. S. Kim, J. G. Na, and S. H. Lee, "Co-combustion of refuse derived fuel with Korean anthracite in a commercial circulating fluidized bed boiler," *Energy*, vol. 35, no. 7, pp. 2814–2818, 2010.

[98] U. Kääntee, R. Zevenhoven, R. Backman, and M. Hupa, "Cement manufacturing using alternative fuels and the advantages of process modelling," *Fuel Processing Technology*, vol. 85, no. 4, pp. 293–301, 2004.

[99] J. Maier, A. Gerhardt, and G. Dunnu, "Experiences on Co-firing Solid Recovered Fuels in the Coal Power Sector," in *Solid Biofuels for Energy*, 1st ed., P. Grammelis, Ed. London: Springer, 2011, pp. 75–94.

[100] R. Sarc, K. Lorber, R. Pomberger, M. Rogetzer, and E. Sipple, "Design, quality, and quality assurance of solid recovered fuels for the substitution of fossil feedstock in the cement industry," *Waste management & research*, vol. 32, no. 7, pp. 565–585, 2014.

[101] FLSmidth A/S and FLSmidth, "HOTDISC combustion device," Copenhagen, Denmark, 2011.

[102] Thyssenkrupp AG, "Prepol-SC," Beckum, Germany.

[103] L. F. De Diego, F. Garcia-Labiano, A. Abad, P. Gaya, and J. Adanez, "Coupled drying and devolatilisation of non-spherical wet pine wood particles in fluidised beds," vol. 65, pp. 173–184, 2002.

[104] E. N. Tackie, A. P. Watkinson, and J. K. Brimacombe, "Experimental Study of the Elutriation of Particles from Rotary Kilns," *The Canadian Journal of Chemical Engineering*, vol. 67, pp. 806–817, 1989.

[105] M. Fardadi, "Modeling Dust Formation in Lime Kilns," PhD Thesis, University of Toronto, 2010.

[106] G. R. Long, "Microstructure and Chemistry of Unhydrated Cements," *Philosphical Transactions of the Royal Society A*, vol. 310, pp. 43–51, 1983.

[107] F. W. Locher, "Influence of burning conditions on clinker characteristics," *World Cement Technology*, vol. 11, no. 2, pp. 67–73, 1980.

[108] M. Ichikawa and Y. Komukai, "Effect of burning conditions and minor components on the color of portland cement clinker," *Cement and Concrete Research*, vol. 23, no. 4, pp. 933–938, 1993.

[109] M. Clark, "Brown cores," *International Cement Review*, pp. 46–47, Dec-2006.

[110] Holderbank Cement, "Holderbank Cement Seminar - Circulation Phenomena in the Clinkerization Process," Holderbank Cement, Jona, Switzerland, 2000.

[111] G.-S. Choi and F. Glasser, "The sulphur cycle in cement kilns: Vapour pressures and solid-phase stability of the sulphate phases," *Cement and Concrete Research*, vol. 18, no. 3, pp. 367–374, 1988.

[112] M. D. M. Cortada Mut, "Interactions between solid fuels and raw materials in cement rotary kilns," PhD Thesis, Technical University of Denmark, 2013.

[113] A. H. Mortensen, A. Hintsteiner, and P. Rosholm, "Converting two kiln lines to 100% high sulphur petroleum coke firing," *ZKG International*, vol. 51, no. 4, pp. 184–196, 1998.

[114] I. R. Dominguez, J. Gómez-Millán, M. Alvarez, S. De Aza, L. Contreras, and A. H. De Aza, "Build-up formation and corrosion of monolithic refractories in cement kiln preheaters," *Journal of the European Ceramic Society*, vol. 30, no. 9, pp. 1879–1885, 2010.

[115] W. Kurdowski and M. Soboń, "Mineral composition of build-up in cement kiln preheater," *Journal of Thermal Analysis and Calorimetry*, vol. 55. pp. 1021–1029, 1999.

[116] H. Bolio-Arceo and F. P. Glasser, "Formation of spurrite, Ca5(SiO4)2CO3," *Cement and Concrete Research*, vol. 20, no. 2, pp. 301–307, 1990.

[117] E. Jøns and M. J. L. Østergard, "Kiln Shell Corrosion," in *IEEE-IAS/PCA Cement Industry Technical Conference*, 2001, pp. 343–359.

[118] A. R. Nielsen, M. B. Larsen, P. Glarborg, and K. Dam-Johansen, "High-temperature release of SO2 from calcined cement raw materials," *Energy and Fuels*, vol. 25, no. 7, pp. 2917–2926,

2011.

[119] M. D. M. Cortada Mut, L. K. Nørskov, F. J. Frandsen, P. Glarborg, and K. Dam-Johansen, "Review: Circulation of Inorganic Elements in Combustion of Alternative Fuels in Cement Plants," *Energy and Fuels*, vol. 29, no. 7, pp. 4076–4099, 2015.

[120] K. Sutoh, M. Murata, and N. Ueno, "Stable kiln operation achived by chlorine bypass system," *World cement*, vol. 29, no. 2, pp. 47–51, 1998.

[121] E. M. Sipple, "The ReduDust process – production of salt in the cement plant," *ZKG International*, 2015. [Online]. Available: http://www.zkg.de/en/artikel/zkg_The_ReduDust_process_production_of_salt_in_the_cement_plant_2452179.html. [Accessed: 01-Jan-2017].

[122] E. M. Sipple and J. Mülnner, "A green building in a grey cement plant – Transforming bypass dust into industrial salt with the ReduDust Process," *ZKG International*, no. 11, 2015.

[123] M. P. Javellana and I. Jawed, "Extraction of free lime in portland cement and clinker by ethylene glycol," *Cement and Concrete Research*, vol. 12, no. 3, pp. 399–403, 1982.

[124] D. Broton and J. I. Bhatty, "Analytical Techniques in Cement Materials Characterization," in *Innovations in Portland Cement Manufacturing*, 1st ed., J. I. Bhatty, F. M. Miller, S. H. Kosmatka, and R. P. Bohan, Eds. Skokie, Illinois, USA: Portland Cement Association, 2011, pp. 1373–1424.

[125] L. J. Struble, L. A. Graf, and J. I. Bhatty, "X-Ray Diffraction Analysis," in *Innovations in Portland Cement Manufacturing*, 1st ed., J. I. Bhatty, F. M. Miller, S. H. Kosmatka, and R. P. Bohan, Eds. Skokie, Illinois, USA: Portland Cement Association, 2011, pp. 1425–1482.

[126] G. Kychakoff and A. F. Hollingshead, "Acoustic Pyrometry in Cement Manufacturing," in *Innovations in Portland Cement Manufacturing*, 1st ed., J. I. Bhatty, F. M. Miller, S. H. Kosmatka, and R. P. Bohan, Eds. Skokie, Illinois, USA: Portland Cement Association, 2011, pp. 557–570.

[127] M. C. Mound and C. Colbert, "Automation and Optimization in the Cement Plant," in *Innovations in Portland Cement Manufacturing*, 1st ed., J. I. Bhatty, F. M. Miller, S. H. Kosmatka, and R. P. Bohan, Eds. Skokie, Illinois, USA: Portland Cement Association, 2011, pp. 823–868.

[128] K. B. Floor and F. M. Miller, "Inlet Gas Analysis in Cement Operations," in *Innovations in Portland Cement Manufacturing*, 1st ed., J. I. Bhatty, F. M. Miller, S. H. Kosmatka, and R. P. Bohan, Eds. Skokie, Illinois, USA: Portland Cement Association, 2011, pp. 571–588.

[129] R. P. Brower, J. P. S. Seinfield, and S. Akhtar, "NOx control and SNCR," in *Innovations in Portland Cement Manufacturing*, 1st ed., J. I. Bhatty, F. M. Miller, S. H. Kosmatka, and R. P. Bohan, Eds. Skokie, Illinois, USA: Portland Cement Association, 2011, pp. 1017–1038.

[130] B. Lin and S. B. Jørgensen, "Soft sensor design by multivariate fusion of image features and process measurements," *Journal of Process Control*, vol. 21, no. 4, pp. 547–553, 2011.

[131] Verein Deutscher Zementwerke (VDZ), "VDZ Activity Report 2005-2007," Düsseldorf, Germany, 2008.

[132] D. Schmidt, "Highly efficient burning of clinker using flame analysis and NMPC," in *2007 IEEE Cement Industry Technical Conference*, 2007, pp. 140–146.

[133] J. P. Kemmerer, "Refractory management with a high speed kiln shell scanner," in *IEEE Technical Conference on cement Industry*, 1990, pp. 237–251.

[134] M. N. Pedersen, M. Nielsen, S. Clausen, P. A. Jensen, L. S. Jensen, and K. Dam-Johansen, "Imaging of Flames in Cement Kilns To Study the Influence of Different Fuel Types," *Energy & Fuels*, vol. 31, no. 10, pp. 11424–11438, 2017.

[135] N. A. Chigier, "Gasdynamics of swirling flow in combustion systems," *Astronautica Acta*, vol. 17, pp. 387–395, 1972.

[136] F. D. Moles, D. Watson, and P. B. Lain, "The aerodynamics of the rotary cement kiln," *Journal of the Institute of Fuel*, pp. 353–362, 1973.

[137] H. E. Borgholm, D. Herfort, and S. Rasmussen, "A New Blended Cement Based on Mineralised Clinker," *World Cement*, no. 8, pp. 27–33, 1995.

[138] G. K. Moir, "Improvements in the Early Strength Properties of Portland Cement," *Philosophical Transactions of the Royal Society A: Mathematical and Physical*, vol. 310, no. 1511, pp. 127–138, 1983.

[139] A. Emanuelson, S. Hansen, and E. Viggh, "A comparative study of ordinary and mineralised Portland cement clinker from two different production units: Part I: Composition and hydration of the clinkers," *Cement and Concrete Research*, vol. 33, no. 10, pp. 1613–1621, 2003.

[140] J. I. Bhatty, "Use of Fluxes and Mineralizers in the Cement Industry: A Survey," Portland Cement Association, R&D Serial 2045; Skokie, Illinois, USA, 1996.

[141] J. Benesty, J. Chen, Y. Huang, and I. Cohen, "Pearson Correlation Coefficient," in *Noise Reduction in Speech Processing*, vol. 2, Berlin: Springer, 2009, pp. 37–40.

[142] W. M. Haynes, Ed., *CRC Handbook of Chemistry and Physics*, 97th ed. Boca Raton, FL, USA: CRC Press/Taylor & Francis, 2016.

[143] B. Liedmann, S. Wirtz, V. Scherer, and B. Krüger, "Numerical Study on the Influence of Operational Settings on Refuse Derived Fuel Co-firing in Cement Rotary Kilns," *Energy Procedia*, vol. 120, pp. 254–261, 2017.

[144] N. Syred and J. M. Beér, "Combustion in Swirling Flows: a Review," *Combustion and Flame*, vol. 23, no. 2, 1974.

[145] FLSmidth A/S, "JETFLEX Burner," Copenhagen, Denmark, 2017.

[146] A. J. Chapman and W. F. Walker, *Introductory Gas Dynamics*, 1st ed. Holt, Rinehart and Winston, Inc, 1971.

[147] J. M. Beér and N. A. Chigier, "Stability and Combustion Intensity of Pulverized-Coal Flames-

Effect of Swirl and Impingement," *Journal of the Institute of Fuel*, vol. 42, no. 347, pp. 443–450, 1969.

[148] A. K. Gupta, D. G. Lilley, and N. Syred, *Swirl Flows*. Tunbridge Wells, UK: Abacus Press, 1984.

[149] P. Geladi and B. R. Kowalski, "Partial least-squares regression: a tutorial," *Analytica Chimica Acta*, vol. 185, no. C, pp. 1–17, 1986.

[150] H. Abdi, "Partial least squares regression and projection on latent structure regression," *Wiley Interdisciplinary Reviews: Computational Statistics*, vol. 2, pp. 97–106, 2010.

[151] S. Wold, M. Sjöström, and L. Eriksson, "PLS-regression: A basic tool of chemometrics," *Chemometrics and Intelligent Laboratory Systems*, vol. 58, no. 2, pp. 109–130, 2001.

[152] T. Kourti and J. F. MacGregor, "Process analysis, monitoring and diagnosis, using multivariate projection methods," *Chemometrics and intelligent laboratory systems*, vol. 28, pp. 3–21, 1995.

[153] L. Eriksson, P. Hagberg, E. Johansson, *et al.*, "Multivariate process monitoring of a newsprint mill. Application to modelling and predicting COD load resulting from de-inking of recycled paper," *Journal of Chemometrics*, vol. 15, no. 4, pp. 337–352, 2001.

[154] B. Lin, B. Recke, J. K. H. Knudsen, and S. B. Jørgensen, "A systematic approach for soft sensor development," *Computers & Chemical Engineering*, vol. 31, no. 5–6, pp. 419–425, 2007.

[155] B. Lin, B. Recke, T. M. Schmidt, J. K. H. Knudsen, and S. B. Jørgensen, "Data-Driven Soft Sensor Design with Multiple-Rate Sampled Data: A Comparative Study," *Industrial & Engineering Chemistry Research*, vol. 48, no. 11, pp. 5379–5387, 2009.

[156] E. Marengo, M. Bobba, E. Robotti, and M. C. Liparota, "Modeling of the polluting emissions from a cement production plant by partial least-squares, principal component regression, and artificial neural networks," *Environmental Science and Technology*, vol. 40, no. 1, pp. 272–280, 2006.

[157] T. Mehmood, K. H. Liland, L. Snipen, and S. Sæbø, "A review of variable selection methods in Partial Least Squares Regression," *Chemometrics and Intelligent Laboratory Systems*, vol. 118, pp. 62–69, 2012.

[158] J. Josse and F. Husson, "Selecting the number of components in principal component analysis using cross-validation approximations," *Computational Statistics and Data Analysis*, vol. 56, no. 6, pp. 1869–1879, 2012.

[159] T. Hastie, R. Tibshirani, and J. Friedman, *The Elements of Statistical Learning*, 2nd ed. New York, USA: Springer, 2009.

[160] European Comittee for Standardization (CEN), "EN 15359 - Solid recovered fuels. Specifications and classes," Brussels, Belgium, 2011.

[161] M. Nakhaei, M. N. Pedersen, H. Wu, *et al.*, "Aerodynamic and Physical Characterization of Refuse Derived Fuel," *Energy and Fuels (Manuscript)*.

[162] B. Liedmann, W. Arnold, B. Krüger, *et al.*, "An approach to model the thermal conversion and flight behaviour of Refuse Derived Fuel," *Fuel*, vol. 200, pp. 252–271, 2017.

[163] B. Liedmann, W. Arnold, S. Wirtz, *et al.*, "Refuse Derived Fuel Co-Firing in Cement Rotary Kilns – A methodology to specify a customized fuel by numerical simulation and fuel characterisation," in *10th European Conference on Industrial Furnaces and Boilers*, 2015, pp. 1–11.

[164] P. Grammelis, P. Basinas, A. Malliopoulou, and G. Sakellaropoulos, "Pyrolysis kinetics and combustion characteristics of waste recovered fuels," *Fuel*, vol. 88, no. 1, pp. 195–205, 2009.

[165] D. Montané, S. Abelló, X. Farriol, and C. Berrueco, "Volatilization characteristics of solid recovered fuels (SRFs)," *Fuel Processing Technology*, vol. 113, pp. 90–96, 2013.

[166] L. Sørum, M. G. Gronli, and J. E. Hustad, "Pyrolysis characteristics and kinetics of municipal solid wastes," *Fuel*, vol. 80, no. 9, pp. 1217–1227, 2001.

[167] J. Brandsch and O. G. Piringer, "Characteristics of Plastic Materials," in *Plastic Packaging: Interactions with Food and Pharmaceuticals*, 2nd ed., O. G. Piringer and A. L. Baner, Eds. Wiley, 2008, pp. 15–61.

[168] S. M. Al-Salem, P. Lettieri, and J. Baeyens, "The valorization of plastic solid waste (PSW) by primary to quaternary routes: From re-use to energy and chemicals," *Progress in Energy and Combustion Science*, vol. 36, no. 1, pp. 103–129, 2010.

[169] Q. Chen and T. Zhao, "The thermal decomposition and heat release properties of the nylon/cotton, polyester/cotton and Nomex/cotton blend fabrics," *Textile Research Journal*, vol. 86, no. 17, pp. 1859–1868, 2016.

[170] G. Dunnu, T. Hilber, and U. Schnell, "Advanced Size Measurements and Aerodynamic Classification of Solid Recovered Fuel Particles," *Energy & Fuels*, vol. 20, no. 4, pp. 1685–1690, 2006.

[171] E. Alakangas, "Quality Guidelines for Wood Fuels in Finland VTT-M-04712-15," Jyvaskyla, Finland, 2015.

[172] P. Rosin and E. Rammler, "Laws governing the fineness of powdered coal," *Journal of the Institute of Fuel*, vol. 7, pp. 29–36, 1933.

[173] P. A. Vesilind, "The Rosin-Rammler particle size distribution," *Resource Recovery and Conservation*, vol. 5, no. 3, pp. 275–277, 1980.

[174] G. M. Savage and G. J. Trezek, "Significance of Size Reduction in Solid Waste Management," Washington, DC, 1980.

[175] H. Lu, E. Ip, J. Scott, P. Foster, M. Vickers, and L. L. Baxter, "Effects of particle shape and size on devolatilization of biomass particle," *Fuel*, vol. 89, no. 5, pp. 1156–1168, 2010.

[176] Z. Lu, J. Jian, P. A. Jensen, H. Wu, and P. Glarborg, "Influence of Torrefaction on Single Particle Combustion of Wood," *Energy and Fuels*, vol. 30, no. 7, pp. 5772–5778, 2016.

[177] UL Prospector, "Polyethylene," 2018. [Online]. Available: https://plastics.ulprospector.com/generics/27/polyethylene-pe. [Accessed: 11-Mar-2018].

[178] M. Imber and V. Paschkis, "A new theory for a rotary-kiln heat exchanger," *International Journal of Heat and Mass Transfer*, vol. 5, no. 7, pp. 623–638, 1962.

[179] J. K. Brimacombe and A. P. Watkinson, "Heat transfer in a direct-fired rotary kiln: I. Pilot plant and experimentation," *Metallurgical Transactions B*, vol. 9, no. 3, pp. 201–208, 1978.

[180] A. P. Watkinson and J. K. Brimacombe, "Heat transfer in a direct-fired rotary kiln: II. Heat flow results and their interpretation," *Metallurgical Transactions B*, vol. 9, no. 3, pp. 209–219, 1978.

[181] J. P. Gorog, J. K. Brimacombe, and T. N. Adams, "Radiative heat transfer in rotary kilns," *Metallurgical Transactions B*, vol. 12, no. 1, pp. 55–70, 1981.

[182] J. P. Gorog, T. N. Adams, and J. K. Brimacombe, "Regenerative Heat Transfer in Rotary Kilns," *Metallurgical Transactions B*, vol. 13, no. 2, pp. 153–163, 1982.

[183] J. P. Gorog, T. N. Adams, and J. K. Brimacombe, "Heat transfer from flames in a rotary kiln," *Metallurgical Transactions B*, vol. 14, no. 3, pp. 411–424, 1983.

[184] P. V. Barr, J. K. Brimacombe, and A. P. Watkinson, "A Heat-Transfer Model for the Rotary Kiln: Part I. Pilot Kiln Trials," *Metallurgical Transactions B*, vol. 20B, no. 3, pp. 391–402, 1989.

[185] P. V. Barr, J. K. Brimacombe, and A. P. Watkinson, "A Heat-Transfer Model for the Rotary Kiln: Part II. Development of Cross Sectional Model," *Metallurgical Transactions B*, vol. 20B, no. 3, pp. 403–419, 1989.

[186] J. M. Beér and N. A. Chigier, *Combustion Aerodynamics*. London, UK: Applied Science Publishers, 1972.

[187] F. P. Ricou and D. B. Spalding, "Measurements of entrainment by axisymmetrical turbulent jets," *Journal of Fluid Mechanics*, vol. 11, no. 1, pp. 21–32, 1961.

[188] J. P. Gorog and T. N. Adams, "Design and Performance of Rotary Lime Kilns in the Pulp and Paper Industry: Part 1 - A Predictive Model for a Rotary Lime Reburning Kiln," in *Kraft Recovery Operations Seminar*, 1987, pp. 41–47.

[189] J. P. Gorog and T. N. Adams, "Design and Performance of Rotary Lime Kilns in the Pulp and Paper Industry: Part 2 - The Effect of Chain System Design and the Refractory Lining on Lime Kiln Performance," in *Kraft Recovery Operations Seminar*, 1986, pp. 45–51.

[190] J. P. Gorog and T. N. Adams, "Design and Performance of Rotary Lime Kilns in the Pulp and Paper Industry: Part 3 - How Flame Characteristics and Product Coolers Affect Lime Kiln Performance," in *Kraft Recovery Operations Seminar*, 1986, pp. 53–60.

[191] J. P. Gorog and T. N. Adams, "Design and Performance of Rotary Lime Kilns in the Pulp and Paper Industry: Part 4 - The Effect of Operating Variables and O2 Enrichment on Lime Kiln Performance," in *Kraft Recovery Operations Seminar*, 1987, pp. 63–68.

[192] J. P. Gorog and T. N. Adams, “Design and Performance of Rotary Lime Kilns in the Pulp and Paper Industry: Part 5 - Heat Transfer, Kiln Geometry, and Lime Kiln Performance Rating,” in *Kraft Recovery Operations Seminar*, 1987, pp. 69–73.

[193] H. A. Spang, “A Dynamic Model of a Cement Kiln,” *Automatica*, vol. 8, no. 3, pp. 309–323, 1972.

[194] G. Locher, “Mathematical models for the cement clinker burning process. Part 1: Reactions and unit operations,” *ZKG International*, vol. 55, no. 1, pp. 29–38, 2002.

[195] G. Locher, “Mathematical models for the cement clinker burning process. Part 2: Preheater, calciner and bypass,” *ZKG International*, vol. 55, no. 1, pp. 39–50, 2002.

[196] G. Locher, “Mathematical models for the cement clinker burning process. Part 3: Rotary Kiln,” *ZKG International*, vol. 55, no. 6, pp. 25–37, 2002.

[197] K. S. Mujumdar and V. V. Ranade, “Simulation of Rotary Cement Kilns Using a One-Dimensional Model,” *Chemical Engineering Research and Design*, vol. 84, no. 3, pp. 165–177, 2006.

[198] K. S. Mujumdar, A. Arora, and V. V. Ranade, “Modeling of rotary cement kilns: Applications to reduction in energy consumption,” *Industrial and Engineering Chemistry Research*, vol. 45, no. 7, pp. 2315–2330, 2006.

[199] J. Haas and R. Weber, “Co-firing of refuse derived fuels with coals in cement kilns: Combustion conditions for stable sintering,” *Journal of the Energy Institute*, vol. 83, no. 4, pp. 225–234, 2010.

[200] F. C. Lockwood and B. Shen, “Performance predictions of pulverised-coal flames of power station furnace and cement kiln types,” in *Twenty-Fifth Symposium (International) on Combustion*, 1994, pp. 503–509.

[201] E. Mastorakos, A. Massias, C. D. Tsakiroglou, D. A. Goussis, V. N. Burganos, and A. C. Payatakes, “CFD predictions for cement kilns including flame modelling, heat transfer and clinker chemistry,” *Applied Mathematical Modelling*, vol. 23, no. 1, pp. 55–76, 1999.

[202] S. Wang, J. Lu, W. Li, J. Li, and Z. Hu, “Modeling of pulverized coal combustion in cement rotary kiln,” *Energy and Fuels*, vol. 20, no. 10, pp. 2350–2356, 2006.

[203] K. S. Mujumdar and V. V. Ranade, “CFD modeling of rotary cement kilns,” *Asia-Pacific Journal of Chemical Engineering*, vol. 3, no. 2, pp. 106–118, 2008.

[204] D. J. Isaac, M. N. Pedersen, D. Grévain, L. S. Jensen, and M. Nielsen, “Numerical Evaluation of Co-Firing Solid Recovered Fuel With Petroleum Coke in a Cement Rotary Kiln - A Case Example,” in *Proceedings of The 12th International Conference on Computational Fluid Dynamics in the Oil & Gas, Metallurgical and Process Industries*, 2017, pp. 613–620.

[205] H. Mikulčić, E. von Berg, M. Vujanović, and N. Duić, “Numerical study of co-firing pulverized coal and biomass inside a cement calciner.,” *Waste Management & Research*, vol. 32, no. 7, pp. 661–669, 2014.

[206] M. Nakhaei, H. Wu, P. Glarborg, K. Dam-johansen, D. Grévain, and L. S. Jensen, "CFD simulation of a full-scale RDF-fired calciner," in *Proceedings of the 2nd International Workshop on CFD and Biomass Thermochemical Conversion*, 2016.

[207] S. Telschow, "Clinker Burning Kinetics and Mechanism," PhD Thesis, Technical University of Denmark, 2012.

[208] P. V. Barr, "Heat Transfer Processes in Rotary Kilns," PhD Thesis, University of British Columbia, 1986.

[209] H. Henein, J. K. Brimacombe, and A. P. Watkinson, "Experimental study of transverse bed motion in rotary kilns," *Metallurgical Transactions B*, vol. 14, no. 2, pp. 191–205, 1983.

[210] W. C. Saeman, "Passage of Solids Through Rotary Kilns," *Chemical Engineering Progress*, vol. 47, no. 10, pp. 508–514, 1951.

[211] J. A. Imlach, "Non-isothermal Investigation of the Clinker Kinetics of Reactions Occuring During Clinker Formation," vol. 6, pp. 797–802, 1976.

[212] A. Khawam and D. R. Flanagan, "Solid-State Kinetic Models: Basics and Mathematical Fundamentals," *The Journal of Physical Chemistry B*, vol. 110, no. 35, pp. 17315–17328, 2006.

[213] W. Jander, "Reaktionen im festen Zustande bei höheren Temperaturen. Reaktionsgeschwindigkeiten endotherm verlaufender Umsetzungen," *Zeitschrift für anorganische und allgemeine Chemie*, vol. 163, no. 1, pp. 1–30, 1927.

[214] B. I. Ginstling, A. M.; Brounshtein, "Concerning the Diffusion Kinetics of Reactions in Spherical Particles," *Journal of Applied Chemistry of the USSR*, vol. 23, pp. 1327–1338, 1950.

[215] O. Levenspiel, *The Chemical Reactor Omnibook*. Corvallis, Oregon, USA: Oregon State University, 2002.

[216] S. Chromy and Z. Hrabe, "Process of Portland clinker formation, reactivity and burnability of cement raw materials - Part 2 Kinetics of clinker formation," *Zement-Kalk-Gips*, no. 7, pp. 368–373, 1982.

[217] G. Locher and M. Schneider, "Modeling in Cement Kiln Operations," in *Innovations in Portland Cement Manufacturing*, 1st ed., J. I. Bhatty, F. M. Miller, S. H. Kosmatka, and R. P. Bohan, Eds. Skokie, Illinois, USA: Portland Cement Association, 2011, pp. 935–972.

[218] N. Rajaratnam, *Turbulent Jets*. Amsterdam: Elsevier, 1976.

[219] A. G. Guruz, H. K. Guruz, S. Osuwan, and F. R. Steward, "Aerodynamics of a Confined Burning Jet," *Combustion Science and Technology*, vol. 9, no. 3–4, pp. 103–110, 1974.

[220] S. H. Park and H. D. Shin, "Measurements of entrainment characteristics of swirling jets," *International Journal of Heat and Mass Transfer*, vol. 36, no. 16, pp. 4009–4018, 1993.

[221] P. J. Mullinger, "Flame control in rotary lime kilns," *World Cement*, vol. 24, no. 6, pp. 20–23, 1993.

[222] I. Akman, U. Durgut, C. G. Manias, and S. T. Hill, "Kiln Burner Design," *World Cement*, no. 12, pp. 53–59, Dec. 2004.

[223] W. Ruhland, "Investigation of flames in cement rotary kilns," *Journal of the Institute of Fuel*, vol. 40, pp. 69–75, 1967.

[224] T. P. Bhad, S. Sarkar, A. Kaushik, and S. V. Herwadkar, "CFD Modeling of a Cement Kiln with Multi Channel Burner for Optimization of Flame Profile," in *Seventh International Conference on CFD in the Minerals and Process Industries*, 2009, pp. 1–7.

[225] N. Orfanoudakis, A. Hatziapostolou, K. Krallis, *et al.*, "Experimental and numerical investigations in the near-burner region of a versatile multi-fuel burner," *Journal of Computational Methods in Sciences and Engineering*, vol. 7, pp. 3–19, 2007.

[226] J. Lehmberg, M. Hehl, and K. Schügerl, "Transverse Mixing and Heat Transfer in Horizontal Rotary Drum Reactors," *Powder Technology*, vol. 18, no. 2, pp. 149–163, 1977.

[227] A. A. Boateng and P. V. Barr, "A thermal model for the rotary kiln including heat transfer within the bed," *International Journal of Heat and Mass Transfer*, vol. 39, no. 10, pp. 2131–2147, 1996.

[228] S. H. Tscheng and A. P. Watkinson, "Convective Heat Transfer in a Rotary Kiln," *The Canadian Journal of Chemical Engineering*, vol. 57, pp. 433–443, 1979.

[229] R. Siegel and J. R. Howell, *Thermal Radiation Heat Transfer*, 3rd ed. Washington, DC, USA: Taylor & Francis, 1992.

[230] K. M. Becker, "Measurement of Convective Heat Transfer from a Horizontal Cylinder Rotating in a Tank of Water," Stockholm, Sweden, 1963.

[231] K. M. Bryden, K. W. Ragland, and C. J. Rutland, "Modeling thermally thick pyrolysis of wood," *Biomass and Bioenergy*, vol. 22, pp. 41–53, 2002.

[232] M. Nakhaei, H. Wu, D. Grevain, *et al.*, "Experiments and Modelling of Single Plastic Particle Conversion in Suspension," *Fuel Processing Technology (Manuscript)*.

[233] C. A. Koufopanos, N. Papayannakos, G. Maschio, and A. Luchessi, "Modelling of the Pyrolysis of Biomass Particles - Studies on Kinetics , Thermal and Heat Transfer Effects," *The Canadian Journal of Chemical Engineering*, vol. 69, no. 4, pp. 907–915, 1991.

[234] S. Hamdi, W. E. Schiesser, and G. W. Griffiths, "Method of lines," 2007. [Online]. Available: http://www.scholarpedia.org/article/Method_of_lines. [Accessed: 01-Oct-2017].

[235] W. E. Ranz and W. R. Marshall, "Evaporation from drops Part 1," *Chemical Engineering Progress*, vol. 48, no. 3, pp. 141–146, 1952.

[236] K. M. Bryden and M. J. Hagge, "Modeling the combined impact of moisture and char shrinkage on the pyrolysis of a biomass particle," *Fuel*, vol. 82, no. 13, pp. 1633–1644, 2003.

[237] J. M. Johansen, "Power Plant Burners for Bio-Dust Combustion Thesis," PhD Thesis, Technical

University of Denmark, 2015.

[238] A. N. Matzakos, “Fundamental Mechanisms of Coal Pyrolysis and Char Combustion,” PhD Thesis, Rice University, 1992.

[239] C. Di Blasi, “Modeling chemical and physical processes of wood and biomass pyrolysis,” *Progress in Energy and Combustion Science*, vol. 34, no. 1, pp. 47–90, 2008.

[240] G. Borghi, A. F. Sarofim, and J. M. Beér, “A model of coal devolatilization and combustion in fluidized beds,” *Combustion and Flame*, vol. 61, no. 1, pp. 1–16, 1985.

[241] D. R. Burgess, “Thermochemical Data,” in *NIST Chemistry WebBook*, P. J. Linstrom and G. W. Mallard, Eds. Gaithersburg, Maryland, USA: National Institute of Standards and Technology, 2018.

[242] N. M. Laurendeau, “Heterogeneous kinetics of coal char gasification and combustion,” *Progress in Energy and Combustion Science*, vol. 4, no. 4, pp. 221–270, 1978.

[243] I. W. Smith, “The combustion rates of coal chars: A review,” *Symposium (International) on Combustion*, vol. 19, no. 1, pp. 1045–1065, 1982.

[244] B. F. Magnussen and B. H. Hjertager, “On mathematical modeling of turbulent combustion with special emphasis on soot formation and combustion,” *Symposium (International) on Combustion*, vol. 16, no. 1, pp. 719–729, 1977.

[245] Y. C. Guo, C. K. Chan, and K. S. Lau, “Numerical studies of pulverized coal combustion in a tubular coal combustor with slanted oxygen jet,” *Fuel*, vol. 82, no. 8, pp. 893–907, 2003.

[246] H. Thunman and B. Leckner, “Thermal conductivity of wood - Models for different stages of combustion,” *Biomass and Bioenergy*, vol. 23, no. 1, pp. 47–54, 2002.

[247] E. N. Fuller, P. D. Schettler, and J. C. Giddings, “A New Method for Prediction of Binary Gas-Phase Diffusion Coefficients,” *Industrial and Engineering Chemistry*, vol. 58, no. 5, pp. 19–27, 1966.

[248] R. Johansson, B. Leckner, K. Andersson, and F. Johnsson, “Account for variations in the H2O to CO2 molar ratio when modelling gaseous radiative heat transfer with the weighted-sum-of-grey-gases model,” *Combustion and Flame*, vol. 158, no. 5, pp. 893–901, 2011.

[249] V. Johansen and J. I. Bhatty, “Fluxes and Mineralizers in Clinkering Process,” in *Innovations in Portland Cement Manufacturing*, 1st ed., J. I. Bhatty, F. M. Miller, S. H. Kosmatka, and R. P. Bohan, Eds. Skokie, Illinois, USA: Portland Cement Association, 2011, pp. 401–438.

[250] Mathworks, “ode15s,” 2018. [Online]. Available: https://se.mathworks.com/help/matlab/ref/ode15s.html. [Accessed: 03-Apr-2018].

[251] A. Kaw, “Shooting Method for Ordinary Differential Equations,” *nm.mathforcollege.com*, 2009. [Online]. Available: http://nm.mathforcollege.com/topics/shooting_method.html. [Accessed: 03-Apr-2018].

[252] “Everything You Need to Know About Operation and Control of Clinker Cooler.” [Online]. Available: http://www.cementequipment.org/. [Accessed: 13-Apr-2018].

[253] S. R. Turns, *An Introduction to Combustion*, 3rd ed. McGraw-Hill, 2012.

[254] R. B. Silva, S. Martins-Dias, C. Arnal, M. U. Alzueta, and M. Costa, “Pyrolysis and char characterization of refuse-derived fuel components,” *Energy and Fuels*, vol. 29, no. 3, pp. 1997–2005, 2015.

[255] J. M. Johansen, P. A. Jensen, P. Glarborg, M. Mancini, R. Weber, and R. E. Mitchell, “Extension of apparent devolatilization kinetics from thermally thin to thermally thick particles in zero dimensions for woody biomass,” *Energy*, vol. 95, pp. 279–290, 2016.

[256] D. D. Evans and H. W. Emmons, “Combustion of wood charcoal,” *Fire Safety Journal*, vol. 1, no. 1, pp. 57–66, 1977.

[257] C. Di Blasi, F. Buonanno, and C. Branca, “Reactivities of some biomass chars in air,” vol. 37, pp. 1227–1238, 1999.

[258] H. Lu, W. Robert, G. Peirce, B. Ripa, and L. L. Baxter, “Comprehensive Study of Biomass Particle Combustion,” no. 4, pp. 2826–2839, 2008.

[259] Y. Kim and W. Parker, “A technical and economic evaluation of the pyrolysis of sewage sludge for the production of bio-oil,” *Bioresource Technology*, vol. 99, pp. 1409–1416, 2008.

[260] A. Demirbas, “Effects of moisture and hydrogen content on the heating value of fuels,” *Energy Sources, Part A: Recovery, Utilization and Environmental Effects*, vol. 29, no. 7, pp. 649–655, 2007.

[261] R. Ahmad, T. A. Khan, and V. Agarwal, “Mass and Energy Balance in Grate Cooler of Cement Plant,” *International Journal of Scientific Engineering and Technology*, vol. 2, no. 7, pp. 631–637, 2013.

[262] K. S. Mujumdar, K. V. Ganesh, S. B. Kulkarni, and V. V. Ranade, “Rotary Cement Kiln Simulator (RoCKS): Integrated modeling of pre-heater, calciner, kiln and clinker cooler,” *Chemical Engineering Science*, vol. 62, no. 9, pp. 2590–2607, 2007.

[263] D. Touil, H. F. Belabed, C. Frances, and S. Belaadi, “Heat Exchange Modeling of a Grate Clinker Cooler and Entropy Production Analysis,” *International Journal of Heat and Technology*, vol. 23, pp. 61–68, 2005.

[264] U. Akay, “The Fons Delta Level Transmitter,” *International Cement Review*, 2013.

12 APPENDICES

The following appendices are included to provide additional clarification and details on certain subjects covered in the thesis.

A. Flame Analysis of Image Intensities

An example of the analysis of changing image intensities is shown here. Three example images consisting of 11x11 pixel are shown in Figure 12-1a-c. In the images the intensity is increased from the top left corner to the bottom right corner. The upper left pixel in Figure 12-1a has a value of 0 (i.e. black), and the bottom right pixel in Figure 12-1c has a value of 255 (i.e. white).

The graphs presented in Figure 12-1d-f are the image intensities in the horizontal and vertical direction of each image in Figure 12-1a-c. The horizontal image intensity profile is taken across the image from left to right in row 6, and the vertical profile is taken from the top to bottom in column 11. The graphs thus indicate how the image intensity changes from the left to the right, and from the top to the bottom. Furthermore it is seen that the intensity is generally higher in Figure 12-1c than in Figure 12-1a.

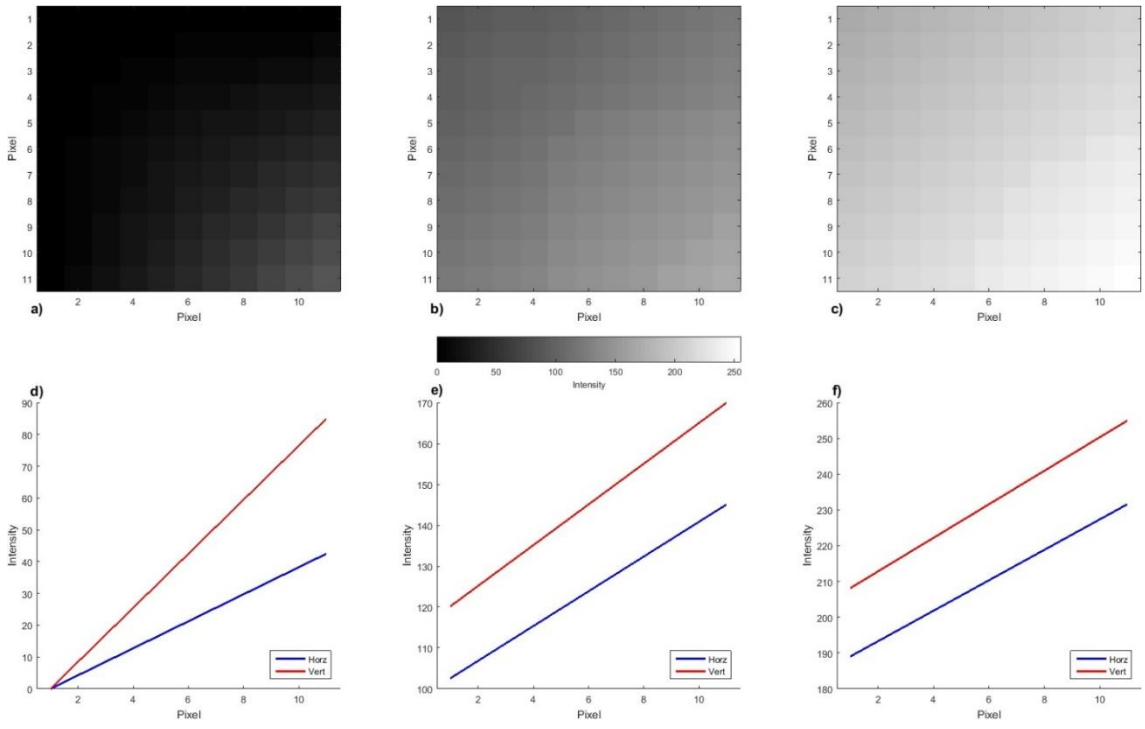

Figure 12-1: a-c) Three example images in grayscale with varying image intensity. The image intensity increases from top left to bottom right in each image. d-f) Image intensities in horizontal direction from left to right, and in vertical direction from top to bottom.

In Figure 12-2 the intensity profiles from Figure 12-1d-f are combined to show how the intensity changes from pixel to pixel in each frame (y-axis), and how it changes

between the frames (x-axis). The color indicates the image intensity from Figure 12-1a-c. Thus it is seen in Figure 12-2a+b how the image intensity increases as the pixel number is increased from 1 to 11, and it can be seen how the general image intensity increases over the three frames.

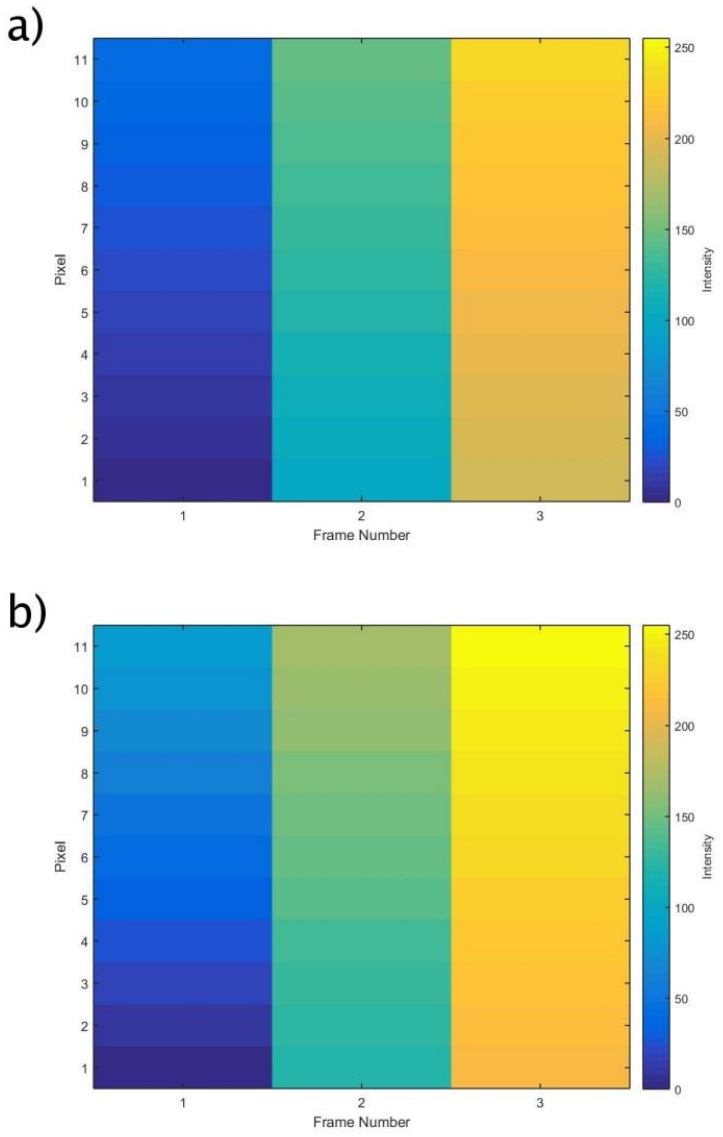

Figure 12-2: Image intensities in the 3 example images. a) in horizontal direction in center of image (pixel 1 is left side of Figure 12-2) , and b) in vertical direction in right most pixel column (pixel 1 is top of Figure 12-2).

The same approach is used for the recorded videos. They just consist of a greater number of frames with a higher resolution than what is exemplified above.

B. Determination of Kinetics for Alite Formation

The burnability of raw meal samples from two different cement plants were determined at the FLSmidth laboratories. The raw meal composition is given in Table 12-1. The minor oxides (MgO, K_2O, etc.) have been grouped as inerts. The loss on ignition is the mass loss due to calcination when the raw meal sample is heated.

Table 12-1: Raw meal composition of test samples.

	Composition	SiO2	Al2O3	Fe2O3	CaO	Inerts	Loss on ignition	Total
Sample 1	wt. %	13.90	3.80	2.56	43.10	1.24	35.20	99.80
Sample 2	wt. %	13.70	3.09	1.76	43.10	2.74	35.50	99.89

The raw meal burnability is tested according to an internal FLSmidth Standard. The samples are burned for 30 minutes at temperatures of 1400, 1450, and 1500 °C. Afterwards the free lime, C_2S, and C_3S content were determined, with the results shown in Table 12-2. It is observed that sample 1 obtains a lower free lime content than sample 2, thus it is easy to burn compared to sample 2.

Table 12-2: Measured CaO, C_2S, and C_3S in burnability tests.

	Temperature (°C)	1400			1450			1500		
	Composition	CaO	C2S	C3S	CaO	C2S	C3S	CaO	C2S	C3S
Sample 1	wt. %	1.8	22	60	1.4	21	60	0.9	20	61
Sample 2	wt. %	4.8	30	52	3.8	23	56	2.5	19	63

The kinetics of Mastorakos [201] were adjusted using a trial and error procedure. The initial adjustment resulted in using the following values for the alite formation, $A = 3*10^8$ m^3/kg/s and $Ea = 440$ kJ/mol. Using these kinetics, the model of alite was compared with the burnability tests for sample 2, as shown in Figure 12-3a. The reaction is too slow at 1400, while it is too fast at 1450 and 1500 °C.

The rate constant for reaction at each of the three temperatures were then adjusted to minimize the difference between the model predictions and the laboratory determined alite content, as shown in Figure 12-3b. An excellent fit is seen between the model and lab measurements of alite content. A deviation is seen in the belite and free lime contents, since the real samples do not behave according to the idealized simplified clinker composition.

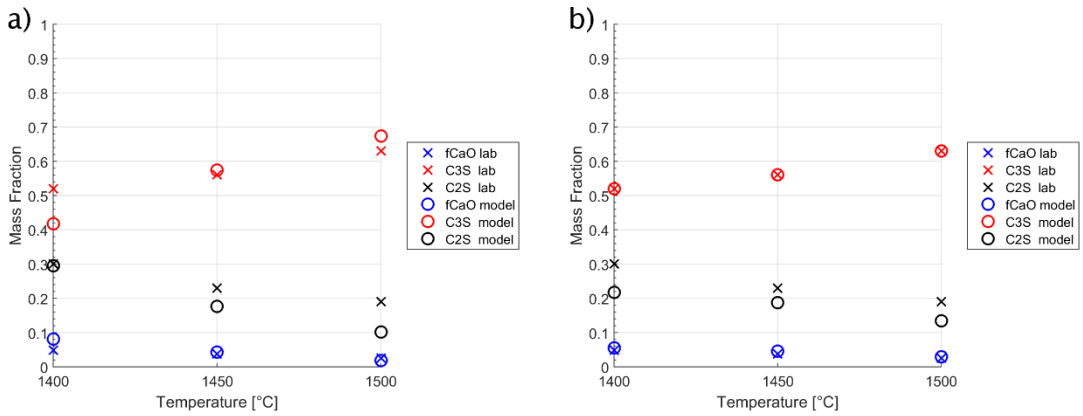

Figure 12-3: Comparison of model predictions with laboratory burnability tests for sample 2. a) Using standard kinetics (A = 3*10⁸ m³/kg/s, Ea = 440 kJ/mol). b) using optimized kinetics.

The optimal rate constants at each temperature have now been determined. Using a fixed activation energy of 440 kJ/mol, the appropriate preexponential factor is determined.

The same procedure can be followed for sample 1, to find the kinetics for an easy burning cement clinker. The optimized best fitting kinetics are given in Table 12-3. A factor 3 difference is seen in the preexponential factor for the two samples. Thus, sample 1 will more easily react, which is consistent with its low burnability.

Table 12-3: Optimized best fitting kinetics for the alite formation.

	A ($m^3/kg/s$)	Ea (kJ/mol)
Sample 1	3.32*10⁸	440
Sample 2	1.10*10⁸	440

C. Determination of View Factors for Radiation

The radiative problem can be sketched as seen in Figure 12-4, where the three surfaces that radiation occurs between are the jet (green circle at center), bed (red line between A1 and A2), and kiln wall (blue outer circle).

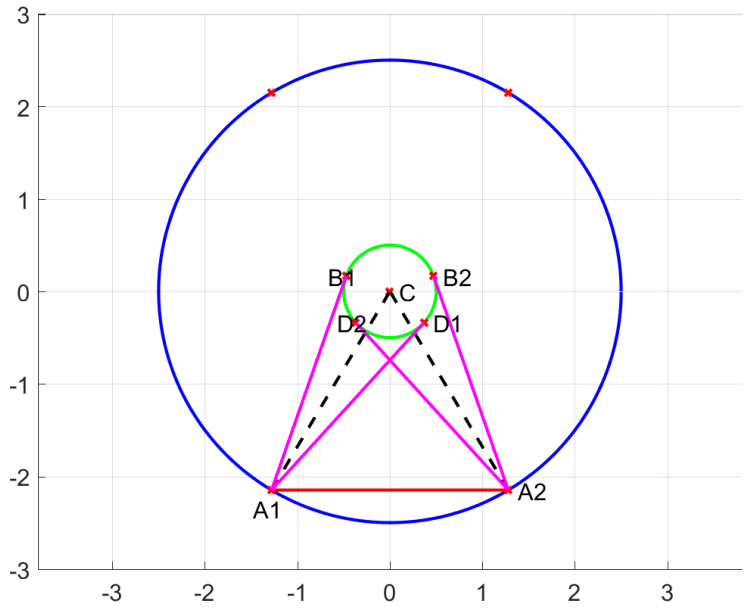

Figure 12-4: Sketch to determine the radiation view factors.

Since it is an enclosure the sum of view factors must be 1. We have for the three surfaces:

$$\boldsymbol{\Omega_{1,1} + \Omega_{1,2} + \Omega_{1,3} = 1} \qquad \textbf{E 12.1}$$

$$\boldsymbol{\Omega_{2,1} + \Omega_{2,2} + \Omega_{2,3} = 1} \qquad \textbf{E 12.2}$$

$$\boldsymbol{\Omega_{3,1} + \Omega_{3,2} + \Omega_{3,3} = 1} \qquad \textbf{E 12.3}$$

Surface 1 (the bed) is flat and surface 3 (the jet) is convex so they can't see themselves and the view factor is 0. In addition the reciprocity relation is given as [229]:

$$\boldsymbol{A_i \Omega_{i,j} = A_j \Omega_{j,i} \Rightarrow \Omega_{i,j} = \frac{A_j}{A_i} = \Omega_{j,i}} \qquad \textbf{E 12.4}$$

This allows the following rewriting of the equations E 12.1-E 12.3:

$$\boldsymbol{\Omega_{1,2} + \Omega_{1,3} = 1} \qquad \textbf{E 12.5}$$

$$\frac{A_1}{A_2}\Omega_{1,2} + \Omega_{2,2} + \Omega_{2,3} = 1 \qquad \text{E 12.6}$$

$$\frac{A_1}{A_3}\Omega_{1,3} + \frac{A_2}{A_3}\Omega_{2,3} = 1 \qquad \text{E 12.7}$$

This results in three equations with four unknown view factors. I.e. it is needed to determine one before the equations can be solved.

The view factor $\Omega_{1,3}$ (between the bed and jet) will be determined by use of Hottel's crossed-string method [229]. From Figure 12-4 the result of the method yields as the problem is symmetrical:

$$A_1 * \Omega_{1,3} = \frac{l_{A1B2} + l_{A2B1} - l_{A1B1} - l_{A2B2}}{2} = \frac{2l_{A2B1} - 2l_{A1B1}}{2} = l_{A2B1} - l_{A1B1} \qquad \text{E 12.8}$$

Since the problem is considered in 2-D only, as only radial heat transfer is considered, the surface area reduces to just the length of the chord between points A1 and A2:

$$A_1 = l_{A1A2} = 2 * sin\frac{\theta}{2} * r_k \qquad \text{E 12.9}$$

Thus equation E 12.8 can be rewritten to:

$$\Omega_{1,3} = \frac{l_{A2B1} - l_{A1B1}}{2r_k * sin\frac{\theta}{2}} \qquad \text{E 12.10}$$

The distance l_{A1B1} can be determined as:

$$l_{A1B1} = \sqrt{l_{A1C}^2 + l_{B1C}^2} = \sqrt{r_k^2 + r_{jet}^2} \qquad \text{E 12.11}$$

This is the Pythagorean theorem as the triangle connecting A1, B1, and the center of the jet forms a right-angled triangle, due to the line A1B1 being a tangent to the jet circle.

The distance $l_{A1D1B2} = l_{A1D1} + l_{D1B2}$ also needs to be determined. Distance $l_{A1D1} = l_{A1B1}$, which is known from E 12.11 is already determined. The distance l_{D1B2} lies on the circle arch and is determined by the angle $\angle B_2CD_1$. The following relation is true for the angle:

$$\angle B_2CD_1 = \angle A_1CA_2 = \theta \quad \text{E 12.12}$$

Thus, the last length can be found as:

$$l_{D1B2} = r_{jet} * \theta \quad \text{E 12.13}$$

And finally, the view factor between bed and jet can be found as:

$$\Omega_{1,3} = \frac{\sqrt{r_k^2 + r_{jet}^2} + r_{jet} * \theta - \sqrt{r_k^2 + r_{jet}^2}}{2r_k * sin\frac{\theta}{2}} = \frac{r_{jet} * \theta}{2r_k * sin\frac{\theta}{2}} \quad \text{E 12.14}$$

With this solved the remaining three view factors can be deduced:

$$\Omega_{1,2} = 1 - \Omega_{1,3} \quad \text{E 12.15}$$

$$\Omega_{2,3} = \frac{A_3}{A_2}\left(1 - \frac{A_1}{A_3}\Omega_{1,3}\right) = \frac{2\pi r_{jet}}{2\pi r_k - r_k\theta}\left(1 - \frac{2r_k * sin\frac{\theta}{2}}{2\pi r_{jet}}\Omega_{1,3}\right) \quad \text{E 12.16}$$

$$\Omega_{2,2} = 1 - \frac{A_1}{A_2}\Omega_{1,2} - \Omega_{2,3} = 1 - \frac{2r_k * sin\frac{\theta}{2}}{2\pi r_k - r_k\theta}\Omega_{1,2} - \Omega_{2,3} \quad \text{E 12.17}$$

The following definitions of areas, that reduces to length chords in 2-D, have been used:

$$A_1 = 2r_k * sin\frac{\theta}{2} \quad \text{E 12.18}$$

$$A_2 = 2\pi r_k - r_k\theta \quad \text{E 12.19}$$

$$A_3 = 2\pi r_{jet} \quad \text{E 12.20}$$

D. Oxygen Requirement for Combustion

The simplified method of calculating the volatile yield includes a heat and mass balance on the char and volatile yield given by the proximate analysis and the heating value.

This results in three products from the devolatilization: carbon monoxide (CO), methane (CH4), as well as remaining char (C).

The oxygen consumption for the combustion, per kg fuel, can then be calculated as:

$$\boldsymbol{n_{O2,req} = \frac{Y_{char}}{M_C} + \frac{Y_{vol}}{M_{CO}} * Y_{vol,CO} + \frac{Y_{vol}}{M_{CH4}} * Y_{vol,CH4} * 2} \qquad \text{E 12.21}$$

Where Y_{char} and Y_{vol} indicate the mass fraction of char and volatiles determined by the proximate analysis, $Y_{vol,CO}$ and $Y_{vol,CH4}$ are the fraction of volatiles present as CO and CH_4.

A more rigorous method is to consider the fuel ultimate analysis where the oxygen consumption can be calculated as:

$$\boldsymbol{n_{O2,reg} = \frac{Y_C}{M_C} + 2\frac{Y_H}{M_H} + \frac{1}{2}\frac{Y_S}{M_S} - \frac{1}{2}\frac{Y_O}{M_O}} \qquad \text{E 12.22}$$

Where Y_C, Y_H, Y_S, and Y_O indicate the mass fraction of carbon, hydrogen, sulfur, and oxygen in the fuel. The nitrogen in the fuel will be assumed released as N_2.

A comparison of the oxygen consumption of the two methods is shown in Table 12-4, for the different fuels used in this study. It is seen that for some fuels there is a considerable difference in the calculated oxygen consumption. This difference in air consumption of the two methods also leads to significant differences in the adiabatic temperature. However, for the coal the difference between the two methods is insignificant. For coal 2 and the SHW the ultimate analysis is not reported in the source material.

In order to compensate for the difference in air consumption between the two methods, extra nitrogen is added to the secondary air. Compensating with nitrogen instead of air, keeps the total flow of oxygen into the kiln constant. The addition of extra nitrogen, will limit the combustion temperatures, which may otherwise be too high, if too little air is admitted to the kiln.

Table 12-4: The proximate and ultimate analysis of the fuels used in the model studies. Including the calculated oxygen consumption and adiabatic temperature by simple (1) and rigorous method (2).

Property	Unit	Fetnuss Coal	Coal 1	MBM	Coal 2	SHW	SRF
LHV	MJ/kg	34.0	28.0	18.5	27.1	15.0	15.4
Moisture	wt%	0.6	1.0	4.0	1.7	30.0	21.4
Ash	wt%	2.8	13.6	27.1	19.4	17.6	17.6
Char	wt%	72.3	62.4	8.0	51.4	1.0	6.1
Volatiles	wt%	24.3	23.0	60.9	27.5	51.4	54.9
Carbon	wt%	85.2	72.9	47.1	-	-	38.5
Hydrogen	wt%	4.6	3.9	6.9	-	-	5.5
Nitrogen	wt%	1.4	1.7	9.7	-	-	0.8
Sulfur	wt%	0.9	1.4	0.5	-	-	0.5
Oxygen	wt%	4.4	5.5	4.7	-	-	15.7
Source		[80]	[81,83]	[81,83]	[82]	[82]	
Oxygen Req. 1	mol/kg	85.5	70.0	43.8	67.8	37.2	37.2
Oxygen Req. 2	mol/kg	81.1	68.9	54.9	-	-	40.9
Adiabatic Temp. 1	K	2038	2038	2071	2040	1920	1971
Adiabatic Temp, 2	K	2122	2060	1726	-	-	1835

E. Validation of Biomass Combustion Model

The biomass combustion model is validated against experiments found in the literature [31,86,87,176]. The results form a good basis for validation since they contain data on devolatilization and char oxidation times for different fuels over a wide range of conditions with varying temperatures and oxygen concentrations.

E.1 Details of Experiments

The experiments from Momeni [86], Lu [176], and Nørskov [31] are performed at the Technical University of Denmark, using the same single particle combustor setup. The fuel particle is inserted into a furnace heated by a gas flame, and the combustion process is monitored by a video camera. The experiments of Mason [87] were performed in the flame of a Meker burner.

The experimental conditions from the different experiments are given in Table 12-5. Five difference conditions are used by Nørskov, while the other sources use only one set of conditions. It is assumed that for the experiments carried out in the single particle combustor (Momeni, Lu, Nørskov), the gas temperature (convective heat transfer) and wall temperature (radiative heat transfer) are equal. The experiments by Mason are performed in an open flame, here it will be assumed that radiation from the particle is governed by the ambient temperature outside the flame.

Table 12-5: Experimental conditions used in literature.

Source	**Experimental condition**	$\mathbf{T_g}$	$\mathbf{T_w}$	$\mathbf{u_g}$	$\mathbf{y_{O2}}$
		°C	°C	m/s	vol%
Momeni	1	1473	1473	3.4	20
Lu	2	1504	1504	2.76	3
Nørskov EC1	3	1200	1200	2	5.8
Nørskov EC2	4	1450	1450	2	2.8
Nørskov EC3	5	1450	1450	2	6.6
Nørskov EC4	6	1475	1475	2	12
Nørskov EC5	7	1550	1550	2	5.9
Mason	8	1550	27	3	10.8

E.2 Fuels Used

The fuels studied include pine wood (Nørskov [31], Momeni [86], Mason [87]), schima wood (Lu [176]), eucalyptus and willow wood (Mason [87]), and sewage sludge (SS) (Nørskov [31]). Details of the fuels are found in Table 12-6. Since the

char content is dependent on the heating rate of the biomass, it will typically be lower than measured in the proximate analysis [96,176]. Here it will be assumed that the char content during experiments is 70 % of the proximate char, on a dry basis.

Table 12-6: Properties of the fuels used in experiments.

		Momeni Pine	Lu Schima	Nørskov Pine	Nørskov SSA	Nørskov SSB	Mason Pine	Mason Eucalyp.	Mason Willow
Fuel Type	Unit	1	2	3	4	5	6	7	8
Proximate Volatiles	wt% dry	85.3	80.0	85.3	73.7	68.2	80.9	82.6	82.0
Proximate Char	wt% dry	14.3	18.7	14.4	7.1	10.2	17.2	16.5	16.1
Proximate Ash	wt% dry	0.3	1.3	0.3	19.1	21.6	2.0	0.9	1.9
Moisture	wt%	9.3	5.6	9.3	6.0	8.0	8.3	8.1	2.8
Volatiles	wt%	81.3	80.8	81.3	71.3	65.5	78.9	80.4	84.4
Char	wt%	9.1	12.4	9.1	4.7	6.6	11.0	10.6	10.9
Ash	wt%	0.3	1.2	0.3	18.0	19.9	1.8	0.8	1.8
Assumed volatiles	wt%	6.4	8.7	6.4	3.3	4.6	7.7	7.5	7.7
Assumed char	wt%	84.0	84.5	84.0	72.7	67.5	82.2	83.6	87.7
Density dry	kg/ m3	600	658	497	696	1136	440	616	505
Density wet	kg/ m3	662	697	548	740	1235	480	670	520
Density char	kg/ m3	42	60	35	24	57	37	50	40
Heat Capacity	J/kg /K	2296	2284	2296	2066	2041	2276	2289	2276

It is assumed that the initial heat capacity is influenced by the ash content of the sample according to E 12.23, and that it is constant during combustion.

$$\boldsymbol{Cp = Cp_1 * (1 - w_{ash}) + Cp_2 * w_{ash}} \qquad \textbf{E 12.23}$$

With $Cp_1 = 2300$ J/kg/K and $Cp_2 = 1000$ J/kg/K.

The particle shape is explicitly stated in the experiments by Momeni, which allows for calculating the particle sphericity. This is not the case for the other experiments, where sphericity will be assumed 1.

E.3 Kinetics Used in Model

The kinetics of the biomass combustion reactions are given in Table 12-7. Some additional physical parameters are also available. The values are based on different literature references.

Table 12-7: Kinetics of biomass combustion reactions and additional physical parameters.

Parameter	Symbol	Unit	Value	Source
Preexponential factor drying	A_{dry}	1/s	$5.13*10^{10}$	[236]
Activation energy char drying	Ea_{dry}	kJ/mol	88	[236]
Preexponential factor devolatilization	A_{devol}	1/s	$1.11*10^{11}$	Low temperature kinetics [255]
Activation energy char devolatilization	Ea_{devol}	kJ/mol	177	Low temperature kinetics [255]
Preexponential factor char oxidation	$A_{char,ox}$	kg/(m²*s*Pa)	$2.54*10^{-3}$	[256]
Activation energy char oxidation	$Ea_{char,ox}$	kJ/mol	81.55	Average values from [257]
Preexponential factor char gasification	$A_{char,gsc}$	m/s	$3.42*T_{char}$	[258]
Activation energy char gasification	$A_{char,\ gsc}$	kJ/mol	130	[258]
Particle emissivity	ε_p	-	0.9	Coal particle [31]
Particle heat conductivity	λ_p	W/(m*K)	0.12	Approximate value based on fuel with 10 % char [255].
Heat capacity of organic fraction	Cp_O	J/(Kg K)	2300	Heat capacity of organic material in range 2.1-2.5 kJ/(kg K) [259]
Heat capacity of ash fraction	Cp_A	J/(Kg K)	1000	Heat capacity of inorganic material in range 0.8-1.3 kJ/(kg K) [259]

E.4 Model Predictions Devolatilization

A comparison of predicted devolatilization times with the experimental results are shown in Figure 12-5. The fit is generally good with average deviations for each fuel type being maximum 15 %. Only the results of Momeni have a larger deviation. This is due to the difficulty of describing the cylinder-shaped particles as an equivalent sphere. Some different approaches were tested to account for the particle shape.

Eventually, it was chosen to increase the particle surface area (for heat transfer and char oxidation) by a factor $1/\varphi$, since this gave the overall best fit.

For the experimental conditions the largest difference is seen for the results of Mason and Nørskov EC2, which are at low oxygen concentration. The oxygen concentration in the experiments have some influence, most likely because a flame is formed above the particle at high O_2 concentrations, which increases the heat transfer. This is not considered in the model.

For the results of Mason, the experiments are made in an open flame, which means the particle radiates heat to cold surroundings outside the flame. This might be difficult to describe exactly with a simple model.

It should also be noted that there is significant scatter in the experimental results, especially seen by Nørskov. The results of Mason have been derived based on regression of several particle conversion times. Results from Momeni and Lu are averages of multiple experiments.

The reason the model appears to work well for very different fuel types is likely the large particles sizes. In this case heat transfer in the particle is more important than the kinetics of devolatilization for the given fuel, which are assumed to be the same in all cases.

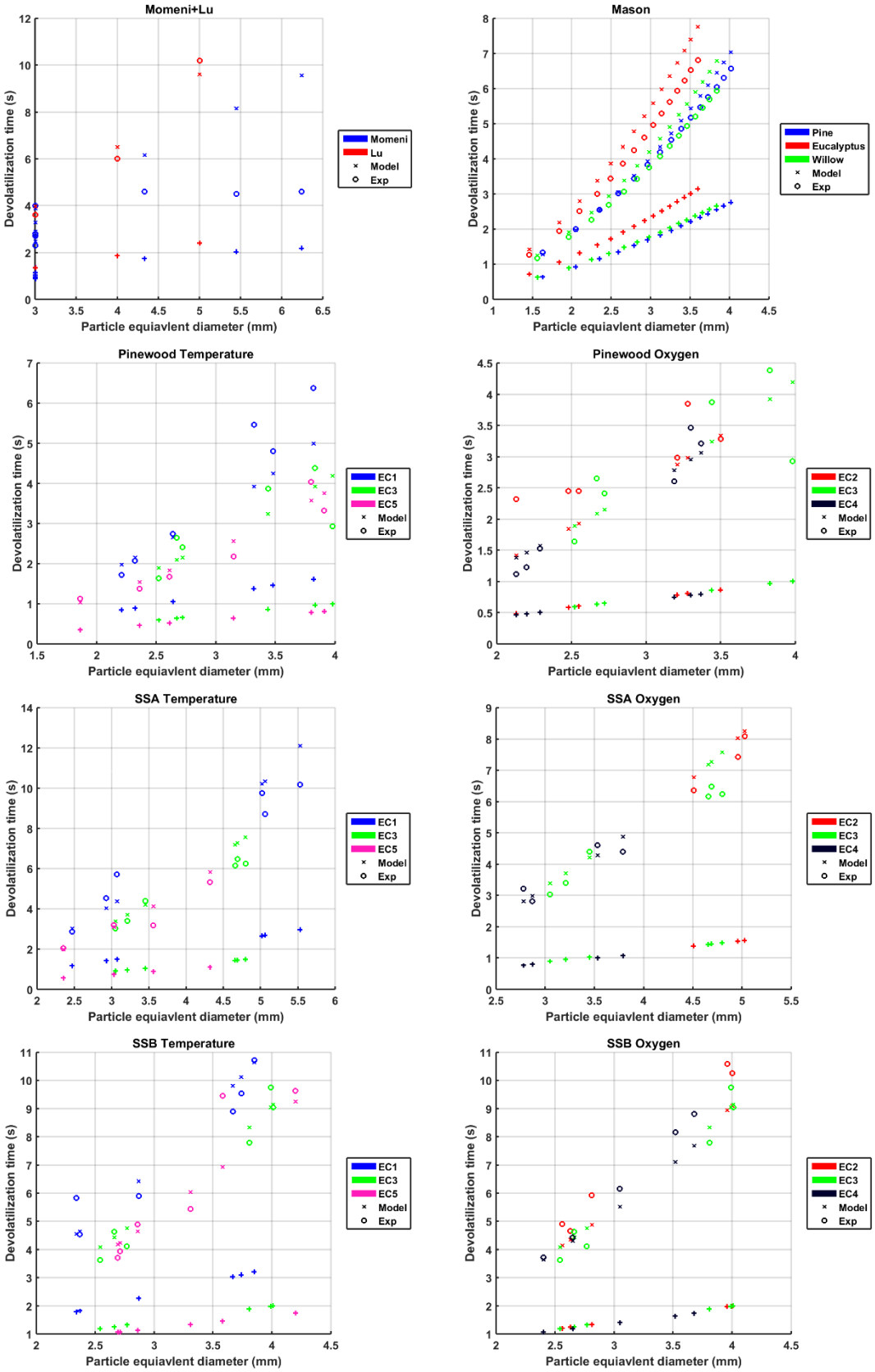

Figure 12-5: Model and experimental comparison for devolatilization.

E.5 Model Predictions Char Oxidation

The comparison of model predictions with experimental results of the char oxidation times are shown in Figure 12-6. The maximum average deviation is 30 % for the pine wood char oxidation of Nørskov. The deviation on the other results are on average below 20 %.

For the experimental conditions the largest problems are seen for Nørskov at low temperature (EC1) or low oxygen concentration (EC2) and for the Mason results, which are also at low temperature. With low temperature the kinetics of the reaction are more important, while at high temperature mass transfer of oxygen to the particle surface is rate limiting. For the low oxygen concentration, gasification with water is also more important. In the cement kiln the combustion temperatures are above 1500 °C and the oxygen concentration is above 5 %, thus the errors seen here should be on the order of maximum 20 %.

For the Mason results it is noticed that the experimental results show a curvature with d_p. For the shrinking core model for kinetically limited reaction, the relationship between particle diameter and conversion time should be linear, as predicted by the model. Perhaps some kind of ash diffusion could be added to get a better fit with the experimental results. This would especially influence the largest particles, where the largest underestimation of char oxidation time is seen.

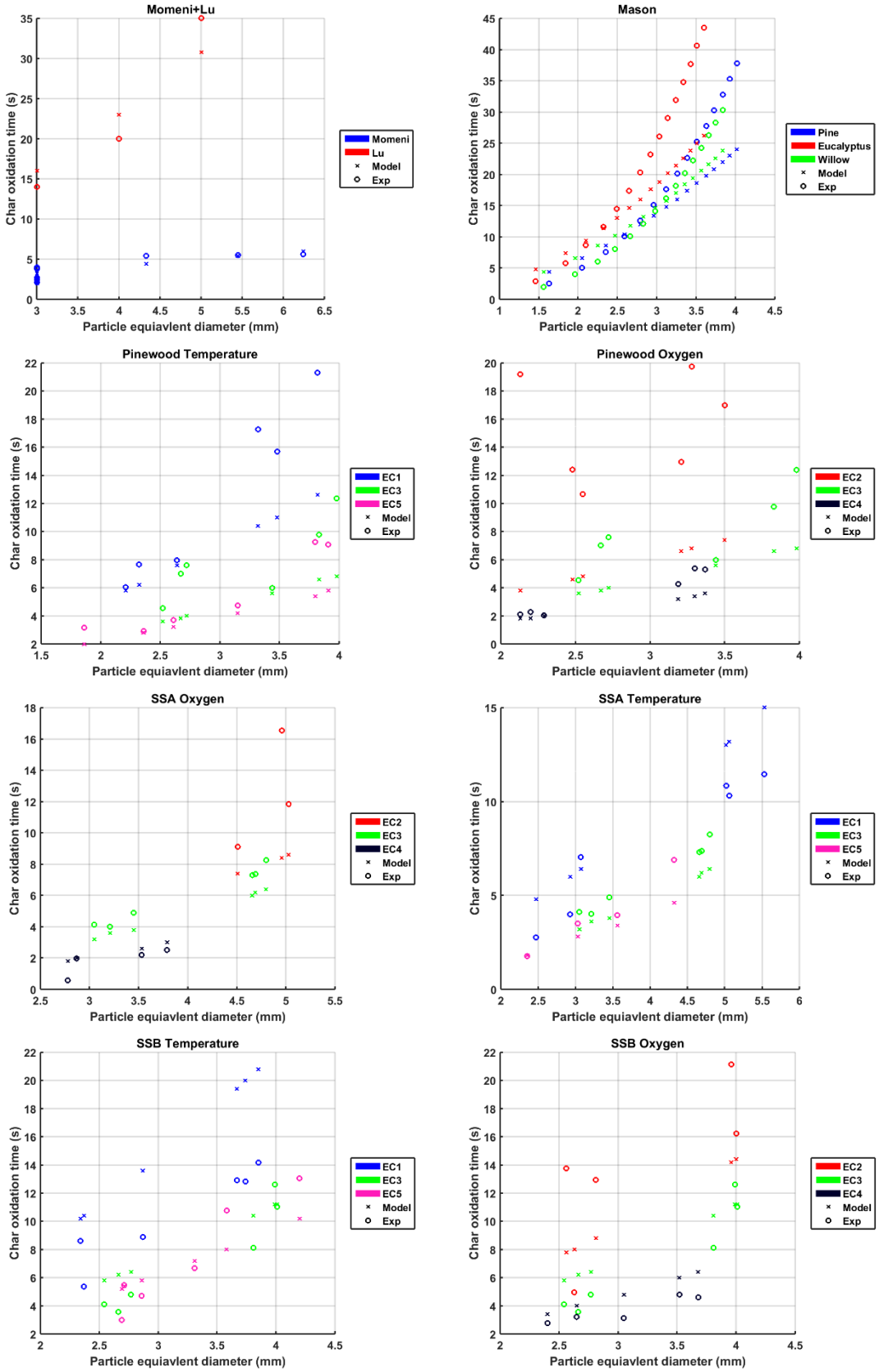

Figure 12-6: Model and experimental comparison for char oxidation.

F. Comparison of Isothermal and Non-Isothermal Devolatilization Model

Since SRF particles are large, internal temperature gradients are present during devolatilization. Thus, it is necessary to somehow account for this in the model. In this chapter a comparison of a 1D model (using the partial differential equation E 8.55) is compared to results using the isothermal particle model (E 8.53).

The partial differential equation used in the 1D model is solved by discretization using the Method of Lines [234]. However, the discretization means that additional equations need to be solved. This may set an additional computational strain on the model; especially as multiple particle sizes are added to the model. Thus, a simple approach to account for the difference between an isothermal and non-isothermal (1D) model, may be of interest.

F.1 Comparison of Models

A comparison of the devolatilization times calculated by the isothermal and non-isothermal model is shown in Figure 12-7. The devolatilization time is here defined as the time it takes for the isothermal particle to reach 99.9 devolatilization, while it for the non-isothermal particles is the center of the particle that should reach 99.9 % conversion.

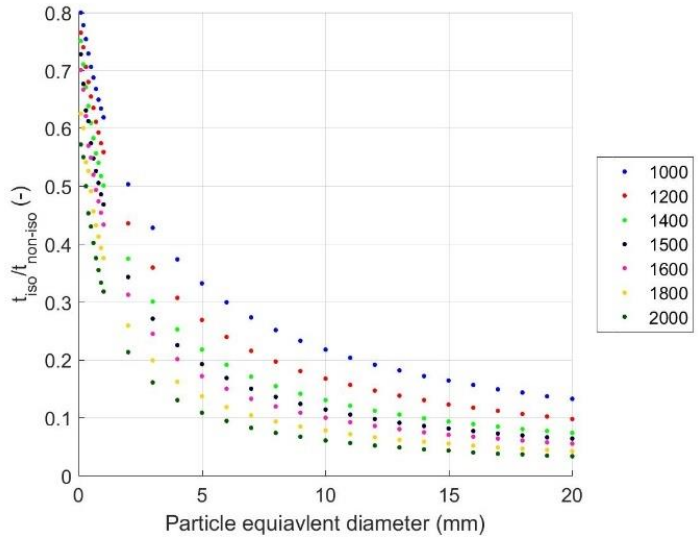

Figure 12-7: Comparison of devolatilization times predicted by isothermal and non-isothermal model for different gas temperatures (°C).

The devolatilization is calculated for particles sizes in the range 0.1-20 mm and temperatures 1000-2000 °C. The devolatilization times predicted by the isothermal model are significantly lower than what is predicted by the non-isothermal model. The error becomes larger as the particle size or gas temperature is increased and temperature gradients in the particle become more pronounced.

A linear relationship between d_p and $t_{iso}/t_{non\text{-}iso}$ is found for particles with $d_p < 1$ mm, for particles with $d_p > 1$ mm a log-log plot reveals a linear relation, as shown in Figure 12-8..

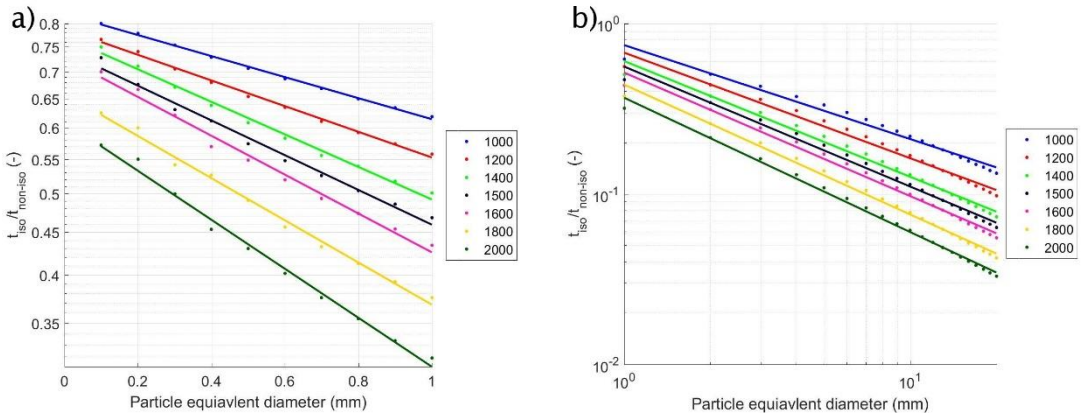

Figure 12-8: Linearized versions of Figure 12-7 for a) $d_p < 1$ mm and b) $d_p > 1$ mm in a log-log plot.

F.2 Adjusting Devolatilization Kinetics of Isothermal Model

Johansen et al. [255] proposed to reduce devolatilization kinetics for larger isothermal particles in order to account for their faster conversion than non-isothermal particles. This can shift the devolatilization to occur at higher temperatures, which will cause a delay in devolatilization. A similar approach is used here, although a more detailed fitting of kinetic parameters is presented.

The basis for the devolatilization kinetics is a preexponential factor of $1.11*10^{11}$ 1/s and an activation energy of 177 kJ/mol [255]. The preexponential factor is first adjusted so that $t_{iso}/t_{non\text{-}iso}$ is independent of particle size, see Figure 12-9a. Next the activation energy is adjusted to make $t_{iso}/t_{non\text{-}iso} = 1$, for all particles and at all temperatures, see Figure 12-9b. One set of parameters is found for particles with d_p between 0.5 and 1 mm, and a second set is found for particles with d_p above 1 mm. For particles below 0.5 mm, the difference between the two models is lower than 0.01 s, and thus adjustments are not deemed necessary.

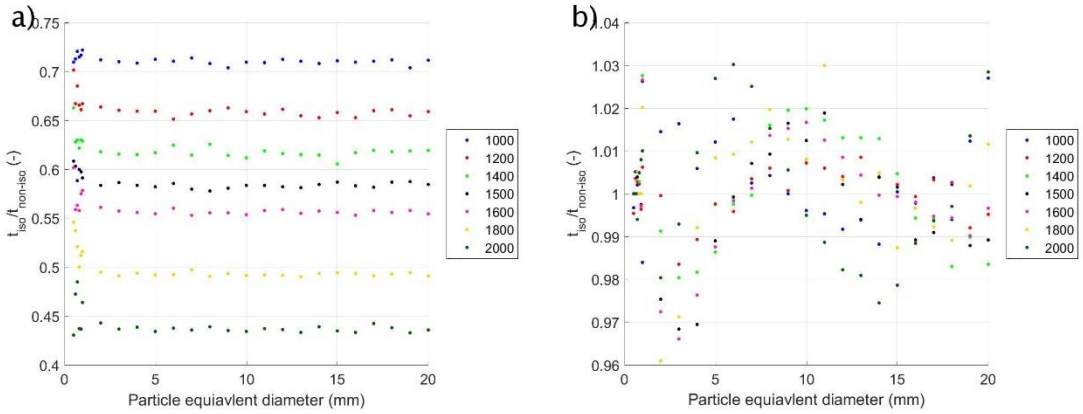

Figure 12-9: Comparison of devolatilization times predicted by isothermal and non-isothermal models after adjustment of preexponential factor (a) and activation energy (b).

The adjusted values of preexponential factor (A_{devol}) and activation energy (Ea_{devol}) are then fitted across particle diameter and gas temperature. The following fits are derived. In the equations d_p should be inserted in mm and T_g in K.

For particles smaller than 1 mm:

The preexponential factor is found by:

$$log(A_1) = a_{A1} * log(d_p) + b_{A1} \quad \text{E 12.24}$$

$$a_{A1} = a_{A1,1} * log(T_g) + a_{A1,2} \quad \text{E 12.25}$$

$$b_{A1} = b_{A1,1} * log(T_g) + b_{A1,2} \quad \text{E 12.26}$$

The activation energy is found by:

$$E_1 = a_{E1} * log(dp) + b_{E1} \quad \text{E 12.27}$$

$$log(-a_{E1}) = a_{E1,1} * T + a_{E1,2} \quad \text{E 12.28}$$

$$log(b_{E1}) = b_{E1,1} * T + b_{E1,2} \quad \text{E 12.29}$$

For particles larger than 1 mm:

The preexponential factor is found by:

$$log(A_2) = a_{A2} * log(dp) + b_{A2} \quad \text{E 12.30}$$

$$a_{A2} = a_{A2,1} * log(T)^2 + a_{A2,2} * log(T) + a_{A2,3} \quad \text{E 12.31}$$

$$b_{A2} = b_{A2,1} * log(T) + b_{A2,2} \quad \text{E 12.32}$$

The activation energy is found by:

$$log(E_2) = a_{E2} * exp(b_{E2} * d_p) + c_{E2} \quad \text{E 12.33}$$

$$a_{E2} = a_{E2,1} * log(T)^2 + a_{E2,2} * log(T) + a_{E2,3} \quad \text{E 12.34}$$

$$b_{E2} = b_{E2,1} * log(T)^2 + b_{E2,2} * log(T) + b_{E2,3} \quad \text{E 12.35}$$

$$c_{E2} = c_{E2,1} * log(T)^2 + c_{E2,2} * log(T) + c_{E2,3} \quad \text{E 12.36}$$

The values of the regression coefficients are found in Table 12-8.

Table 12-8: Values for regression parameters to determine isothermal kinetics.

	1	2	3
For d_p < 1 mm			
a_{A1}	-17.39	52.01	-
b_{A1}	-5.36	27.10	-
a_{E1}	1.19E-03	2.14	-
b_{E1}	1.64E-04	5.10	-
For d_p > 1 mm			
a_{A2}	13.68	-90.95	147.24
b_{A2}	-8.60	36.94	-
a_{E2}	-1.44	9.85	-16.66
b_{E2}	-1.55	9.99	-16.09
c_{E2}	2.40	-15.56	30.45

Using the fitted kinetics for the isothermal model, isothermal and non-isothermal devolatilization times are compared in Figure 12-10. The deviation is generally lower than 10 %. For particles smaller than 0.5 mm, the error is larger, but they were not included in the optimization.

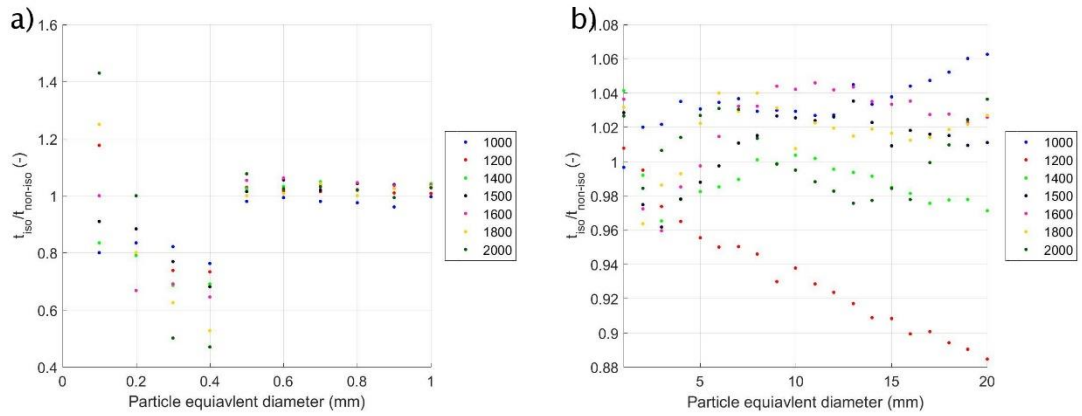

Figure 12-10: Comparison of devolatilization times predicted by isothermal and non-isothermal models using adjusted kinetics for a) $d_p < 1$ mm and b) $d_p > 1$ mm.

It should be noted that this fitting approach only shifts the devolatilization for isothermal particles to occur at higher temperatures. In this way the devolatilization time of isothermal particles is delayed to coincide with that of non-isothermal particles. It is purely a mathematic manipulation of the kinetics to make the devolatilization times match. There is no physical basis for the shape of the regression equations. In a non-isothermal particle outer layers may start devolatilization before the inner layers. This could e.g. affect ignition of the fuel. This has not been considered in this data fitting. Thus, using this approach could result in a changed onset of devolatilization between isothermal and non-isothermal particles.

G. Bed and Gas Phase Energy Balances

G.1 Energy Balance for the Bed Phase

The equation for the bed temperature is derived based on an energy balance. The balance is performed observing a control volume of length Δx in the axial direction of the kiln, as shown in Figure 8-11.

The energy entering the control volume is given by the clinker flow plus the energy contained in the clinker melt:

$$E_{in} = u_b(x) * A_b(x) * \rho_b(x) * \Delta t * [Cp_b * T_b(x) + \Delta H_{melt} * X_{melt}(x)] \quad \text{E 12.37}$$

The energy leaving the control volume is similarly given by the clinker flow:

$$E_{out} = u_b(x+\Delta x) * A_b(x+\Delta x) * \rho_b(x+\Delta x) * \Delta t * [Cp_b * T_b(x+\Delta x) + \Delta H_{melt} * X_{melt}(x+\Delta x)] \quad \text{E 12.38}$$

In the equations X_{melt} is the fraction of melt in the kiln, which is assumed to change linearly, being 0 at a certain temperature and $X_{melt,max}$ at another temperature, i.e.:

$$X_{melt} = X_{melt,max} * \frac{T_b - T_{melt,1}}{T_{melt,2} - T_{melt,1}} \quad \text{E 12.39}$$

And the rate of melt formation for later use is:

$$\frac{d}{dx} X_{melt} = \frac{X_{melt,max}}{T_{melt,2} - T_{melt,1}} * \frac{d}{dx} T_b \quad \text{E 12.40}$$

With the following limitations:

$$X_{melt} = 0 \; for \; T_b < T_{melt,1} \quad \text{E 12.41}$$

$$X_{melt} = X_{melt,max} \; for \; T_b > T_{melt,2}$$

The energy formed and consumed by reactions in the control volume is:

$$E_r = \sum_{i=1}^{N_r} R_i * \Delta H_{r,i} * A_b * \Delta x * \Delta t \quad \text{E 12.42}$$

The energy transferred to and away from the clinker bed:

$$E_{ht} = \sum_{i=1}^{N_{ht}} q_i * l_i * \Delta x * \Delta t \quad \text{E 12.43}$$

The energy lost from the clinker bed due to CO_2 release from the calcination reaction:

$$E_{loss} = R_{CO2} * H_{CO2} * A_b * \Delta x * \Delta t \quad \text{E 12.44}$$

The energy balance can now be derived by considering the balance equation:

$$Out - In = Produced \quad \text{E 12.45}$$

The equations E 12.37, E 12.38, and E 12.42-E 12.44 combine to:

$$\begin{aligned} & u_b(x+\Delta x) * A_b(x+\Delta x) * \rho_b(x+\Delta x) * \Delta t \\ & \quad * [Cp_b * T_b(x+\Delta x) + \Delta H_{melt} * X_{melt}(x+\Delta x)] \\ & \quad - u_b(x) * A_b(x) * \rho_b(x) * \Delta t \\ & \quad * [Cp_b * T_b(x) + \Delta H_{melt} * X_{melt}(x)] \\ & \quad = \sum_i^{N_r} R_i * \Delta H_{r,i} * A_b * \Delta x * \Delta t + \sum_i^{N_{ht}} q_i * l_i * \Delta x * \Delta t \\ & \quad - R_{CO2} * H_{CO2} * A_b * \Delta x * \Delta t \end{aligned} \quad \text{E 12.46}$$

The *Δt's* cancel out and the limit of the *Δx* is taken to yield:

$$\begin{aligned} & \frac{d}{dx}(u_b * A_b * Cp_b * \rho_b * T_b + \rho_b * \Delta H_{melt} * X_{melt}) \\ & \quad = \sum_{i=1}^{N_r} R_i * \Delta H_{r,i} * A_b + \sum_{i=1}^{N_{ht}} q_i * l_i - R_{CO2} * H_{CO2} * A_b \end{aligned} \quad \text{E 12.47}$$

Assuming that the bed velocity, cross sectional area, and heat capacity are constant the equation simplifies to:

$$\begin{aligned} & u_b * A_b * \left[Cp_b * \frac{d}{dx}(\rho_b * T_b) + \Delta H_{melt} * \frac{d}{dx}(\rho_b * X_{melt}) \right] \\ & \quad = \sum_{i=1}^{N_r} R_i * \Delta H_{r,i} * A_b + \sum_{i=1}^{N_{ht}} q_i * l_i - R_{CO2} * H_{CO2} * A_b \end{aligned} \quad \text{E 12.48}$$

The following rewriting is performed on the left-hand side of the equation to simplify the differential expression:

$$Cp_b * \frac{d}{dx}(\rho_b * T_b) + \Delta H_{melt} * \frac{d}{dx}(\rho_b * X_{melt}) \quad \text{E 12.49}$$

This can be rewritten using the product rule

$$Cp_b * \rho_b \frac{d}{dx}(T_b) + Cp_b * T_b \frac{d}{dx}(\rho_b) + \Delta H_{melt} * \rho_b \frac{d}{dx}(X_{melt}) + \Delta H_{melt} * X_{melt} \frac{d}{dx}(\rho_b) \quad \text{E 12.50}$$

Inserting the expression for the rate of melt change from E 12.40 and collecting the derivatives gives:

$$\left(Cp_b * \rho_b + \Delta H_{melt} * \rho_b * \frac{X_{melt,max}}{T_{melt,2} - T_{melt,1}}\right)\frac{d}{dx}(T_b) + (Cp_b * T_b + \Delta H_{melt} * X_{melt})\frac{d}{dx}(\rho_b) \quad \text{E 12.51}$$

Equation E 12.51 is now inserted into E 12.48, which yields the expression:

$$\left(Cp_b * \rho_b + \Delta H_{melt} * \rho_b * \frac{X_{melt,max}}{T_{melt,2} - T_{melt,1}}\right)\frac{d}{dx}(T_b) + (Cp_b * T_b + \Delta H_{melt} * X_{melt})\frac{d}{dx}(\rho_b) = \frac{1}{u_b * A_b}\left(\sum_{i=1}^{N_r} R_i * \Delta H_{r,i} * A_b + \sum_{i=1}^{N_{ht}} q_i * l_i - R_{CO2} * H_{CO2} * A_b\right) \quad \text{E 12.52}$$

The rate of density change is caused by decomposition of $CaCO_3$ according to:

$$\frac{d\rho_{cl}}{dx} = -\frac{1}{u_b} * R_1 * \frac{M_{CO2}}{M_{CaCO3}}\left[\frac{kg}{m^3 m}\right] \quad \text{E 12.53}$$

And the rate of CO_2 release is given as:

$$R_{CO2} = R_1 * \frac{M_{CO2}}{M_{CaCO3}}\left[\frac{kg}{m^3 s}\right] \quad \text{E 12.54}$$

The definitions of E 12.53 and E 12.54 are used in E 12.52 yielding:

$$\left(Cp_b * \rho_b + \Delta H_{melt} * \rho_b * \frac{X_{melt,max}}{T_{melt,2} - T_{melt,1}}\right)\frac{d}{dx}(T_b) - (Cp_b * T_b + \Delta H_{melt} * X_{melt}) * \frac{1}{u_b} * R_1 * \frac{M_{CO2}}{M_{CaCO3}} = \frac{1}{u_b * A_b}\left(\sum_{i=1}^{N_r} R_i * \Delta H_{r,i} * A_b + \sum_{i=1}^{N_{ht}} q_i * l_i - R_1 * \frac{M_{CO2}}{M_{CaCO3}} * H_{CO2} * A_b\right) \quad \text{E 12.55}$$

Assuming that the CO_2 has a similar constant heat capacity to that of the clinker the enthalpy for CO_2 can be written as:

$$H_{CO2} = Cp_b * T_b \quad \text{E 12.56}$$

Inserting this knowledge leads to:

$$\left(Cp_b * \rho_b + \Delta H_{melt} * \rho_b * \frac{X_{melt,max}}{T_{melt,2} - T_{melt,1}}\right)\frac{d}{dx}(T_b) = \frac{1}{u_b * A_b}\left(\sum_{i=1}^{N_r} R_i * \Delta H_{r,i} * A_b + \sum_{i=1}^{N_{ht}} q_i * l_i\right) - \left(\frac{1}{u_b} R_1 * \frac{M_{CO2}}{M_{CaCO3}} * Cp_b * T_b\right) + (Cp_b * T_b + \Delta H_{melt} * X_{melt}) * \frac{1}{u_b} * R_1 * \frac{M_{CO2}}{M_{CaCO3}} \quad \text{E 12.57}$$

And the right-hand side of the equation can be simplified to:

$$\left(Cp_b * \rho_b + \Delta H_{melt} * \rho_b * \frac{X_{melt,max}}{T_{melt,2} - T_{melt,1}}\right)\frac{d}{dx}(T_b) = \frac{1}{u_b * A_b}\left(\sum_{i=1}^{N_r} R_i * \Delta H_{r,i} * A_b + \sum_{i=1}^{N_{ht}} q_i * l_i\right) + (\Delta H_{melt} * X_{melt}) * \frac{1}{u_b} * R_1 * \frac{M_{CO2}}{M_{CaCO3}} \quad \text{E 12.58}$$

The temperature derivative can now be isolated:

$$\frac{d}{dx}T_b = \frac{1}{\left(Cp_b * \rho_b + \Delta H_{melt} * \rho_b * \frac{X_{melt,max}}{T_{melt,2} - T_{melt,1}}\right)} \frac{1}{u_b * A_b} \left(\sum_{i=1}^{N_r} R_i * \Delta H_{r,i} * A_b + \sum_{i=1}^{N_{ht}} q_i * l_i + (\Delta H_{melt} * X_{melt}) * A_b * R_1 * \frac{M_{CO2}}{M_{CaCO3}}\right) \quad \text{E 12.59}$$

The equation is further simplified to:

$$\frac{d}{dx}T_b = \frac{1}{\dot{m}_b\left(Cp_b + \Delta H_{melt} * \frac{X_{melt,max}}{T_{melt,2} - T_{melt,1}}\right)} \left(\sum_{i=1}^{N_r} R_i * \Delta H_{r,i} * A_b + \sum_{i=1}^{N_{ht}} q_i * l_i + (\Delta H_{melt} * X_{melt}) * A_b * R_1 * \frac{M_{CO2}}{M_{CaCO3}}\right) \quad \text{E 12.60}$$

If melting does not occur the equation simplifies to:

$$\frac{d}{dx}T_b = \frac{1}{\dot{m}_b Cp_b}\left(\sum_{i=1}^{N_r} R_i * \Delta H_{r,i} * A_b + \sum_{i=1}^{N_{ht}} q_i * l_i\right) \quad \text{E 12.61}$$

G.2 Energy Balance for the Gas Phase

The energy balance for the gas phase is made for the primary air jet flow. The gas phase energy balance is derived in a similar manner to that of the solids, based on Figure 8-12.

The energy entering the control volume by the gas flow:

$$E_{in} = u_g(x) * A_g(x) * Cp_g(x) * \rho_g(x) * T_g(x) * \Delta t \quad \text{E 12.62}$$

The energy leaving the control volume by the gas flow:

$$E_{out} = u_g(x + \Delta x) * A_g(x + \Delta x) * Cp_g(x + \Delta x) * \rho_g(x + \Delta x) * T_g(x + \Delta x) * \Delta t \quad \text{E 12.63}$$

The energy released by the combustion reactions:

$$E_r = \sum_{i=1}^{N_r} R_i * \Delta H_{r,i} * A_g * \Delta x * \Delta t \quad \text{E 12.64}$$

The energy transferred to and away from the gas phase:

$$E_{ht} = \sum_{i=1}^{N_{ht}} q_i * l_i * \Delta x * \Delta t \quad \text{E 12.65}$$

The energy obtained from the clinker bed due to CO_2 formed in the calcination reaction:

$$E_{CO2} = R_{CO2} * H_{CO2} * A_b * \Delta x * \Delta t = R_1 * \frac{M_{CO2}}{M_{CaCO3}} * Cp_b * T_b * A_b * \Delta x * \Delta t \quad \text{E 12.66}$$

The energy obtained from the fuel due to gas release from the fuel

$$E_{fg} = R_{fg} * H_{fg} * A_g * \Delta x * \Delta t \quad \text{E 12.67}$$

The energy obtained from the entrained secondary air:

$$E_{ent} = R_{ent} * Cp_{sec} * T_{sec} * A_g * \Delta x * \Delta t \quad \text{E 12.68}$$

The energy balance can now be derived by considering the balance equation:

$$Out - In = Produced \quad \text{E 12.69}$$

The equations can be written as:

$$\begin{aligned} & u_g(x+\Delta x) * A_g(x+\Delta x) * Cp_g(x+\Delta x) * \rho_g(x+\Delta x) \\ & * T_g(x+\Delta x) * \Delta t - u_g(x) * A_g(x) * Cp_g(x) * \rho_g(x) \\ & * T_g(x) * \Delta t \\ & = \sum_{i=1}^{N_r} R_i * \Delta H_{r,i} * A_g * \Delta x * \Delta t + \sum_{i=1}^{N_{ht}} q_i * l_i * \Delta x * \Delta t \\ & + R_1 * \frac{M_{CO2}}{M_{CaCO3}} * Cp_b * T_b * A_b * \Delta x * \Delta t + R_{fg} * H_{fg} \\ & * A_g * \Delta x * \Delta t + R_{ent} * Cp_{sec} * T_{sec} * A_g * \Delta x * \Delta t \end{aligned} \quad \text{E 12.70}$$

The Δt's cancel out and the limit of the Δx is taken to yield:

$$\frac{d}{dx}\left(u_g * A_g * Cp_g * \rho_g * T_g\right) = \sum_{i=1}^{N_r} R_i * \Delta H_{r,i} * A_g + \sum_{i=1}^{N_{ht}} q_i * l_i + R_1 * \frac{M_{CO2}}{M_{CaCO3}} * Cp_b * T_b * A_b + R_{fg} * H_{fg} * A_g + R_{ent} * Cp_{sec} * T_{sec} * A_g \quad \text{E 12.71}$$

Assuming a constant heat capacity, the derivative on the left-hand side of E 12.71 can be rewritten as:

$$\frac{d}{dx}\left(A_g * v_g * Cp_g * \rho_g * T_g\right) = Cp_g \frac{d}{dx}\left(T_g * \dot{m}_g\right) = \dot{m}_g * Cp_g \frac{d}{dx} T_g + Cp_g * T_g \frac{d}{dx} \dot{m}_g \quad \text{E 12.72}$$

Thus, the expression for the gas temperature becomes:

$$\frac{d}{dx} T_g = \frac{1}{\dot{m}_g * Cp_g}\left[\sum_{i=1}^{N_r} R_i * \Delta H_{r,i} * A_g + \sum_{i=1}^{N_{ht}} q_i * l_i * + R_1 * \frac{M_{CO2}}{M_{CaCO3}} * Cp_b * T_b * A_b + R_{fg} * H_{fg} * A_g + R_{ent} * Cp_{sec} * T_{sec} * A_g - Cp_g * T_g \frac{d}{dx} \dot{m}_g\right] \quad \text{E 12.73}$$

H. Model Parameters for Industrial Combustion Simulations

This appendix contains information of the parameter values used for the modeling of MBM, SHW, and SRF co-firing.

H.1 Standard Kiln Parameters

Data concerning the kiln size and various other properties used in the industrial scale model validation can be found in Table 12-9.

Table 12-9: Parameters for the kiln in industrial scale validation. Parameters marked by * have been assumed.

Parameter	Symbol	Unit	Value	Ref.
Dimensions				
Inner diameter of kiln	d_k	m	3.9	[83]
Outer diameter of kiln	$d_{k,o}$	m	4.4	[83]
Length of kiln	L_k	m	68	[83]
Pressure	P	Pa	101325	[83]
Radius of burner	r_{burner}	m	0.22	[83]
Location of burner tip relative to kiln clinker exit	x_{burner}	m	5	[83]
Thermal Parameters				
Ambient air temperature	T_{amb}	K	293	*
Emissivity of kiln walls	ε_w	-	0.8	[31]
Heat conductivity of clinker coating	λ_{coat}	W/(m*K)	2.7	[31]
Heat conductivity of kiln walls	λ_w	W/(m*K)	2.7	[31]
Kiln Residence Time				
Rotational speed of kiln	n	1/s	0.05	*
Kiln angle	ψ	°	2.5	*
Bed angle of repose	ξ	°	46	*
Residence time of clinker	τ	s	1838	Calc.
Coating				
Distance to which kiln coating has full thickness	$L_{coat,1}$	m	15	*
Distance where kiln coating has 0 thickness	$L_{coat,2}$	m	20	*
Kiln coating thickness	l_{coat}	m	0.25	*

Data pertaining to the kiln residence time, such as kiln inclination and rotational speed were not reported by Ariyaratne [83], thus appropriate values were assumed.

A coating with a thickness of 0.25 m is assumed to be present in the first 1 meters of the kiln. A linear decrease in thickness is assumed between 15 and 20 m, until the coating thickness is 0 m.

H.2 Standard Gas Parameters

Parameters for the inlet gas flow conditions can be found in Table 12-10.

Table 12-10: Parameters for the primary and secondary air inlet for industrial scale model validation.

Parameter	Symbol	Unit	Value	Ref.
Primary and Secondary Air				
Flowrate of primary air	$\dot{m}_{g,prim}$	kg/s	2.08	[83]
Primary air temperature	$T_{g,prim,0}$	K	323	[83]
Heat capacity of primary air	$Cp_{g,prim}$	J/(kg K)	1290	Calc.
Flowrate of secondary air	$\dot{m}_{g,sec}$	kg/s	19.4-26.1	Calc.
Standard temperature for secondary air	$T_{g,sec,0}$	K	1023	[83]
Heat capacity of secondary air	$Cp_{g,sec}$	J/(kg K)	1154	Calc.
Oxygen gas concentration in flue gas	y_{O2}	-	0.035	[84]
Burner Parameters				
Burner momentum	I	N/MW	5.8	[83]
Burner swirl number	S	-	0.261	[83]
Entrainment rate	$K_{ent,jet}$	-	0.195	Calc.
Constant for ε/k calculation	$K_{edr,1}$	1/s	101.6	Calc.
Constant for ε/k calculation	$K_{edr,2}$	-	-1.50	Calc.

The parameters are primarily based on data as reported by Ariyaratne et al. [83]. Based on the reported axial momentum and swirl number, the entrainment constant rate and constants for the eddy dissipation rate can be calculated. The oxygen concentration at the kiln inlet is attempted maintained at 3.5 %, and the secondary airflow is changed to match this, based on the oxygen requirements of the fuel (see appendix D). The secondary air flows and oxygen concentrations for the MBM, SHW, and SRF simulation cases can be found in Appendices H.5-H.7.

The heat capacities of the two gas streams are assumed constant. The value for secondary air is calculated for atmospheric air at the inlet temperature 1023 K, and the heat capacity for the primary air is calculated at 1200 K.

H.3 Standard Parameters for Fuel

The standard values for various fuel properties can be found in Table 12-11. MBM and SHW are assumed to have the same properties as the biomass, except for the density, which is changed to 1354 kg/m^3 for MBM and 620 kg/m^3 for SHW.

Table 12-11: Standard parameters for fuels used in the simulations.

		Coal		**Biomass**		**Plastic (solid/ liquid)**	
Parameter	Unit	Value	Ref.	Value	Ref.	Value	Ref.
Kinetics							
A_{dry}	1/s	5.13*10^6	[31]	5.13*10^{10}	[236]	5.13*10^{10}	[236]
Ea_{dry}	kJ/mol	87.9	[31]	88	[236]	88	[236]
ΔH_{evap}	kJ/kg	2257	[260]	2257	[260]	2257	[260]
A_{devol}	1/s	9.59*10^4	[31]	1.11*10^{11}	[255]	4.8*10^{22}	[232]
Ea_{devol}	kJ/mol	82.6	[31]	177	[255]	3.49*10^5	[232]
ΔH_{devol}	kJ/kg	0		0		365	[232]
$A_{char,ox}$	kg/(m^2*Pa*s*)	1*10^{-2}	[31]	2.54*10^{-3}	[256]	-	
$Ea_{char,ox}$	kJ/mol	105	[31]	81.6	[257]	-	
$A_{char,gsc}$	m/s	-		3.42*T_{char}	[258]	-	
$Ea_{char,gsc}$	kJ/mol	-		130	[258]	-	
A_{melt}	1/s	-		-		2.17*10^{44}	[232]
Ea_{melt}	kJ/mol	-		-		353	[232]
ΔH_{melt}	kJ/kg	-		-		207	[232]
Others							
λ_f	W/(m*K)	-		0.12	[255]	-	
ε_f	-	0.9	[31]	0.9	[31]	Depends on particle	[232]
ρ_f	kg/m^3	1336	[31]	600	[86]	950	[232]
Cp	J/(Kg K)	1400	[31]			1900/2200	[232]
Cp_1	J/(Kg K)	-		2300	[259]	-	
Cp_2	J/(Kg K)	-		1000	[259]	-	

For biomass, MBM, and SHW the fuel heat capacity is calculated based on the fuel ash content:

$$Cp_f = (1 - w_{ash})Cp_1 + w_{ash}Cp_2 \quad \text{E 12.74}$$

H.4 Standard Parameters for Clinker

The standard parameters for the clinker bed used in the kiln model can be found in Table 12-12.

Table 12-12: Standard parameters for the clinker/kiln bed. Parameters marked by * have been assumed.

Parameter	Symbol	Unit	Value	Ref.
Heats of reactions				
Heat of reaction for limestone calcination	ΔH_{R1}	kJ/(kg $CaCO_3$)	1780	[217]
Heat of reaction for alite formation	ΔH_{R2}	kJ/(kg C2S)	-732	[217]
Heat of reaction for belite formation	ΔH_{R3}	kJ/(kg C3S)	59.0	[217]
Heat of reaction for aluminate formation	ΔH_{R4}	kJ/(kg C3A)	-33.5	[217]
Heat of reaction for ferrite formation	ΔH_{R5}	kJ/(kg C4AF)	-38.8	[217]
Melting Parameters				
Temperature where clinker starts to melt	$T_{melt,1}$	K	1553	[217]
Temperature where clinker is fully molten	$T_{melt,2}$	K	1723	[217]
Heat of clinker melt	ΔH_{melt}	kJ/ (kg clinker)	600	[217]
maximum fraction of clinker melt	$X_{melt,max}$	-	0.2	*
Physical Parameters				
Heat capacity of clinker bed	Cp_b	J/(kg*K)	1500	[201]
Emissivity of clinker bed	ε_b	-	0.8	[183]
Thermal conductivity of clinker bed	λ_b	W/(m*K)	0.5	[198]
Bulk density of clinker bed	ρ_b	kg/m³	1200	[201]
Calcination degree at kiln raw material inlet	-	-	0.965	[82]

H.5 Parameters for MBM Simulations

Additional parameters used in the MBM co-firing simulations are shown in Table 12-13. These show the calculated secondary air flows and temperatures, and the oxygen mole fraction at the kiln clinker inlet. The secondary air temperatures are calculated based on the simplified cooler model described in Appendix J.

Table 12-13: Flows of fuel and secondary air with secondary air temperature and oxygen concentration (mol%) in flue gas for the MBM simulations.

Case	Coal Flow	MBM Flow	Secondary Air Flow	Secondary Air Temperature	y_{O2} kiln clinker inlet
	kg/s	kg/s	kg/s	°C	%
1	2.2	0.0	23.1	750	3.5
2	1.8	0.6	24.0	717	3.4
3	1.5	1.1	25.1	680	3.3
4	1.3	1.4	25.2	671	3.2
5	1.1	1.7	25.8	654	3.2
6	0.9	1.9	26.1	642	3.1
7	0.9	1.9	26.1	642	3.1

The applied particle sizes are shown in and Table 12-14.

Table 12-14: Particle diameter of coal and MBM particles used in simulations.

Particle Group	Coal	MBM
	µm	µm
1	2	38
2	5	118
3	10	208
4	16	311
5	23	431
6	32	576
7	44	756
8	61	999
9	87	1,375
10	172	2,478

H.6 Parameters for SHW Simulations

Additional parameters used in the SHW co-firing simulations are shown in Table 12-15.

Table 12-15: Flows of fuel and secondary air with secondary air temperature and oxygen concentration (mol%) in flue gas for the SHW simulations.

Case	Coal Flow	SHW Flow	Secondary Air Flow	Secondary Air Temperature	y_{O2} kiln clinker inlet
	kg/s	kg/s	kg/s	°C	%
1	2.1	0.0	21.8	750	3.5
2	1.9	0.1	20.8	763	3.5
3	1.9	0.3	20.7	763	3.5
4	1.8	0.4	20.7	762	3.5
5	1.6	0.6	19.4	786	3.5
6	1.6	0.7	19.9	774	3.5
7	1.6	0.7	20.9	759	3.5
8	1.6	0.7	20.9	756	3.5
9	1.6	0.8	21.1	749	3.5
10	2.1	0.0	21.1	762	3.5

The applied particle sizes are shown in and Table 12-16.

Table 12-16: Particle diameter of coal and SHW particles used in simulations.

Particle Group	Coal	SHW
	µm	µm
1	2	327
2	5	848
3	10	1,218
4	16	1,567
5	23	1,921
6	31	2,299
7	43	2,725
8	58	3,239
9	83	3,945
10	160	5,621

H.7 Parameters for SRF Simulations

Additional parameters used in the SRF co-firing simulations are shown in Table 12-17.

Table 12-17: Flows of fuel and secondary air with secondary air temperature and oxygen concentration (mol%) in flue gas for the SRF simulations.

Case	Coal Flow	SRF Flow	Biomass Flow	Plastic Flow	Secondary Air Flow	Secondary Air Temperature	y_{O2} kiln clinker inlet
	kg/s	kg/s	kg/s	kg/s	kg/s	°C	%
1	2.2	0.0	0.0	0.0	23.1	750	3.5
2	2.0	0.4	0.2	0.1	23.4	738	3.5
3	1.7	0.8	0.5	0.2	23.6	723	3.5
4	1.5	1.2	0.7	0.2	23.8	708	3.4
5	1.3	1.6	0.9	0.3	24.0	697	3.4
6	1.1	2.0	1.2	0.4	24.2	687	3.4
7	0.9	2.4	1.4	0.5	24.4	678	3.4
8	0.7	2.8	1.6	0.5	24.6	671	3.4
9	0.4	3.2	1.9	0.6	24.8	665	3.3
10	0.2	3.5	2.1	0.7	25.0	659	3.3
11	0.0	3.9	2.4	0.8	25.3	655	3.3

The applied particle sizes are shown in and Table 12-18.

Table 12-18: Particle diameter of coal and SRF particles used in simulations.

Particle Group	Coal	Biomass	Plastic
	µm	µm	µm
1	2	1.0E+03	1.0E+03
2	5	2.8E+03	2.4E+03
3	10	3.9E+03	3.5E+03
4	16	4.3E+03	4.1E+03
5	23	6.6E+03	6.8E+03
6	32	1.3E+04	9.7E+03
7	44	-	-
8	61	-	-
9	87	-	-
10	172	-	-

I. Details of Combustion Simulations

In chapter 9, the free lime content has been shown as the result of simulations. In addition, select temperature profiles of the gas and bed have been shown, to further explain the differences observed in the various simulation cases. However, many additional parameters are calculated by the model. This appendix contains a more in-depth discussion of select parameters calculated by the model. As an example, further discussions are made for the coal case simulations from the MBM and SRF test scenario and the 30 % SRF energy input co-firing scenario.

I.1 Details of Coal Combustion Simulation

Figure 12-11 shows the calculated temperatures through the kiln for the coal simulations case of Test 1-1. The kiln burner is protruding 5 meters into the kiln. As soon as the air and fuel leave the burner it is quickly heated by radiation and entrainment of the secondary air, which initiates the devolatilization of the coal. The combustion of volatiles increases the temperature to around 2200 °C.

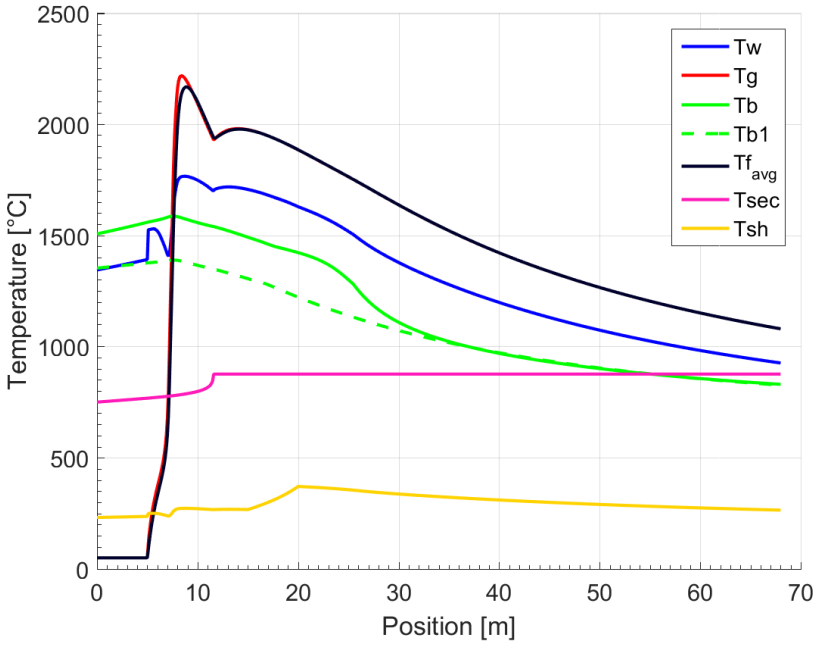

Figure 12-11: Temperatures through the kiln of the wall, gas, bed (without clinker reactions as dashed line), fuel average temperature, secondary air, and outer shell.

After the initial peak, the temperature decreases as remaining secondary air, which is now colder than the flame, is entrained into the flame. The entrainment is complete at around 11 m, where the temperature begins to increase again. A second

peak is seen as the coal char is combusted at around 15 m from the kiln burner end. Afterwards, the temperature decreases as heat is transferred to the clinker bed and lost to the surroundings. The gas and average fuel temperatures are very similar, due to the small size of the coal particles.

The secondary air temperature increases slightly during the first 12 meters of the kiln. The secondary air is assumed to be radiatively clear, as it only consists of oxygen and nitrogen. Thus, it is assumed to only be heated by convection which is a slower mode of heat transfer than radiation. At 12 meters, all the secondary air is entrained. The temperature change is no longer tracked, and the temperature is thus shown as constant in Figure 12-11.

The pre-calcined raw meal is admitted from the other end of the kiln. The temperature is initially only increasing slowly. 30 meters from the burner end the bed temperature increases rapidly, due to the exothermic formation of belite (C_2S). The temperature continues to increase reaching a maximum around 1600 °C at 7-8 m from the clinker outlet. The bed temperature then decreases as heat is transferred to the secondary air, to the walls and to the burner tip. For the sake of comparison, the dashed green line shows the bed temperature without clinker reactions. It is seen that the exothermic formation of belite has a high impact on the temperature in the bed.

The wall temperature is seen to initially change very drastically. Since the wall temperature is only determined based on a heat balance based on the heat transfer to the wall and heat transfer through the wall, it has no thermal inertia. Consequently, the temperature can change drastically in the axial direction. For the 5 initial meters of the kiln, the burner tip is exposed. The burner is assumed to have the same temperature as the secondary air, and an emissivity similar to that of the kiln walls (0.9). At this point the temperature of the wall is between that of the bed and secondary air. After the 5 m, the wall temperature quickly approaches that of the bed. The primary air initially has an emissivity and absorptivity of 0, since no water or CO_2 is present. Thus, the heat transfer between the wall and bed will dominate the wall temperature, and it obtains a temperature close to that of the bed. As water and CO_2 is released during the fuel devolatilization and combustion, radiation between the wall and primary air jet becomes more influencing, and the wall temperature ends up in between that of the bed and the gas.

Lastly, Figure 12-11 also shows the temperature of the outer kiln shell. It is seen to generally follow the trend of the kiln wall temperature. Between 15 and 20 m the shell temperature increases rapidly. A kiln coating of 25 cm thickness is assumed to be present in the initial 15 m of the kiln, which reduces the heat loss and shell temperature. At 15 m, the kiln coating thickness begins to decrease reaching a thickness of 0 m at 20 m. As the coating thickness decreases, the heat transfer through the wall increases, and the shell temperature is increased.

Figure 12-12 shows the different clinker phases through the kiln. The position is made to be consistent with Figure 12-11, thus the figure has the raw meal inlet on the right-hand side, and the clinker travels left through the kiln.

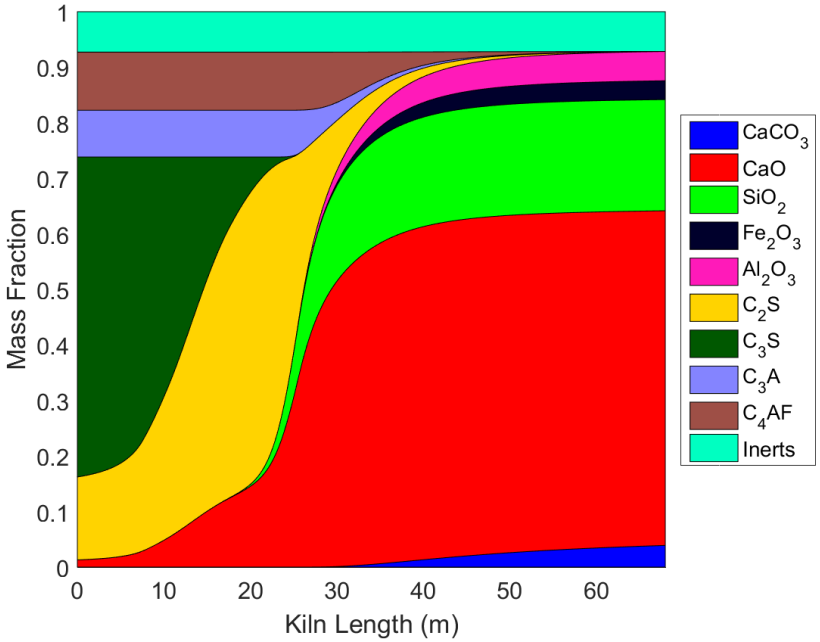

Figure 12-12: The mass fraction of the different clinker phases through the kiln.

The pre-calcined raw meal enters the kiln at a temperature of 830 °C. Some residual $CaCO_3$ is left. In the kiln the limestone slowly decomposes, and is fully converted at 30 m, where the temperature of the bed is around 1100 °C. The formation of C_3A and C_4AF starts almost immediately, but the formation rate increases between 30-40 m, where the temperature is between 1000 and 1100 °C. This consumes all the Fe_2O_3 and Al_2O_3 and some of the CaO.

C_2S is rapidly formed from the 30 m mark, where the temperature is around 1100 °C. The SiO_2 is consumed, and the CaO content also decreases rapidly. The formation of C_2S is exothermic, and the reaction quickly increases the bed temperature. At

around 20 m from the clinker outlet, the concentration of C_2S reaches its maximum, as C_3S begins to form. The formation of C_3S occurs rapidly from 20 m, where the temperature is above 1400 °C and plenty of CaO is available. In the last 5 m of the kiln, the formation rate decreases as the most of the CaO has been used, and the temperature is lowered.

The concentration of the gasses N_2, O_2, CO_2, H_2O, CH_4, and CO through the kiln are shown in Figure 12-13. The oxygen concentration is seen to decrease sharply at around 7 m, where the coal devolatilization and volatile combustion occurs. The oxygen concentration then slightly increases from 8 to 12 m, as the secondary air is entrained into the flame. From 12 m, the concentration slowly decreases as char oxidation of the larger coal particles take place.

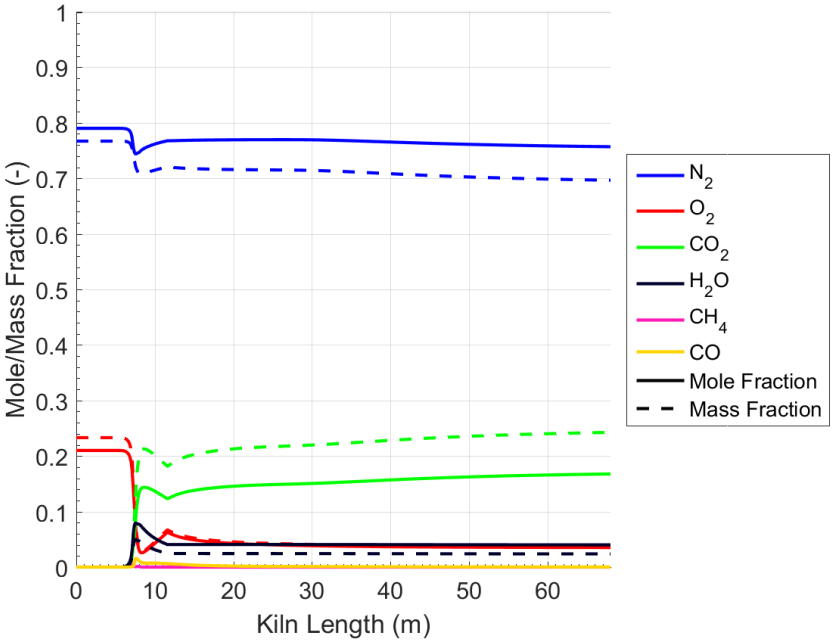

Figure 12-13: The mole and mass fraction of N_2, O_2, CO_2, H_2O, CH_4 and CO through the kiln for a coal fired simulation.

The CO and CH_4 concentration are seen to have a small spike at around 8 m due to the rapid devolatilization. However, the gasses are quickly combusted, and the concentration decrease to 0. H_2O is seen to be mainly formed at around 8 m, due to the combustion of CH_4. CO_2 is also increased rapidly as CO and CH_4 is oxidized. The CO_2 concentration keeps increasing after 12 m due to oxidation of the remaining char, but also caused by the decomposition of $CaCO_3$ in the bed.

Figure 12-14 shows the temperatures and conversion of each of the 10 discrete particle size classes. The smallest particles have a diameter of 1.6 µm and the largest 170 µm. All particles, except the largest, are heated very quickly and almost follow the gas temperature.

The drying and the conversion of the particles occur rapidly within 10 m, due to the fast heating rate of the small particles. The size does not have a large impact on this. The char oxidation is seen to occur rapidly for the 5 smallest particle groups, where they are fully converted within 10 m. The largest particle group takes much longer to be converted, and full conversion is not reached in the kiln.

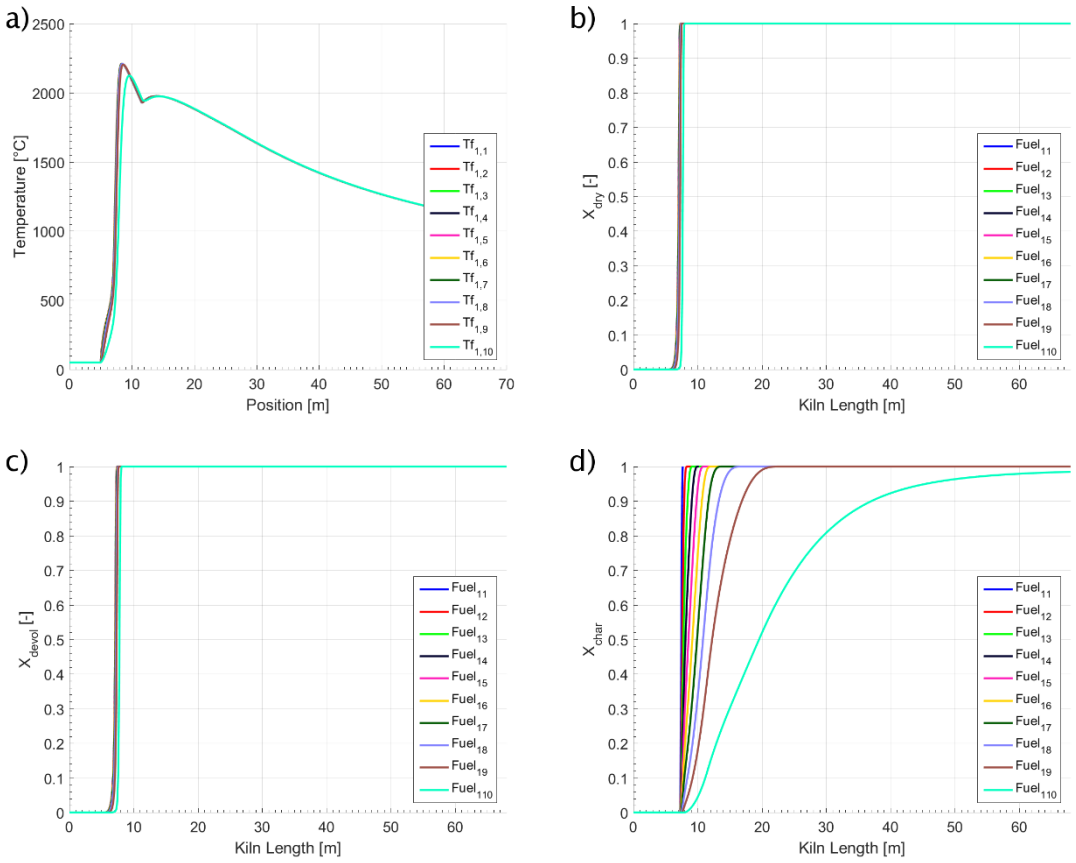

Figure 12-14: Temperatures (a), extent of drying (b), extent of devolatilization (c), and extent of char oxidation (d) for the 10 discrete particle size classes of coal particles.

I.2 Details of SRF Co-Firing Simulation

In this chapter additional details of the SRF co-firing scenario, with 30 % SRF by energy, are discussed. The trends of the graphs are similar to those explained in Appendix I.1, and only the major differences will be described.

Figure 12-15 shows the different temperatures through the kiln. It is noticed how the peak temperature is decreased compared to the coal case. Instead the peak gas temperature occurs at around 25 m, which is after the largest particles of SRF have been converted.

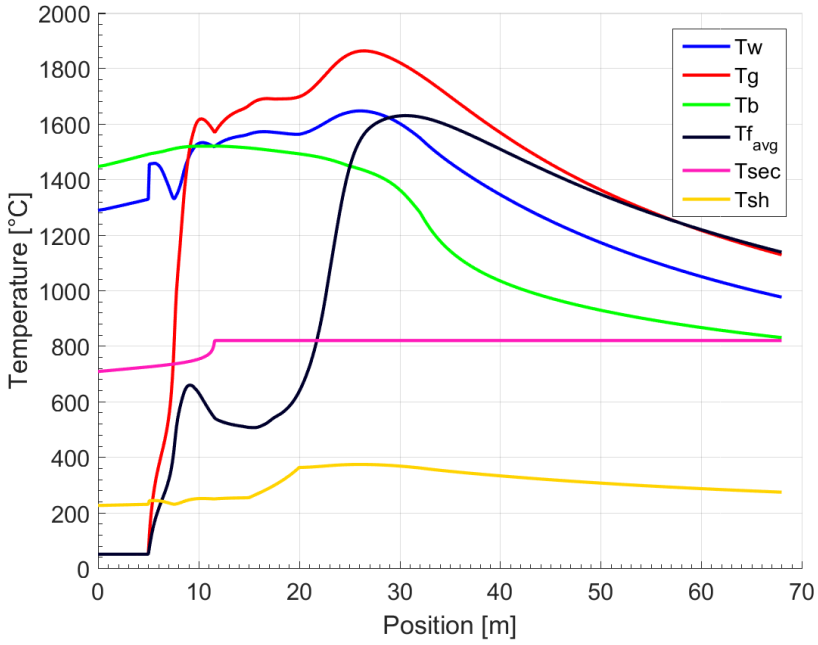

Figure 12-15: Temperatures through the kiln of the wall, gas, bed fuel average temperature, secondary air, and outer shell.

The average fuel temperature in Figure 12-15 is also significantly different. It only approaches the gas temperature after 25 m, where only the ash particles are remaining, which results in a rapid heating. Initially, an increase is seen in the average fuel temperature followed by a decrease. The temperature is a mass-based average. Initially, the coal particles are quickly heated, which increases the average temperature. However, as the coal particles lose mass during the combustion, the average temperature becomes dominated by the SRF particles, which are only heated slowly.

The clinker phase composition is shown in Figure 12-16. Compared to the coal case, belite is formed earlier, from around the 35 m mark. This is caused by a more rapid heating of the bed, due to higher gas temperatures at the clinker inlet.

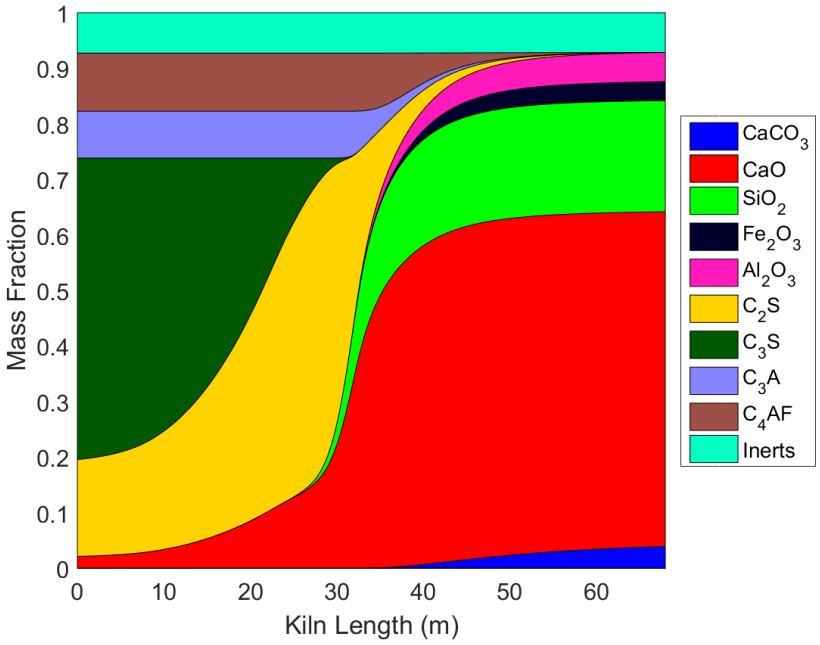

Figure 12-16: The mass fraction of the different clinker phases through the kiln.

Figure 12-17 shows the various gas concentrations accounted for in the kiln model. The main difference to the coal case is a slower consumption of oxygen due to the slower combustion rate of the alternative fuels. Furthermore, the water concentration is higher at 7.5 mol% compared to 4.0 mol% in the coal case. This is caused by the high water content in the SRF of 20 wt% compared to 1 wt% in coal.

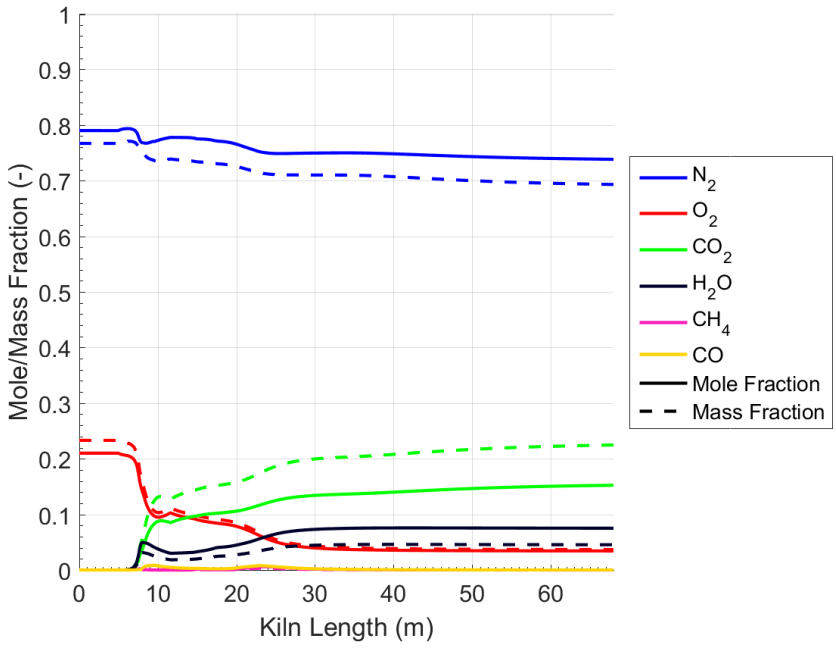

Figure 12-17: The mole and mass fraction of N_2, O_2, CO_2, H_2O, CH_4 and CO through the kiln for a coal fired simulation.

The fuel temperatures and conversion of the coal particles, biomass particles, and plastic particles are shown in Figure 12-18, Figure 12-19, and Figure 12-20. The temperatures of the coal particles follow the gas temperatures. The drying and devolatilization occurs rapidly, and char oxidation is only slow for the larger coal particles.

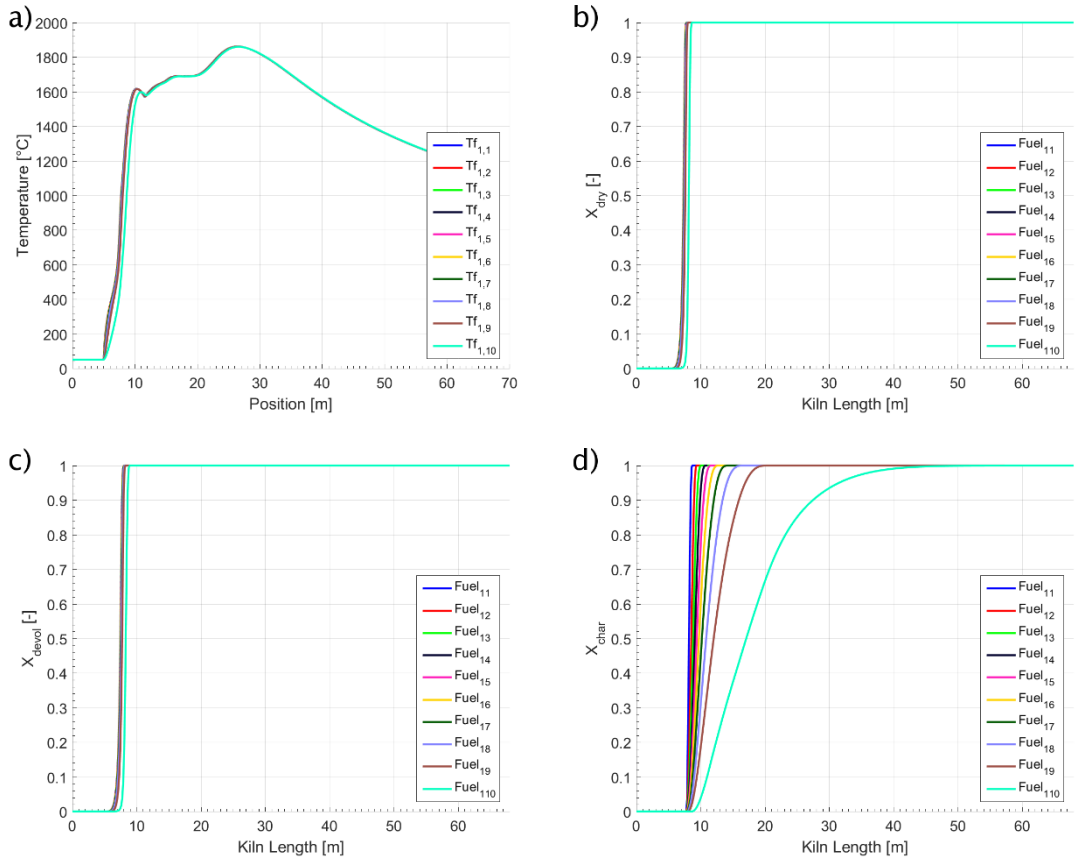

Figure 12-18: Temperatures (a), extent of drying (b), extent of devolatilization (c), and extent of char oxidation (d) for the 10 discrete particle size classes of coal particles.

The temperatures and conversion of the biomass particles in the SRF are shown in Figure 12-19. The markers in the graphs indicate the location where the fuel particles drop into the bed. The biomass particles are initially heated slowly, due to their high water content. It is only when the water has been evaporated that the temperatures increase more rapidly, which leads to devolatilization of the two smallest particle size groups. It is only the two smallest particle groups that undergo devolatilization, while they are in suspension, and only the smallest group, where the char is also oxidized to some extent. The inflection point on the char conversion graph, indicates when the particles enter the bed. These particles groups

correspond to the fines and the particles with a terminal velocity lower than 2 m/s, as determined in the wind sieve. The larger particles are converted, as they enter the clinker bed.

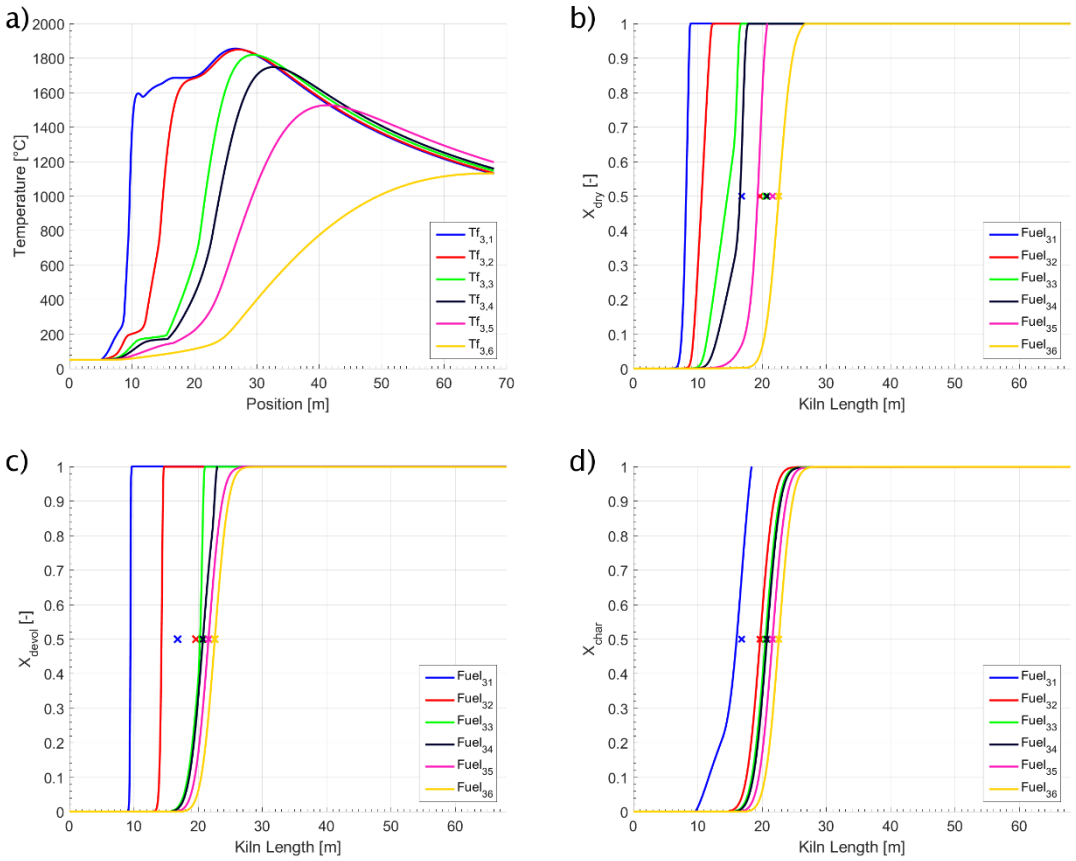

Figure 12-19: Temperatures (a), extent of drying (b), extent of devolatilization (c), and extent of char oxidation (d) for the 6 discrete particle size classes of biomass particles in SRF. 'x'-markers indicate the distance of fuel landing in the clinker bed.

The temperatures and conversion of the plastic particles of the SRF are shown in Figure 12-20. The curves are somewhat similar to those seen for the biomass temperatures and conversion. The drying of the plastic particles take slightly longer, as they undergo melting while they are drying, which also requires energy. Only the smallest particle group is fully devolatilized while in suspension. These correspond to the fines (<2 mm) separated from the wind sieve. The other particle groups are devolatilized as they enter the clinker bed, as indicated by the location of the markers.

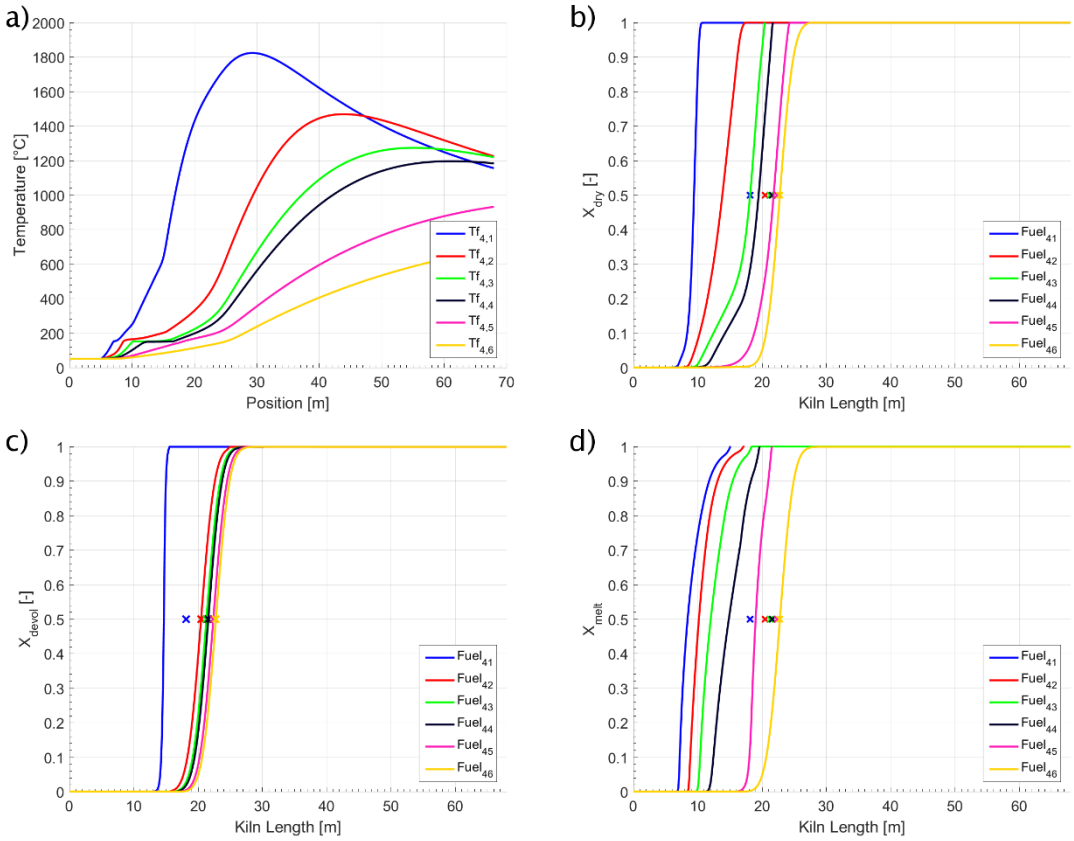

Figure 12-20: Temperatures (a), extent of drying (b), extent of devolatilization (c), and extent of melting (d) for the 6 discrete particle size classes of plastic particles in SRF. 'x'-markers indicate the distance of fuel landing in the clinker bed.

J. Model for the Clinker Cooler

The temperature and flow of the clinker that leaves the kiln has a direct impact on the heat recuperation in the clinker cooler, and the secondary air temperature. The secondary air temperature is used as an inlet condition to the model. Thus, one of the outlet conditions (the bed temperature) is coupled to one of the inlet conditions (the secondary gas temperature). To describe the impact, a simple model for the clinker cooler is developed.

Modern clinker coolers are grate coolers, see Figure 12-21, which function as a form of cross-flow cooler. The clinker is moved along the cooler by reciprocating grates. Meanwhile cooling air is forced through the bed, cooling the clinker and heating the air, which is used as secondary air in the kiln [33,261].

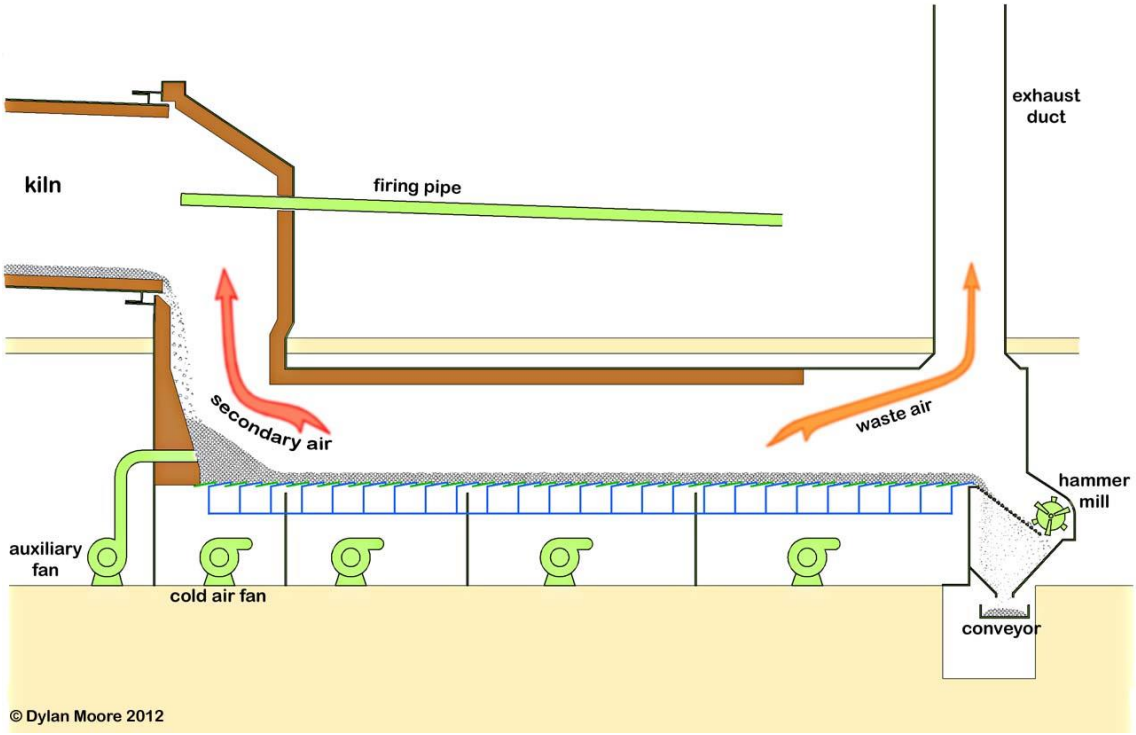

Figure 12-21: A grate cooler in a cement plant. The clinker is moved forward by reciprocating grates. Cooling air is forced through the clinker bed by air fans. The heated air is used as secondary air in the cement kiln [33].

Modeling of the clinker cooler is discussed by e.g. Ahmad et al. [261], Mujumdar et al. [262], and Touil et al. [263], but a simpler approach is pursued here.

A simplified model of the cooler can be obtained by dividing the cooler into a number, N_{cooler}, of segments as shown in Figure 12-22. In each segment the clinker moves in the axial x-direction, while gas moves in the vertical y-direction. The

clinker enters the cooler at a temperature of $T_{b,in}$ and is cooled in each segment by the gas flow, and exits the cooler at a temperature of $T_{b,out}$.

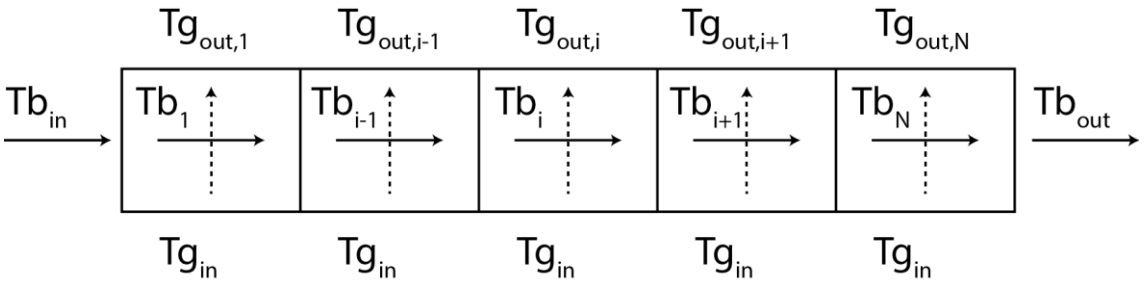

Figure 12-22: Sketch of a simplified cooler model divided into N_{cooler} segments.

As a simplification it will be assumed that the clinker temperature is constant in each segment, while only the gas temperature increases in the y-direction. Thus, the following temperature equation can be formulated for the gas temperature in a given segment (assuming constant heat capacity and flow).

$$\frac{dT_{g,i}(y)}{dy} = \frac{1}{F_{g,i} * Cp_g} * h_{conv} * \left(T_{b,i} - T_{g,i}(y)\right) * l_{gb} \qquad \text{E 12.75}$$

$F_{g,i}$ is the gas mass flow in the i'th segment, Cp_g the gas heat capacity, h_{conv} the convective heat transfer coefficient, and l_{gb} is the contact area between gas and bed per unit height of the bed [m²/m].

Since neither the value of l_{gb} or h_{conv} is known, they are combined into a single constant H_{cooler} [W/m/K], which is the cooler heat transfer coefficient.

$$\frac{dT_{g,i}(y)}{dy} = \frac{1}{F_{g,i} * Cp_g} * H_{cooler} * \left(T_{b,i} - T_{g,i}(y)\right) \qquad \text{E 12.76}$$

If the segments are small enough the bed temperature in each segment can be assumed constant. The bed temperature in one segment will be assumed equal to the outlet temperature of the previous segment. The temperature difference between the inlet and outlet of a section can be found from a heat balance considering the heat transfer in the segment.

$$T_{b,i} = T_{b,out,i-1} = T_{b,i-1} - \frac{Q_{ht,i-1}}{F_b * Cp_b} \qquad \text{E 12.77}$$

The heat transfer in the segment can be calculated based on the gas flow and temperature of the segment:

$$Q_{ht,i} = \left(T_{g,out,i} - T_{g,in}\right) * F_{g,i} * Cp_g \quad \text{E 12.78}$$

The differential equation in E 12.76 can be solved directly to yield the gas temperature through the y-direction of the segment:

$$T_{g,i}(y) = T_{b,i} - exp\left(\frac{-H_{cooler}}{F_{g,i} * Cp_g} * y\right)\left(T_{b,i} - T_{g,in}\right) \quad \text{E 12.79}$$

It is assumed that the clinker bed height is constant through the cooler with a value of 0.8 m [264]. If this value is inserted into E 12.79, then it is possible to determine the gas outlet temperature of the i'th segment.

J.1 Determining the Cooler Heat Transfer Coefficient

The main form of heat transfer in the cooler is convection when the gas is forced through the bed. The convective heat transfer coefficient is a function of Reynolds and Prandtl number [262,263]. However, here the cooler heat transfer coefficient, H_{cooler}, will be assumed constant in all segments of the cooler. Furthermore, it is only desired to model the first part of the cooler, in order to determine the secondary air temperature.

To determine the value of the heat transfer coefficient, a base case is needed to calibrate the model. For this is it is needed to know corresponding values of the inlet and outlet temperatures. The coal fired model validation case Test 1-1 (see chapter 9.2) is used as the calibration case. The conditions for this case are given in Table 12-19. For this case the bed inlet temperature to the cooler is calculated in the kiln model to 1506 °C. The inlet temperature of the gas is assumed to be 25°, and the secondary air temperature is given as 750 °C. The outlet temperature of the bed can be calculated using an overall heat balance via equations E 12.77 and E 12.78, assuming 1 stage in the cooler.

Table 12-19: Cooler conditions for the calibration calculations based on coal validation case Test 1-1.

	Mass Flow	Inlet Temperature	Outlet Temperature	Heat Capacity
	kg/s	°C	°C	J/kg/K
Bed	39.1	1506	1176	1500
Gas	23.2	25	750	1154

In the following an example using 5 segments of the clinker cooler is shown. The secondary air temperature is equal to the average of outlet temperatures from each segment. Thus, the optimal value of H_{cooler} can be found by a trial and error method to minimize the value of the equation:

$$abs\left(T_{sec} - \frac{1}{N_{cooler}} * \sum_{i}^{N_{cooler}} T_{g,out,i}\right) \qquad \text{E 12.80}$$

Figure 12-23 shows the value of E 12.80 as a function of H_{cooler} and it is determined that a value of around $5.2*10^3$ results in the correct temperature of the gas leaving the cooler.

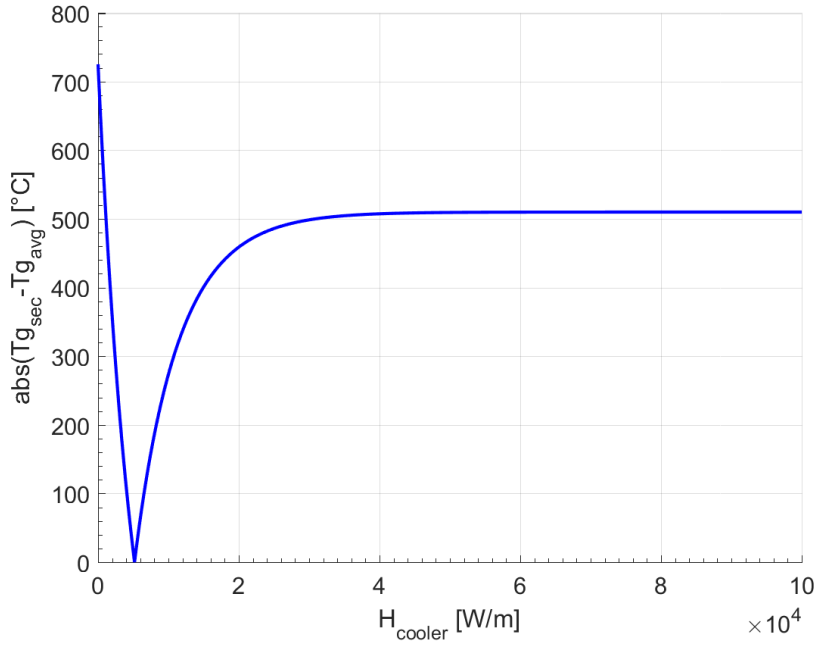

Figure 12-23: Absolute difference between the secondary air temperature and the average air temperature out of the cooler as function of H_{cooler}.

Using the optimal value of clinker cooler heat transfer coefficient, H_{cooler}, the temperature through each segment of the cooler can be calculated. Figure 12-24 shows the gas and bed temperatures through each segment of a clinker cooler divided into 5 segments. The gas temperature is seen to increase through each segment, while the bed temperature in each segment is fixed. The average outlet temperature of the five gas streams is 750 °C.

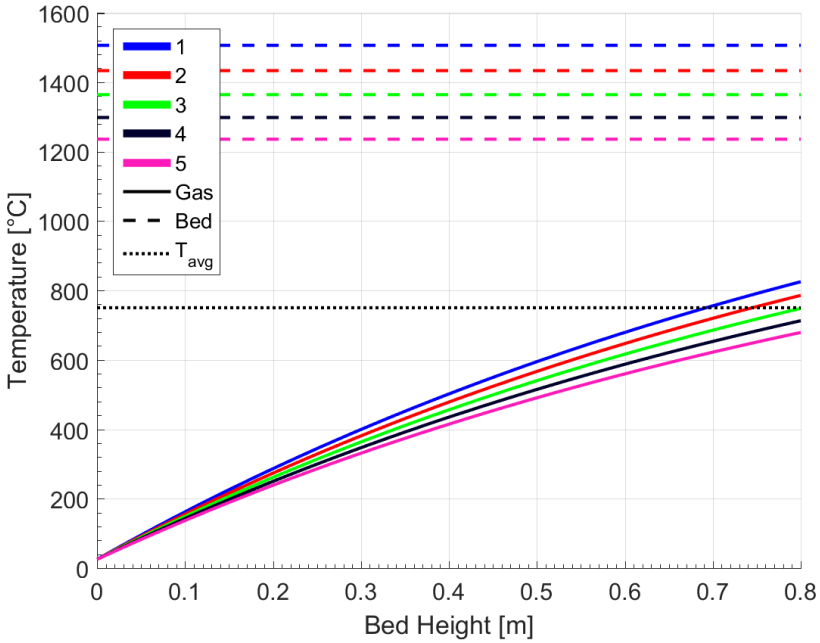

Figure 12-24: The gas temperatures (solid lines) through the 5 bed segments, with bed temperatures (dashed lines) and the average gas outlet temperature (dotted line).

Using the calibrated value of the heat transfer coefficient, it is possible to calculate different values of the secondary air temperature if there are changes in the temperature of the clinker from the kiln, the flow of the clinker, or the flow of secondary air.

In this example the clinker cooler was divided into 5 segments. In the actual simulations, 1000 segments are used. With this number of segments, the temperature of the clinker decreases by less than 1 °C in each segment, and the assumption of constant temperature is acceptable.

Department of Chemical and Biochemical Engineering - CHEC
Technical University of Denmark
Søltofts Plads, Building 229
2800 Kgs. Lyngby
Denmark
Phone: +45 45 25 28 00
Web: www.kt.dtu.dk